AD-A251 843

PAGE

1. AGENCY USE ONLY (Leave blank)	2. REPORT DATE April 23, 1992	3. REPORT TYPE AND DATES COVERED Final REport July 1990 – April 1991

4. TITLE AND SUBTITLE
The Unsteady Aerodynamics of a Delta Wing Undergoing
Large Amplitude Pitching Motions

5. FUNDING NUMBERS
PE: 61102F 2307 / CS

AFOSR-90-0321

6. AUTHOR(S)
Dr. Robert C. Nelson and Dr. Scott A. Thompson

7. PERFORMING ORGANIZATION NAME(S) AND ADDRESS(ES)
Hessert Center for Aerospace Research, Building 66
Department of Aerospace and Mechanical Engineering
University of Notre Dame
Notre Dame, INDIANA 46556

8. PERFORMING ORGANIZATION REPORT NUMBER

AFOSR-TR· 92 0500

9. SPONSORING / MONITORING AGENCY NAME(S) AND ADDRESS(ES)
AFOSR / NA
Building 410
Bolling AFB, DC 20332-6448

NA

10. SPONSORING / MONITORING AGENCY REPORT NUMBER

AFOSR-90-0321

11. SUPPLEMENTARY NOTES

DTIC
ELECTE
JUN 17 1992
S C D

12a. DISTRIBUTION / AVAILABILITY STATEMENT

Unlimited

12b. DISTRIBUTION CODE

13. ABSTRACT (Maximum 200 words)

The goal of this study was to examine the relationship between the aerodynamic loads and the vortex flow characteristics of a highly swept delta wing (70° sweep) undergoing both steady and unsteady pitching motions. The effects of several parameters were examined, including motion amplitude, pitching frequency, Reynolds number, and leading edge geometry.

The unsteady surface pressure data could be separated into two regimes dependent on the angle of attack range: a regime where quasi-steady behavior occurred, and a regime where significant unsteady effects occurred. The first regime included angle of attack ranges which precluded the occurrence of vortex breakdown, and ranges for which breakdown existed on the wing throughout the motion. The second regime included angle of attack ranges where breakdown moved onto or off of the wing, and ranges which included very high angles of attack involving full scale leeward flow separation.

For the second regime, the unsteady effects occurred in the form of a hysteresis in the surface pressures relative to the steady case. It appeared that either the onset of breakdown or the reformation of the vortex system (at very high incidences) was responsible for the unsteady effects.

14. SUBJECT TERMS
Unsteady Aerodynamics   Dynamic Stall
Slender Wings
Flow Visualization

15. NUMBER OF PAGES
243

16. PRICE CODE

17. SECURITY CLASSIFICATION OF REPORT	18. SECURITY CLASSIFICATION OF THIS PAGE	19. SECURITY CLASSIFICATION OF ABSTRACT	20. LIMITATION OF ABSTRACT
Unclassified	Unclassified	Unclassified	Unclassified

FOREWORD

This report consists of the doctoral dissertation of Scott A. Thompson. The dissertation is submitted as the final contract report for the research effort entitled "The Unsteady Surface Pressure on a Delta Wing Undergoing an Unsteady Pitching Maneuver." The research was sposored by the Air Force Office of Scientific Research, Bolling Air Force Base, during the period from January 1990 to May 1992, under research grant AFOSR-90-0321. Major Daniel Fant and Captain Henry Helin were the technical monitors.

THE UNSTEADY AERODYNAMICS OF A DELTA WING UNDERGOING LARGE
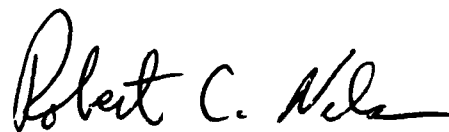AMPLITUDE PITCHING MOTIONS

A Dissertation

Submitted to the Graduate School

of the University of Notre Dame

in Partial Fulfillment of the Requirements

for the Degree of

Doct of Philosophy

by

Scott A. Thompson, B.S.M.E., M.S.A.E.

<u>*Robert C. Nelson*</u>

Dr. Robert C. Nelson, Director

Department of Aerospace and Mechanical Engineering

Notre Dame; Indiana

April, 1992

THE UNSTEADY AERODYNAMICS OF A DELTA WING UNDERGOING LARGE

AMPLITUDE PITCHING MOTIONS

Abstract

by

Scott A. Thompson

An experimental wind tunnel investigation was performed using a series of 70°
sweep delta wings. The goal was to examine the relationship between the aerodynamic
loads and the vortex flow characteristics of a highly swept wing undergoing both steady
and unsteady pitching motions. Extensive testing was conducted consisting primarily of
the measurement of surface pressure and vortex breakdown location as functions of angle
of attack. The effects of several parameters were examined, including motion amplitude,
pitching frequency, Reynolds number, and leading edge geometry. The data obtained was
then correlated to data from the literature on the aerodynamic loads and the surface flow
characteristics for similar wings. The effects of wing size and blockage were also
examined.

The steady and unsteady flow visualization data indicated that the trailing edge of
the wing significantly influences the smooth forward or aft motion of breakdown when
breakdown is near the trailing edge. The data indicated that this may be caused by the
pressure gradient downstream of the wing.

Scott A. Thompson

The unsteady surface pressure data could be separated into two regimes, dependent on the angle of attack range: a regime where quasi-steady behavior occurred, and a regime where significant unsteady effects occurred. The first regime included angle of attack ranges which precluded the occurrence of vortex breakdown, and ranges for which breakdown existed on the wing throughout the motion. The second regime included angle of attack ranges where breakdown moved onto or off of the wing, and ranges which included very high angles of attack involving full scale leeward flow separation

For the second regime, the unsteady effects occurred in the form of a hysteresis in the surface pressures relative to the steady case. Lags in the unsteady breakdown location relative to the steady location were also measured. It appeared that either the onset of breakdown or the reformation of the vortex system (at very high incidences) was responsible for the unsteady effects.

The size of the model relative to the wind tunnel was seen to affect the magnitude of the surface pressure coefficients. However, the qualitative trends were not changed significantly.

TABLE OF CONTENTS

LIST OF TABLES

LIST OF FIGURES

NOMENCLATURE

Symbols

c   = root chord length, in., mm

f   = dimensional pitch rate, Hz

k   = nondimensional (or reduced) pitch frequency, $k = \dfrac{2\pi fc}{U}$

P   = pressure, lb/in^2, Pa

q   = freestream dynamic pressure, $q = \frac{1}{2}\rho U^2$

s   = trailing edge span length, in., mm

t   = dimensional time, s

t*   = nondimensional time, $t^* = \dfrac{t}{\Delta t}$

U   = freestream velocity, ft/s, m/s

v   = absolute speed of vortex breakdown, ft/s, m/s

x   = distance from apex of model parallel to the root chord, in., mm

y   = distance from root chord of model parallel to the trailing edge, in., mm

z   = perpendicular distance from surface of model, in., mm

Greek Symbols

α = angle of attack, deg.

ε = bluff body blockage factor (from Maskell, 1963)

γ = $\cos^{-1}(\cos\alpha\,\sin\Lambda)$, deg.

μ = viscosity of freestream air, lb/ft s, kg/m s

θ = angle vortex core makes with wing surface, deg.

ρ = density of freestream air, lb/ft^3, kg/m^3

Δt = temporal duration of a pitching maneuver, s

Abbreviations

A/D = analog to digital

C_p = pressure coefficient, $C_p = \dfrac{P_{tap}-P_\infty}{q_\infty}$

C_{Pc} = corrected pressure coefficient (from Maskell, 1963)

LVDT = linear variable differential transformer

Re = Reynolds number, based on root chord for a delta wing, $Re = \dfrac{\rho U c}{\mu}$

rpm = revolutions per minute

SCR = silicon control rectifier

Subscripts

∞ = Denotes freestream condition

o = Denotes stagnation condition

tap = Denotes conditions at a pressure orifice

total = Denotes stagnation condition

ACKNOWLEDGEMENTS

I   INTRODUCTION

1.1   Prologue

In September 1930 the Fifth Volta Conference was held in Rome, Italy; the topic was "High Velocities in Aviation." At this conference, a German engineer named Dr. Adolph Busemann officially introduced the concept of a swept wing aircraft. This idea was considered valuable enough that within a year of this conference the German Luftwaffe had designated the swept wing concept as a classified military secret. Dr. Busemann proposed that by sweeping the wing (that is, putting the leading edge at an angle relative to the flow direction), compressibility effects over the wing could be delayed and the high speed wave drag could be reduced (Greenwood, 1989).

During the next year, 1931, a small machine designed by another German engineer, Dr. Alexander Lippisch, was flown for the first time. This event proved to be significant in that it was the first flight of a practical delta wing aircraft. Dr. Lippisch's aircraft utilized trailing edge ailerons and wing tip rudders, and was powered by a 31 horsepower engine with a pusher-type propeller (Lippisch, 1981; Gibbs-Smith, 1970). This aircraft is shown in Fig. 1.1.

Like Dr. Busemann, Dr. Lippisch was interested in increasing flight speeds. Although Dr. Busemann is typically credited with originating the concept of a swept wing (Heiman, 1963), Dr. Lippisch had been experimenting with swept wing aircraft and tailless aircraft for several years before the flight in 1931, all in an attempt to reduce aerodynamic drag and produce higher flight velocities (Lippisch, 1981).

This desire to increase flight speeds could be found in many sectors of the aviation industry during this time. Manufacturing methods were improved, and higher quality steel and lighter weight aluminum began to be available to the aircraft industry. The all metal airplane came into widespread use. Streamlining was emphasized, and with it engine

1

nacelles, cockpit cowling, and retractable landing gear were all introduced. Maximum thrust could be obtained at a variety of flight conditions by the use of variable pitch propellers. The development of aviation engines also advanced, and with more powerful engines came the potential for faster flight speeds. Trailing edge flaps were implemented to allow for lift retention at low speeds (Gibbs-Smith, 1970).
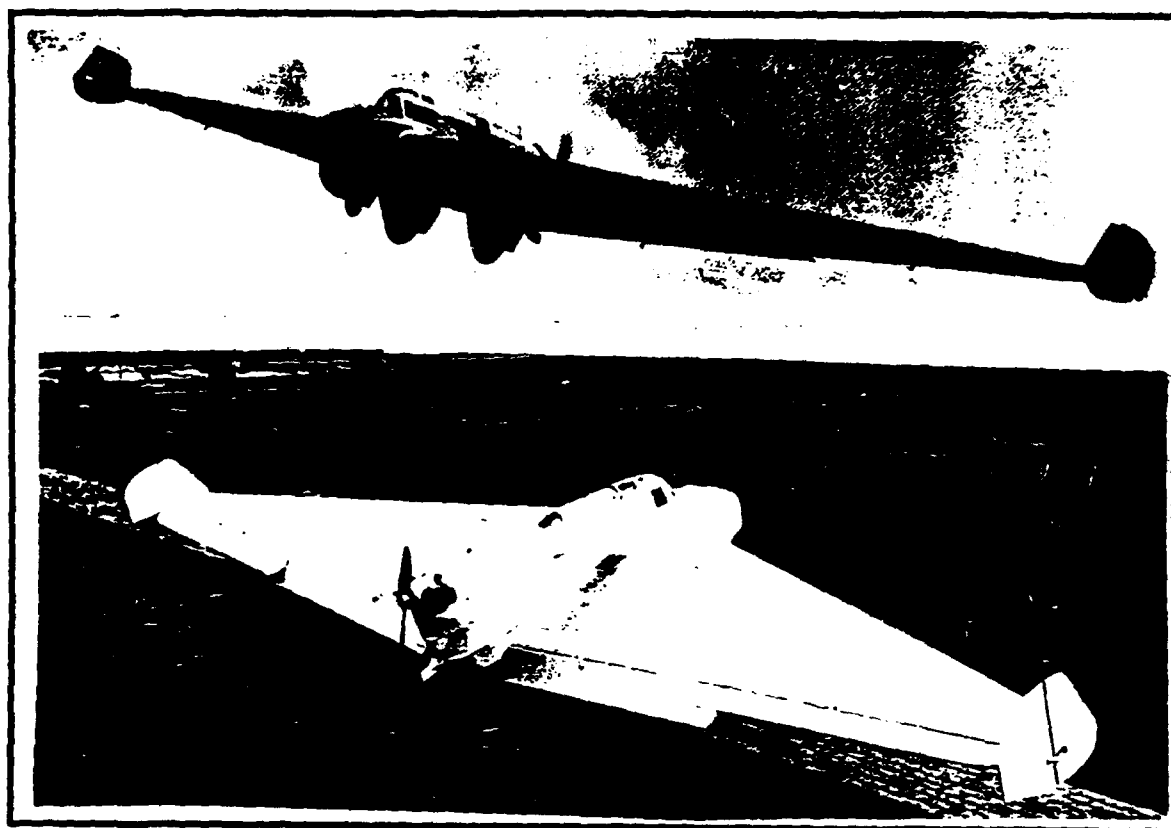
Figure 1.1   Photographs of *Delta I* (1931); in flight and on the ground. Photos from Lippisch, 1981.

The 1931 flight of Dr. Lippisch's delta wing aircraft was evidence of the practicality of swept- and delta wing aircraft; however, this concept was not exploited to its fullest potential until the development of the jet engine in the early 1940's. The jet engine made transonic flight speeds more easily attainable. The first experimental turbojet airplane was the German Heinkel He 178, flown in August of 1939. This was followed by an Italian Caproni-Campini in 1940, a British Gloster E28/29 in 1941 (developed by Frank Whittle), and a German Messerschmitt Me 262 in 1942. When the latter plane entered service in 1944 it was the first practical jet airplane, using two axial flow turbojets and having a top speed of 525 mph (Gibbs-Smith, 1970). Now that aviation propulsion was capable of transonic speeds, the amount of research investigations on triangular delta wings and swept rectangular wings soon began to increase.

The desire for increased speed, maneuverability and efficiency have characterized the evolution of manned flight. These goals have resulted in the use of swept wings and highly swept wing extensions. This trend has currently reached a point where flight envelopes are beginning to encompass very high angles of attack; and it is in the high angle of attack regime where swept wings have unique characteristics. This flight regime is frequently encountered during the landing and takeoff portions of a flight, and in the case of military applications, during combat maneuvering. Combat flight maneuvers such as velocity vector turning, fuselage axis reversal, and nose pointing (point-and-shoot) involve high angle of attack excursions. These types of maneuvers typically belong to the category of "supermaneuverability," a term that implies control of an airframe at and beyond stall angles. The unsteady aerodynamics at such angles are difficult to quantify or predict. Considering the current and future emphasis of these flight regimes, and that both maneuvering flight and high angle of attack flight are intrinsically transient, the understanding of the influence of unsteady motions on swept wing performance is essential.

1.2   Fundamentals of Steady Delta Wing Aerodynamics

A delta wing refers to a wing whose planform resembles an isosceles triangle, with the apex of the wing pointing into the freestream flow. In 1929, when Dr. Lippisch first designed a flying wing with a triangular planform, the aircraft was designated the *Delta I* (Lippisch, 1981). Successive versions of this aircraft over the next five years were also given this name (each with a different numerical designation). It is from the name given to these early airplanes that the term "delta" wing evolved. It was subsequently picked up by H. J. Stewart in his paper regarding the analytic evaluation of the supersonic lift characteristics of a delta wing (Stewart 1946). The term was then used by A. Robinson in several papers involving the analytic evaluation of the supersonic characteristics of delta wings. (Robinson; May 1946, Sept. 1946, Oct. 1947, Dec. 1947). Within a few years the term "delta wing" was commonplace for referring to a wing with a triangular planform.

When considering the capability of a swept wing aircraft at large angles of attack, the presence of the leading edge vortices must be taken into account. This understanding can be furthered by the study of simple delta wings. The flow phenomenon observed over simple delta wings is representative of that seen for many airframes currently in use, including the NASA space shuttle and several U.S. military aircraft. In addition, current design concepts for the National Aerospace Plane (NASP) and the high speed civil transport employ delta wing planforms.

At small angles of attack, the flow over a delta wing resembles the flow over a flat plate or a conventional wing. However, as the angle of attack increases, two large scale, stable vortices are formed over the suction surface of the wing. These vortices lie roughly along a straight line from the apex to the trailing edge. The angle of attack at which these vortices first form is primarily a function of the wing sweep angle. The sweep angle is typically defined as 90° minus half the included apex angle.

The vortices are formed due to the flow separation that occurs at the sharp leading edge. At moderate angles of attack, the incoming flow impinges on the pressure surface of the wing and is swept outboard towards the leading edge. When the leading edge is encountered, the flow separates from the wing surface. A free shear layer is formed which wraps over the leading edge to a position above the suction side of the wing. This shear layer then rolls into a vortex. This occurs from both of the leading edges, resulting in two counter-rotating vortices. The freestream flow moving over these vortices is entrained and drawn towards the surface of the wing. This flow attaches to the wing and is swept downstream and outboard, beneath the leading edge vortices (also known as the primary vortices). The adverse pressure gradient between the primary vortex and the leading edge is sufficient to cause this flow to separate, resulting in a second vortex beneath each primary vortex. This secondary vortex is typically smaller and weaker than the primary, rotates in a direction opposite to the primary vortex above it, and occupies a position beneath and outboard of the primary. The main effect of the secondary vortices is to displace the primary vortices inboard and upward. This system of vortices can exist in a coherent state up to very high angles of attack (Payne, 1987). A schematic of this vortex system is shown in Fig. 1.2.

Angle of Attack

Flat Plate Sharp-Edged Delta Wing

Primary Vortex ———
Secondary Vortex ———
Feeding Sheet ———
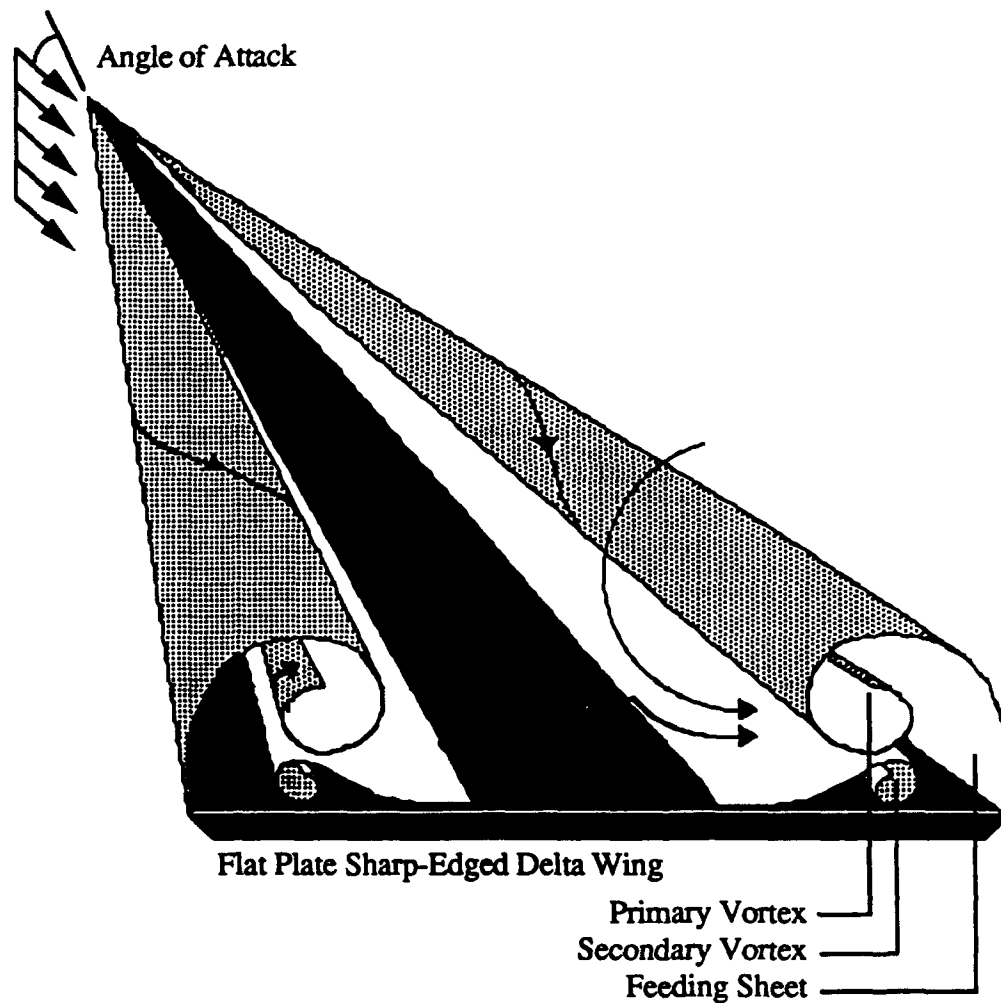
Figure 1.2   Schematic of Leading Edge Vortex Formation on a Flat Plate Sharp-Edged

Delta Wing.

The leading edge vortices account for the high lift coefficient achieved by a delta

wing at a large angle of attack. The velocity of the fluid within the vortices causes a

significant decrease in the surface pressure, hence the large lift (Wilson, 1947). This lift

increment can result in stall angles for simple delta wings as high as 35°. Figure 1.3 shows

the lift coefficient as a function of angle of attack for a series of three sharp-edged delta

wings. Wings with leading edge sweep angles of 60°, 70°, and 80° are shown. Note that

the stall angle varies from 30-40° angle of attack. Also shown on Fig. 1.3 is the angle of attack at which vortex breakdown crosses the trailing edge. O'Neil et al. (1989) found that this angle was well correlated with the stall angle for wings with sweep angles greater than 70°. As shown in Fig. 1.3, breakdown occurs over the 60° wing at an angle considerably smaller than the stall angle.
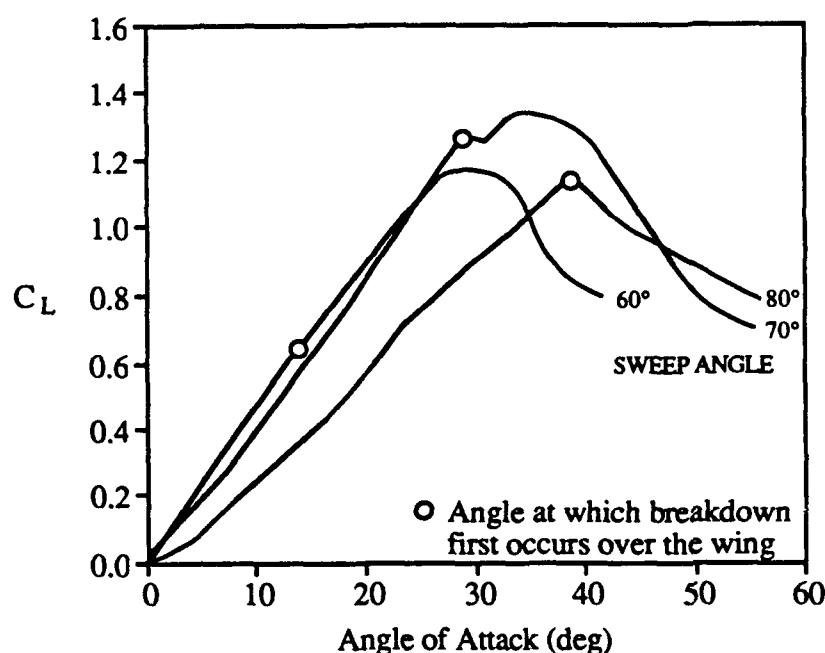
Figure 1.3   Lift Coefficient for a Thin, Sharp-Edged Delta Wing. Three Sweep Angles Shown. Data from O'Neil et al., 1989

The additional lift due to the leading edge vortices is typically known as vortex lift or nonlinear lift. The difference between the two is shown in Fig. 1.4. The total lift has been defined by Polhamus (1971) to be the sum of the potential lift and the vortex lift increment. This method is referred to as the leading edge suction analogy. The nonlinear

lift increment is also shown in Fig. 1.4 to demonstrate the difference. Additional discussion of this figure can be found in Hemsch and Luckring (1990). Note that the curve shown in Fig. 1.4 has been calculated for a 75° sweep delta wing at a Mach number near zero.
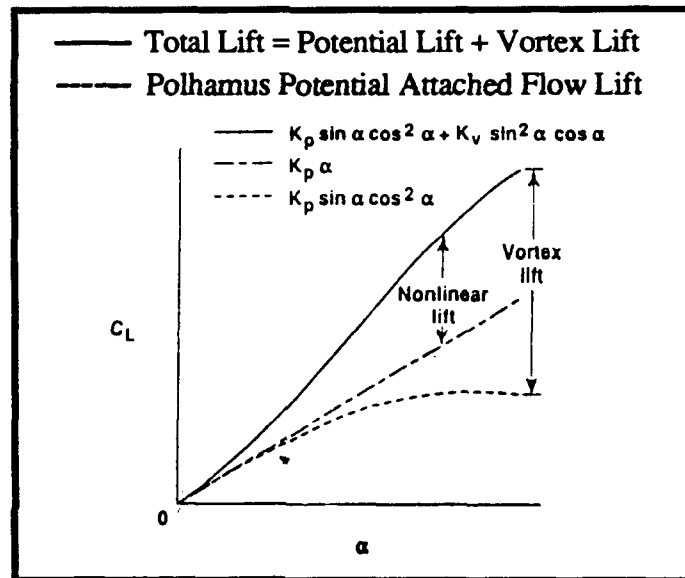
Figure 1.4   Vortex and Nonlinear Lift. Figure from Hemsch and Luckring, 1990

The character of a flat plate delta wing flowfield is typically considered to be a strong function of the angle of attack and the angle of sweep of the wing. The wing thickness and leading edge geometry are additional factors. However, the dependence on Reynolds number (typically defined using the wing centerline or root chord length) is not as strong. This is due to the fact that the primary flow separation point is fixed at the leading edge, regardless of Reynolds number (this is typical for sharp leading edges at angle of attack). However, some Reynolds number effect has been detected in the shape,

edge definition, and velocity gradients of the free shear layer forming off the sharp leading edge (Earnshaw, 1961). In addition, the secondary separation point (on the suction surface of the wing), as well as the transition of the secondary surface flow from laminar to turbulent, does depend on the Reynolds number (Lee, 1951). The transition of the secondary flow to turbulent flow moves the primary vortices downward and outboard (Erickson, 1981; Thompson, 1985; Carcaillet, Manie, Pagan, and Solignac, 1986). This Reynolds number sensitivity is then reflected in the strength and location of the secondary vortices, and thus influences (although to a much lesser extent) the primary vortices.

This effect on the primary and secondary vortices in turn influences the surface pressure distribution. The suction peak due to the primary vortex is more defined for the turbulent case since the primary core lies closer to the wing surface. In addition, the secondary vortex is smaller for the turbulent case and thus its effect on the surface pressure distribution is decreased (Hummel, 1978). For the laminar case the suction peak due to the secondary vortex can overlap the peak due to the primary vortex, in effect smearing the distinct suction peak seen in the turbulent case. However, the aerodynamic loads such as lift and moment do not change substantially with Reynolds number, particularly compared to stronger factors such as incidence and wing sweep (Hummel, 1978; Erickson, 1981; O'Neil et al., 1989).

1.3   Vortex Breakdown

At sufficiently large angles of attack the leading edge vortices undergo a transition known as vortex breakdown or vortex bursting. The flow in the vortex undergoes an abrupt deceleration of the axial velocity, an increase in its diameter, and an expansion around a stagnation point (Lambourne and Bryer, 1961). Upstream of the breakdown, the vortex core is tightly bound; downstream the vortex is swirling and highly turbulent. However, the "vortex" continues to be stable and organized. Figure 1.5 shows two

examples of vortex breakdown. The photograph on the left shows a top view of a simple 65° delta wing with the leading edge vortex cores visualized by dye. Vortex breakdown is occurring for both the left and right side vortices. The photograph on the right shows an in-flight F-16 aircraft at angle of attack. The leading edge vortices formed by the leading edge extensions (or strakes) have been visualized by natural condensation. Breakdown is occurring near the apex of the strakes thus the majority of the vortices appears turbulent.
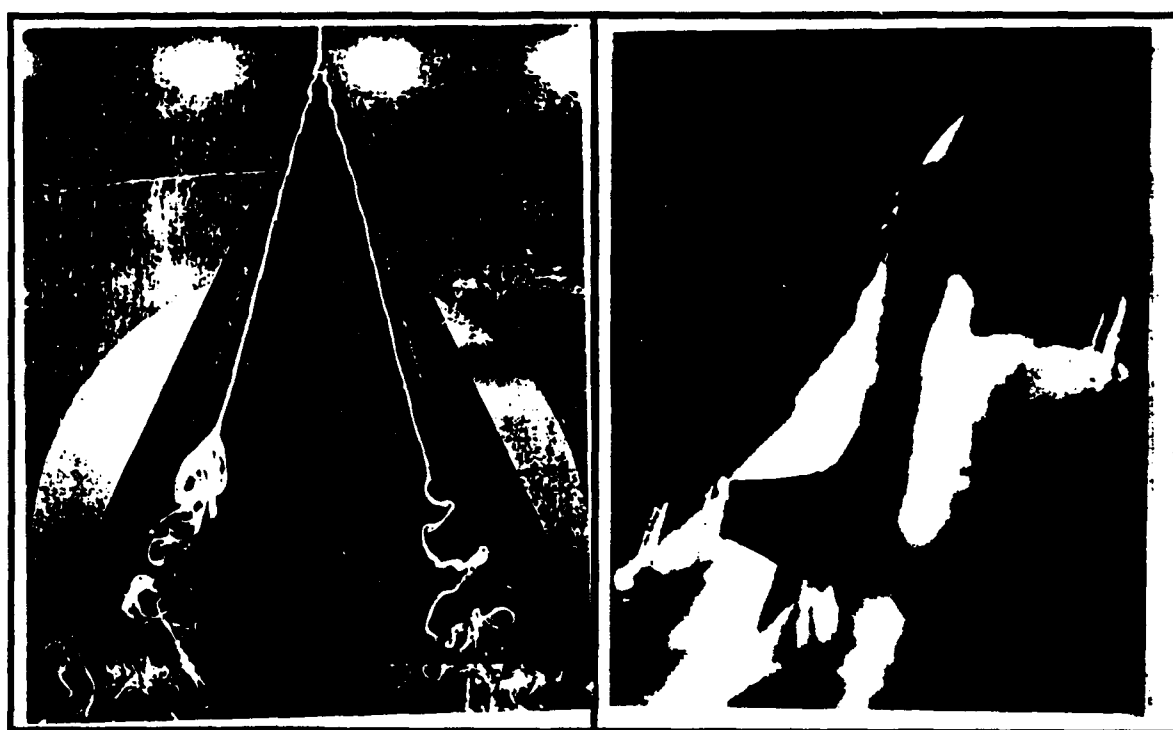
Figure 1.5   Photographs of Leading Edge Vortex and Vortex Breakdown occurring over a Simple Delta Wing and a Swept Wing Aircraft (F-16). Delta Wing Photograph from Lambourne and Bryer, 1961. F-16 Photograph from NASA High-Angle-of-Attack Technology Conference, 1990.

The angle of attack at which this occurs depends on the sweep angle, and to lesser extent, the wing thickness and leading edge shape. The breakdown of the two leading edge vortices can occur symmetrically or asymmetrically. Breakdown first occurs near the trailing edge, then moves forward with increasing incidence (Elle, 1958). When breakdown reaches the vicinity of the apex, a further increase in incidence will result in the loss of a coherent vortex field over the wing, leading to total separation of the flow. At this point the leeward surface flow resembles a bluff body type of wake.

Figure 1.6 shows the breakdown location as a function of angle of attack for a series of three sharp-edged delta wings. Data for wings with three leading edge sweep angles is shown. These data clearly show the forward progression of the breakdown with
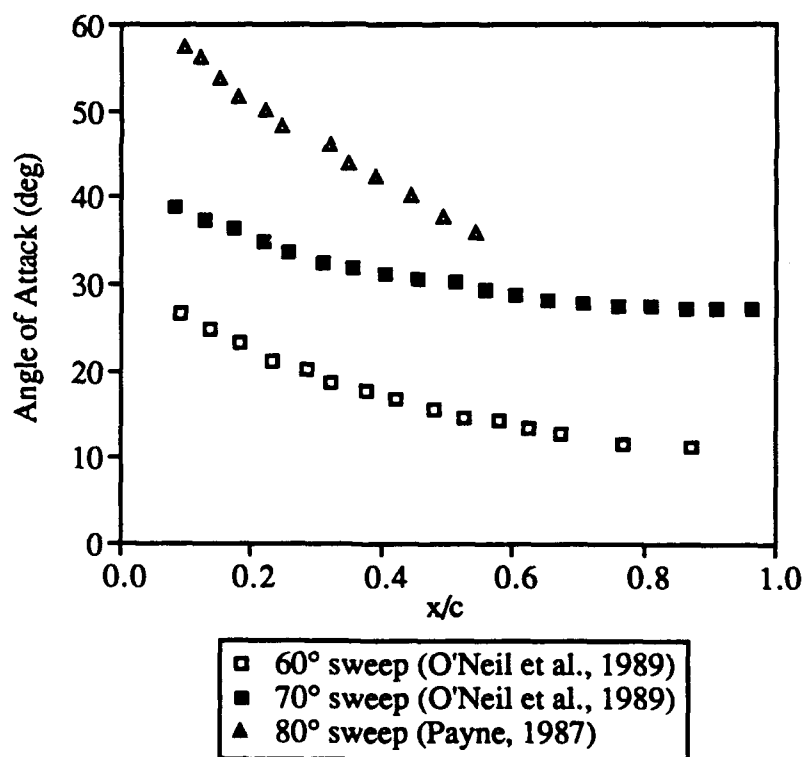
Figure 1.6   Steady Vortex Breakdown Location for a Sharp-Edged Delta Wing. Three Sweep Angles Shown

increasing incidence. Note that an increase in sweep angle results in a higher angle of attack necessary for the onset of breakdown. Also, breakdown of the left and right side vortices can be asymmetrically located for wings with sweep angles greater than 80°; only data for the left side vortex is shown in Fig. 1.6.

Vortex breakdown typically takes place over a small area rather than at a point. It has been seen to be sensitive to downstream pressure gradient and leading edge geometry (Hummel and Srinivasan, 1967; Kegelman and Roos, 1989; Earnshaw and Lawford, 1964; Ng and Malcolm, 1990). Furthermore, the breakdown has been seen to oscillate fore and aft for a steady wing attitude. The amount of this oscillation is typically within three to five percent of the root chord length (LeMay, 1988; Thompson, Batill, and Nelson, 1991).

The effect of Reynolds number on vortex breakdown is unclear. The majority of researchers have concluded that the breakdown is insensitive to Reynolds number (Lambourne and Bryer, 1961; Wolffelt, 1986; Magness, Robinson, and Rockwell, 1989; Roos and Kegelman, 1990). However, some researchers have documented a Reynolds number effect (Lambourne and Bryer, 1961; Earnshaw, 1968; LeMay, Batill, and Nelson, 1990).

The type of Reynolds number effect seen was typically a discrete change in the breakdown location due to the increase of Reynolds number beyond a critical value. In other words, the breakdown location was insensitive up to a certain Reynolds number, at which a change in location occurred, then it was insensitive again. This type of behavior suggests a flow transition or a change in the development of the flow. The Reynolds number at which this has been seen varies among the sources in the literature by an order of magnitude and is probably a function of several factors including model geometry, angle of attack, freestream turbulence level, and Mach number (Elsenaar and Hoeijmakers, 1990).

This effect of Reynolds number on breakdown location is possibly due to the secondary flow characteristics. The transition of the secondary separation from laminar to

turbulent is dependent on Reynolds number. It is also known that the trajectory of the primary vortices is effected by the secondary flow. It has also been documented that the occurrence of breakdown and the location of the secondary separation line (Lambourne and Bryer, 1961) are interrelated. Thus it stands to reason that the transition of the secondary flow could alter the change in breakdown position for sufficiently high angles of attack.

Another interesting characteristic of vortex breakdown is the existence of a steady hysteresis in breakdown location. At a given incidence, the location of breakdown over the wing can be different depending on whether the wing has been brought up or down to that angle of attack. This is typically seen near the angle at which breakdown first appears over the wing; that is, angles where breakdown is near the trailing edge. This type of behavior has been documented for changes in attitude in both yaw (Elle, 1961) and pitch (LeMay, Batill, and Nelson, 1988).

1.4   Research on Steady Delta Wing Aerodynamics

Presented in this section is a synopsis of the some of the pioneering research on steady delta wing aerodynamics. Representative research investigations from the end of World War II through the 1980's are summarized. Some of these are presented to illustrate the advancement of knowledge, while others are presented due to their applicability to the current investigation.

Among the first researchers to identify some of the fundamental characteristics of delta wing aerodynamics were Wilson and Lovell. In 1947 they conducted an experimental investigation using a German glider with a 60° sweep delta wing. They made the following observations, which would prove to be the foundation of delta wing research:

- At moderate angles of attack the upper surface flow field is dominated by two large scale vortices produced by the sharp leading edge.

- The presence of these leading edge vortices maintains an orderly flow over the wing even at large angles of attack.

- As a result of this orderly flow, delta wings are capable of generating large lift coefficients relative to wings with conventional planforms. However, the corresponding angle of attack is much larger for a delta wing than for a conventional wing.

The development of the leading edge vortices was also described by G. H. Lee in 1955, who used a 70° sweep wing in a low speed wind tunnel. Lee also conducted a series of surface flow visualization experiments to examine the effect of Reynolds number on the leeward surface flow. Angles of attack up to 34.5° were used. Lee found that the only apparent effect of Reynolds number was a change in the location of the secondary separation line; otherwise the Reynolds number effects were not substantial over the range of 100,000-500,000.

In 1958, B. J. Elle conducted an experiment using full- and half-span delta wings with sweep angles from 60°-76°. Using smoke visualization, Elle recorded the vortex core trajectory for various angles of attack. He was also one of the first researchers to note the high angle of attack existence of vortex breakdown. He recorded the general appearance of the breakdown area, as well as its upstream movement with increasing incidence.

One of the first efforts to obtain comprehensive surface pressure measurements for a delta wing was conducted by Peckham in 1958. Using a wind tunnel he examined twelve flat plate, swept wings (a combination of gothic [a swept wing with a continuously curved leading edge] and delta wings) and three thick simple delta wings. Peckham obtained extensive surface pressure distributions over a wide range of angles of attack, and

calculated the centers of pressure. He found that both increasing aspect ratio and increasing thickness move both the secondary separation line and the suction peak outboard.

Static pressure distributions were taken through and along the vortex by Lambourne and Bryer in 1959. They made measurements on a 65° sweep wing using a five-tube pressure probe. A favorable pressure gradient was measured along the vortex core, as well as an increasing axial velocity (in the streamwise direction). Axial core velocities as high as three times the freestream were measured. Also, in 1961, Lambourne and Bryer conducted an investigation into the nature of vortex breakdown by using flow visualization methods. They noted that breakdown causes a loss of suction pressure and a flattening of the leeward pressure distribution. They also noted that the location of breakdown was sensitive to the axial pressure gradient along the vortex core, and that a reduction of this gradient could result in a new position of breakdown, downstream of the original location.

In 1961, P. B. Earnshaw examined the structure of leading edge vortices using a 76° sweep wing in a wind tunnel. He took total and static pressure measurements through the vortex at three chordwise stations. Earnshaw identified three distinct, concentric regions of the leading edge vortex: the free shear layer, the rotational core, and the viscous subcore. The speculative shapes of these three regions are shown schematically in Fig. 1.7. The free shear layer, or vortex sheet, emanates from the leading edge and wraps into the rotational core; viscous dissipation then diffuses the sheet within the core. Earnshaw described the rotational core flow as being conical and occupying approximately thirty percent of the local semi-span. The diameter of the viscous subcore varied with the square root of the downstream distance, and was approximately five percent of the local semi-span in diameter. This part of the vortex rotates as a solid body. Earnshaw noted axial velocities in the subcore as high as 2.3 times the freestream velocity. Axial velocities as high a three times the freestream have been since documented by many researchers (Lambourne and Bryer, 1961; Kegelman and Roos, 1990). It is this high velocity fluid

that is typically believed to cause the large pressure drop (and thus high lift) over the wing, even to large angles of attack.

Free Shear Layer
Rotational Core
Viscous Subcore
Secondary Vortex
Wing
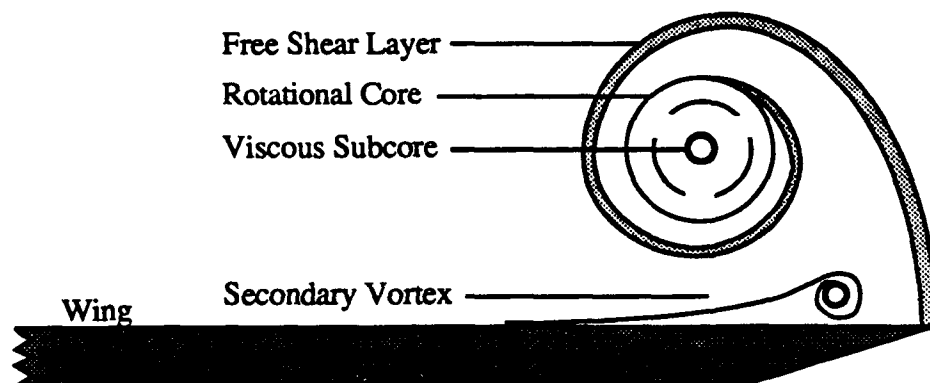
Figure 1.7   Leading Edge Vortex Cross Section. Figure Adapted from Payne, 1987.

In 1964, Earnshaw and Lawford measured the aerodynamic loads on six delta wings of varying sweep angle (45° to 76°). They took steady data up to 60° angle of attack, and also noted the location of breakdown and the surface flow patterns. They found that a larger sweep angle resulted in a higher angle of attack necessary for complete leeward flow separation. They also found that the angle necessary for the onset of vortex breakdown increases with increasing sweep angle.

A review of slender wing characteristics was published by A. G. Parker in 1976. Parker discussed both experimental and theoretical findings, and compared the two. Parker noted that the line of attachment of the freestream flow moving over and being entrained by the primary vortices moves inboard with increasing incidence. Parker concluded by pointing out that the majority of experimental studies had been conducted at Reynolds numbers far below actual flight Reynolds numbers, and that despite the apparently small

effect of Reynolds number, research should still be done in this area. He also pointed out that few studies existed (at that time; 1976) on the unsteady characteristics of delta wings.

In 1978 Hummel published some of the results of an extensive investigation of the flowfield around a 76° delta wing at 20.5° angle of attack. Surface pressure measurements, static pressure measurements within the vortex core, force measurements, surface flow patterns, velocity measurements, and boundary layer measurements were all obtained. Hummel documented a difference in the surface pressure field as a result of a laminar or turbulent boundary layer (as discussed in section 1.2). He also found that the inboard and upward displacement of the primary vortex caused by the secondary vortex is less for a turbulent boundary layer than for a laminar boundary layer.

Earlier, Hummel and Srinivasan (1967) had measured the lift and moment on a series of slender delta wings. They correlated the onset of vortex breakdown with a decrease in the slope of the lift and moment curves. This phenomenon was also examined as a function of the leading edge sweep angle.

In 1981 Erickson published a comprehensive flow visualization study on the characteristics of leading edge vortices. He found the location of the primary vortex core to be different for laminar or turbulent secondary surface flow. This was caused by a change in location of the secondary vortex. However, the change on the integrated loads was negligible. Erickson also noted an oscillation of the vortex core due to the presence of breakdown at some downstream position. He concluded that when comparing experimental data, qualitative (rather than quantitative) comparisons should be stressed due to the sensitivity of the leading edge vortices to a wide variety of factors, including support interference, freestream flow aberrations, and model irregularities.

1.5   Fundamentals of Unsteady Delta Wing Aerodynamics

The unsteady response of the vortical flow over a delta wing can, in general, be divided into two categories: low angle of attack motions, and high angle of attack motions. In general the point of division between these two is the occurrence of vortex breakdown. Typically, very different behavior is seen for motions including and excluding the presence of breakdown. For low angle of attack motions, the reaction of the flowfield is typically quasi-steady, while hysteresis effects are often seen for high angle of attack motions, assuming comparable rates of motion. This difference in behavior is particularly true for pitching oscillations (Ashley, Jarrah, Katz, and Vaneck, 1990). The flowfield is incapable of precisely tracking an unsteady maneuver, but rather will take time to adjust to the new wing attitude. At low angles of attack this time lag can delay flow separation, while at higher angles of attack it can delay the occurrence of vortex breakdown.

However, the delay is typically not considered to be a convective delay; significant lags in flow development have been measured for reduced pitching frequencies on the order of 0.1. This delay, or lag, in the formation or motion of vortex breakdown is related to the unsteady effects seen in the aerodynamic loads. For a sudden increase in angle of attack, the breakdown is located aft of its steady state location, and a coherent vortex exists over a greater part of the wing, hence the suction pressure is greater and the lift is higher (all relative to the steady case). The opposite situation exists for a decrease in incidence; the breakdown is farther upstream, thus the suction pressure is less and the lift is lower. For an oscillatory pitching motion this results in an unsteady hysteresis in both the breakdown location and the loads (LeMay, Batill, and Nelson 1988; Bragg and Soltani, 1988). For excursions to very high angles of attack, the occurrence of leeward flow separation increases this effect, as there is a delay in the reformation of an organized leeward surface flow from a bluff body type of wake.

This type of behavior has been documented for several different characteristics: core location, breakdown location, surface pressure, lift, drag, pitching moment, and normal force. For the aerodynamic loads the unsteady effects are typically manifested as an overshoot or undershoot relative to the steady case. For an angle of attack increase, the loads can be larger in magnitude (hence the term overshoot) than in the steady case. The undershoot then occurs during a decrease in incidence, when the loads are smaller than for the steady case.

Figure 1.8 shows an example of this type of unsteady data. This figure shows the normal force coefficient as a function of angle of attack, for a 70° sweep delta wing. Unsteady data for two pitch frequencies are shown, as well as the steady case (which shows both angle of attack statically increasing and decreasing). The hysteresis (overshoot and undershoot) of the unsteady case is readily apparent.
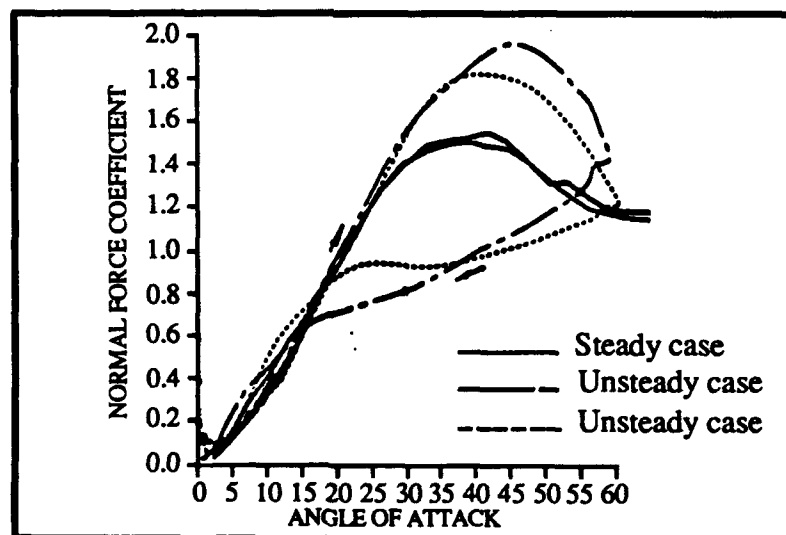
Figure 1.8   Unsteady Normal Force Coefficient during Angle of Attack Oscillation.
Figure from Jarrah, 1988. Data for Two Pitch Rates Shown.

The unsteady response of the leading edge vortex flowfield has been seen to be very sensitive to the initial conditions of the flow. The magnitude of both the overshoot and the undershoot can change. For example, a pitching oscillation of constant amplitude can result in significantly different unsteady effects depending on the initial angle of attack, even for initial angles varying by less than five degrees (Wolffelt, 1986; Brandon and Shah, 1988). Furthermore, at angles where breakdown exists over the wing, the behavior can be different even for the same initial angle of attack, depending on the initial instantaneous location and velocity of vortex breakdown (Magness, Robinson, and Rockwell, 1989; Thompson, Batill, and Nelson, Jan. 1989).

The overshoots and undershoots seen in the aerodynamic loads occur for both oscillatory and transient motions. Several researchers have investigated the response of the leading edge vortex system to a transient or impulsive motion, and have documented trends similar to those seen for oscillatory motion. One valuable aspect of utilizing a transient motion is that information can be obtained on the length of time necessary for the flowfield to return to the steady case upon completion of the maneuver. Typically this is measured in terms of convective time units, where one convective time unit is the amount of time it takes the freestream flow to travel the length of the wing (Reynolds and Abtahi, 1987). An interesting note involves the comparison of the vortex behavior for a transient motion to that for an oscillatory motion. It is possible to subject the wing to a transient motion that is a portion of an oscillatory motion. However, the flowfield behavior will not necessarily be the same for the two cases (Magness, Robinson, and Rockwell, 1989; Thompson, Batill, and Nelson, 1989 and 1991). This phenomenon demonstrates the very strong dependence of the leading edge vortices and their unsteady aerodynamic effects to the exact motion history.

1.6   Research on Unsteady Delta Wing Aerodynamics

Research involving unsteady swept wing motions began in the early 1950's. However, these early investigations focused on motions at small angles of attack. Tests using high angle of attack excursions (and thus involving the leading edge vortices) were not conducted until several years later, and the bulk of that research has been conducted in the past ten years. This section presents a brief overview of the research conducted to date involving unsteady delta wing fluid dynamics. Data from several of these research efforts will be used as a basis for comparison with the current study.

In 1954 W. R. Laidlaw investigated the unsteady aerodynamic loads on a rectangular wing, a swept wing, and a delta wing. He measured the surface pressure as the wings underwent either a sinusoidal pitching motion or a pure vertical translation. Laidlaw then integrated the surface pressures to estimate the lift, then compared this to a theoretical evaluation of the unsteady lift. He found moderate agreement; however, he examined only small angles of attack, thus the formation of the leading edge vortices was not a factor.

This was also the case for L. Woodgate in 1963. Woodgate measured the pitching moment derivatives on a 70° sweep wing undergoing small amplitude pitching oscillations in a wind tunnel. The amplitude of motion varied from 0.5-1.5°, with mean angles of attack from 0-15°. Woodgate found a Reynolds number effect to exist between the range of 1.28-2.56 million (based on root chord). He attributed this to a difference in the state of the boundary layer of the secondary flow. By using trip wires he was able to eliminate the effect. Furthermore, he found no apparent difference due to a change in amplitude, but considering the small range of amplitudes, and the low mean angles of attack, this is to be expected. In addition, the lack of difference due to amplitude is not indicative of the behavior at very high angles of attack, where breakdown is present over the wing.

In 1985, Gad-el-Hak and Ho examined a 45° wing and a 60° wing being pitched sinusoidally in a towing tank, at Reynolds numbers from 25,000-35,000. Pitching

amplitudes of 5°, 10°, and 15° were used. Using flow visualization, they documented a hysteresis in the development of the leading edge vortices during the unsteady motion. This was also seen by Atta and Rockwell in 1987, for a 52° sweep wing. Gad-el-Hak and Ho noted that this hysteresis was a strong function of the nondimensional pitching frequency.

In 1986 Wolffelt tested a 60° delta wing undergoing pitching and plunging oscillations in a water tunnel. Wolffelt noted hysteresis in the breakdown location for angle of attack ranges of 0-20°, 5-25°, and 10-30°. He also noted that the unsteady values were sometimes displaced relative to the steady values; that is, the unsteady hysteresis loop did not necessarily encompass the steady data. Wolffelt also used a wind tunnel to repeat some of the tests at a Reynolds number an order of magnitude larger than that of the water tunnel tests. An example of Wolffelt's data is shown in Fig. 1.9. Breakdown location is shown for both steady and unsteady cases, for three angle of attack ranges. Note the substantial difference in the unsteady behavior depending on the initial angle of attack.
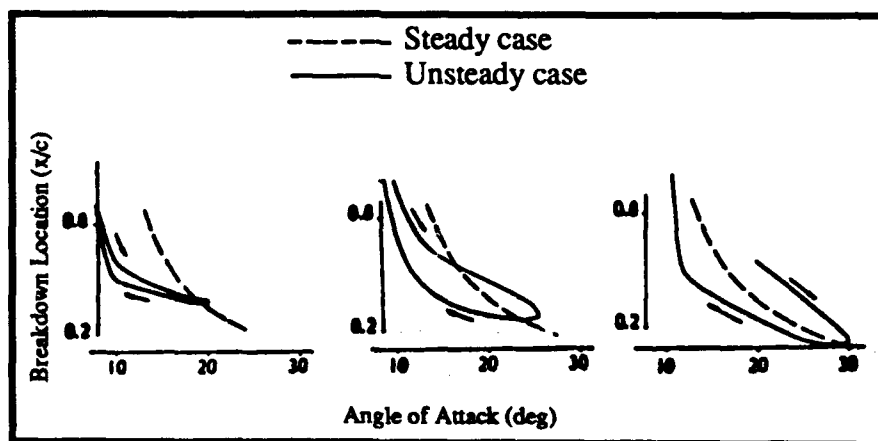
Figure 1.9   Unsteady Vortex Breakdown Location during Angle of Attack Oscillation.
Figure from Wolffelt, 1986.

Wolffelt also found a consistent difference in the steady location of breakdown. However, he dismissed this as possibly being a Reynolds number effect, citing differences in the data reduction process. However, in light of subsequent research, it seems possible that this was indicative of a differences in the surface flow boundary layer., which *can be* a Reynolds number effect.

In 1988 LeMay (see also LeMay, Batill and Nelson, 1988 and 1990) examined the dynamic location of vortex breakdown during a sinusoidal pitching oscillation, using flow visualization methods and a 70° sweep wing. LeMay carefully documented hysteretic behavior for the chordwise location of breakdown over an angle of attack range of 29-39°. This data compared well with the findings of Wolffelt (1987). LeMay also found that the amount of lag between the steady and unsteady positions increased with increasing nondimensional pitch rate. This has been seen by several other researchers, including Manor, Miller, and Wentz (1990). LeMay also documented a consistent Reynolds number effect over the range of 175,000-260,000. This was manifested as a chordwise change in the dynamic breakdown location for the entire pitching motion. This change was a discrete downstream shift from 175,000 to 260,000. LeMay also documented a steady hysteresis at the angle of attack where breakdown first appeared over the wing.

Also during 1988 Bragg and Soltani measured the unsteady forces and moments on a pitching 70° wing. Both sinusoidal and ramp motions were used over the range of 0-55° angle of attack, and at several pitch rates. Bragg and Soltani found significant lift overshoots relative to the steady case, with the magnitude of the overshoot being a strong function of pitch rate. They attributed these overshoots to a lag in the formation and upstream progression of the vortex breakdown. They used reduced pitching frequencies less than 0.1, hence the lag is probably not due to a convective delay. They also recorded undershoots in the loads as the incidence was decreasing; this was attributed to a delay in the flow reattachment. Their conclusions correlated well with the actual flow visualization data obtained by LeMay (LeMay, 1988).

Jarrah (1988 and 1989) drew similar conclusions from his tests involving a series of three delta wings being sinusoidally pitched over three angle of attack ranges: 0-30°, 0-60°, and 0-90°. Rate dependent hysteresis loops in both the unsteady forces and the unsteady breakdown location were documented by Jarrah. He observed overshoots of the lift coefficient of up to 50% of the steady value. No substantial Reynolds number effect was seen over the range of 420,000-840,000.

The conclusions of both Bragg and Soltani (1988) and Jarrah (1988) compared well with the conclusions of both Brandon and Shah (1988), who measured the unsteady normal force on a pitching 70° wing. They used a range of motion of ±18° about mean angles of attack of 22°, 27°, 32°, and 37°. Like Bragg and Soltani (1988) they attributed the observed hysteresis in the loads to lags in the breakdown location, and to lags in the flow separation and reattachment. Brandon and Shah also noted a strong dependence on the mean angle of attack. They found that as the mean angle of attack increased, the magnitudes of the over- and undershoots increased. The largest unsteady effects were noted when the motion encompassed the static stall angle. Brandon and Shah later published a report evaluating the potential for exploitation of the dynamic lift overshoot (Brandon and Shah, 1990). They used a fighter model with a highly swept leading edge extension; a geometry that is known to cause leading edge vortex formation at large incidence. They used both sinusoidal and ramp motions. They found that the unsteady lift increment persisted for up to fifty convective time units (reinforcing Bragg and Soltani's finding that the lags in the breakdown motion were not due to a convective delay). They then examined the possibility of utilizing the unsteady effects to improve the aircraft performance during two high alpha maneuvers; nose pointing (a rapid large amplitude pitch up) and velocity vector turning (a rapid low radius turn). Brandon and Shah found that the unsteady effects on the pitching moment could be detrimental to the nose pointing maneuver. They also concluded that a persistence of fifty convective time units was insufficient to improve the turn performance.

A study involving the reaction of the vortex breakdown to a ramp pitching motion was conducted by Reynolds and Abtahi in 1987. They used a 75° flat plate delta wing oscillating from 30-50° in a water tunnel, at several pitch rates. They found that twenty to thirty convective time units were needed for the breakdown to reach a steady position. This compares well to the findings of Brandon and Shah (1990). Reynolds and Abtahi also noted that during a pitch-down motion, the breakdown propagated downstream with a speed less than one-tenth the convective speed. They also suggested that, compared to tests using transient motions, tests involving oscillatory motions may not be as well suited to studying the potential of exploiting the unsteady effects, due to the large time scales involved.

Magness, Robinson, and Rockwell (1989) also studied the effect of ramp motions on a 75° wing in a water tunnel. They suggested that the lags seen in the breakdown position could be exploited to obtain optimal wing loading. They noted that upon completion of the pitching motion, the breakdown could move as much as half the chord length to its equilibrium position. An example of their data is shown in Fig. 1.10. Data for the transient case, oscillatory case, and the steady case are all shown. Magness et. al. also noted that the trailing edge presented a discontinuity of the boundary conditions, where the breakdown propagation speed was low. They conducted tests using a continuous motion, but in the form of a sawtooth wave rather than a sine wave. They found that this type of motion could result in an upstream motion of the breakdown with a decrease in incidence (opposite the steady behavior), an effect of not allowing the breakdown to return to the steady-state position.

Vortex Breakdown Location x_b/C

1.000
0.800
0.600
0.400
0.200
0.000

▲ Pitch up
▼ Pitch down
○ Continuous pitch up and down

$\dot{a}C/2U_\infty = 0.025$

Static

Angle of Attack α

10   15   20   25   30   35   40   45
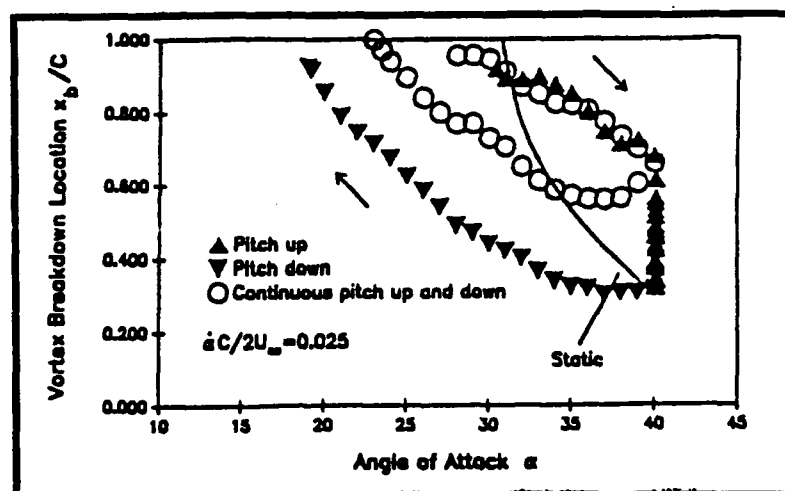
Figure 1.10   Breakdown Location for Transient and Oscillatory Motions. Figure from

Magness, Robinson, and Rockwell, 1989

A similar trend was seen by Thompson, Batill, and Nelson in 1989 (see also Thompson, Batill, and Nelson, 1991). They recorded the motion of the vortex breakdown for a 70° wing being pitched from 30-40° in pitch-up and pitch-down motions, for several pitch rates. They noted that upon completion of the motion, the breakdown had typically travelled 80% of the distance to the steady state location, however, a large time lag (relative to the convective speed of the flow) was involved for the remaining 20% to be recovered. The magnitude of the lag of the unsteady location from the steady location was seen to be a function of the pitch rate. No consistent Reynolds number effect was seen. Thompson et. al. also discussed some of the problems in obtaining and evaluating this type of data, considering the many factors influencing the breakdown behavior.

In 1989 Cunningham published a report that was a summary of an extensive test program performed with a straked (or double-delta) wing. Flow visualization data, six-component force measurements, and surface pressures measurements were all obtained. Pitch rate dependent hysteresis loops were documented as for the researchers mentioned previously. Cunningham also noted that vortex breakdown was seen to effect the surface

pressure at upstream locations. This was attributed to a change in the vertical location of the vortex core caused by the breakdown.

Cunningham and Bushlow then performed a similar study in 1990 using a water tunnel. They utilized both flat plate and three dimensional subscale fighter models in an effort to compare the water tunnel data with the previously obtained wind tunnel data. They found excellent agreement in the steady forces and moments. For the unsteady data, good agreement was found upon applying a dynamic blockage correction (this will be discussed in additional detail in section 4.4.4 on blockage corrections).

Unsteady surface pressure measurements were obtained by Thompson, Batill, Nelson in 1990. They used a 70° sweep wing undergoing sinusoidal pitching oscillations over several angle of attack ranges, both including and excluding such occurrences as vortex breakdown, dynamic stall, and full scale leeward flow separation. Several pitch rates and Reynolds numbers were examined. This data has been presented in several publications, including Thompson, Batill and Nelson, Jan. 1990 and Aug. 1990; Thompson, Arena, Nelson, and Batill, Oct. 1990. Considering the similarity of these investigations with the current study, they will not be presented here; but will rather be presented in conjunction with the presentation of the current experimental results.

1.7   Scope of Current Research

The steady-state characteristics of delta wings and leading edge vortices have been well documented in the literature, with both experimental and analytic investigations. However, this is not true for the unsteady characteristics. At present the number of unsteady, high angle of attack delta wing studies is limited. In general, the unsteady effects at low angles of attack (angles where breakdown does not occur) are small; the behavior is quasi-steady. However, high angle of attack unsteady delta wing aerodynamics is characterized by hysteretic behavior. The location of vortex breakdown during an unsteady

motion has been seen to involve hysteresis effects, and dynamic overshoots in the aerodynamic loads (relative to the steady case) have been documented in the literature. It is this overshoot that holds the potential for exploitation. Dynamic lift has the potential for expanding the maneuvering envelope of swept wing aircraft. However, to achieve this it would be necessary to monitor the conditions over the wing. This could be done in a practical manner by use of surface pressure sensors, which could provide feedback to the flight control system. In addition, maneuvering at large angles of attack may require control of the leading edge vortices to avoid unwanted loading, or to increase control authority. Several aircraft experience a substantial loss of yaw control at high angles of attack due to the location of the vertical tail(s) in the wake of the airframe. By employing leading edge vortex control, it may be possible to restore some of this lost control. In either case, an understanding of the relation between the surface pressure distribution and the vortical flow field becomes necessary for unsteady conditions.

This research has been designed to experimentally investigate the relationship between the aerodynamic loads and the vortical flow characteristics of a highly swept wing undergoing unsteady angle of attack excursions. The research focuses on angles of attack large enough to include the formation of the leading edge vortices, the onset of vortex breakdown, and the onset of fully separated flow. A delta wing with a 70° leading edge sweep has been used to increase the amount of comparative data available in the literature.

Two primary experimental methods have been used: flow visualization tests, and surface pressure measurement tests. For the most part, the flow visualization tests have been used to obtain data on the vortex core and vortex breakdown positions. The surface pressure data have been used to examine the aerodynamic loads. This research focuses on unsteady motions, but steady data (for both flow visualization and surface pressure) have been obtained for comparison with the unsteady data.

This research is of the first experimental studies to obtain unsteady surface pressures for a pitching delta wing. This was accomplished for several angle of attack ranges and surface locations.

For an unsteady pitching motion, the response of the vortical flowfield depends on many parameters; range of motion, mean angle of attack, pitch rate, motion history, Reynolds number, wing geometry, and pitch axis, as well as others. This research involves an extensive series of tests designed to examine the effect of these parameters on the unsteady flow characteristics of a delta wing. In order to maintain a reasonable test program some of these factors have been examined in lesser depth than others.

While the acquisition of the vortex trajectory data and the surface pressure data was one of the primary goals of this research; another was to examine this information relative to each other, and attempt to correlate the response of the vortex breakdown with the change in the pressure field. Thus, the flow visualization tests have been used to help interpret the surface pressure data. Finally, comparable data available in the literature have been mentioned wherever applicable, and agreement or discrepancies have been noted. In addition, data from the literature on the steady and unsteady aerodynamic loads have been used.

II EXPERIMENTAL EQUIPMENT

2.1 Wind Tunnel Specifications

The primary experimental facility used during this research was a subsonic indraft wind tunnel located at the Hessert Center for Aerospace Research University of Notre Dame. This tunnel contains a 22:1 contraction ratio inlet, a working section, and a diffuser section. A schematic of this is shown in Fig. 2.1. The contraction section has four steel screens and eight nylon screens mounted at the inlet to reduce the scale of the irregularities in the freestream flow. Directly behind the contraction section is the interchangeable working section, typically with a cross section of 2 ft. by 2 ft. (61 cm by 61 cm). This is followed by a diffuser section with a length of 14 ft. 8 in. (4.47 m) and an angle of divergence of 4.2°. The fan and motor are located at the end of the diffuser; the motor is an 18.6 kW AC motor. The motor drives an eight bladed fan with a blade diameter of 4 ft. (1.22 m). A rubber gasket was located between the test section and the diffuser to reduce any possible effects of vibrations from the motor.

The wind tunnel exhausts into the motor room, which has both an exhaust fan and vents to the outside atmosphere; thus the tunnel is well suited for the use of various types of smoke visualization. Contamination of the freestream flow due to recirculation of the smoke particles is not a concern. The susceptibility of this tunnel to disturbances in the test section due to outside wind gusts can be minimized by adjusting the louvers. A flow restrictor could be also used to minimize this effect.; however, such a restrictor was not used during this research so that the desired freestream velocities could be obtained. Tests were thus conducted with the motor room sealed off or only when outside atmospheric conditions were calm.

30
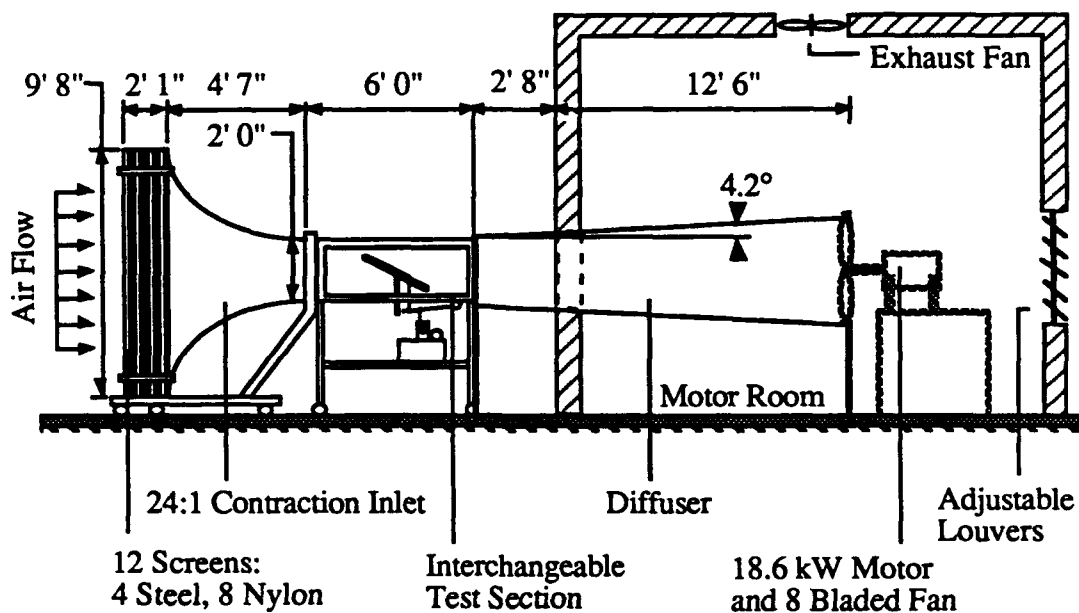
Figure 2.1   Subsonic Wind Tunnel Facility

The turbulence intensity of this tunnel has been determined to be less than 0.5% for all speeds and test section configurations. For a clean test section the turbulence level is less than 0.1% for disturbances with frequencies greater than 10 Hz. Additional details can be found on this subject in Brendel and Huber (1984).

2.2   Test Section Specifications

A single test section was used throughout this research. A schematic is shown in Fig. 2.2. This section had a length of 6 ft. (1.83 m) and a cross section of 2 ft. by 2 ft. (61 cm by 61 cm). The top and one side of the section had glass plates installed to facilitate illumination and viewing of the model. The opposite side was hinged to allow access to the interior of the section. A shelf was installed beneath the working section to allow for the

REAR SIDE

TOP

FRONT SIDE
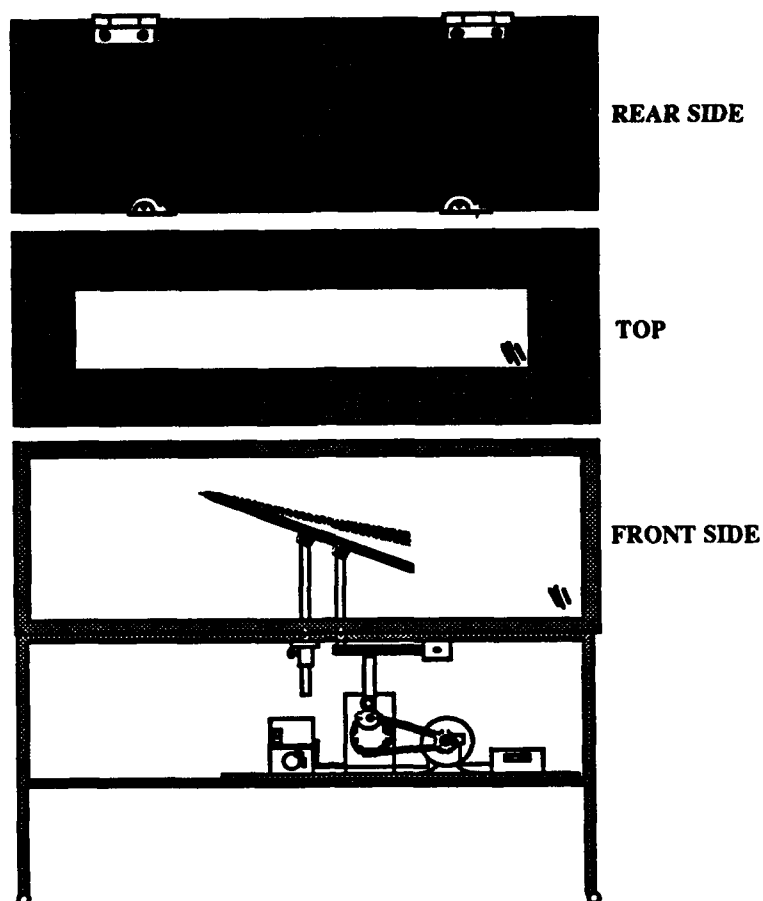
Figure 2.2   Test Section Schematic

placement of necessary equipment. A pitot static tube was mounted through the floor of the

section such that the head was located between the section walls, 4 in. (10.2 cm) above the

floor, and 6 in. (20.3 cm) aft of the contraction section. Test models were strut mounted in

the test section using a 0.75 in. (1.9 cm) diameter aluminum sting mounted to the floor of

the section. The length of the sting was adjusted so that the model was centered in the test

section cross sectional area. In addition a $\frac{1}{2}$ in. by 3 in. (1.3 by 7.6 cm) slot was cut

through the floor to allow for the parts of the unsteady pitching mechanism and the removal

of instrumentation leads. The unused portion of this slot was covered from the inside of

the test section during testing. The interior of the section was painted flat black to provide high contrast with the white smoke used during flow visualization experiments. Black felt was attached to the interior of the rear wall for this same purpose.

2.3 Delta Wing Model Specifications

Over the course of this research, several delta wing models were designed and fabricated. Some of these wings were built for a specific test, while some were built to be used in several tests. Each model was a flat plate delta wing with a sweep angle of 70°. The thicknesses and leading edge geometries varied among the different wings. A schematic of each of the wings is shown in Figs. 2.3a-d. The geometric parameters of the wings are summarized in Table 2.1. The primary models used during the current study were the three models with single bevel leading edge geometries.

TABLE 2.1

DELTA WING WIND TUNNEL MODELS

All wings have a leading edge sweep of 70°; aspect ratio = 1.46.

Root Chord c	Span s	Thickness t	Thickness Ratio t/c (%)	Material	Leading Edge Geometry	Type of Tests
$16\frac{5}{16}$"	$11\frac{15}{16}$"	$\frac{1}{2}$"	3.1	Aluminum	2 Bevel	Flow vis
$16\frac{7}{16}$"	12"	$\frac{3}{4}$"	4.6	Plexiglas	2 Bevel	Pressure, Flow vis.
$16\frac{7}{16}$"	12"	$\frac{3}{4}$"	4.6	Plexiglas	1 Bevel	Pressure, Flow vis.
$10\frac{15}{16}$"	8"	$\frac{1}{2}$"	4.6	Plexiglas	1 Bevel	Blockage Study
$8\frac{3}{16}$"	6"	$\frac{3}{8}$"	4.6	Plexiglas	1 Bevel	Blockage Study

2.3.1 Flow Visualization Models

Initially, a delta wing model was fabricated strictly for use in flow visualization experiments. This wing is illustrated in Fig. 2.3a. It was made from 0.5 in. (1.27 cm) thick aluminum and was beveled to 25° on both the windward and leeward surfaces, on all three sides. The root chord length was $16\frac{5}{16}$ in. (41.4 cm). A channel 5 in. by $\frac{3}{8}$ in. (12.7 cm by 0.95 cm) was cut out of the bottom of the model to house the plastic tubing used to deliver the smoke particles to the wing apex. A 0.08 in. (0.20 cm) diameter hole was then drilled from this channel to the upper surface of the model, to a position near the apex found to be advantageous for injecting smoke particles into the leading edge vortex. This was only done on one side of the model. In addition, three screw holes were drilled in the centerline of the model to allow for the wing to be mounted to the sting. The model was then painted flat black to provide contrast with the smoke used during visualization experiments.

It was later found that the pressure models could be adapted for use with flow visualization experiments. Consequently, two of the pressure models were used for the flow visualization experiments. These two models are detailed in the following section.

Model made of aluminum

70°

Smoke injection ports

Smoke injection tubing channel (bottom surface)

Sting mounting plate (bottom surface)

16.3125"

11.9375"

0.5"

23°
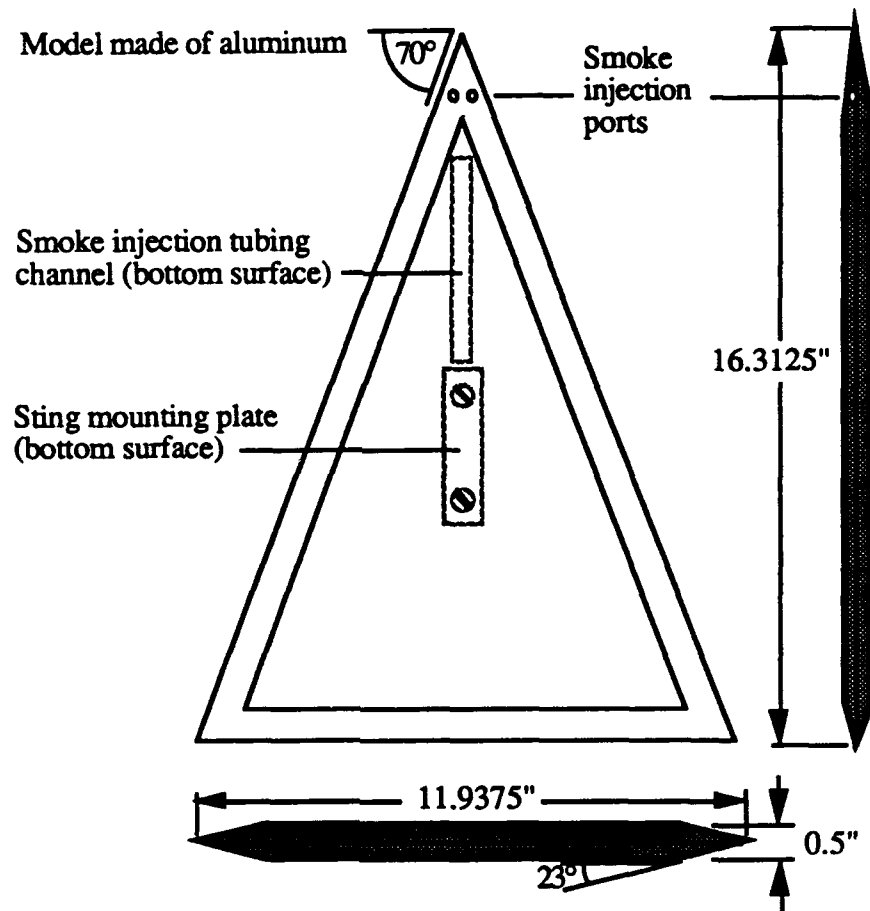
Figure 2.3a   Delta Wing Model: Double Bevel Flow Visualization Model

2.3.2   Surface Pressure Models

The first pressure model built was cut from plexiglass and designed to approximately replicate the flow visualization model described above. Thus this wing also had a root chord length of $16\frac{7}{16}$ in. (41.8 cm), and was beveled to 25° on both leeward and windward surfaces on all three side. Pressure orifices were drilled into the leeward surface of this wing in the form of 0.08 in (0.20 cm) diameter holes. Three lines of pressure orifices existed in this wing as shown in Fig. 2.3b. One set was placed at a constant local semi-span location of $y/s = 0.60$. Due to the width of the upper surface bevel, one of these

x = Local chordwise distance
y = Local spanwise distance
c = Root chord length
s = Trailing edge semi-span
Model made of Plexiglas

70°

y/s = 0.60

x/c = 0.50

x/c = 0.75

16.44"

Removeable top plate

12.0"

Hollow cavity

23°

0.75"

PRESSURE TAP LOCATIONS		
y/s = 0.60	x/c = 0.50	x/c = 0.75
x/c = 35%	y/s =0%	y/s =0%
40%	±12%	±9%
45%	±24%	±18%
50%	±36%	±26%
55%	±48%	±34%
60%	±60%	±43%
65%		±51%
70%		-56%
75%		±60%
80%		-64%
85%		±68%
90%		-76%
		-84%
		-90%
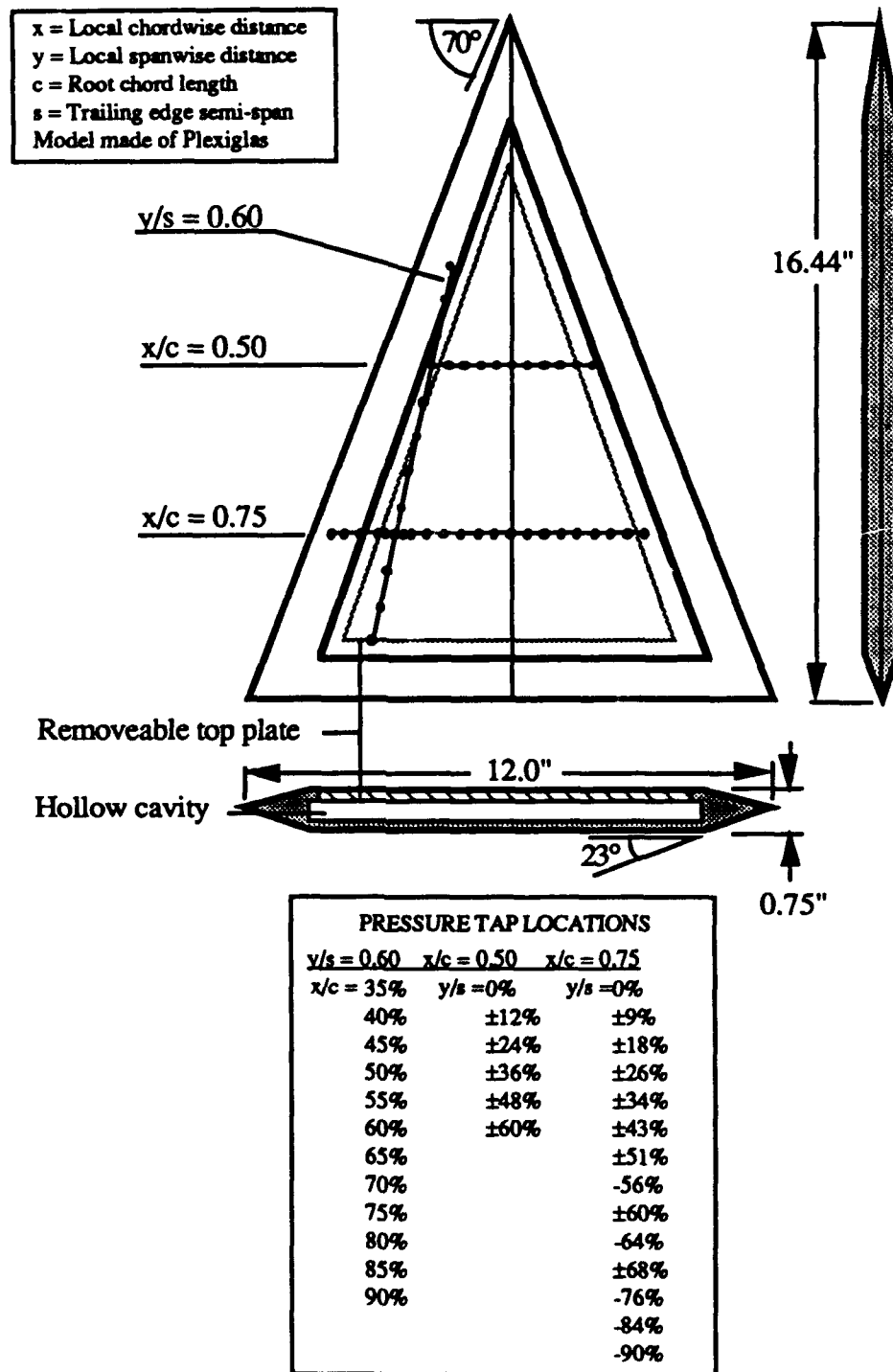
Figure 2.3b   Delta Wing Model: Double Bevel Pressure Model and Pressure Orifice

Locations

pressure orifices was located on the face of the bevel rather than on the flat upper surface. Two additional rows of orifices were placed at constant chord locations of x/c = 0.50 and 0.75. A total of 31 orifices were placed in the wing; the specific locations are noted in Fig. 2.3b. In addition, 23 orifices were drilled into the right side of the model, in positions symmetric to those already on the left side of the wing. This was done to examine the symmetry of the pressure field. In order to differentiate between the left and right sides of the model, negative semi-span values will hereafter be used to denote values on the left side of the model, relative to a view from the top.

In order to house the instrumentation leads, the model was 0.75 in. (1.9 cm) thick, with a 0.25 in. (0.64 cm) thick cavity in the center of the model. A removeable top plate allowed for access to the interior of the model. Holes were drilled to accommodate the sting mounting plate and the removal of the instrumentation leads. This model was also adapted for use in flow visualization experiments by drilling a hole beginning at the cavity inside the model and ending at the leeward surface of the wing, near the apex. This modification was similar to the flow visualization model described above. Thus smoke could be delivered to a location where it would be entrained into the leading edge vortex.

A second pressure model was built, also made of plexiglass, this one having the same chord length and thickness as the previous model. However, the leading edge geometry was different; this model was built with a bevel of 45° on the windward side only, and the trailing edge was left blunt. As before this model had a hollow interior and a removeable top plate. Lines of pressure orifices were again placed at y/s = -0.60, x/c = 0.50 and x/c = 0.75. The specific locations of the orifices are noted in Fig. 2.3c. More pressure orifices were placed on this model in an effort to obtain more detailed pressure profiles. No orifices were placed on the right side of the wing. This model was also modified to allow for flow visualization experiments.

In addition to being able to examine the effect of the leading edge geometry on the surface pressure, this second, single bevel model was constructed to allow for comparison

x = Local chordwise distance
y = Local spanwise distance
c = Root chord length
s = Trailing edge semi-span
Model made of Plexiglas

70°

y/s = 0.60

x/c = 0.50

x/c = 0.75

16.44"

Removeable top plate

12.0"

Hollow cavity

45°

0.75"

PRESSURE TAP LOCATIONS		
y/s = 0.60	x/c = 0.50	x/c = 0.75
x/c = 25%	y/s =0%	y/s =0%
30%	10%	10%
35%	20%	20%
40%	30%	30%
45%	40%	40%
50%	50%	50%
55%	60%	60%
60%	70%	70%
65%	80%	80%
70%	90%	90%
75%		
80%		
85%		
90%		
95%		
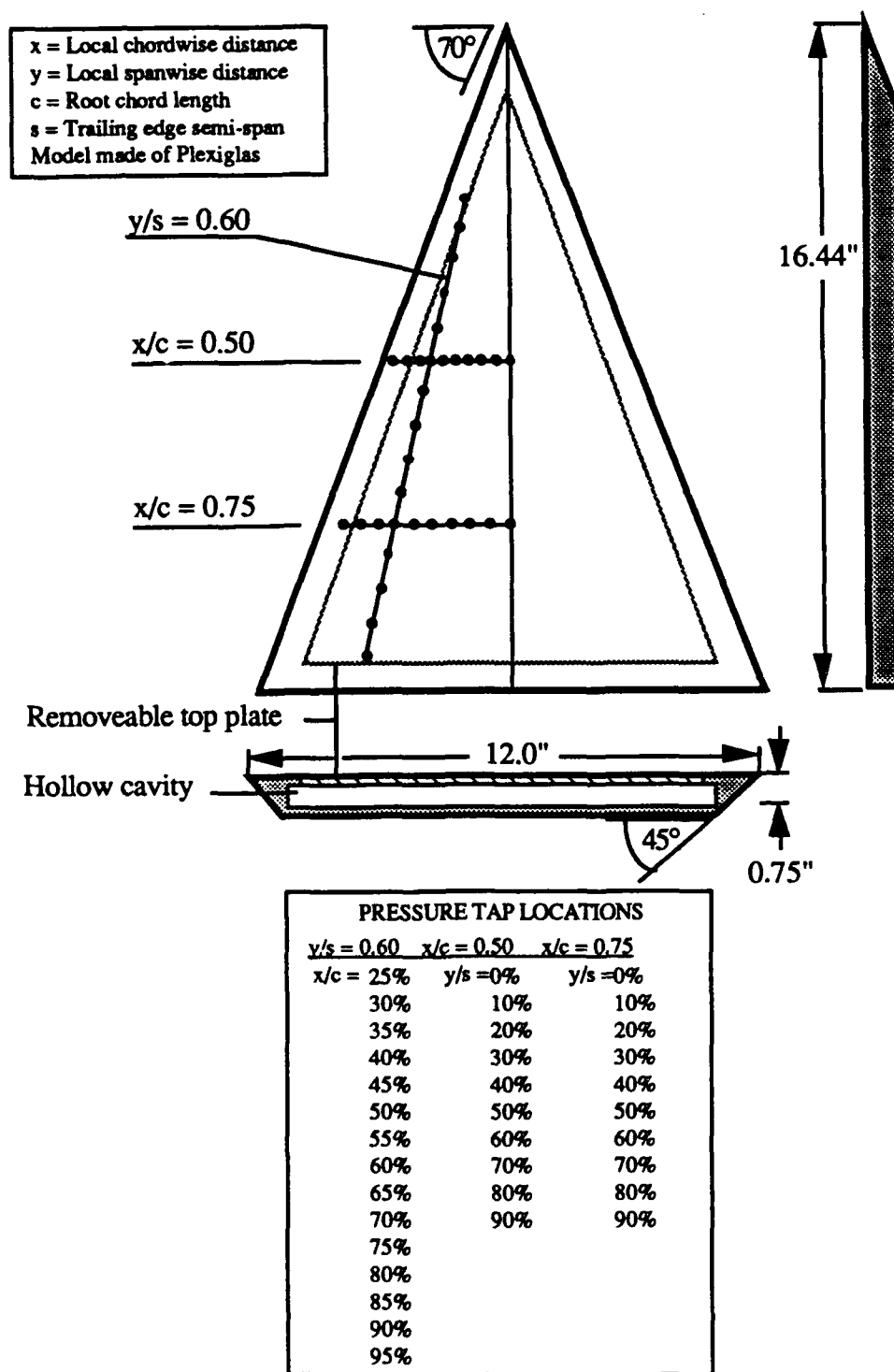
Figure 2.3c   Delta Wing Model: Single Bevel Pressure Model and Pressure Orifice

Locations

with data available in the literature (including aerodynamic force data obtained by Jarrah, 1988 and 1989). A much greater amount of information is available for delta wings with only a windward surface bevel. Thus to increase the generality of this research, the single bevel model was built.

2.3.3 Blockage Effects Models

Two additional models were built in order to study the effect of blockage at very high angles of attack. These are illustrated in Fig. 2.3d. Both these wings were made of plexiglass. These models were scaled to the single bevel pressure model but with different chord lengths. Thus the thickness and span length were appropriately reduced to maintain similarity. Chord lengths of $10\frac{15}{16}$ in. (27.8 cm), and $8\frac{3}{16}$ in. (20.8 cm) were used, with thicknesses of $\frac{1}{2}$ in. (1.27 cm) and $\frac{3}{8}$ in. (0.95 cm). Thus, relative to the largest wing, one wing was two-thirds that size and one was one-half that size. As with the full scale wing, the bevel angle for each of the three wings was $45°$. Thus they were exactly geometrically similar to the full scale wing.

These models were used primarily for pressure tests although they were also used to obtain a limited amount of flow visualization data. Pressure orifices, noted in Fig. 2.3d, were placed at locations matching many of those on the single bevel pressure model. However, these subscale models did not have an interior cavity; they were solid plexiglass. Thus, an alternative method was used to connect the surface orifices to a pressure transducer. A piece of $\frac{1}{8}$ in (0.32 cm) square brass tubing was embedded in the model beneath the surface locations where pressure data was desired. Pressure orifices were then drilled through the wing surface and into the brass tubing. The brass tubing was then connected to a transducer by plastic tubing. Thus all the pressure orifices were drilled into a common chamber. When one orifice was being sampled the remainder were sealed off with adhesive tape.
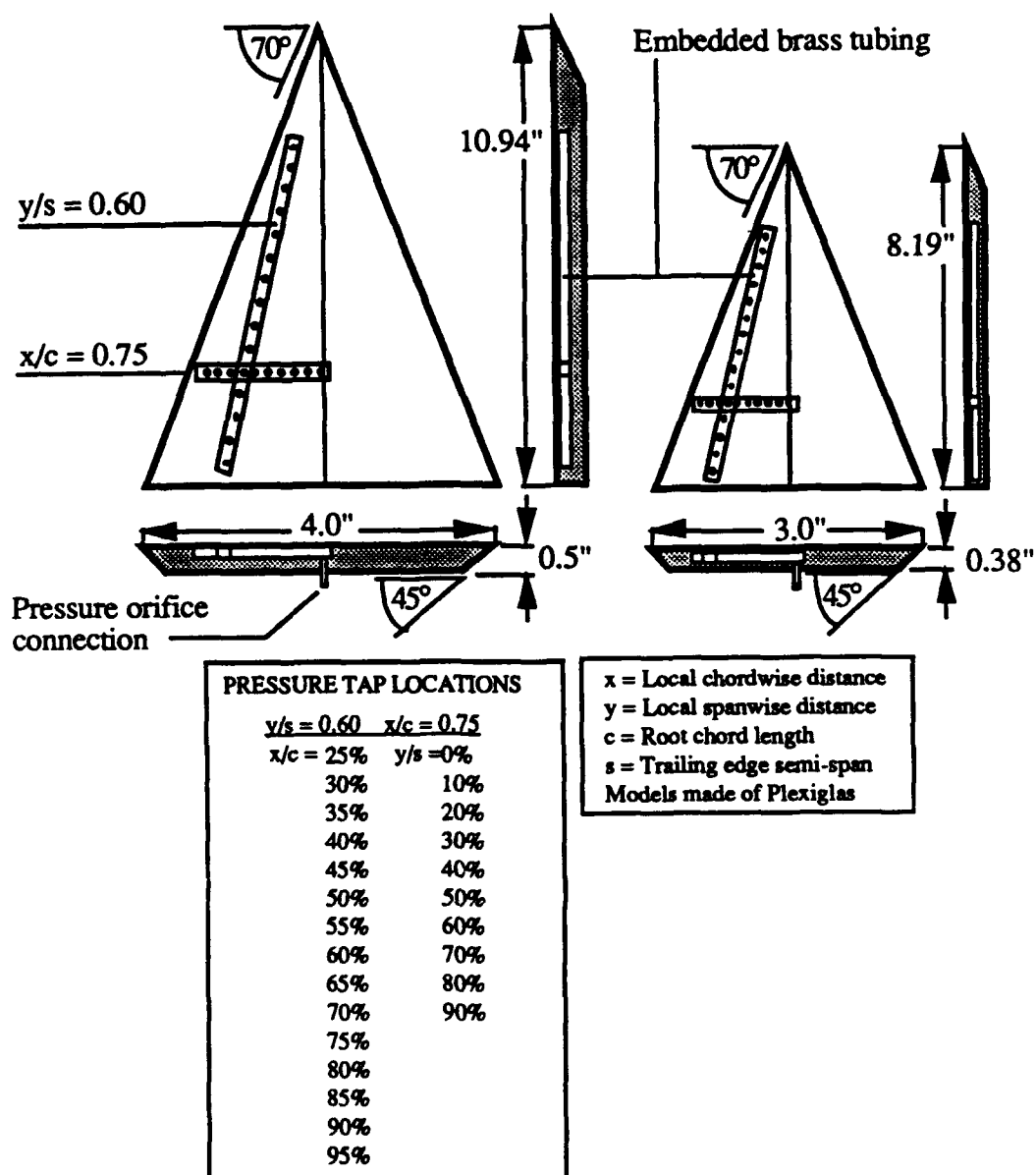
Figure 2.3d   Delta Wing Model: Subscale Blockage Effect Test Models

2.4   Unsteady Pitching Mechanism

In order to produce the unsteady pitching motion, a drive system was designed and built. A schematic of this system is shown in Fig. 2.4. Details on the design can be found in LeMay (1988). The mechanism consisted of a five bar linkage powered by a DC motor. The system was designed to allow for a variety of angle of attack ranges and pitch rates.
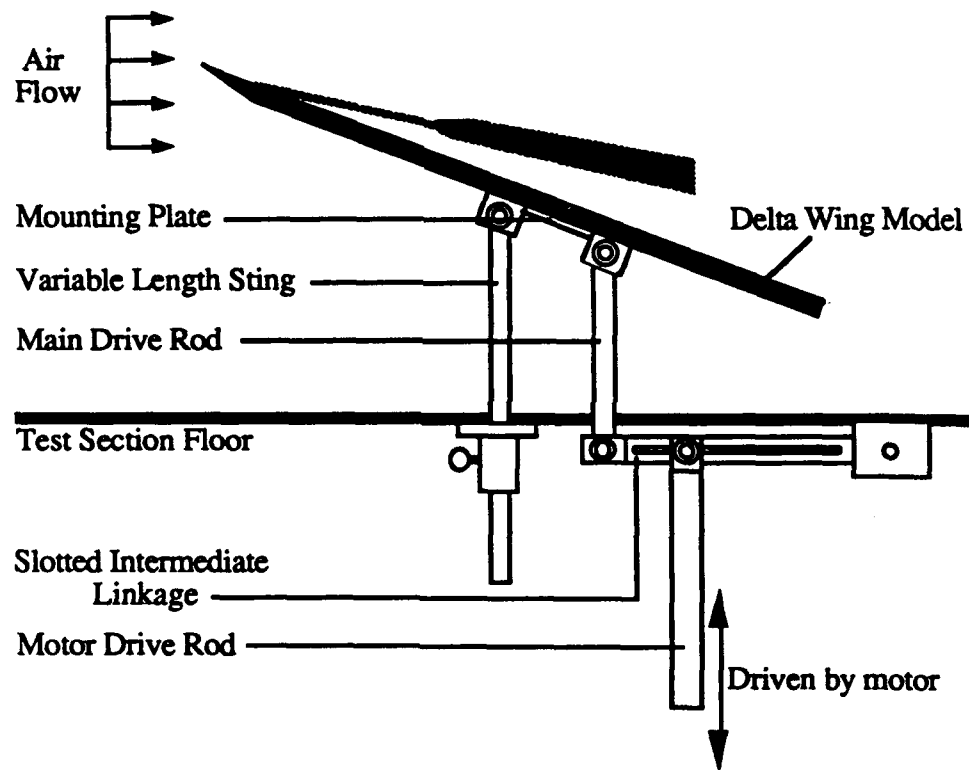
Figure 2.4   Unsteady Pitching Mechanism

2.4.1 Support and Drive Mechanism

The unsteady pitching mechanism consisted of a five bar linkage: one member was the mounting plate for the test models, one was the sting, one was the test section floor, one was a slotted pivot arm, and one was the model drive rod, powered by the motor. The entire linkage was made from aluminum. The mounting plate was 3.5 in. (8.9 cm) long and was used to attach the delta wing model to the pitching mechanism. The pivot point of the wing was located $\frac{5}{8}$ in. (1.6 cm) below the bottom surface of the model. The model was usually mounted such that this pivot point was located at the $x/c = 0.50$ point, although not for every test. An aluminum plate that mated to the mounting plate was glued to the bottom surface of each model, in order to attach the model to the support. By altering the length of the sting, a wide range of mean angles of attack could be achieved. The linkage was driven by a motor drive rod which was attached to the slotted pivot arm. By altering this point of attachment, the range of travel of the mounting plate could be changed, effectively yielding a variety of angle of attack ranges. A maximum range of travel of 60° could be obtained.

2.4.2 Motor and Gear Box

Powering the five bar linkage was a 1 hp 90V DC electric motor connected to the linkage through a gear box and a drive rod. This is shown in Fig 2.5. The motor was manufactured by Dayton Electric, model 2M170C, and was controlled by a silicon control rectifier (SCR) motor controller, Dayton Electric model 2M171C. The SCR controller was capable of controlling the speed and direction of the motor rotation. A change in the motor speed corresponded to a change in the pitch rate of the model. The motor was then connected by a drive belt to a gear box. A gear box was used in the system so that higher motor speeds could be used, thus yielding a smoother operation of the entire system. Gear

ratios of 14.22:1 and 26.66:1 were used, depending on the desired pitch rate. Smooth model motion with pitch rates up to 2.2 Hz could be achieved with this system. However, this is dependent on the range of travel; as the range increases the maximum pitch rate which can be used without distortion decreases.

Connected to the motor was an incremental optical encoder, used to measure motor speed. The speed was read by a digital counter. This counter provided a resolution of 1 rpm.
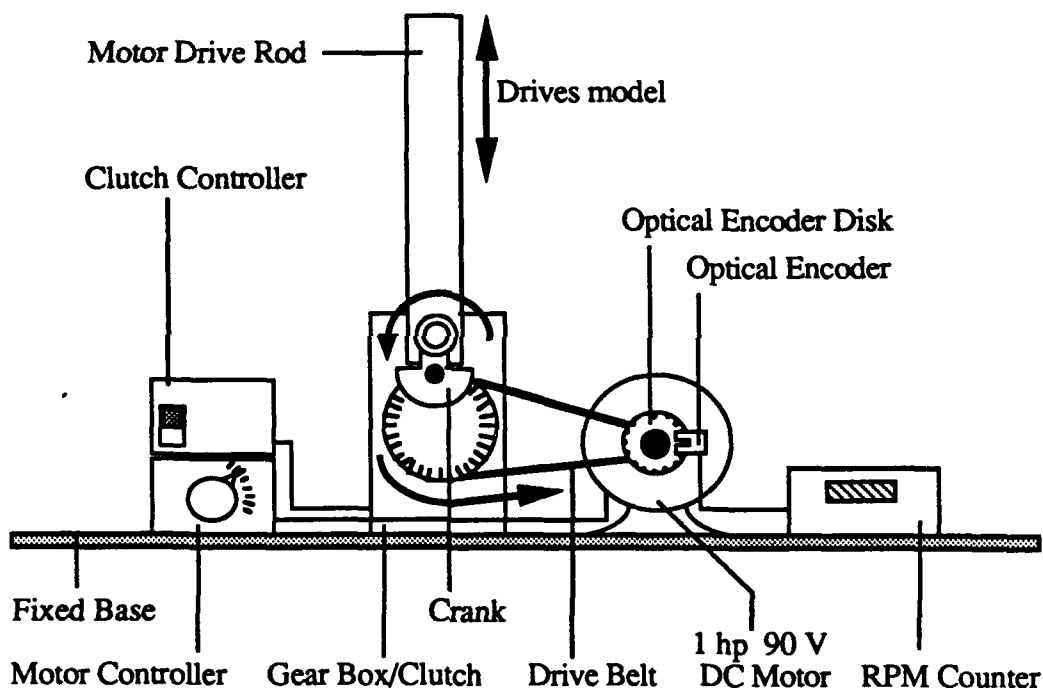
2.5   Schematic of Motor and Gear Box Arrangement

A gear box was designed that contained both a brake and an electric clutch. Thus the motor could be allowed to run continuously regardless of the model motion. To operate the electric clutch, a control box was built that allowed for the clutch to be engaged either

continuously or for a portion of the cycle. This control box contained a trigger which was connected to a potentiometer. By changing the value of the potentiometer the time duration of the clutch engagement could be changed, thus changing the extent of the model motion. Thus the model could be oscillated in a continuous sinusoidal motion, or in a portion of a sine wave. For additional information on this mechanism see Thompson, Batill, and Nelson (1989 and 1991) or LeMay (1988). The entire motor, controller, and gear box assembly was mounted beneath the test section.

2.4.3 Linear Variable Differential Transformer and Power Supply

The angle of attack of the wing was measured using a linear variable differential transformer (LVDT). This transducer was a Trans-Tek Series 240, model 0245-0000. This piece of equipment operates by emitting a voltage that is linearly proportional to the amount of displacement of the core, which is a piece of 0.12 in. (0.30 cm) diameter steel rod. Additional information on this can be found in LeMay (1988). The LVDT has an input voltage range of 5-30 V DC; 15 V was chosen to maximize the resolution of the output voltage while staying within the voltage limit of the computer analog-to-digital hardware. A Hewlett-Packard dual output regulated power supply, model 6234A, was used to power the LVDT.

The LVDT was mounted on the same shelf as the motor, and the core was connected to the model drive rod. Thus the core was free to move vertically as the model pitched. As the angle of attack range increased, the increasing amount of angular motion of the drive linkages resulted in an increased horizontal component of the model drive rod. This could be detected in the calibration of the LVDT and will be discussed in section 3.1, Equipment Calibration. Both the LVDT and the power supply were found to be very reliable.

2.4.4 Harmonic Distortion

By recording the LVDT time history during sinusoidal pitching oscillations it is possible to analyze the accuracy of the pitching mechanism in creating a sinusoidal variation in angle of attack. The can be done by examining the power spectral density of the LVDT signal as a function of frequency. The power of the harmonics can then be expressed as a percentage of the power of the fundamental frequency (i.e., the pitching frequency). This is similar to the method used and described by LeMay (1988). By doing this for several different ranges of motion and pitching frequencies, it was found that for all configurations the harmonic distortion was less 8%.

2.5 Flow Visualization Equipment

Flow visualization was used in several different manners during the course of this research. Smoke particles were entrained into the leading edge vortex to mark its trajectory as well as the location of vortex breakdown. In addition, streaklines were visualized to aid in understanding the effects caused by blockage of the delta wing model at high angles of attack. Two types of smoke flow visualization were employed; titanium tetrachloride ($TiCl_4$) and kerosene.

The method of using titanium tetrachloride has been documented by Visser, Ng, and Nelson (1988). In general, the method is as follows. An inert gas, in this case nitrogen, is pumped into a flask containing titanium tetrachloride, a colorless liquid. The vapor pressure of the $TiCl_4$ is low enough that it is absorbed into the nitrogen. The mixture is then pumped through plastic tubing to the point at which the streakline is desired. Upon contact with air, the $TiCl_4$ reacts with the water vapor in the ambient air to form titanium dioxide particles in the form of a dense white smoke, and hydrochloric acid vapor. Due to

the presence of the hydrochloric acid vapor the resultant smoke is both toxic and corrosive. The majority of the titanium dioxide particles are from 0.5-1.0 μm in diameter.

Kerosene smoke was formed by dripping the kerosene onto electric strip heating elements, thus vaporizing it and forming a white smoke. This smoke was then blown through a series of pipes designed to cool the smoke, thus eliminating buoyancy effects. The smoke was introduced into the flow upstream of the contraction section. A complete discussion of this system, along with schematics, can be found in Mueller (1978).

During the flow visualization experiments, illumination was provided by a 1000 watt lamp. This lamp was typically placed above the test section, pointing down through the glass section onto the model.

2.6   Videotape Equipment

In order to analyze the flow visualization experiments, and obtain quantitative information such as vortex breakdown location, the experiments were recorded on video tape. Two video cameras were available, and each was used at a different stage in the research.

One camera used was a Panasonic Digital WV-D5000 System camera with a 10.5-126 mm zoom lens. This camera was capable of inverted image and an effective exposure duration of a minimum of one-thousandth of a second (with a frame rate of one-thirtieth of a second). Another camera used was a Sony SSC-S20 video camera. This camera used a $\frac{1}{2}$ in. charge-coupled device (CCD). It had a resolution of 460 television lines, an effective exposure duration of a minimum of one ten-thousandth of a second, an f/1.2 aperture lens, and was capable of sensing a minimum illumination of 4 lux.

Two video recorders were also available to record the videotape. The first was a Panasonic NV-8950 video recorder used with standard VHS videotape. The second was a Panasonic 7750 video recorder. This unit could be used with either standard or super VHS

videotape; super VHS was typically used to improve the image quality. This unit also made possible precise control over the videotape playback rate and single frame advance.

The first sets of experiments were performed using the Panasonic camera and Panasonic NV-8950 recorder; these were the replaced by the Sony camera and Panasonic 7750 recorder for improved videotape quality. As the flow visualization data is discussed the specific system used to record it will be noted.

2.7   Pressure Transducers

For the majority of this research three electronic manometers manufactured by Setra Systems were used to measure pressures, both steady and unsteady. Each of these units contains a differential pressure transducer, conversion circuitry, a digital display (in inches of water), an adjustable bias, and an analog output connection; all encased in a metal housing. Two of these had a range of 0-0.2 psi (0-1370 Pa), while one had a range of 0-0.02 psi (0-137 Pa). The former were model 339H while the latter was a model 339B. The low range manometer was used to measure the freestream dynamic pressure while the two high range manometers were used to measure the delta wing surface pressures.

An additional pressure transducer was used during a portion of this research. It was chosen so that it could fit within the delta wing model. A Nova Sensor differential pressure transducer, model NPH-8-2.5DH, was built into one of the pressure models. Its range was 0-0.36 psi (0-2491 Pa). This transducer consisted of a body that was 0.45 in. (1.14 cm) in diameter and 0.27 in. (0.69 cm) long and a tube coming out from the sensing element that was 0.19 in. (0.48 cm) in diameter and 0.47 in. (1.19 cm) long. A 0.125 in. (0.32 cm) diameter reference pressure tube was attached to the rear of the transducer. The full scale output was 43 millivolts, yielding a sensitivity of 4.3 millivolts per psi (the nominal full scale output of this model is 50 mV). The transducer was powered by a constant current supply rather than a constant voltage supply to minimize the drift due to

temperature. A current supply of 1.5 milliamps was used. A circuit board was designed to contain the current supply and the analog output signal hardware.

2.8   Data Acquisition Equipment

To analyze the flow visualization experiments, a Data Translation Quickcapture frame acquisition board was used. This board could be used with either an Apple Computer MacIntosh II or a DTK 486 computer. The MacIntosh II was used initially, along with software developed in-house to acquire coordinates from the captured images. This system was later upgraded to a professional image processing center with the DTK 486. The software used on this system was Global Lab Image. The specific system used will be noted as the data is discussed.

The pressure data was acquired using a MacIntosh II and a National Instruments analog-to-digital board. This board was an NB-MIO-16H 12 bit board with an A/D conversion rate of 9 μsec. An input voltage range of -10 to +10 volts was used, yielding a resolution of 4.88 mV with a gain of one. Programmable gain settings of 1, 2, 4, and 8 were available. Due to hardware limitations the different channels of data were sampled sequentially rather than simultaneously. The software used to control the data acquisition was written in part using National Instruments LabView 2.0.

III   EXPERIMENTAL PROCEDURE AND DATA REDUCTION

3.1   Equipment Calibration

The following pieces of equipment required calibration prior to conducting an experiment: the linear variable differential transformer (LVDT), the Setra electronic manometers, and the Nova pressure transducer.

The LVDT was calibrated throughout the angle of attack range to be used. Angle of attack was obtained by measuring the incidence of the model relative to the wind tunnel floor. The output voltage of the LVDT was then measured. Thus, during an unsteady motion, the instantaneous angle of attack could be obtained by measuring the instantaneous LVDT output voltage and converting it to angle of attack.

For angle of attack ranges of approximately 15° or less, the calibration of the LVDT was linear. The LVDT is connected to the model drive rod in such a way as to measure the vertical displacement only. For a range of motion of 15° or less the model drive rod moves primarily vertically, with a negligible horizontal component. Thus, the correspondence of the LVDT voltage to the angle of attack is linear. However, angle of attack ranges of up to 60° were used during the course of this research. As the range of motion increases, the horizontal component of the model drive rod increases, which the LVDT is not capable of resolving. Thus the linearity of the calibration decreases. This was also noted by LeMay (1988). However, this did not cause a problem in the measurement of angle of attack. A representative calibration curve is shown in Fig. 3.1. A curve fit is shown along with the set of measured calibration points. This curve fit is a third order equation. Note that even with the nonlinearity of the data (particularly at very large angles of attack), a very good curve fit can be applied. The curve fit was within 0.2° of the measured angles of attack.

49
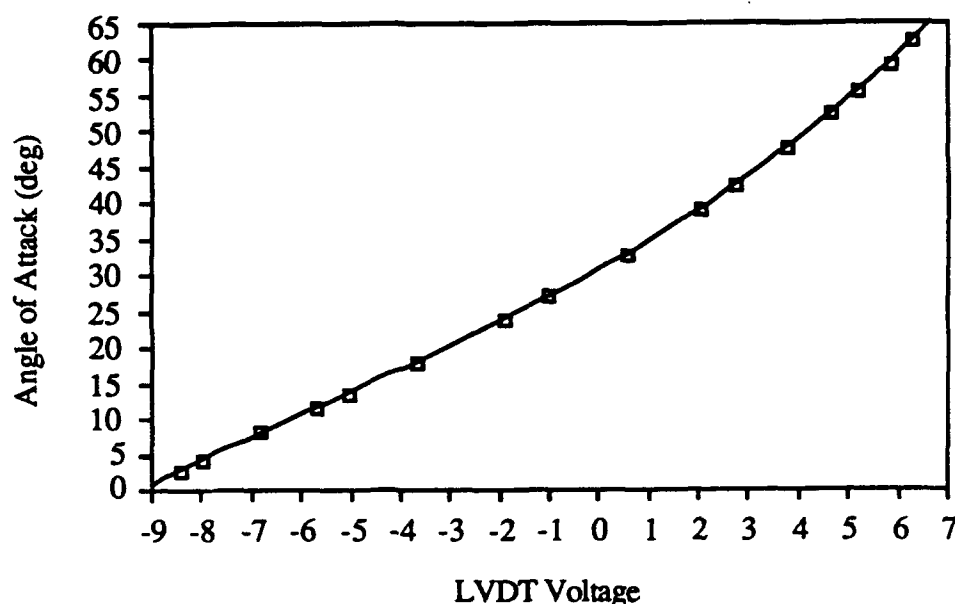
Figure 3.1   Representative LVDT Calibration Curve: 2-60° Range of Motion

The LVDT was typically calibrated prior to each set of tests. This calibration consisted of ten to fifteen points measured over the angle of attack range to be used. Repeated measurements were taken during the testing to check the alignment of the LVDT. No significant change in the calibration occurred either during the testing or between tests.

The Setra electronic manometers were calibrated prior to testing. This was accomplished by subjecting the manometers to a pressure source which was also measured with an inclined water manometer. Thus, the pressure could be read directly in inches of water, then compared to the output voltage of the manometer (measured with a voltmeter). Repeated calibration measurements were made several times and the calibration constants of these instruments were found to be very repeatable; within the uncertainty of the calibration measurements. Any drift due to temperature could be removed with the adjustable bias on the front panel. A side note regarding the use of these instruments involves the front panel display of the pressure. It was found that the display circuitry did not accurately convert

the measured voltage to units of pressure, hence a calibration would be required for the display. However, the voltage was measured directly, bypassing the use of the front panel display.

The Nova pressure transducer was calibrated in the same manner, by referencing it to a water manometer connected to a common pressure source. However, for this case the voltage was measured using the computer data acquisition system (as opposed to a voltmeter which was used when calibrating the Setra manometers). Thus, the signal from the Nova transducer could be amplified to increase the resolution; a gain of eight was used. The Nova transducer was calibrated prior to each set of tests, and repeated calibration measurements were performed prior to each individual test. This transducer was also found to have a calibration constant that was repeatable within the uncertainty of the measurements. Unlike the Setra manometers, the Nova transducer had a zero pressure offset which could not be adjusted. This offset varied slightly with temperature and thus was measured before each test. The measured offset was consistent with the manufacturer's specification of ± 4 mV.

The accuracy with which these instruments could be calibrated is discussed in section 3.5.

3.2   Flow Visualization Procedure

Titanium tetrachloride (TiCl$_4$) was used as the flow visualization method for the vortex breakdown location experiments. A plastic tube was connected on one end to the flask of TiCl$_4$, then passed along the model support through the tunnel floor, then connected on the other end to a stainless steel tube (0.072 in. diameter, 0.18 cm) embedded in the model. Tygon brand plastic tubing was used throughout the flow visualization system (this same brand of tubing was used during the surface pressure testing, as pressure lines). The steel tube exited from the model near the apex; the location had been previously

seen to be good for entraining smoke particles into the leading edge vortex core. Thus when nitrogen was supplied to the $TiCl_4$ from an adjacent tank, the mixture of nitrogen and $TiCl_4$ was fed to the apex of the model where the resulting smoke particles visualized the leading edge vortex. Nitrogen was used as an inert gas capable of absorbing the $TiCl_4$. The leading edge vortex on only the left side of the model was marked with smoke. This was the side that the glass window and the camera were located on. Since the model was positioned at zero sideslip (within $0.3°$ uncertainty) it is assumed that the leading edge vortices are symmetric, thus the behavior of only one vortex was recorded (however, the possibility of flow asymmetry was examined during the surface pressure tests).

After exiting the model and marking the vortex, the smoke was then convected downstream where is was exhausted to the atmosphere. Periodic cleaning or replacing of the plastic tubing was required to maintain consistent smoke generation. The flow visualization quality depended on several factors, including freestream air humidity, freestream air velocity, proper lighting, and condition of flow visualization equipment. The quality (essentially the density) of the smoke typically degraded with increasing wind speed. Other factors being optimal, useful flow visualization could be conducted for freestream velocities up to roughly 55 ft/s (15.2 m/s).

The video camera was placed on a tripod located close enough to the test section that the full field of view was utilized while ensuring that the model would be visible throughout the full range of motion. This was roughly 6 ft (1.83 m) from the test section. The camera lens was placed even with and centered on the pitch axis of the model. A flood light was placed above the test section to illuminate both the smoke and the model while leaving the background dark. The exact location was adjusted until a video image with good contrast was obtained.

After the experiments were conducted, the videotapes were digitized one frame at a time to obtain vortex breakdown location as a function of angle of attack, for both the steady and unsteady case. This was accomplished by acquiring the video image from the

video recorder with the video frame acquisition board. The video recorder was equipped with a video output connection for this type of transferral. Each captured frame was then analyzed to obtain pertinent information such as angle of attack and breakdown location. Typically this was accomplished by digitizing five points on each frame; two on the sting, one at the model apex, one at the model trailing edge, and one at the breakdown location. This is shown in Fig. 3.2.

A-B : Establishes vertical reference line
C-D : Establishes incidence and chord line
E   : Establishes vortex breakdown location
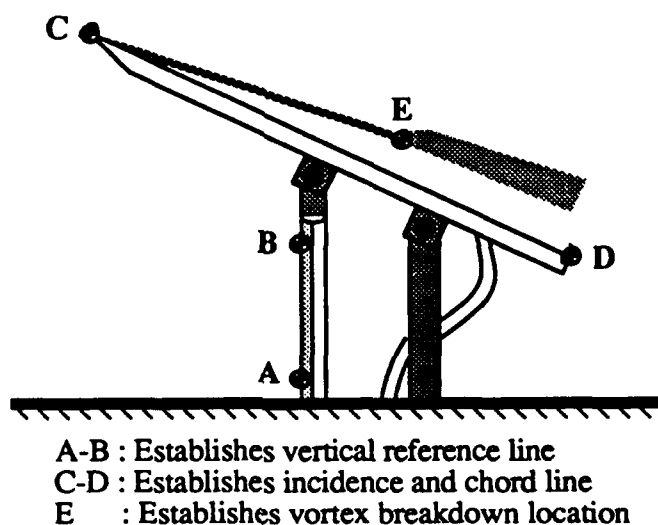
Figure 3.2   Digitized Points from Flow Visualization Videotape

For the steady cases, from 10-30 frames were digitized at each steady angle of attack in order to obtain an average value of the breakdown location. The amount of deviation from this mean value was also calculated for these frames of data. For the unsteady cases, from 35-45 cycles of motion were analyzed for each case, with 20-35 frames digitized per cycle (depending on the pitch rate and the quality of the flow visualization). The breakdown location data could then be ensemble averaged if desired. This entails averaging the breakdown location from each cycle at matching angles of attack,

giving an average location for each instantaneous angle of attack during the unsteady motion. However, for some very large angle of attack excursions the scatter in the data was often such that ensemble averaging led to misleading results; thus the data was left as individual cycles.

Section 3.5 contains a discussion of the accuracy of the digitization process and the subjectivity in choosing a specific point to represent vortex breakdown.

3.3   Acquisition of Steady Pressures

The delta wing surface pressures were obtained by using two electronic manometers, a pitot-static probe located in the freestream flow, and the surface pressure orifices located on the delta wing model. A schematic of the experimental setup is shown in Fig. 3.3. The pitot-static probe was connected to one of the manometers using plastic tubing. The difference between the freestream static pressure and the freestream total pressure was then measured, giving the freestream dynamic pressure, q. Note that the freestream total pressure is not necessarily the same as the atmospheric total pressure due to a total pressure loss through the wind tunnel screens (located at the contraction section inlet). Quantitative information on this subject exists in Thompson, Batill, and Nelson (July, 1989). Thus to obtain an accurate reading of the freestream dynamic pressure the total pressure needs to be measured inside the test section.

The second manometer was used to measure the delta wing surface pressures. The difference between the surface static pressure and the freestream total pressure was measured by this manometer. The freestream total pressure was obtained by connecting the total pressure tube from the pitot-static probe to a manifold, allowing the total pressure to be connected to both manometers (as shown in Fig. 3.3).

Pitot-static probe

Pressure lines connected
to surface pressure orifices

Four-way manifold

A: $P_{total} - P_{\infty} = q_{\infty}$

B: $P_{total} - P_{tap}$

C: $P_{total} - P_{tap}$

Electronic manometers
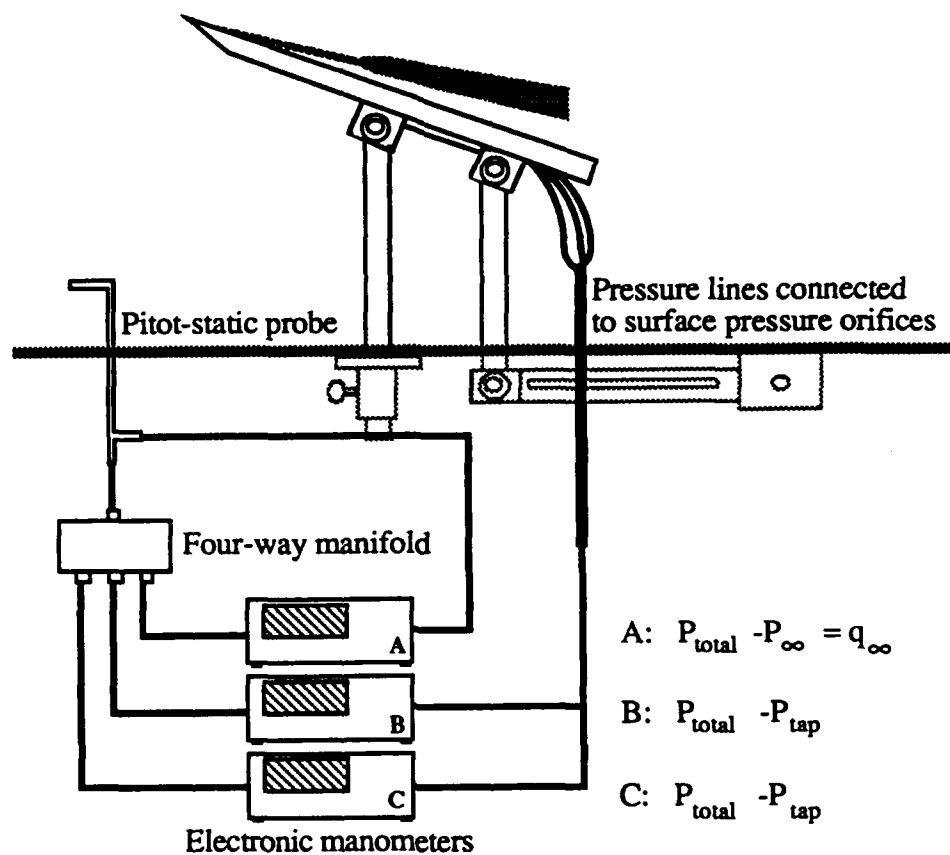
· Figure 3.3   Schematic of Steady Pressures Experimental Setup

The pressure coefficient C_p was defined in the following characteristic manner:

$$C_p = \frac{P_{tap} - P_{\infty}}{q_{\infty}}$$

(3.1)

where P_{tap} is the local static pressure at a specific pressure orifice, P_{∞} is the ambient static pressure, and q_{∞} is the freestream dynamic pressure.

Equation 3.1 can be rewritten in terms of the quantities measured by the manometers:

$$C_p = 1 - \frac{P_{total} - P_{tap}}{P_{total} - P_{\infty}} \qquad (3.2)$$

where P_{total} is the freestream total (or stagnation) pressure.

The numerator term in Equation 3.2 was the quantity measured by the second manometer while the denominator term was measured by the first manometer. Thus, by connecting the two manometers in the manner described above, the calculation of the pressure coefficient Cp was made very straightforward.

Typically during the steady pressure acquisition, two manometers were used to measure the surface pressures. Thus, the pressures from two surface locations could be measured during each test, thereby decreasing the time required to obtain a complete pressure profile. A four-way manifold was used to direct the freestream total pressure into three separate tubes (one for each manometer).

Thus, during a typical steady pressure experiment, four quantities were recorded: angle of attack, freestream dynamic pressure, and the surface pressures from two surface pressure taps. This was done by connecting the analog output of each instrument to the appropriate channel of the computer analog-to-digital circuit board. These quantities were each measured as a voltage (either from the LVDT or the electronic manometers) which then had to be converted to the appropriate units. Software was written to control the data acquisition process and parameters such as sampling rate and sample size. For the steady pressures, typically 2000 samples were obtained at a sampling rate of 1000 Hz. This combination was found to provide a repeatable mean while minimizing data acquisition and conversion time. The average and standard deviation of the 2000 samples were then calculated.

In order to obtain the steady pressure profile along an entire line of pressure taps, the above process was repeated two pressure taps at a time, until all the surface locations had been sampled. The model was outfitted with a separate plastic tube for each pressure tap; this bundle of tubes then passed from the model to the manometers. The entire set of pressure taps could be alternately sampled by selecting the appropriate tube from the bundle. The pressure taps not currently being sampled were sealed off at the model surface with a piece of adhesive tape. The selection of the desired tube was accomplished by hand; a multiplexer or computer controlled stepping valve was not used.

A survey of the steady surface pressures was taken prior to the unsteady testing. This data was obtained to be used as a comparison to both data available in the literature (an extensive amount of steady pressure data exists) and to the unsteady pressure data. Steady pressure profiles were obtained on each of the delta wing models along several lines of pressure taps. Angles of attack ranging from zero to sixty degrees were used, as well as Reynolds numbers ranging from 150,000-500,000.

The accuracy with which these pressure measurements could be made, as well as the standard deviation of the averaging process is discussed in section 3.5.

3.4   Acquisition of Unsteady Pressures

The general setup for the unsteady pressure acquisition was similar to that described above for the steady pressures. The same arrangement of pitot-static probe, electronic manometers, and plastic tubing was used (as shown in Fig. 3.3). The definition of pressure coefficient was also the same. The primary difference between the two experimental methods involves the software used to control the data acquisition. Note that when making unsteady pressure measurements, the size of the plastic tubing used to measure the pressures is important. This issue will be addressed in section 4.1.

Making measurements of a system undergoing an unsteady motion introduces the additional variable of time. It is necessary to be able to correlate the pressure measurements with the time history. To do this the instantaneous angle of attack must be measured as the surface pressures are being measured. The freestream dynamic pressure must also be simultaneously sampled in order to compute the pressure coefficient. However, simultaneous data sampling could not be achieved with the available computer hardware. Thus sequentially sampling was used with a sampling rate that was extremely high compared to the rate of unsteadiness; larger by four orders of magnitude. A preliminary experiment was conducted to determine if this was sufficient to approximate simultaneous sampling. It was found that with a sampling rate that high, the time interval between the sampling of each channel could not be detected in a given unsteady signal.

Sampling at such a high rate for the duration of an entire pitching cycle resulted in a large data sample, on the order of 10^4. This large number of data points was then substantially reduced (for example by only using every hundreth point) to facilitate graphing.

Unsteady pressure data was obtained during twenty five cycles of motion. This number was found to provide a representative average while reducing computational requirements and time. These twenty five cycles of data were then ensemble averaged by averaging the twenty five pressure readings at each instantaneous angle of attack. The standard deviation was also calculated for each point, providing a measure of the relative fluctuation of the pressures at each point in the pitching cycle.

This was performed using two surface pressure taps at a time. The test would then be repeated at the same conditions (Reynolds number and pitch rate) for another two pressure taps. This was repeated until an entire pressure distribution was obtained. By fitting the model with pressure tubes for each tap it was not necessary to open the test section (thus disturbing the flow) in between tests.

When quantifying the level of unsteadiness of an unsteady motion, it is typical to use a nondimensional pitching frequency. This quantity is often termed the reduced frequency and has a definition similar to that of the Strouhal number (another dimensional variable used with oscillating flows). The reduced frequency k is defined by:

$$k = \frac{2\pi f c}{U}$$
(3.3)

where f is the pitching frequency, c is the root chord length, and U is the freestream velocity. This parameter is a measure of the unsteadiness of the model relative to the convective time of the flow. Thus k can be separated into these two components:

$$k = 2\pi f \text{ (frequency of oscillation)} * \frac{c}{U} \text{ (convective time)}$$
(3.4)

Some of the unsteady delta wing research available in the literature defines k without the factor of two in the numerator. When making comparisons with data from the literature the reduced frequency will be converted to the definition given in Equation 3.3 if it was originally defined differently.

The pressure model was outfitted with three lines of pressures taps: one at a constant span location and two at constant chord locations. A constant span location of y/s = -0.60 was chosen due to its proximity to the leading edge vortex core. It has been seen by several researchers (Payne, 1987; LeMay, 1988; Roos and Kegelman, 1990) that the vortex core lies roughly at this span location for a wing with a leading edge sweep angle of 70°; the exact position is a function of several parameters including angle of attack and leading edge geometry. Two additional lines of pressure taps were added in order to define the spanwise pressure distribution; these taps were placed at constant chord locations of x/c = 0.50 and x/c = 0.75.

During the course of the experiments there were three primary factors that were investigated: angle of attack range, pitch frequency, and Reynolds number. The possible angle of attack ranges were divided into three categories: ranges that did include vortex breakdown, ranges over which breakdown existed over the wing for the entire motion, and ranges over which breakdown moved onto and off of the wing. The Reynolds number range selected was limited by two factors. First, the high end of the Reynolds number range was limited by the maximum capacity of the wind tunnel given the current experimental setup. Second, the low end of the Reynolds number range was determined so that the freestream velocity was large enough to ensure a sufficient resolution of the surface pressures by the pressure transducers. This resulted in a range of possible Reynolds numbers of approximately 75,000-600,000. Pitch frequencies of up to 2.2 Hz could be attained with the unsteady pitching mechanism. However, for large ranges of motion such as 0-60°, the practical limit is 1.2 Hz before the smooth performance of the pitching mechanism degrades due to the inertia of the model (thus higher frequencies could have been obtained for a model of less weight). Several pitch frequencies were chosen over this range. In addition, some pitch frequencies were chosen in order to correlate the results with data available in the literature. Table 3.1 contains a list of dimensional pitch rates for several values of Reynolds number and the reduced frequency k.

TABLE 3.1

DIMENSIONAL PITCH RATE AS A FUNCTION OF REYNOLDS NUMBER AND

REDUCED PITCH FREQUENCY

Value are the dimensional pitch rate f in Hz.

All values are for the full scale wing, chord length = $16\frac{7}{16}$ in.

Reduced frequency k is defined by: $k = \frac{2\pi f c}{U}$

k :	Reynolds Number (Freestream Velocity) :		
	150,000 (18 ft/s)	250,000 (30 ft/s)	500,000 (60 ft/s)
0.03	0.063 Hz	0.104 Hz	0.209 Hz
0.06	0.126	0.209	0.417
0.09	0.188	0.314	0.626
0.12	0.251	0.417	0.835

3.5   Uncertainty Analysis

This section contains an analysis and discussion of the uncertainties in the experimental parameters, including equipment, measurement uncertainty, mathematically propagated errors, statistical uncertainty, and repeatability. The section begins with a discussion of the calibration of the pressure transducers. Following this is a discussion of the uncertainty in the Reynolds number and pitch frequency. The uncertainty in the flow visualization and surface pressure methods are then discussed. The section closes with discussions of the statistical uncertainty and the repeatability of the data.

3.5.1 Calibration of Pressure Transducers

The electronic manometers were calibrated by measuring ten points and fitting a straight line to those points; the slope of the line is then the calibration constant. During the calibrations it was found that the output voltage of the electronic manometers could be measured within 0.09 volts, and the pressure from the inclined water manometer could be measured within 0.08 inches of water (0.042 psf, 2.0 Pa). For the electronic manometer this corresponds to a maximum error of 1.1-17.0% over the full range of the manometer, depending on the magnitude of that measurement. For the inclined water manometer this range is 0.1-13.3% for any given pressure measurement.

These error ranges are on each point calibration individually; the ultimate goal is the slope of the line fit to the points as a whole. This is obtained by a linear curve fit which has associated with it a standard error of the fit. Fitting a line to all ten calibration points, it was found that the maximum possible error in the slope of that line was 0.9%. Thus the maximum possible error in the calibration constant is 0.9%.

The Nova pressure transducer was calibrated in the same manner, thus the error in measuring the pressure (from the inclined water manometer) is the same as for the Setra manometers. The output voltage of the Nova transducer could be measured within 0.1 mV (this represents the accuracy of the 12 bit A/D conversion hardware). During the calibration, from 20-25 measurements were made, each at a different pressure. After subtracting the zero pressure offset value, the calibration constant was then calculated for each point. The average of these was then used as the calibration constant. Each of the 20-25 points was found to vary less than 2% about the mean value. Note that any error made in measuring the zero pressure offset would be apparent when the calibration constant was computed; a constant difference would be visible in each data point. Thus the error in measuring the offset did not effect the accuracy of the calibration constant.

3.5.2 Reynolds Number and Pitch Frequency

Prior to a specific experiment, the nominal Reynolds number is specified and the appropriate freestream velocity calculated and set by adjusting the wind tunnel fan speed. Then during the course of the experiment, the Reynolds number is checked, and the freestream velocity is manually changed if the measured value is not within the uncertainty of the nominal value.

Throughout this research the Reynolds number has been calculated using the standard equation:

$$Re = \frac{\rho U c}{\mu} \qquad (3.5)$$

where c is the wing centerline or root chord length.

By using the method of Kline (1985), an estimate can be derived on the uncertainty of the Reynolds number (as determined from the measured freestream dynamic pressure). This is done by estimating the uncertainty of the measurement of each of the variables in Equation 3.5. A more complete description of this method is given in section 3.5.4. By using this method it can be determined that the measured Reynolds number is accurate within 11%. This value was used as the criterion for adjusting the freestream flow during testing. Note that when the experimental data is discussed, it will be referred to by the nominal Reynolds number.

The accuracy with which the pitch frequency could be set depended on two parameters: the accuracy of the optical encoder used to measure the motor speed, and the reliability of the motor itself. The optical encoder system had a resolution of ±1 rpm. It was found that the motor itself could be held to ±3 rpm about a given setting, hence the resolution of the encoder was within the consistency of the motor. The range of pitching

frequencies used during this research corresponded to a range of motor speeds of 90-1200 rpm. Thus the motor speed was accurate within 3.3% of the specified setting. This corresponds to a maximum possible error in the stated value of the reduced frequency (defined by Equation 3.3) of 3.4%. This would occur at the lowest reduced frequency; as the reduced frequency increases, the possible error decreases. At the largest reduced frequency the possible error is only 0.33%.

3.5.3 Flow Visualization Method

There are several important factors affecting the accuracy of the digitization of the flow visualization videotapes. The first is the inherent unsteadiness of the vortex breakdown. The shape of the vortex breakdown smoke pattern was seen to vary between individual frames of a videotape. In some cases the vortex core could be seen to expand suddenly from a tightly rolled core to a wider breakdown region. In other cases the core would gradually expand into the breakdown region.

This is shown in Fig. 3.4, which shows the breakdown at the same steady angle of attack, but in two different forms. A sudden expansion of the core is shown on the left while a gradual expansion is shown on the right. The lower half of Fig. 3.4 shows how the specific "point" of breakdown was chosen. The intersection of the vortex core with the breakdown area is indicated with an arrow; this intersection has been used as the point of breakdown.

Thus some subjectivity exists in the digitization of a single point to represent the location of breakdown. Note that this is increased for a poorly-defined breakdown, as shown in the right half of Fig. 3.4. Uncertainty due to subjectivity was minimized by the consistency resulting from the analysis of numerous frames.
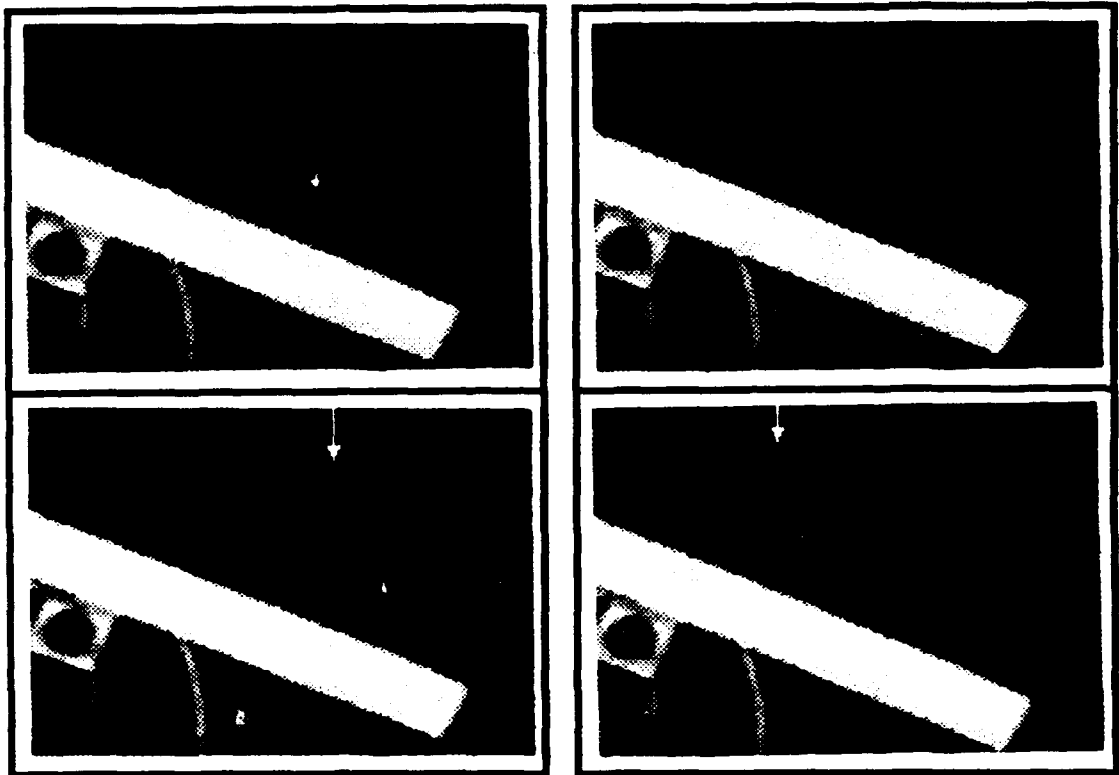
Figure 3.4   Examples of Well-Defined Vortex Breakdown (left) and Poorly-Defined

Breakdown (right). Method of Pinpointing Breakdown Shown in Lower Half.

In addition, at a steady angle of attack the breakdown can be seen to oscillate up to

as much as ±4% of the root chord from its mean position. This unsteadiness is indicative

of the extreme sensitivity of the breakdown location to such flowfield conditions as

downstream pressure gradient and flow irregularities. The effect of this steady state

oscillation was minimized by digitizing from ten to thirty frames of the video tape at each

steady angle of attack. Thus an average steady breakdown location was obtained (as well

as the amount of variation from that position for the digitized frames). Figure 3.5 shows

an example of the individual data points and the mean value. This figure shows breakdown

location (of a representative case) as a function of time for a steady angle of attack. The mean location is x/c = 0.396, yet the actual location varies from 0.35 to 0.43.
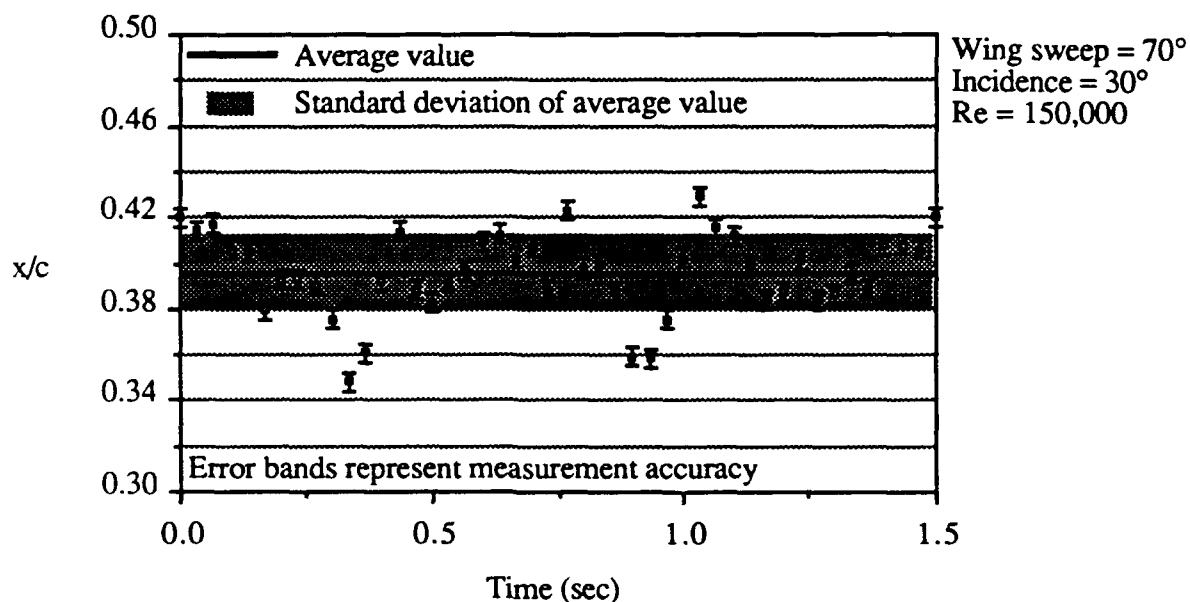
Figure 3.5   Steady Vortex Breakdown Location as a Function of Time with Average Location Shown

Included on this figure are error bands on each point; this is a representation of the uncertainty of each individual measurement. By digitizing the same frame several times an estimate could be obtained of the accuracy of the digitizing process. This was performed several times, digitizing the same frame fifty times. It was found that the breakdown location could be measured within 0.4% of the chord length, while a given angle of attack could be measured within 0.2°. These values were reduced slightly with the upgrade in image analysis hardware (as described in sections 2.6 and 2.8). Using the new equipment, the chord location could be measured within 0.2%, and the angle of attack within 0.15°.

These two values thus represent the accuracy with which a single measurement can be made, and are shown as the error bands in Fig. 3.5. On a frame by frame basis these values vary somewhat due to lighting, flow visualization quality, shape of breakdown smoke pattern, and subjectivity in defining the point of breakdown. This accuracy is consistent with that documented by Wolffelt (1987) and LeMay, Batill, and Nelson (1988). Wolffelt noted an accuracy of 2-3% of the root chord, while LeMay et al. noted an accuracy of 1%. Wolffelt also noted that his accuracy decreased as breakdown moved closer to the apex due to the proximity of the two leading edge vortices to each other near the apex.

Note that the mean value shown in Fig. 3.5 also has an error band; this is the standard deviation of the breakdown location for the individual data points shown. This is shown as a gray zone across the graph. This zone represents the amount of fluctuation in the breakdown position, not the accuracy of the measurement. Thus the accuracy with which the breakdown location can be measured is within the range of scatter due to the unsteadiness of the breakdown; this can be seen in Fig. 3.5.

3.5.4 Temporal and Statistical Uncertainty

It is important to consider that the pressures being measured in this research are fluctuating, time dependent quantities. Even for the case of a steady angle of attack, the surface pressure fluctuates somewhat; the leeward flow field is inherently dynamic and this is reflected in the surface pressure field. During the data acquisition process, an averaging is performed twice. First, when the voltage from the pressure transducer is sampled. Several thousand samples are taken and averaged, yielding a single data point (as described in section 3.3). Second, for the unsteady pressure data acquisition, typically twenty five cycles of data are ensemble averaged together (as described in section 3.4). During each of these averaging processes a standard deviation was computed to quantify the amount of

fluctuation of the data points about the mean. The standard deviation was defined in two ways:

$$\sigma_x = \sqrt{\frac{1}{n} \sum (x - \bar{x})^2} \qquad (3.6)$$

and:

$$s_x = \sqrt{\frac{1}{n-1} \sum (x - \bar{x})^2} \qquad (3.7)$$

where $\bar{x}$ is the average of n values of x.

The difference between Equations 3.6 and 3.7 is that the first is the true population standard deviation, while the second is the standard deviation of a given sample. The values of these two definitions approach the same value as the number of samples (n) increases. For fifty samples the values of σ_x and s_x are within 1% of each other.

The true population standard deviation, Equation 3.6, is used during the steady pressure data acquisition. Two thousand samples are taken at each angle of attack, hence the difference between the two definitions is negligible. However, for the ensemble averaging of the unsteady pressures, only twenty five samples were obtained. Thus the sample standard deviation, Equation 3.7, is used.

Having calculated the standard deviation, it is then possible to define the standard error, which can then be used to define a confidence interval if a normal distribution of the data is assumed. A 95% confidence interval about the mean is given as $1.96 \frac{\sigma_x}{\sqrt{n}}$, thus (Wonnacott and Wonnacott, 1984):

$$x = \bar{x} \pm 1.96 \frac{\sigma_x}{\sqrt{n}} \qquad \text{(with 95\% confidence interval)} \qquad (3.3)$$

This implies that there is a 95% confidence that the value of x will lie within $\pm 1.96 \frac{\sigma_x}{\sqrt{n}}$ of the mean value $\bar{x}$, where x is defined in the following characteristic manner:

$$\bar{x} = \frac{1}{n} \sum_{i=1}^{n} x_i \tag{3.9}$$

level that the actual mean is within the given amount of the calculated mean, $\bar{x}$. Note that the constant 1.96 varies as a function of the number of samples n. For values of n greater than one hundred, the value of this function is 1.96. The validity of assuming a normal distribution and using this equation is discussed in the section 3.6 on graphic presentation. Note that in Equation 3.8, s_x can be substituted for σ_x if appropriate.

3.5.5   Pressure Measurement and Pressure Coefficient Calculation

The uncertainty in the value of pressure coefficient stems from the following sources:

1)   Uncertainty in the calibration of the instruments

2)   Uncertainty in measurement of the surface pressure

3)   Uncertainty in measurement of the freestream dynamic pressure

4)   Computer A/D conversion hardware accuracy

5)   Propagation of the above errors through the calculation of pressure coefficient, Equation 3.2.

The first of these sources, the error in calibration, has been previously discussed. For the Setra manometers the calibration constant used for the conversion from voltage to

pressure has a maximum error of 0.9%. For the Nova transducers this value is 2%. The Setra manometers were used for the majority of the pressure acquisition; the Nova transducers were used to measure pressure only during a preliminary study; this will be discussed in section 4.1. Thus only the Setra manometers will be discussed here.

The second and third sources represent the data acquisition precision. During the current experiments a voltage range of -10 to +10 volts was used with gains of 1 on each channel. Thus with a 12 bit A/D converter the precision was 4.88 mV. For the range of surface pressures recorded, this value corresponds to 0.1-0.9% of the measurement. For the range of freestream dynamic pressures recorded, the precision is 0.1-1.0% of the measurement.

The fourth source is the A/D conversion accuracy. For the hardware used this value is ±1 bit. Thus this error has the same maximum error as the machine precision; ±4.88 mV.

To estimate the effect of the propagation of these errors on the calculation of pressure coefficient the method of Kline (1985) can be used. Using the formula for pressure coefficient defined in Equation 3.2, the uncertainty U_{C_p} of this equation is defined as:

$$U_{C_p} = \sqrt{ \left(U_{(P_o - P_{tap})} \frac{\partial C_p}{\partial (P_o - P_{tap})} \right)^2 + \left(U_{(P_o - P_\infty)} \frac{\partial C_p}{\partial (P_o - P_\infty)} \right)^2 } \qquad (3.10)$$

Equation 3.10 can then be rewritten as:

$$U_{C_p} = \sqrt{ \left(\frac{U_{(P_o - P_{tap})}}{(P_o - P_\infty)} \right)^2 + \left(\frac{(P_o - P_{tap}) \, U_{(P_o - P_\infty)}}{(P_o - P_\infty)^2} \right)^2 } \qquad (3.11)$$

where $U_{(P_o-P_{tap})}$ and $U_{(P_o-P_\infty)}$ are the uncertainties in the two pressure measurements.

Note that Equation 3.11 is dimensionless but does not represent a percentage error; rather it represents the absolute error in the pressure coefficient; itself a dimensionless quantity. This includes the uncertainty in the calibration as well as in the measurement itself. This is an 0.9% maximum error in the calibration constant, and a 0.1-1.0% maximum error in the pressure measurements (as discussed above). Thus the terms $U_{(P_o-P_{tap})}$ and $U_{(P_o-P_\infty)}$ each have a maximum value of 1.0-1.9% of the actual measurement. The approximate range of C_p magnitudes measured during this research was 0.1-6.0. Thus using Equation 3.11, it can be seen that the uncertainty over this range of pressure coefficients is from 1.6-19.2%. The largest error is associated with the smallest magnitude pressure coefficient.

3.5.6 Repeatability

The precision of a measured value is not necessarily indicative of its repeatability. The flow field over as delta wing at large incidence is a dynamic system even at steady angles of attack. Thus, the repeatability of the data obtained during this research becomes important. The confidence in a given measurement can be more a function of the repeatability than the precision; this is particularly true when measuring the location of vortex breakdown. In order to quantify the repeatability, spot checks and repeated measurements were taken whenever possible during the course of the experiments. Repeated measurements were made on separate occasions for the majority of the pressure measurements. Similarly, an ensemble average was obtained of the unsteady data; in order to remove the transients and obtain data that could be repeated. The repeatability of the data presented here will be discussed in chapters 4 and 5, when the results of each test are discussed.

3.6 Graphic Presentation

When the pressure data is presented graphically, several options are available for displaying error bands on the data. The error bands can represent the uncertainty in the pressure measurement (sections 3.5.1 and 3.5.4), the standard deviation of the averaged data points (section 3.5.5), or a confidence interval of a specified amount (section 3.5.5). In addition, each of these can be combined to give an overall estimate of the uncertainty. The following series of figures depicts the effects of each of these options as well as the relative magnitude of each type of error.

Figures 3.6-3.10 each show unsteady surface pressure data from the same case: Reynolds number of 500,000, reduced frequency of 0.09, and a surface location of $x/c = 0.25$ and $y/s = -0.60$. Figure 3.6 shows the unsteady pressure coefficient as a function of time, where Δt is the temporal duration of a single pitching motion. This curve is the result of ensemble averaging twenty five cycles (as discussed in section 3.4). This figure contains no error bands and is provided as a reference for the following figures.

Figure 3.7 again shows the unsteady pressure coefficient data. The error bands on this figure represent the uncertainty in the pressure measurement and the calculation of pressure coefficient. The values have been computed using Equation 3.11. The error shown in this figure ranges from 1.7% to 10.3%. The highest percent error corresponds to the smallest pressure differential; this is a reflection of the resolution of the measurement system for smaller pressure differentials. Note that for cases using lower Reynolds numbers, the suction pressures are smaller. This results in a lower resolution of the pressure transducers and thus a somewhat larger error. However, the amount shown in Fig. 3.7 is indicative. Furthermore, this amount is negligible relative to the temporal uncertainty and the repeatability of the data.

Figure 3.8 shows the unsteady surface pressure and freestream dynamic pressure (q) as functions of time. During the ensemble averaging process the standard deviation cf

73
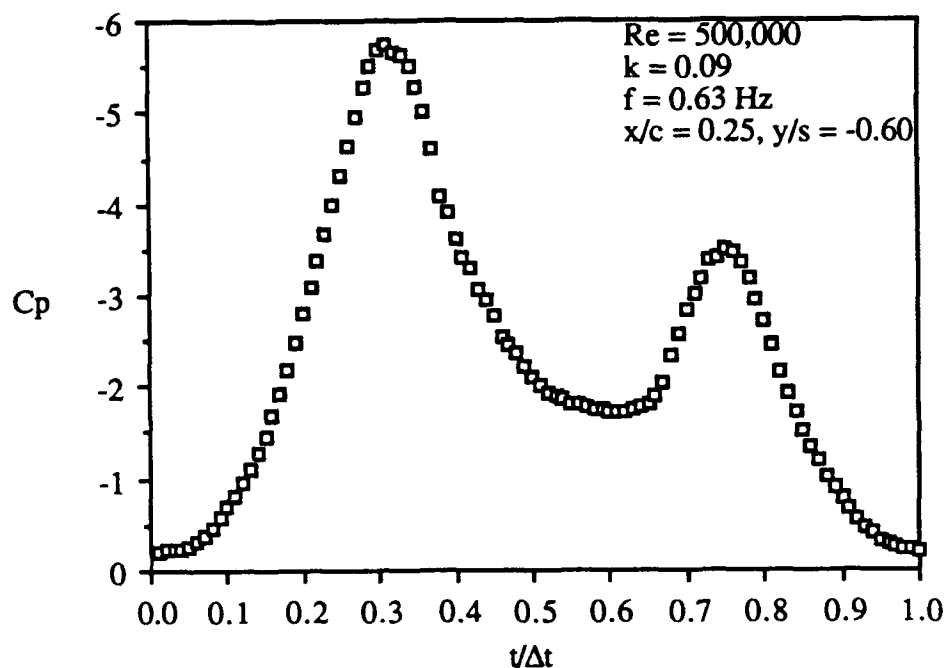
Figure 3.6   Unsteady Surface Pressure Coefficient Time History: Ensemble Average of

25 Cycle of Motion
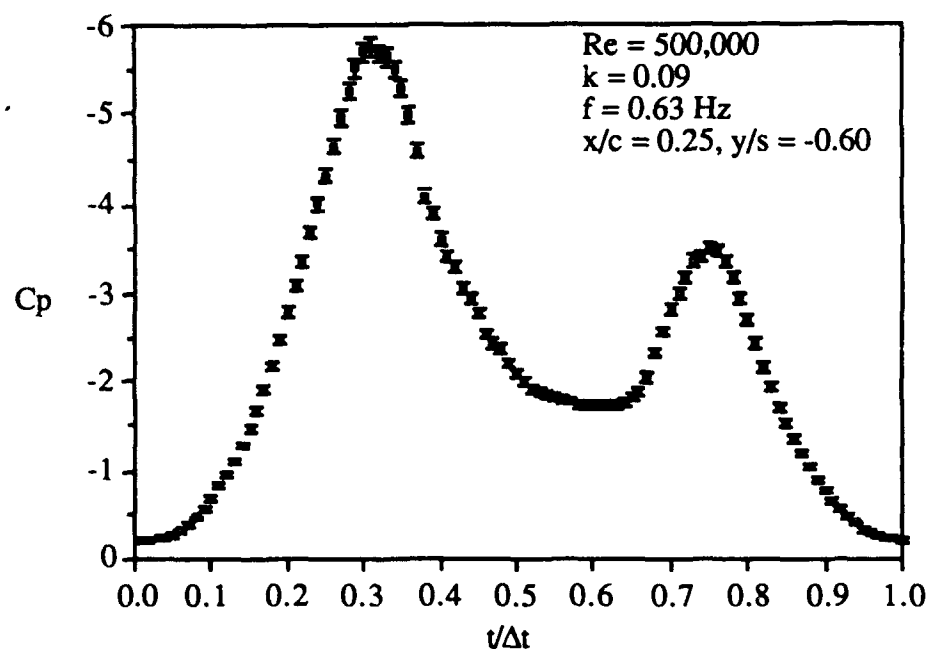
Figure 3.7   Unsteady Surface Pressure Coefficient Time History: Ensemble Average of

25 Cycles and Measurement and Calculation Uncertainty
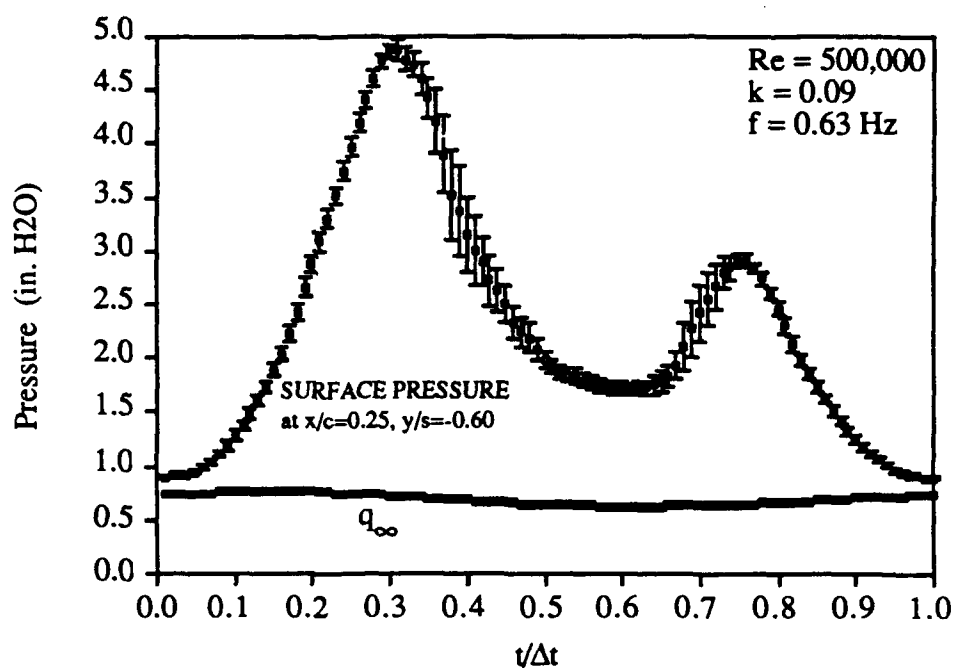
Figure 3.8   Unsteady Surface Pressure and Freestream Dynamic Pressure Time

History: Ensemble Average and Standard Deviation of 25 Cycles

each point was computed (using Equation 3.7) and those values are presented in Fig. 3.8 as error bands. Note that for the q data these bands are smaller than the size of the symbol used hence the bands are not visible. From Fig. 3.8 it can be seen that the largest uncertainty in the data occurs between the two suction peaks, roughly from $t/\Delta t = 0.32$-0.74. In the previous figure the magnitude of the error was a function of the magnitude of the measurement; thus this region of increased uncertainty is not present in Fig. 3.7.

This increase in the standard deviation is indicative of an increased difference between the individual cycles that were averaged together. Figure 3.9 illustrates this by showing the ensemble average as well as one individual cycle of data. The most significant deviation between the two curves is between the two suction peaks; the increase in standard deviation over this range indicates that for the most part this is true of each of the cycles used in the averaging process.
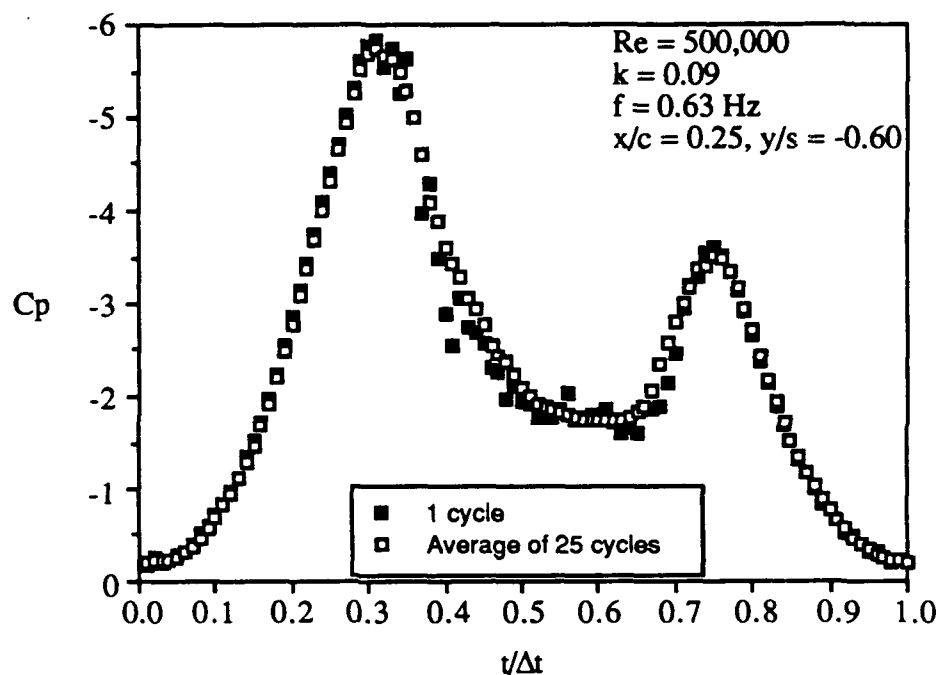
Figure 3.9   Unsteady Surface Pressure Coefficient Time History: One Cycle and

Ensemble Average of 25 Cycles

The previous three figures indicate the precision of the measurement and of the averaging process. Figure 3.10 gives an indication of the repeatability of the measurement. This figure shows a repeated measurement made of the same case; the data used in the previous figures (and shown alone in Fig. 3.6) is shown as the open symbols in Fig. 3.10. The repeated measurement was made during a separate wind tunnel entry. The difference between these two curves is indicative of the repeatability of the unsteady pressure data.

By comparing Fig. 3.10 with Fig. 3.8 it can be seen that the scatter due to the averaging process is roughly the same as the uncertainty due to the repeatability. In addition, either of these is larger than the uncertainty due to either the pressure measurement or the calculation of the pressure coefficient. Thus these two factors, the
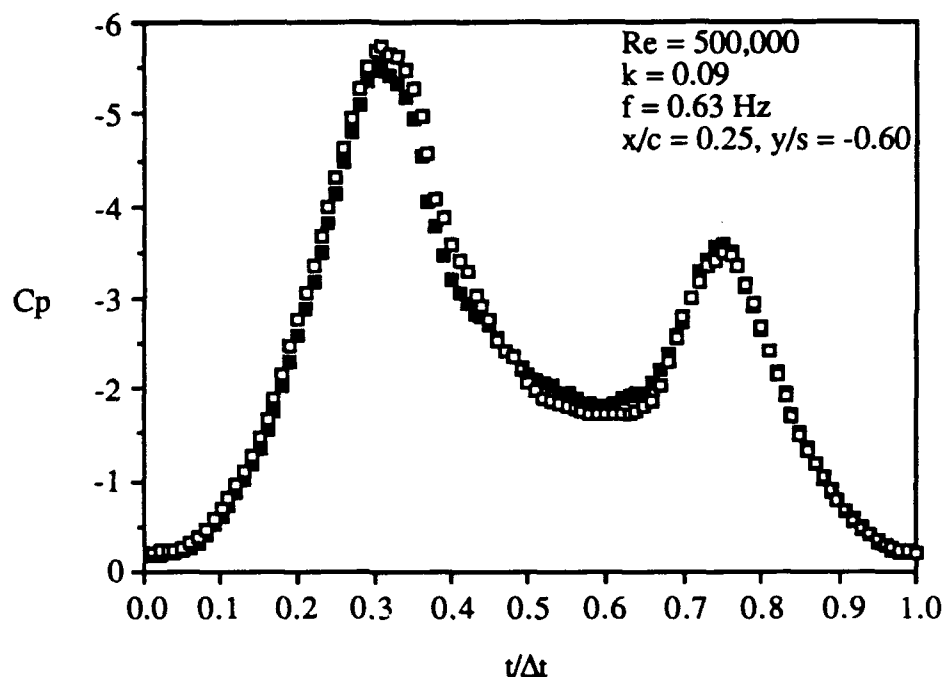
Figure 3.10   Unsteady Surface Pressure Coefficient Time History: Repeated

Measurement and Ensemble Average of 25 Cycles

repeatability and the standard deviation of the mean, are the limiting factors on the

confidence in the data. A confidence interval could be defined (as discussed in section

3.5.5) but would not be effective for the following reason: using a confidence interval (as

defined in Equation 3.8) does not affect the repeatability, which would still be limiting

factor.

The data shown in Figs. 3.6-3.10 was chosen as it is representative of all the

unsteady pressure data. Putting error bands on each point of each data set results in very

cluttered graphs; thus the majority of the data will not be presented in that fashion. Instead,

Figs. 3.6-3.10 can be used as a reference throughout the discussion of the experimental

results.

IV   VALIDATION TESTS: PROCEDURE AND RESULTS

Two sets of experiments were conducted in order to validate the experimental procedure used during the acquisition of the steady and unsteady surface pressures. The first of these consisted of an experimental evaluation of the dynamic response of the pressure measurement system. The second set examined the effect of the variation in wind tunnel blockage caused by both the steady and unsteady motion of the delta wing model.

4.1   Determination of Pressure Measurement System Dynamic Response

This section examines the dynamic characteristics of the measurement system used during this research to obtain dynamic data. An introduction to the problem and the experimental procedure is presented first. This is followed by the results of the investigation and then a summary of the conclusions.

4.1.1   Introduction and Procedure

When attempting to make measurements of a dynamic system, the dynamic characteristics of the measurement system itself must be considered. In this case the system includes the pressure transducer and the plastic tubing used to connect the transducer to the pressure orifice on the model surface.

Two options existed for the location of the pressure transducers: within the delta wing model, mounted directly to the pressure orifice; and outside the working section, connected to the orifice by plastic tubing. The advantage to putting a transducer directly at the pressure orifice is that the surface pressure can then be measured directly, without

77

concern for dynamic effects other than those of the transducer itself. The Setra pressure transducers used during this research have a nominally rated natural frequency of 2000 Hz. Considering that the maximum pitch frequency used during this research was 2.1 Hz, this frequency resolution is sufficient to accurately measure the fluctuating pressures.

The disadvantage of directly mounted transducers is the cost and complexity of their use. In order to measure the pressure at several different surface locations, either several transducers must be used, or a given test must be interrupted in order to reconnect the transducer to a new pressure tap. The former is cost prohibitive while the latter is time consuming and disruptive of the test conditions. Both these complications can be avoided by using a limited number of transducers located outside the working section. Tubing can then be connected from the transducer to the pressure taps; the number of taps is limited only by the amount of tubing that can fit within the model. The pressure tap being sampled can then be varied by changing which tube is connected to the transducer; the conditions in the test section are not affected.

However, this connecting tubing will alter the dynamic pressure signal. Thus, it is necessary to examine the amplitude attenuation and phase shift of this system, particularly over the frequency range of interest. This was accomplished by two experimental procedures. The first examined the dynamic response of the tubing over a range of frequencies. The second involved mounting a transducer directly at the wing orifice and measuring the unsteady pressure, then comparing this to the signal measured by a transducer connected to the pressure tap by plastic tubing. The first experiment was similar to this, only a controlled pressure source was used rather than the actual delta wing surface pressure.

A schematic of the setup for the first experiment is shown in Fig. 4.1. Two pressure transducers were mounted on one end of a cylindrical chamber; one flush with the surface of the cylinder and one connected by a length of plastic tubing (the same length to be used when measuring the delta wing surface pressures). The opposite end of the

chamber was a flexible diaphragm that was driven by an MB Dynamics Modal Exciter and Power Amplifier. This exciter was driven by a Scientific Atlanta Spectral Dynamics SD380 Signal Analyzer, which was capable of producing a single frequency signal or broadband noise. The output from the two transducers was then measured and compared by the SD380. Thus, the amplitude attenuation and phase shift due to the tubing could be quantified. This could be done for either a single frequency or broadband noise. By using broadband noise, the transfer function for the tubing could be determined (over a frequency range of interest) by treating the directly measured pressure as the input and the remotely measured pressure as the output. Additional information on this experiment can be found in Thompson, Batill, and Nelson (Jan., 1990).

Power Amplifier with
Broadband Frequency
Output

Modal Exciter

Test Chamber :
- Flexible Diaphragm
- Two Pressure Orifices

Direct Mounted Pressure
Transducer

Remotely Mounted Pressure
Transducer

Signal Analyzer

Transfer Function and Phase Shift
Due to Connecting Tubing
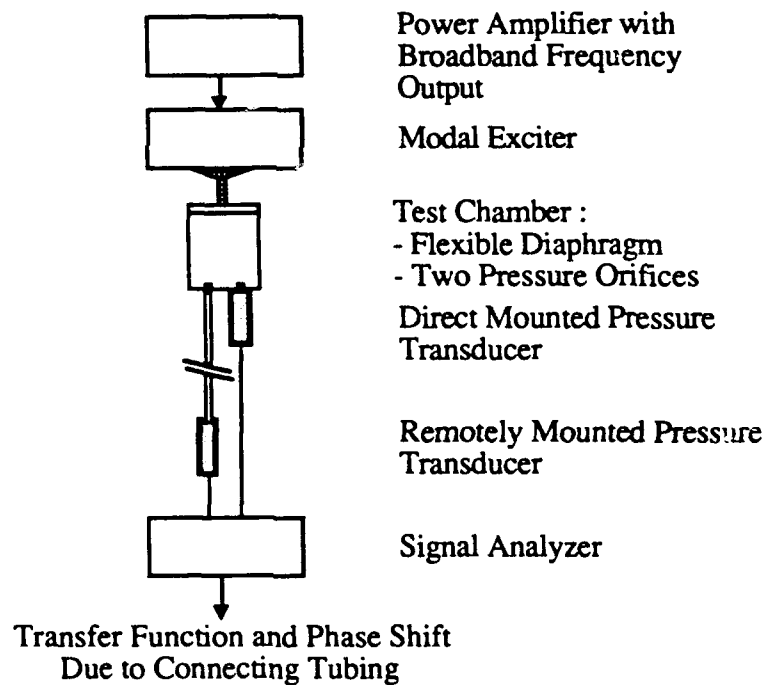
Figure 4.1   Experimental Setup For Determination of Pressure Measurement System

Dynamic Response

The second experiment involved the use of the Nova pressure transducer. This transducer was small enough to fit within the hollow cavity in the delta wing model. Thus it was mounted in the wing, approximately 1 in. (2.54 cm) from a pressure orifice. The orifice located at x/c = 0.25 and y/s = -0.60 was chosen for this purpose. Since this orifice was located farther forward than the others it would experience one of the largest pressure differences, thus a greater amount of the full range of the pressure transducer would be used, increasing the signal resolution. The pressure at that same tap was then measured by using a remotely located transducer along with the connecting tubing. Thus, the effect of the tubing on the actual unsteady pressure signal could be estimated. It is assumed that rated frequency response range for the Nova transducer was sufficient to accurately measure the unsteady surface pressure. The experiment was conducted as follows.

The Nova transducer was first calibrated and placed in the model at the x/c = 0.25 position (y/s = -0.60). A freestream velocity, pitch frequency, and angle of attack range were then chosen for the experiment. A large freestream velocity (relative to the majority of tests conducted during this research) was chosen in order to achieve the largest possible pressure differential. Two pitch frequencies were chosen that were representative of the range of pitch frequencies used throughout the research. A large angle of attack range was used, also to maximize the unsteady effects.

Having chosen these, unsteady pressure data then was obtained using the procedure described in section 3.4.

The Nova transducer was then disconnected from the orifice and removed from the model. It was then placed outside the test section and reconnected to the same orifice with plastic tubing. The experiment was then repeated using identical parameters. This procedure required that the test section be opened so that the model could be reconfigured. Thus, the freestream flow was disturbed between tests; however, this was seen to have no measurable effect. The test was then conducted using the same parameters. The pressure

data from the two cases could then be compared to estimate the effect of the connecting tubing.

4.1.2 Results

When determining the transfer function of the connecting tubing, the actual pieces of tubing to be used in the experiment were tested. This data has been previously presented in Thompson, Batill, and Nelson (July, 1989 and Jan., 1990); only the important conclusions will be cited here. It was found that the tubing behaved as a second order system, in that the input signal was amplified up to a certain natural frequency. Beyond this point the amplification decreased, then the signal was attenuated. This can be seen in the frequency response curve shown in Fig. 4.2. This figure shows the amplitude ratio (output divided by input) and phase shift (in degrees) as a function of signal frequency up to 100 Hz. Notice from this figure that the phase angle plot shows characteristics similar to that of a second order system, where the phase angle asymptotically reaches 180°. Note that the natural frequency of the system occurs near 50 Hz. For frequencies up to 25 Hz, the signal retains 95% of its magnitude with a maximum phase lag of 30°. Below 10 Hz the signal retains 99% of its magnitude with a maximum phase lag of 10°.

The curves presented in these figures do not include the uncertainty of the measured values. The uncertainty of these values is a function of several factors including the sampling parameters, the dynamic response of the transducer itself, and the accuracy of the SD380 Signal Analyzer. However, due to the preliminary nature of this transfer function determination experiment, uncertainties of the transfer function data were not calculated. This experiment was conducted as a quick preliminary test to determine the validity of making remote pressure measurements. Because the results seemed to indicate that the integrity of the unsteady pressure signal could be maintained, a second, more complex test was performed.
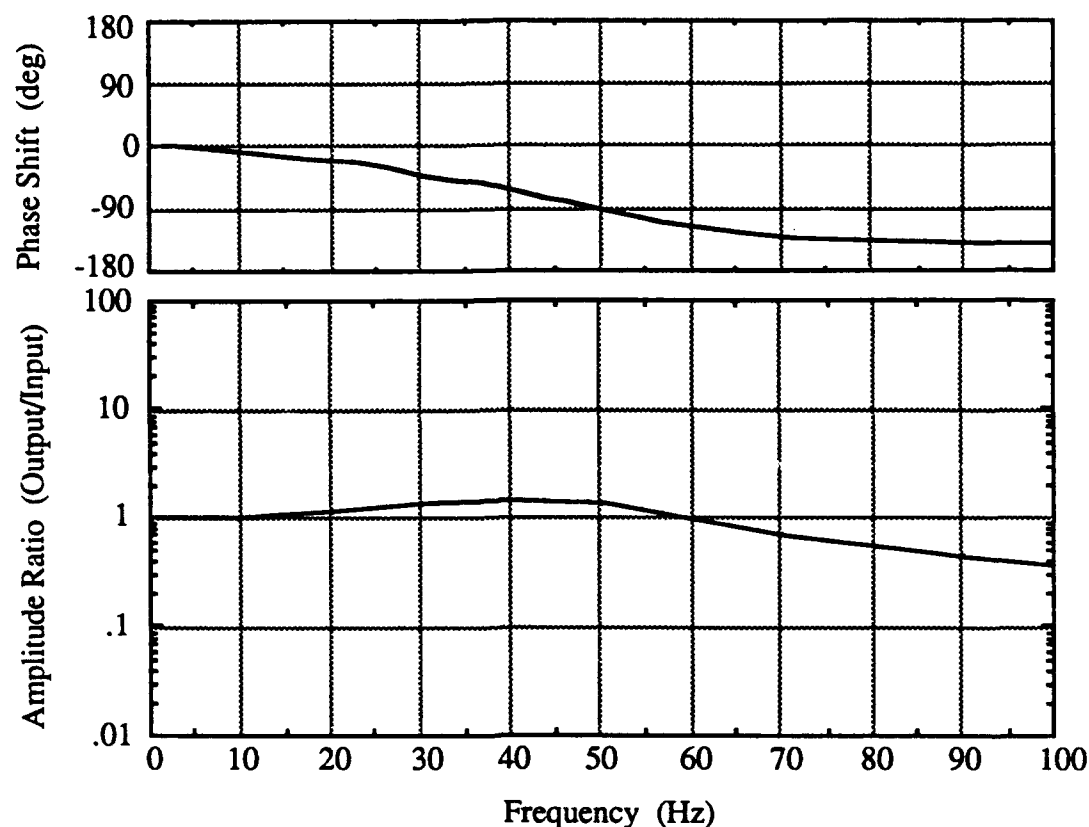
Figure 4.2   Transfer Function for Tubing used with Transducers: Amplitude Ratio and

Phase Shift

For the experiments using a Nova transducer located within the delta wing model, a single Reynolds numbers was used: 575,000. This corresponded to a freestream velocity of approximately 69 ft/s (21 m/s). Reduced frequencies of k = 0.03 and 0.15 were used. These values of Reynolds numbers and reduced frequencies were chosen to provide as wide a range as possible while staying within the practical limits of the wind tunnel facility and the pitching mechanism. An angle of attack range of 0-60° was used throughout the tests.

Representative data is shown in Figs. 4.3a and 4.3b. This figure is for the Re = 575,000 case, with a reduced frequency of k = 0.15. This corresponds to a pitch rate of

1.2 Hz. Note that this data is the ensemble average of data from twenty five cycles of motion. The higher pitch frequency case is shown in Figs. 4.3a-b to better illustrate the unsteady effects; the lower pitch frequency cases showed similar trends. Figure 4.3a shows the time history of the pressure coefficient during the pitching motion where time has been nondimensionalized by the duration of one cycle of motion. From this figure it can be seen that effectively no discernable phase shift or amplitude attenuation exists at this pitch frequency. The suction peaks coincide very well. The only consistent difference between the two curves exists at the "trough" between the two suction peaks, approximately from $t/\Delta t = 0.55$-0.65. At this point the directly measured pressures are slightly lower. This corresponds to the portion of the motion where vortex breakdown is reforming over the wing and rapidly moving aft and into the wake (this phenomenon and its effect on the surface pressure field will be discussed in sections 7.4 and 7.5). This is the portion of the motion with the largest uncertainty in the pressure measurements.
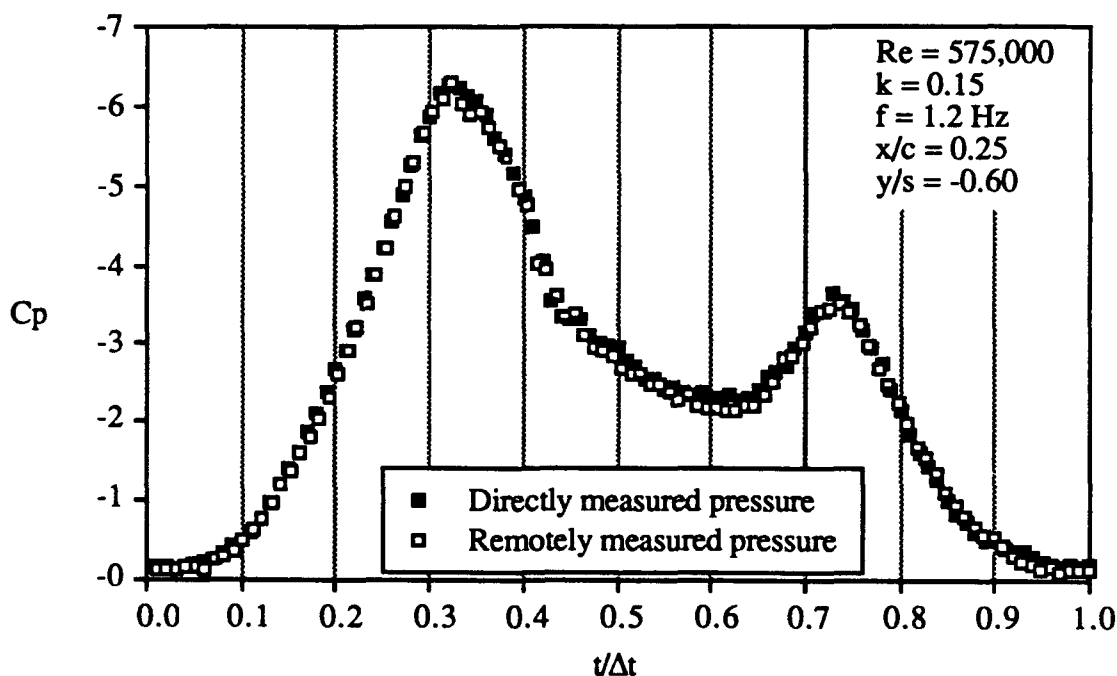
Figure 4.3a   Comparison of Directly Measured Pressure and Remotely Measured Pressure. Pressure Coefficient as a Function of Nondimensional Time

The difference between the directly measured pressures and the remotely measured pressures is small; even including the errant points not smoothed out by the ensemble averaging process the difference is less than 10% for pressure coefficients below 1.5. This amount is within both the uncertainty and the repeatability of the measurements.
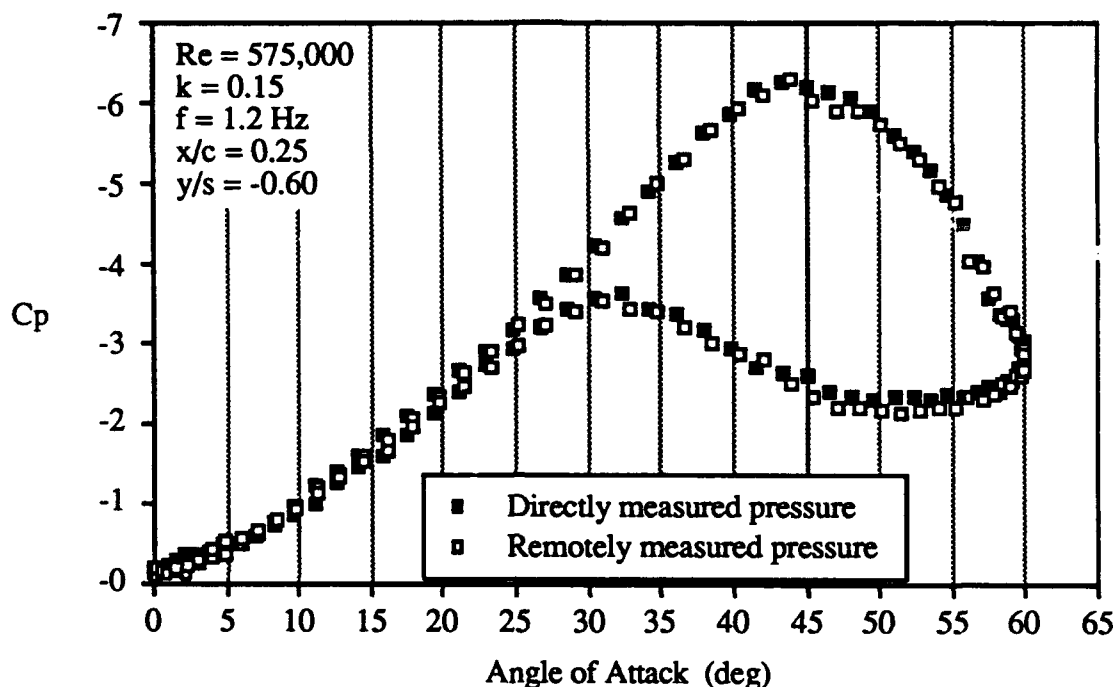
Figure 4.3b   Comparison of Directly Measured Pressure and Remotely Measured Pressure. Pressure Coefficient as a Function of Angle of Attack.

Figure 4.3b shows the same data plotted as a function of instantaneous angle of attack. As with Fig. 4.3a, this figure shows the similarity of the remotely measured pressures as compared to the directly measured pressures. Here the difference in the two curves is manifested as a slight narrowing of the hysteresis loop for the directly measured pressures from 55-40° (angle of attack decreasing).

From the transfer function shown in Fig. 4.2, an amplitude attenuation of up to 2% and a phase shift of up to 4° could have been expected in the dynamic data (for a frequency of approximately 1 Hz). These amounts are not consistently visible in Figs. 4.3a-b,

particularly in the two peaks. A phase shift of 4° roughly corresponds to the amount of time between any two data points (t/Δt = 0.01) shown in Fig. 4.3a. Hence, a phase shift of this size would appear as a consistent shift in the curve of roughly the width of the symbol of one data point.

4.1.3 Conclusions

The initial experiments involving the empirical determination of the measurement system transfer function successfully estimated the amplitude attenuation and phase shift of an unsteady signal. The system was seen to behave similar to a second order system. In effect this results in the system acting as a low pass filter for any given unsteady signal; very high frequencies will be strongly attenuated.

The natural frequency of the system was near 50 Hz. This value is an order of magnitude above the highest frequency of oscillation to be used in this research. Thus these results indicated that any attenuation or amplification of the unsteady effects would be minimal over the frequency range of interest. With this in mind, the effect of the connecting tubing was measured for an actual unsteady pressure signal. This data showed no consistent difference between the remotely measured pressures and the directly measured pressures. The differences that did exist were not sufficient to indicate a dynamic effect of the connecting tubing.

Considering these results, the unsteady pressure data obtained during this research was not corrected for the existence of the connecting tubing. It is assumed that the dynamic effect on the pressure signal is negligible for the levels of unsteadiness used here. Additionally, it was found during the course of these initial tests that the procedure of directly measuring the surface pressures is more complex and has several additional sources of uncertainty (these stem primarily from the increased need to calibrate the transducer and reconfigure the pressure model).

4.2   Blockage Effects: Introduction

In 1957 a study was conducted by Peckham and Atkinson using a 13'x9' wind tunnel and a gothic wing (a swept wing with a continuously curved leading edge) with an area of 16 ft^2 (1.49 m^2). Six component force measurements were made. Angles of attack up to 36° were used, resulting in a maximum frontal blockage of roughly 8%. Peckham and Atkinson found that the tunnel interference could be significant despite the relatively small size of the model. This indicates the potential sensitivity of the leading edge vortex to blockage effects.

Very large angle of attack excursions were used during the course of this research. The majority of the tests were performed in a test section with a cross sectional area of 4 ft^2 (0.37 m^2), and with a delta wing model with a planform area of 0.685 ft^2 (0.064 m^2). The percent frontal area blockage that this model presents is shown in Table 4.1 for several representative angles of attack. Note that this does not include the blockage due to the model support strut, which alone presents a frontal area blockage of 1.6%. Note also that the blockage at 0° represents the frontal area projected by the thickness of the model, 0.75 in. (1.9 cm). The values in Table 4.1 above 0° do not take into account the thickness of the model.

As can be seen in Table 4.1, the blockage exceeds 10% for angles of attack above 36°. This percentage is often considered an upper limit for which blockage corrections need not be applied. However, tests conducted during this research utilized angles of attack up to 60°. Complicating this is the fact that the blockage was a dynamic quantity; it changed as the model oscillated. In order to examine the implications of this dynamic blockage, two additional delta wing models were manufactured.

TABLE 4.1

PERCENT FRONTAL AREA BLOCKAGE FOR 70° DELTA WING

Test section frontal area : 576 in.^{2}

Delta wing model planform area : 98.6 in.^{2}

Delta wing model chord length : $16\frac{7}{16}$ in.

Angle of Attack	Frontal Area of Wing (in.^{2})	Percent Blockage ± 0.3% [*]
0	9.0	1.6
10	17.1	3.0
20	33.7	5.9
30	49.3	8.6
35	56.6	9.8
40	63.7	11.0
50	75.6	13.1
60	85.4	14.8
65	89.4	15.5
70	92.7	16.1

[*] Does not include model support strut blockage of 1.6±0.3%

These two additional wings were geometrically similar to the pressure model but had chord lengths one-half and two-thirds that of the pressure model (these two models are described in section 2.3.2). The percent frontal blockage these two wings is shown in Table 4.2, along with the blockage of the baseline (or full scale) pressure model (taken from Table 4.1). This same information is presented graphically in Fig. 4.4, which shows the percent frontal blockage for each of the three models. Note that the blockage for the two subscale models is below 10% even at very high angles of attack.

TABLE 4.2

PERCENT FRONTAL AREA BLOCKAGE FOR SUB-SCALE WINGS

Test section frontal area : 576 in.^{2}

Delta wing model planform areas : 43.5 in.^{2} and 24.4 in.^{2}

Delta wing model chord lengths : $10\frac{15}{16}$ in. and $8\frac{3}{16}$ in.

Angle of Attack Percent Blockage $\pm$ 0.3% *

	Full Scale Wing	Two-Thirds Scale Wing	One-Half Scale Wing
0	1.6	0.7	0.4
10	3.0	1.3	0.7
20	5.9	2.6	1.4
30	8.6	3.8	2.1
40	11.0	4.9	2.7
50	13.1	5.8	3.2
60	14.8	6.5	3.7
70	16.1	7.1	4.0

* Does not include model support strut blockage of 1.6±0.3%
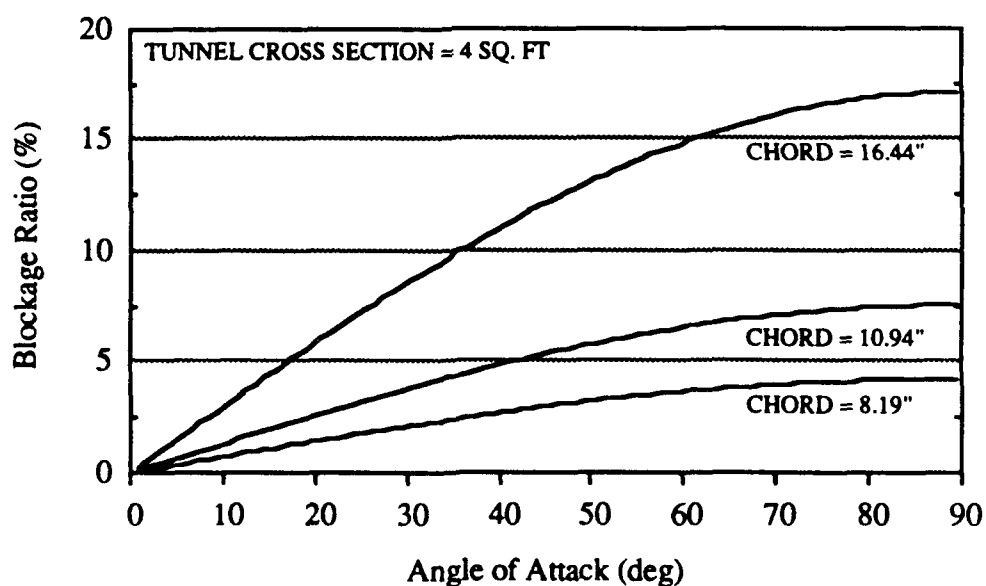
Figure 4.4   Percent Frontal Blockage for Three Geometrically Similar 70° Flat Plate

Delta Wings with Different Chord Lengths

Thus, two sets of tests were conducted to examine the blockage effects. First, the variation of the freestream velocity was examined as a function of varying angle of attack (and thus varying blockage) for the full scale wing. This was done for both steady and unsteady cases. Second, the steady and unsteady pressures were measured on each of the three wings in order to examine the effect of the varying blockage on the surface pressures. In addition, a limited amount of flow visualization data (steady and unsteady) was also obtained for the sub-scale wings.

4.3   Blockage Effects: Variation of Freestream Velocity

This section examines the response of the freestream conditions as the delta wing model undergoes a pitching motion. Both the steady and unsteady cases are examined. An introduction to the problem and the experimental procedure is presented first. This is followed by the results of the investigation and then a summary of the conclusions.

4.3.1   Introduction and Procedure

The pitot static tube used to measure the freestream dynamic pressure was located 2.5 ft (0.76 m) upstream of the delta wing strut, at the entrance to the test section. At this point it was possible to detect a fluctuation of the freestream dynamic pressure during the unsteady delta wing motion. This fluctuation has been quantified (in terms of velocity) for several ranges of motion and pitch frequencies. The steady tests consisted of measuring the change in freestream conditions as a result of changing the steady angle of attack. The unsteady tests consisted of measuring the freestream velocity throughout a pitching motion for several values of pitch frequency and nominal freestream velocity.

It should be noted that the accuracy with which the pitot-static probe could measure a fluctuating pressure was not quantified. The dynamic effects of the plastic tubing

connecting the probe to the transducer was quantified (see Section 4.1), but any dynamic effects of the internal tubing of the pitot-static probe was not considered.

Using the same experimental setup used here, LeMay, Batill, and Nelson (1988) quantified the freestream fluctuation for an oscillating wing using two angle of attack ranges: 29-39° and 0-45°. Several pitch frequencies were examined for each range. It was found that for the smaller angle of attack range, the freestream dynamic pressure fluctuated by less than 1.4% from the mean value, while for the larger range the fluctuation was less than 3.8%. It was also seen that an increase in pitch frequency caused a decrease in percent fluctuation and an increase in phase lag (relative to the motion of the wing).

As a brief additional experiment, the pitot-static tube was moved to a different location in the wind tunnel. This new location was still along the tunnel centerline but only a few inches in front of the model. The variation of the freestream dynamic pressure was then measured as before. The goal of this experiment was to examine the local freestream dynamic pressure experienced by the wing. It was seen that q varied in a manner the same as the results to be presented. This experiment did not account for any change in direction of the freestream flow due to the presence of the model.

4.3.2 Results

Figure 4.5 shows data on the change in freestream dynamic pressure (for a fixed wind tunnel fan speed) with a steady change in angle of attack. These data was obtained using the full size pressure model (chord length of 16.44 in.) at four Reynolds numbers. Note that the vertical scale is different for each of the four parts of Fig. 4.5; this has been done to emphasize the similarity of the four cases. An increase in angle of attack caused a reduction in dynamic pressure; for each of the four Reynolds numbers (and hence dynamic pressures) tested, this reduction was from 12-14% by an incidence of 60°. This amount
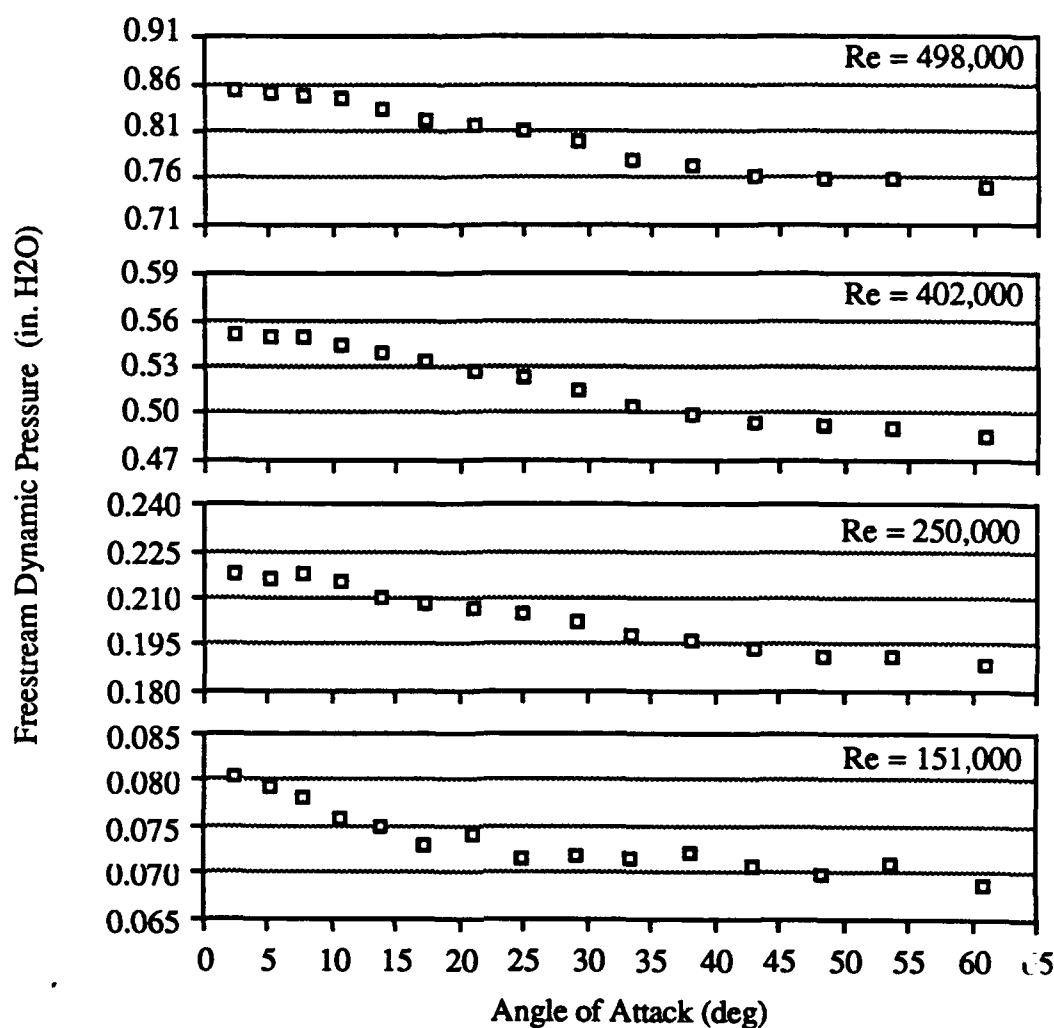
Figure 4.5   Effect of Steady Variation of Angle of Attack on Freestream Dynamic
Pressure. Wing Chord Length = 16.4375 in.

corresponds to a reduction in freestream velocity from 6.2-7.3%. Note that this is a steady
state reduction.

Figure 4.6 shows data on the change in freestream dynamic pressure with an
unsteady change in angle of attack. This figure shows the effect of a 0-60° oscillation at
three different pitch frequencies. The lower portion of this figure is a schematic of the
unsteady model motion, shown for reference. The beginning value of the dynamic
pressure is also shown; this value is the steady dynamic pressure with the wing at 0° angle
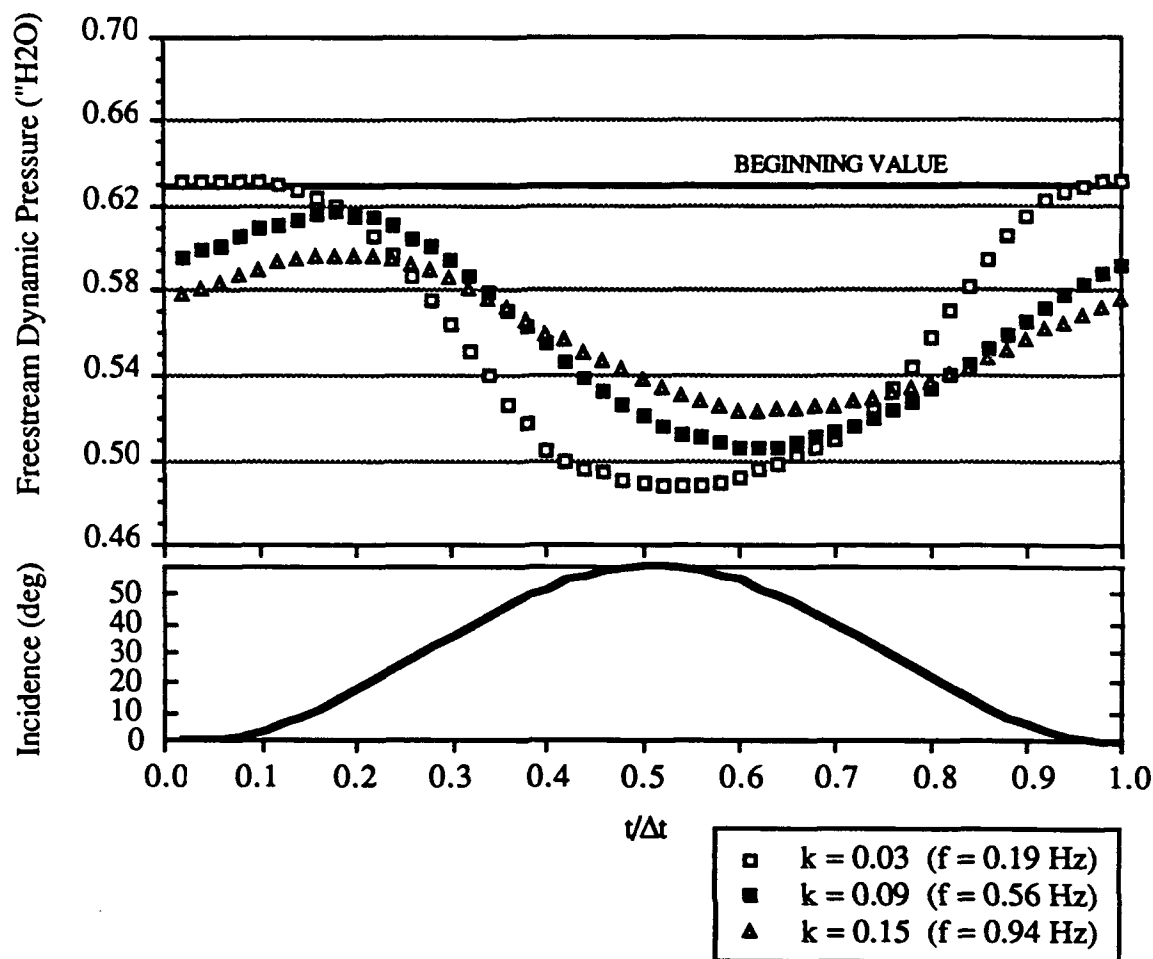
Figure 4.6   Effect of Unsteady Variation of Angle of Attack on Freestream Dynamic

Pressure. Wing Chord Length = 16.4375 in. Re = 450,000.

of attack. It is the value at which the tunnel is set prior to the test. As with the previous

figure the data shown is for the full scale wing.

It can be seen in Fig. 4.6 that the dynamic pressure does not fluctuate about the

beginning value; the mean of the fluctuating signal is lower than the beginning value. This

is to be expected since the fan is turning at a constant speed; a feedback control system is

not employed. Thus, the fan does not accelerate to overcome the additional restriction

caused by the model at high angles of attack.

Furthermore, as seen by LeMay, Batill, and Nelson (1988), an increase in pitch frequency reduces the amount of fluctuation and increases the phase lag (relative to the motion of the wing). For the lowest pitch frequency case, $k = 0.03$, the fluctuation is 21-22%. This amount decreases with increasing pitch frequency. Note that the amount of fluctuation for the $k = 0.15$ case is 12-13%, which is roughly the same as the fluctuation for the steady case.

Tests were conducted for five Reynolds numbers ranging from 150,000 to 550,000. Figure 4.6 is a representative case. This information is summarized in Table 4.3, which shows the percent fluctuation of each case of the five Reynolds numbers and three pitch frequencies tested. The case shown in Fig. 4.6 is included in this table. Notice that, as with the steady data (Fig. 4.5), the trends were relatively Reynolds number independent over the range of 150,000-500,000.

TABLE 4.3

CHANGE IN FREESTREAM DYNAMIC PRESSURE WITH UNSTEADY ANGLE OF ATTACK OSCILLATION FROM 0° TO 60° FOR FULL SCALE WING

Full scale wing chord length : $16\frac{7}{16}$ in.

Values are percent fluctuation of the freestream dynamic pressure relative to the nominal value.

Reynolds Number:	% Fluctuation:		
	$k = 0.03$	$k = 0.09$	$k = 0.15$
150,000	21	18	13
250,000	22	17	12
350,000	21	17	12
450,000	22	18	12
550,000	22	17	12

Figure 4.7 shows steady blockage data for the sub-scale wings as well as the full scale wing. This figure shows the change in freestream dynamic pressure as the wing is changed from a steady angle of attack of 0° to a steady angle of attack 60°. Notice that the data for the half-scale wing has a slope close to one, indicating that any change in the freestream dynamic pressure as a result of the wing angle of attack is small. However, as the wing size increases the effect becomes more noticeable.
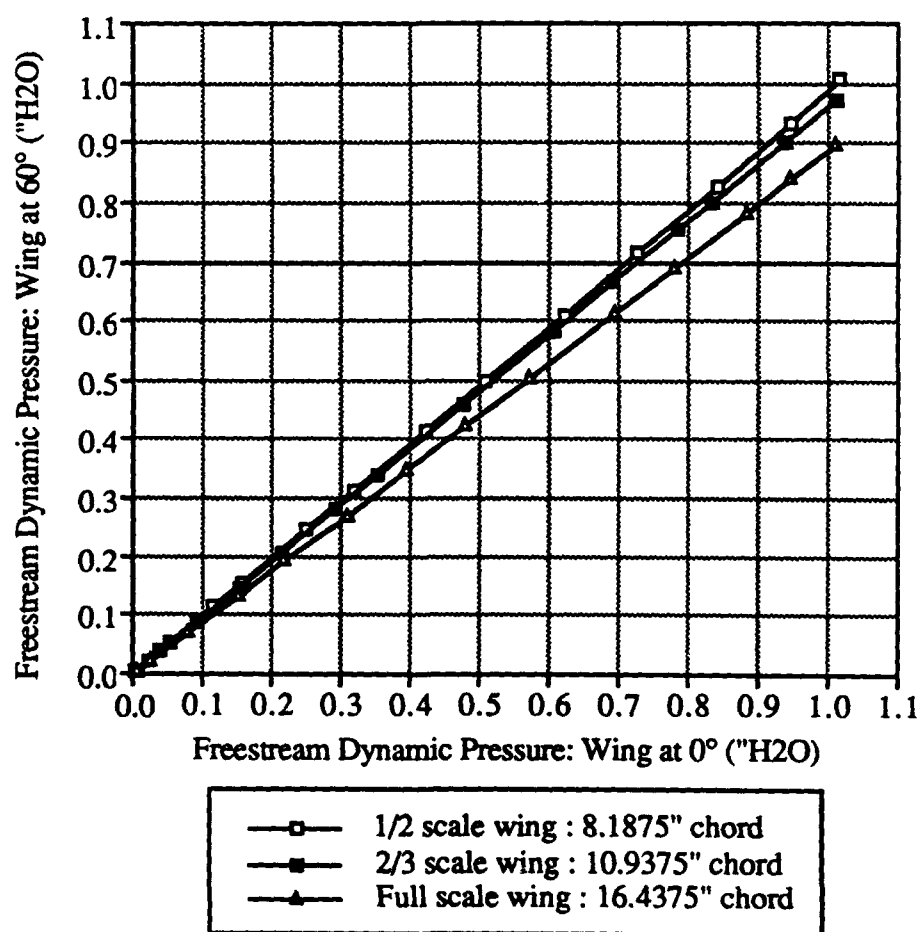
Figure 4.7   Change in Freestream Dynamic Pressure due to Steady Change in Angle of Attack from 0° to 60° for Full-Scale and Sub-Scale Wings

This effect is summarized in Table 4.4, which shows the percent change of the freestream dynamic pressure from 0° to 60° for each of the three wings. Note that the data for the full scale wing is the same data shown in Fig. 4.5. The higher Reynolds number cases could not be tested using the sub-scale wings due to the prohibitively large flow velocities required. From Table 4.4 it can be seen that the reduction in model scale strongly alters the blockage effect; the variation of the dynamic pressure for the one-half scale wing is less than 2%. This is within the accuracy of setting nominal dynamic pressure. Interestingly, this fluctuation is roughly the same magnitude as that reported by LeMay, Batill, and Nelson (1988) for a full scale wing with a much smaller angle of attack range (29-39°).

TABLE 4.4

CHANGE IN FREESTREAM DYNAMIC PRESSURE WITH STEADY CHANGE IN ANGLE OF ATTACK FROM 0° TO 60° FOR FULL SCALE AND SUB-SCALE WINGS

Full scale wing chord length : $16\frac{7}{16}$ in.

Two-thirds scale wing chord length : $10\frac{15}{16}$ in.

One-half scale wing chord length : $8\frac{3}{16}$ in.

Values area percent reduction of freestream dynamic pressure as steady wing incidence is increased from 0° to 60°.

Reynolds Number:	% Reduction:		
	Full scale wing	$\frac{2}{3}$ scale wing	$\frac{1}{2}$ scale wing
150,000	13.8	4.0	1.7
250,000	13.3	3.5	1.6
400,000	12.0	*	*
500,000	12.1	*	*

*Measurement not obtained

Steady blockage tests were conducted using the sub-scale wings as shown in Fig. 4.7 and Table 4.4. In addition to this data, a limited amount of unsteady blockage data exists for the sub-scale wings, although no test was conducted explicitly for this purpose. The data from the unsteady pressure tests performed using these wings contains useful information. When the unsteady pressure tests were conducted the freestream dynamic pressure was measured as a function of time (for use in nondimensionalizing the pressure data). By examining this data the unsteady response of the freestream can be estimated for the sub-scale wings.

The data for the sub-scale wings had characteristics similar to those seen in the data for the full scale wing. An increase in pitch frequency caused a decrease in the freestream fluctuation and an increase in the phase shift (relative to the wing motion), while a change in Reynolds number did not have a noticeable effect. The two-thirds scale wing caused unsteady freestream dynamic pressure fluctuations of up to 5.4%; while the one-half scale wing caused fluctuations of up to 2.3%. Comparatively, the full scale wing caused unsteady fluctuations of up to 20% (as shown in Table 4.3).

4.3.3 Conclusions

As expected, both the steady and unsteady pressure data appears to be reaching an asymptote as the model size decreases. The differences seen (in the surface pressures and freestream dynamic pressures) between the two-thirds scale wing and the one-half scale wing are consistently less than those between the full scale wing and the two-thirds scale wing.

An important note involves the effect of the model support hardware as the model size decreases. The same size model strut and model mounting plate were used regardless of model size, thus the relative size increases. For the smallest wing, the one-half scale wing, the mounting plate is over one half the chord length and when mounted on the wing

it spans all the way to the trailing edge. The pressure surface flow for a delta wing is critical in the formation of the leading edge vortices, and the possible disruption caused by the presence of the support hardware has not been investigated.

4.4 Blockage Effects: Effect of Model Size

This section examines the change in blockage effects as the result of a change in model size (for the same test section cross sectional area). An introduction to the problem and the experimental procedure is presented first. This is followed by a presentation of the results for the steady (model at constant angle) case. Then the unsteady case is presented. This is followed by a discussion of blockage corrections, then by a summary of the conclusions.

4.4.1 Introduction and Procedure

Both the two-thirds scale model and the one-half scale model were equipped with two lines of pressure orifices at the same relative locations as those on the full scale wing. The accuracy with which these orifices could be placed is different for each wing. A given surface location could be measured within $\frac{1}{32}$ in. Thus, the chordwise accuracy of a given tap location is $\pm 0.2\%$, 0.3%, and 0.4% for the full, two-thirds, and one-half scale models, respectively. The spanwise accuracy varies with the local span length. The accuracy decreases with decreasing span length; and thus with decreasing chord position. For the three wings the ranges of spanwise accuracy are ± 0.3-1.1%, 0.4-1.6%, and 0.6-2.1%.

This accuracy needs to be considered when comparing pressure data from the three wings that was obtained at nominally identical surface locations. The position accuracy increases the uncertainty of the comparison. This will be discussed further during the presentation of the blockage correction methods (section 4.4.4).

Both steady and unsteady pressures were obtained on all three wings for identical flow conditions. Due to the design of the subscale wings, with the embedded brass tubing acting as a manifold for all of the pressure orifices, only one orifice could be monitored at any given time. During a specific test the remaining orifices were kept sealed with adhesive tape. Based on the results from the tests involving the remotely placed pressure transducers, it is assumed that the internal manifold did not adversely effect the unsteady surface pressure signal.

Reynolds numbers were matched for all cases, and for the unsteady cases the reduced frequencies were matched (defined in Equation 3.3) as well. Thus, the results from the three wings could be compared to examine the effect of changing blockage.

All three wings were tested at Reynolds numbers of 150,000 and 250,000; for both the steady and unsteady cases. Steady pressures were measured at 15 angles of attack ranging from 2-61°. Pressures were measured at all 23 of the pressure orifices located on the two-thirds and one-half scale wings, as well as the corresponding locations on the full scale wing.

For the unsteady cases, three different reduced frequencies were tested at each Reynolds number: $k = 0.03$, 0.06, and 0.09 for $Re = 150,000$, and $k = 0.06$, 0.09, and 0.12 for $Re = 250,000$. These values of Reynolds numbers and reduced frequencies were chosen to provide as wide a range as possible while staying within the practical limits of the wind tunnel facility and the pitching mechanism. Unsteady pressures were measured only at the following five surface locations, all at $y/s = -0.60$: $x/c = 0.25$, 0.30, 0.35, 0.90, and 0.95. An angle of attack range of 0-60° was chosen to maximize the effect of the varying blockage. It is assumed that any blockage effect seen would be less for smaller ranges of motion.

4.4.2 Steady Effects: Flow Visualization and Surface Pressure

A study on the effect of tunnel blockage on the location of vortex breakdown was conducted by Weinberg in 1991. Weinberg used three 70° wings of exact geometric similarity but with varying chord length, as has been done in the current study. He conducted flow visualization experiments in a water tunnel at a freestream velocity of 4.33 in./s (cm/s). The Reynolds number range was 16,000-64,000. Note that Weinberg tested each wing at the same velocity and thus different Reynolds numbers. However, he tested the smallest wing over Reynolds numbers from 6,000-31,000 and found no effect on breakdown location. Weinberg found that as the wing size decreased the location of breakdown moved upstream for a given angle of attack. Weinberg concluded that a change in the effective wing camber was occurring due to the presence of the tunnel walls. Weinberg also tested a series of 60° wings and found similar but less consistent results.

In addition to his experimental study, Weinberg also developed a model for the test section wall interference using one set of image vortices for each of the four walls. He found that this caused an upwash which was became more pronounced with increasing chord location, effectively resulting in a positively cambered wing. This effect then increased with wing size. Positive camber has been seen to move the breakdown location aft (Lambourne and Bryer, 1959). Thus, Weinberg's experimental data reinforced the validity of his analytic model. However, his model was qualitative only; he did not attempt to correct flow visualization data for blockage effects.

Figures 4.8a and 4.8b show the steady vortex breakdown location from the current experiments as a function of angle of attack for each of the three delta wing models. Figure 4.8a is for increasing (quasi-static) angle of attack, while Fig. 4.8b is for decreasing angle of attack. The data has been separated in this manner to clarify the curves. The Reynolds number for each curve is 150,000. Measurements were also obtained at a Reynolds number of 250,000; no consistent effect on the breakdown location was seen. Each data
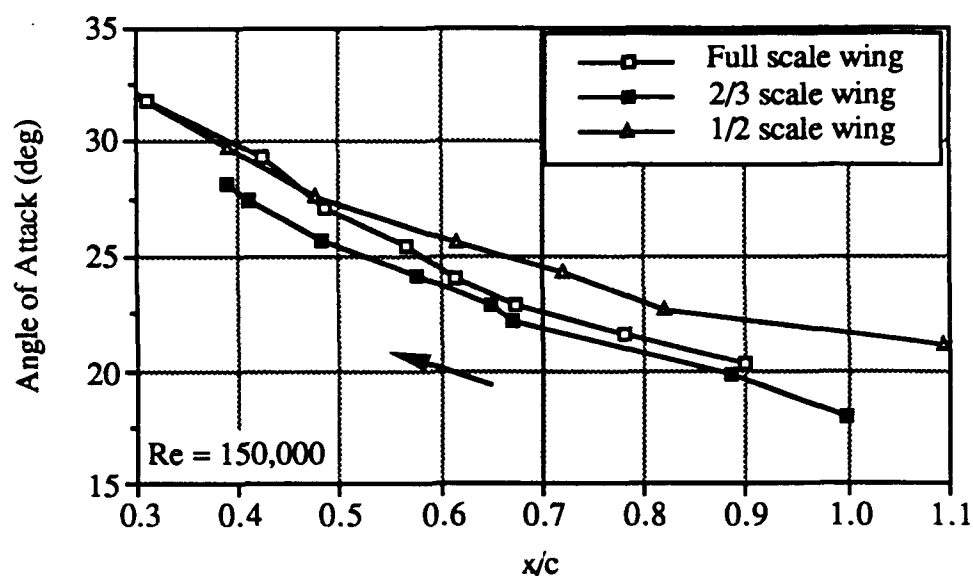
Figure 4.8a   Steady Location of Vortex Breakdown for Full and Sub-Scale Wings.

Angle of Attack Increasing.
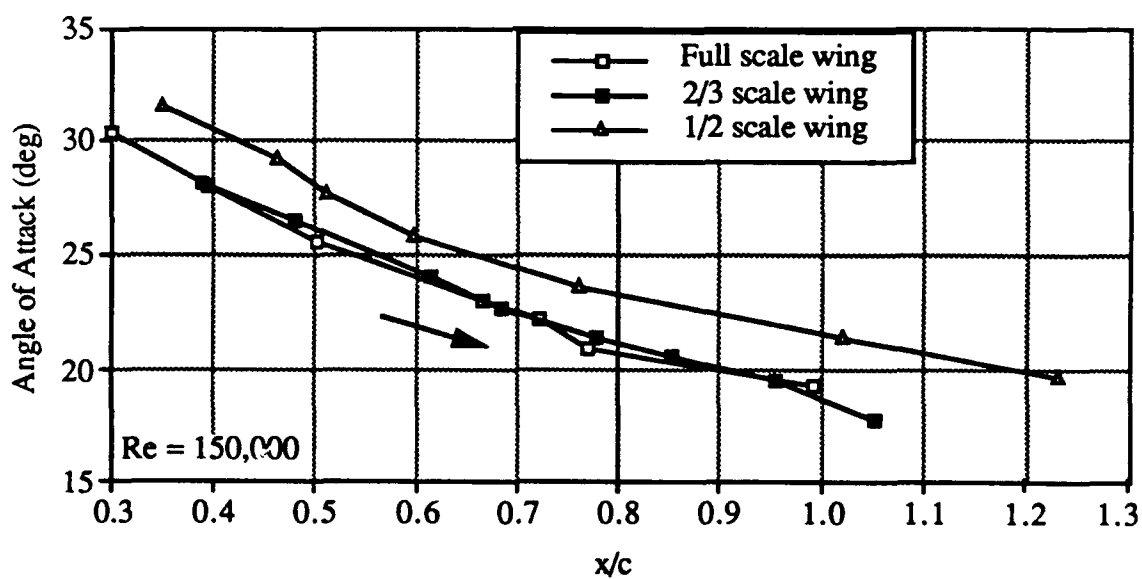
Figure 4.8b   Steady Location of Vortex Breakdown for Full and Sub-Scale Wings.

Angle of Attack Decreasing.

point shown in Figs. 4.8a-b represent the average chord location of ten measurements taken (at a specific angle of attack). The breakdown location can be expected to oscillate from 3-5% about the mean values shown.

Since the sub-scale wings were not originally designed as flow visualization models, the amount of data on these two wings (shown in Figs. 4.8a-b) is limited. The figures show the forward most location of breakdown as x/c = 0.35-0.40; however this is not as far as breakdown moves on the sub-scale wings. Rather this is farthest forward point at which data could be obtained for these two wings due to the location of the smoke injection port. Note that for the full scale wing data was obtained over the entire range of motion from vortex formation to full scale separation.

Figure 4.8a shows some differences between the data for each of the three wings. However, the differences between the full scale wing data and the two-thirds scale wing data cannot be completely attributed to the difference in chord length. Taking the unsteadiness of the breakdown location (at steady incidence) into account, those two curves become similar enough that a significant difference cannot be confidently concluded. However, the one-half scale wing does show a consistent difference for angles less than 25°. The breakdown location for the one-half scale wing is consistently aft of the location for the larger wings; by as much as 15% of the chord. Repeated measurements were made to ensure that this difference was not a result of the digitization or any bias in angle of attack.

A similar trend exists in Fig. 4.8b, for decreasing angles of attack. The data for the full scale curve and the two-thirds scale curve effectively lie on the same curve, reinforcing the similarity of the two for the angle of attack increasing data. Again, the one-half scale breakdown location consistently lags that of the larger wings.

This trend is different than the trend seen in Weinberg's experimental data (Weinberg, 1991). Weinberg documented a forward motion of breakdown with decreasing wing size; Figs. 4.8a and b show an aft motion.

One possible cause of the difference is that Weinberg used a Reynolds number an order or magnitude less than the current study. The effect of this is unknown. In addition, Weinberg used a constant velocity while the current data is for a constant Reynolds number. However, despite the differences, neither Weinberg nor the current study revealed an effect on breakdown due to a change in velocity, over their respective velocity ranges.

In addition, the frontal area blockage for Weinberg's largest wing is roughly twice (26%) that of the blockage for the largest (full scale) wing used here. The other two wings present a blockage comparable to that of the sub-scale wings used here. Also, Weinberg compared his data to data from the literature for wings of similar blockage. The difference between Weinberg's data and the comparative data was the same magnitude as the difference in Weinberg's data for the three different wings.

Interestingly, Weinberg noted a trend for the 60° wing that is similar to that seen in Fig. 4.8b. Weinberg found that the breakdown location was the same for the two largest wings, but different for the smallest wing. He concluded that this indicated that a change in effective camber was not the only effect of the tunnel walls.

An additional difference between the three wings can be detected in Fig. 4.8a; this is in the location of breakdown when it first occurs. The breakdown first occurs farther aft on the wing with decreasing wing size. The first data point for the full scale wing is located at $x/c = 0.9$, for the two-thirds wing this is $x/c = 1.0$ (the trailing edge), and for the one-half scale wing the breakdown first appears in the wake, at $x/c = 1.1$, before moving over the wing. A similar trend occurs during decreasing angle of attack, as seen in Fig. 4.8b. Here a decrease in wing size results in the breakdown coming to a final position farther into the wake. For the one-half scale wing the final steady state data point is almost 25% of the chord length into the wake.

Typically for the full scale wing (as well as the flow visualization model of similar chord length) when breakdown first occurred it was located over the wing. Upon reaching

the critical angle of attack, a slight increase in angle, less than 0.5°, would result in breakdown forming in the wake and immediately moving onto the wing before settling into a steady state position. Similarly, for decreasing angles of attack, the breakdown would reach a location near the trailing edge, then with a slight decrease in incidence, would move off the wing and far into the wake before disappearing. Similarly, Earnshaw (1968) noted that he could not obtain breakdown positions near the trailing edge. This effect is considered to be a reaction of the breakdown to the pressure gradient at the trailing edge.

However, in the present study this trend became less apparent as the model size decreased. For the smallest wing the breakdown appeared to be insensitive to the presence of the trailing edge. Notice from Fig. 4.8a that breakdown first appears 10% of the chord length into the wake. It then smoothly proceeded forward onto the wing with increasing incidence. Similar behavior was seen for decreasing angles of attack, where for the smallest wing the breakdown could be held to a position 25% of the chord length into the wake.

This difference in the trailing edge behavior of the vortex breakdown could be an effect of the varying tunnel blockage. It may be possible that for the full scale wing, the blockage is large enough that the freestream flow is significantly accelerated around the wing, resulting in a pressure gradient at the trailing edge which is sufficient to retard the streamwise motion of the breakdown. However, the blockage and freestream flow acceleration decreases with decreasing wing size. Thus for the smallest wing the resulting trailing edge pressure gradient has decreased enough to allow for breakdown to exist in a steady state both at the trailing edge and in the wake.

A difference also exists in Figs. 4.8a-b in the location of breakdown over the wing for the one-half scale wing. This is not necessarily an effect of decreasing blockage, considering that the two-thirds scale wing shows does not show a consistent difference from the full scale wing. However, it could be an effect of the wing mounting hardware. This was briefly mentioned in section 4.3.3.

As the wing size decreases the relative size of the mounting hardware increase; for the one-half scale wing the mounting plate is over half the chord length. This could cause a significant effect of the windward surface flow, which is in turn instrumental in the formation of the the leading edge vortices over the suction surface. A significant disruption of the lower surface flow could result in less fluid being swept outboard to the leading edges, thus causing weaker leading edge vortices, which would in turn result in the breakdown location being aft of its normal position at a given angle of attack. This is the behavior seen in Figs. 4.8a-b.

Figures 4.9a and 4.9b show some of the steady pressure data for the three different size wings. These two figures show comparisons of the pressure at two specific surface locations as functions of angle of attack, for each wing. Both these figures are for a Reynolds number of 250,000. Steady pressures are shown as a function of angle of attack
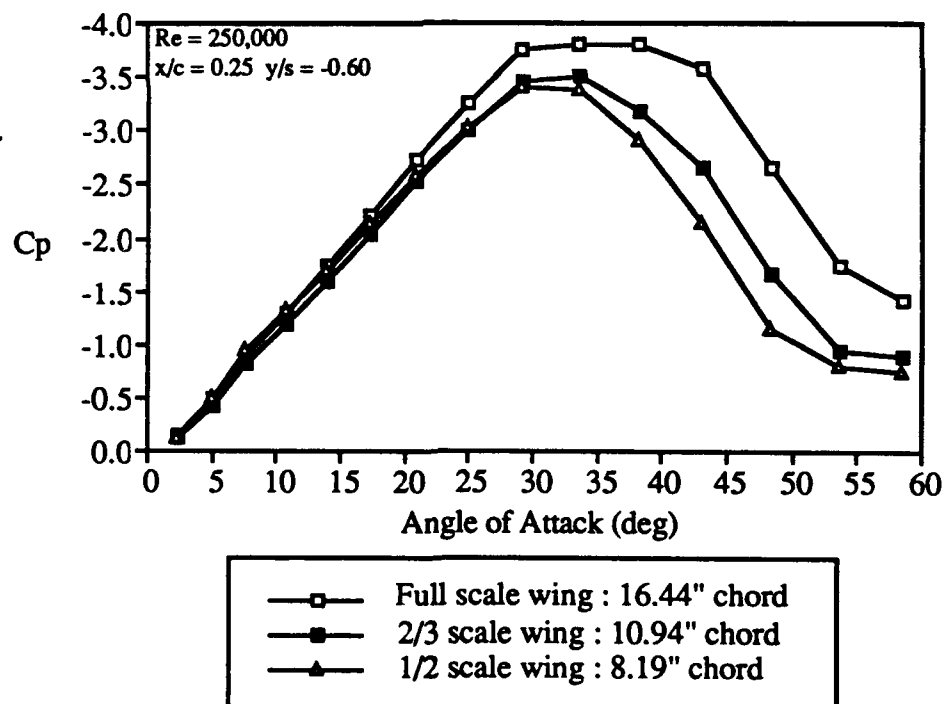
Figure 4.9a   Comparison of Steady Pressure Distributions for Full and Sub-Scale Wings at x/c = 0.25.
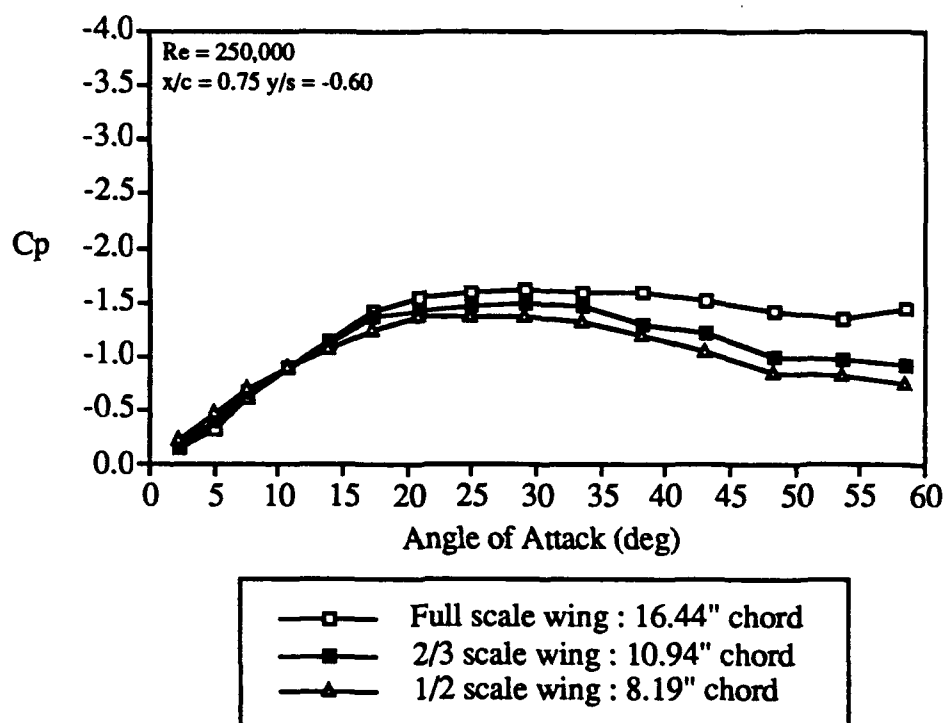
Figure 4.9b   Comparison of Steady Pressure Distributions for Full and Sub-Scale Wings

at x/c = 0.75.

for two surface locations: x/c = 0.25 and 0.75 (both at y/s = -0.60). These two figures qualitatively show the effect seen at each of the surface locations examined. The pressure over each wing remains effectively the same up to a certain angle of attack; at x/c = 0.25 (Fig. 4.9a) this is approximately 21°, while for x/c = 0.75 (Fig. 4.9b) this is approximately 17°. Recalling Fig. 4.8a, this is within a few degrees of the angle at which vortex breakdown first occurs on each wing. Above this point the curves separate, with increasing wing size resulting in a lower pressure at a given incidence. This continues up to the maximum angle examined, 61°. Note that above 45°, the difference between the curves remains approximately the same.

At 21° the blockage ratios for the three wings are 6.0%, 2.7%, and 1.5% respectively. However, at this point the data for the two sub-scale wings is still the same.

From Fig. 4.9a, the full scale data becomes distinct at 21° (blockage of 6.0%), while the two-thirds scale data becomes distinct at 33° (blockage of 4.0%). However, it is more difficult to pinpoint these values in Fig. 4.9b. From looking at the steady pressure data for each of the three wings over the entire range of angles of attack, it is difficult to associate a particular blockage ratio with the point at which the curves begin to separate.

The trend seen in the difference between the steady pressures from each of the three wings is to be expected. An increase in wing size results in an increased blockage, and thus an increase in the local acceleration of the flow. This is turn causes higher flow velocities and thus lower surface pressures. This effect does not appear to be significant for angles below 15° (or blockage ratios below 4.5%).

In addition, it can be seen in Figs. 4.9a and 4.9b that the difference between the data for the full scale wing and that for the two-thirds scale wing is less than the difference between the two sub-scale wings. It appears that the data is reaching an asymptote as the wing chord size decreases in size from $16\frac{7}{16}$" to $8\frac{3}{16}$".

Figures 4.10a and 4.10b also shows comparisons of the pressure distributions for the three different wings. The pressure distribution at a specific angle of attack has been shown for each of the three wings. In Fig. 4.10a the chordwise pressure distribution (at y/s = -0.60) has been shown at an angle of attack of 43.1°. The differences seen between the curves in Fig. 4.9a and 4.9b are repeated here. A larger wing size results in a lower surface pressure. Note that this effect is consistent at each of the fifteen chord locations sampled (from x/c = 0.25-0.95). This trend continues to the maximum angle of attack examined, 61°, and was also seen at Re = 150,000. The percent difference between these three curve is roughly the same at each chord location. The difference between the full scale wing and the two-thirds scale wing is approximately 20% (of the full scale values), while for the full scale and the one-half scale wings the difference is approximately 30%. At x/c = 0.25 and 0.30 the difference is larger, 30% and 40% respectively.
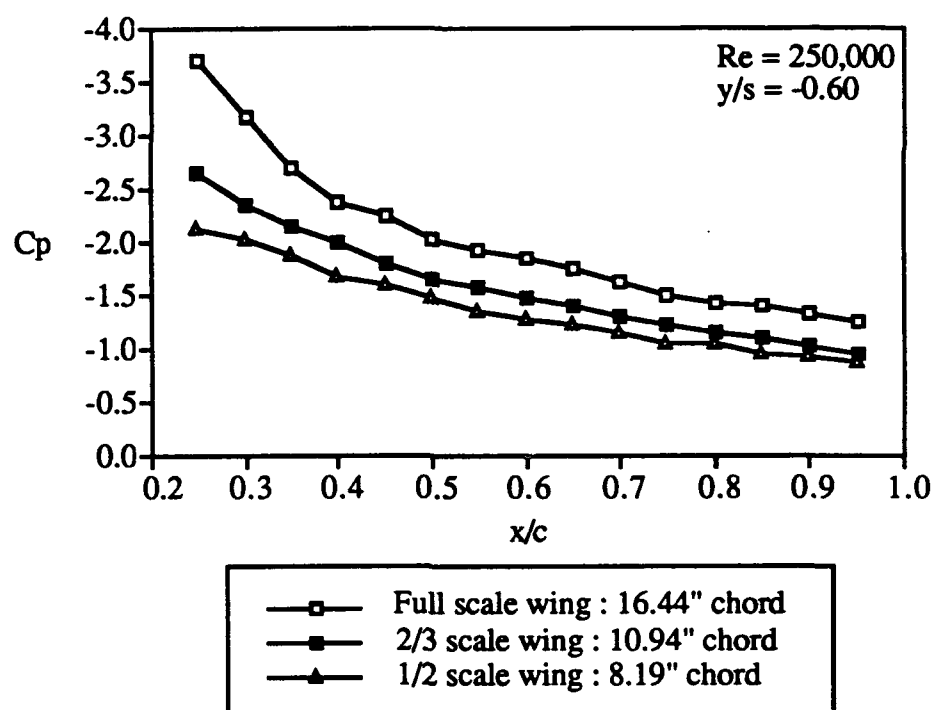
Figure 4.10a   Comparison of Steady Chordwise Surface Pressure Distributions for Full

and Sub-Scale Wings at an Angle of Attack of 43.1°.

Figure 4.10b shows the spanwise pressure distribution at 43.1°, at a constant chord location of x/c = 0.75. At this angle of attack the pressure profiles are essentially flat for each of the three wings. This indicates that at this chord location the leading edge vortex system is relatively weak, if it exists in a coherent state at all. As in the previous figures, the larger wing results in a lower pressure. The difference between the full scale wing and the two-thirds scale wing is approximately 17%; for the full scale and the one-half scale wing this value is 28%. The difference between the two-thirds scale curve and the one-half scale curve is within the repeatability of the measurement; but considering the consistency of this trend throughout the data, the difference is considered to be significant.
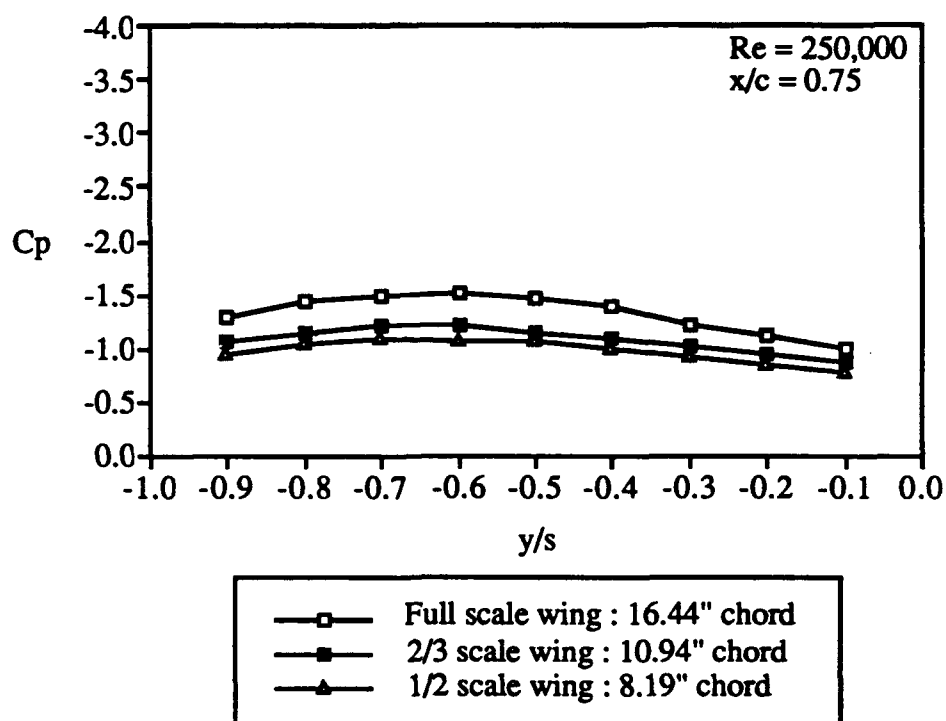
Figure 4.10b   Comparison of Steady Spanwise Surface Pressure Distributions for Full

and Sub-Scale Wings at an Angle of Attack of 43.1°.

4.4.3   Unsteady Effects: Flow Visualization and Surface Pressure

Unsteady pressure data was obtained with all three wings at five surface locations, for two Reynolds numbers and three reduced frequencies. This information is summarized in Table 4.5. The data from these tests can be concisely presented due to the similarity of the results. Of the two Reynolds numbers tested, no significant difference was detected. Quantitative differences existed in the magnitudes of the surface pressures and the pressure coefficients as would be expected for different pitch frequencies. However, of the three reduced pitch frequencies tested the unsteady effects were qualitatively very similar. Thus

only one case will be presented here: x/c = 0.25, k = 0.09, and Re = 250,000. The qualitative results of this case can be assumed to apply to all cases and surface locations.

TABLE 4.5

TEST CONDITIONS FOR SUB-SCALE UNSTEADY PRESSURE TESTS

Tests were conducted using all three wings: full scale, two-thirds scale, and one-half scale.

Surface locations:	y/s	x/c
	-0.60	0.25
	"	0.30
	"	0.35
	"	0.90
	"	0.95

k	Reynolds Number/1000	
0.03	*	250
0.06	150	250
0.09	150	250
0.12	150	*

*Measurement not obtained

Figure 4.11 shows a comparison of the unsteady location of vortex breakdown for each of the three wings. The Reynolds number is 150,000, and the reduced frequency is 0.03, which corresponds to a dimensional pitch frequencies of 0.314, 0.707, and 1.26 Hz for the full scale, two-thirds scale, and one-half scale wings, respectively. The data shown was obtained during a sinusoidal oscillation of angle of attack from 0-60°. The steady case for the full scale wing (as shown in Fig. 4.8b) is shown for reference. The difference between the data for angle of attack increasing and decreasing is indicated on Fig. 4.11 by

arrows showing the direction of motion. Note that although the model pitches from 0-60°, breakdown only exists over the wing for a portion of the motion, thus Fig. 4.11 only shows angles of attack from 14-40°. Note also that the number of data points shown decreases with decreasing wing size. This is due to the higher dimensional pitch frequency for the smaller wings, and thus the shorter time duration of a pitching cycle. Since the frame rate of the video camera is constant, less frames of videotape exist to be digitized.
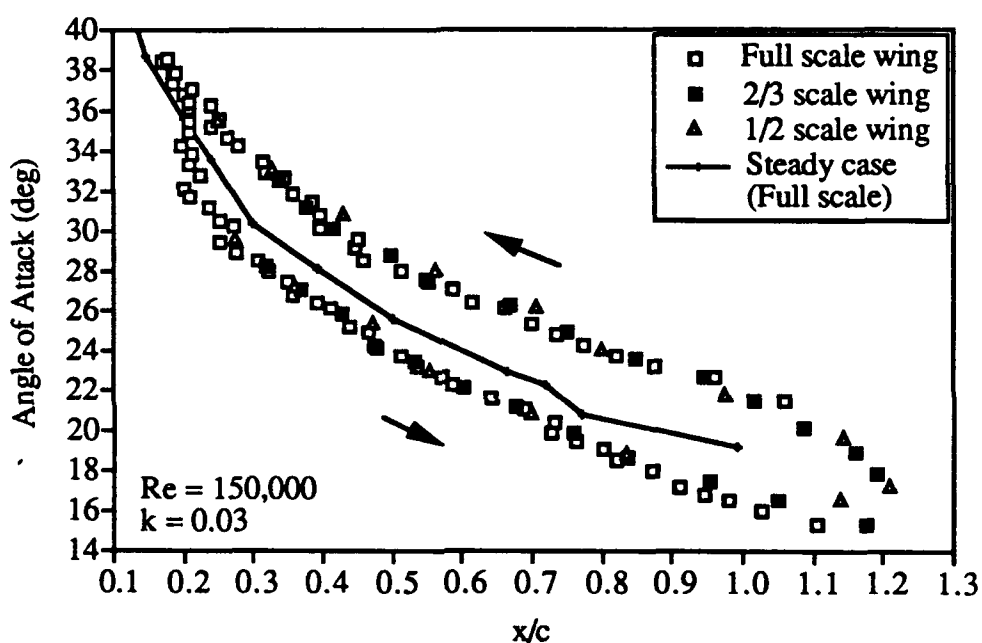
Figure 4.11   Unsteady Location of Vortex Breakdown for Full Scale and Sub-Scale Wings.

From Fig. 4.11 it can be seen that the unsteady data brackets the steady data as is typically seen for large range of motion unsteady pitching oscillations. As a result, the location of breakdown at an instantaneous angle of attack varies by as much as 30% of the chord length, depending on whether the angle of attack is increasing or decreasing. When the wing begins pitching down the breakdown reforms near $x/c = 0.22$. It remains there

while the wing pitches from 37° to 31°. This introduces a lag that remains throughout the remainder of the downstroke (angle of attack decreasing).

It can be seen in Fig. 4.11 that the unsteady characteristics of the breakdown are effectively the same regardless of wing size. The data is the same for each of the three wings, within the repeatability of each point. Similar behavior was seen at a higher reduced frequency of $k = 0.09$. Note that for the two subscale wings additional data points exist near the trailing edge of the wing and in the wake. A similar effect was seen in the steady data.

Figures 4.12a-c show a comparison of the unsteady pressures for the three wings. The pressure coefficient is shown as a function of nondimensional time (Δt is the duration of one pitching motion) in Fig. 4.12a, and as a function of instantaneous angle of attack in Fig. 4.12b. The reduced pitch frequency of $k = 0.09$ corresponds to a dimensional pitch frequency of 0.19 Hz. Fig 4.12a shows two suction peaks during the unsteady motion, at approximately 41° and 25°. A more complete discussion and physical interpretation of this data will be presented in chapter 7.

The magnitudes of both the peaks and the pressures between the peaks decrease with decreasing wing size. This is the high angle of attack portion of the motion, where the blockage ratios are largest and thus the largest blockage effects would be expected. Recalling Fig. 4.6, the effect on the freestream velocity was similarly largest during this portion of the motion.

Figure 4.12b shows the same set of data as a function of instantaneous angle of attack. Notice that the three curves in Fig. 4.12b are very similar qualitatively. From this figure it can be seen that the surface pressures are comparatively the same up to 21°; at this point the curves begin to diverge. Similar behavior was seen in the steady pressure data. Furthermore, although the steady data was excluded from the figure to maintain clarity, it does match the unsteady data up to 21°.
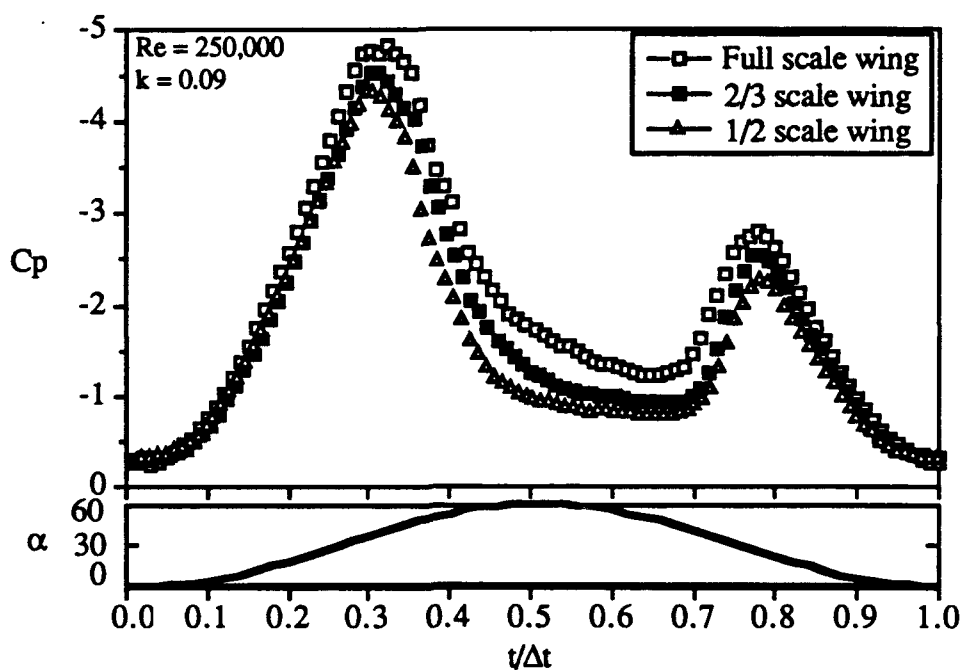
Figure 4.12a   Unsteady Pressure Data for Full Scale and Sub-Scale Wings at x/c = 0.25,

y/s = -0.60. Instantaneous Angle of Attack also Shown.
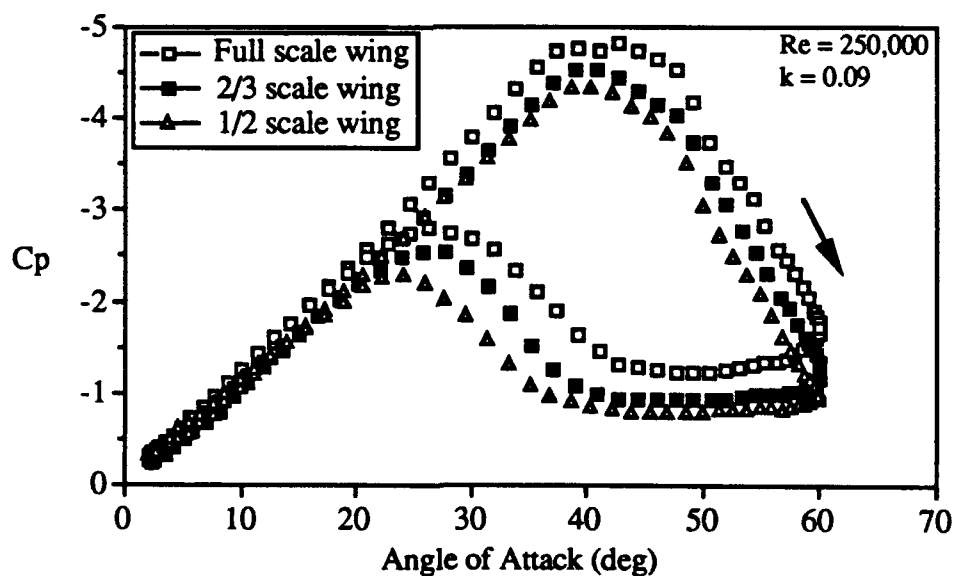
Figure 4.12b   Unsteady Pressure Data for Full Scale and Sub-Scale Wings at x/c = 0.25,

y/s = -0.60.

The unsteady data contains trends similar to the those of the steady data (section 4.4.2). First, the blockage effects are most significant at high angles of attack.. This is expected since the increase in blockage increases the local flow velocity and thus decreases the surface pressures. Second, comparing the data for all three wings suggests the possible existence of an asymptote for which the blockage effects are negligible.

Figure 4.12c again shows the data as a function of nondimensional time; however in this figure the pressures { $(P_{total}-P_{tap})$ } have been nondimensionalized by the total change in pressure { $\Delta(P_{total}-P_{tap})$ } rather than the instantaneous freestream dynamic pressure. Hence, the pressures oscillate from zero to one. By doing this the effect of the varying freestream velocity (as shown in Fig. 4.6) is removed from Fig. 4.12a. This illustrates the effect due to the freestream variation, as opposed to the effect due to the wing size variation.
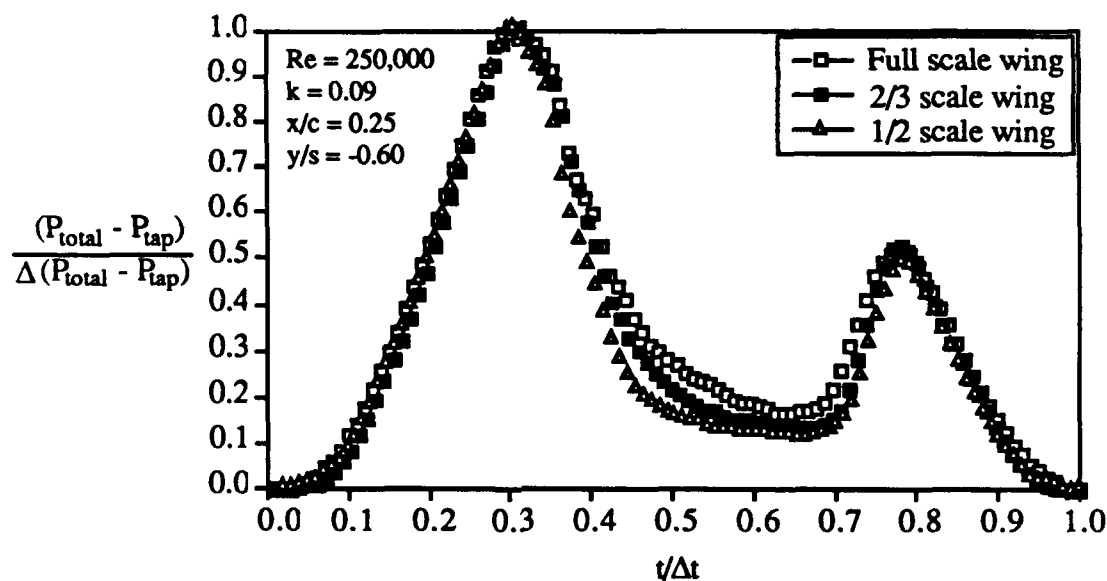
Figure 4.12c   Unsteady Pressure Data for Full Scale and Sub-Scale Wings. Nondimensionalized without Freestream Conditions.

In Fig. 12a, the main difference between the data existed from $t/\Delta t = 0.3$-0.8. Comparing with Fig. 4.12c it can be seen that these differences have been significantly reduced. However, consistent differences exist between the three wings, particularly at the high angles of attack. During the upstroke this corresponds to full separation of the flow, and for the downstroke this corresponds to reformation of the leading edge vortex system.

4.4.4 Blockage Corrections

A method of correcting the steady surface pressures and aerodynamic coefficients for blockage effects was put forth by E. C. Maskell in 1963. This method has been used by several high angle of attack delta wing research papers in the literature (see Pass, 1987; Jarrah, 1988 and 1989; O'Neil et al., 1989; Roos and Kegelman, 1990; and Gili et al., 1990) and has been discussed in textbooks on wind tunnel methods (see Pope and Harper, 1966; and Rae and Pope, 1984). Some discussion of Maskell's method is included here as a prelude to its use. Note that this method applies to the steady aerodynamic loads; vortex trajectories and unsteady conditions are not included.

Maskell's theory was developed using a momentum balance outside of the wake. Using some empirical data, he then derived corrections for a thin flat plate normal to the freestream. These corrections relate the change in freestream dynamic pressure to the drag caused by the separated flow. In order to apply these corrections, the following pieces of information are needed: the blockage ratio, the drag coefficient, and the base pressure. The base pressure is the surface pressure on the leeward side of the plate directly opposite the stagnation point. This parameter can then be expressed in terms of the bluff body blockage factor, ε. Maskell's equation for the corrected surface pressure can be expressed as:

$$\frac{1 - C_P}{1 - C_{P_c}} = 1 + \varepsilon C_D \frac{S}{C} \qquad (4.1)$$

where C_p is the pressure coefficient, C_{p_c} is the corrected pressure coefficient, C_D is the drag coefficient, and $\frac{S}{C}$ is the frontal area blockage ratio. For a wing of finite span, C_{D_s} should be used in place of C_D, where C_{D_s} is the drag due to the separated flow (the total measured drag C_D is the sum of the separation drag and the induced drag). Maskell noted an uncertainty in Equation 4.1 on the order of the square of the blockage ratio.

In order to quantify this parameter, Maskell suggested plotting the square of the lift coefficient (C_L^2) as a function of the total drag coefficient (C_D). The linear portion of this curve is then extrapolated to find the induced drag (C_{D_i}) and the separation drag (C_{D_s}). This method is shown in Fig. 4.13.
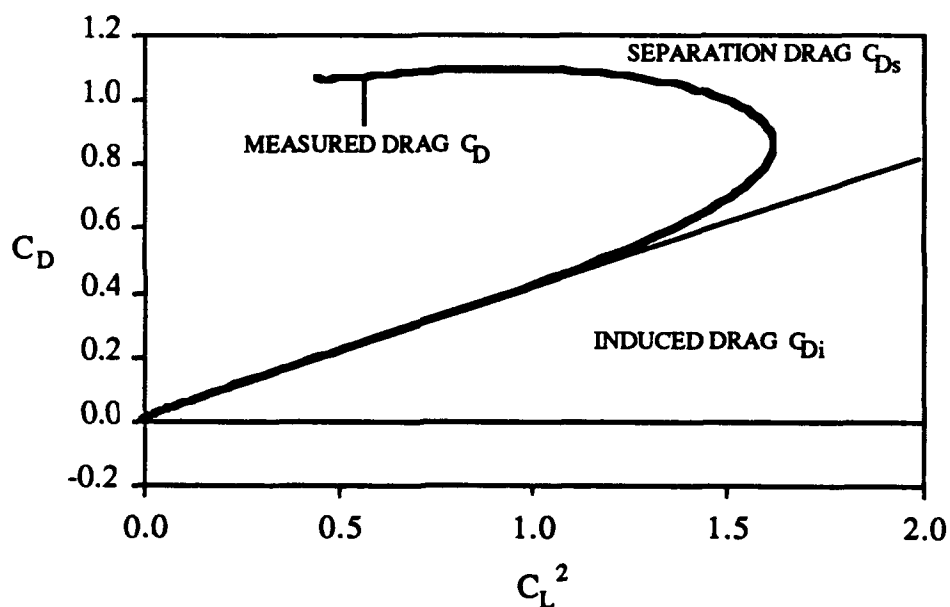
Figure 4.13   Graphic Method of Determining Drag Components. Method from Maskell (1963), data from Jarrah (1988).

As a side note, it should be mentioned that it may be possible to estimate the base pressure coefficient for the current delta wing model from the current steady pressure distributions obtained (to be discussed in Chapter VI). It was found that at an angle of

attack of 60° the leeward pressure field was approximately uniform along a line of pressure taps at a constant semispan location of y/s = 0.60. The pressure coefficient was approximately -1.5. This value could be used as a first approximation of the base pressure coefficient.

Maskell experimentally determined the blockage factor ϵ for a series of flat plates of varying aspect ratio. He empirically found that the value of ϵ varied from 2.77-2.13 as the aspect ratio varied from one to ten. For the current study (aspect ratio 1.5) it was empirically determined that a value of ϵ = 2.75 resulted in the best agreement of the data. Lower values did not sufficiently correct the high angle of attack data (over 30°), while larger values tended to overcorrect the data at low angles of attack. A similar problem was seen by C. Q. Pass (1987); he noted that this was a result of ϵ not being a function of angle of attack. Pass also noted that Maskell's equations were valid for blockages up to about 10%. He concluded that Maskell's equations were suitable for bluff body flow only and needed to be adapted for situations involving a range of angles of attack.

Pass first investigated a series of non-lifting flat plates positioned normal to the flow. Doing this, he successfully verified Maskell's method. Pass then investigated a series of lifting wings over a range of angles of attack. Using empirical data for flat plate rectangular and triangular wings, Pass adapted Maskell's equations to provide useful corrections for his data involving blockage ratios over 20%. Pass used wings of different sizes, and assumed that the data for the smallest wing was free of blockage effects. He then altered Maskell's equations until he found acceptable agreement between the data.

Since it is based on Maskell's method, Pass' method also serves to estimate the change in freestream dynamic pressure due to a change in the blockage ratio. Pass's method of correction involves several different equations. The appropriate equation depends on the type of wing and the value of the separation drag coefficient. The aspect ratio, blockage ratio, and separation drag coefficient all need to be supplied for Pass'

equations. These equations then yield the value of the unknown term on the right-hand side of Equation 4.1.

Thus, it is necessary to obtain the separation drag coefficient in order to apply Pass' equations to the current problem of a delta wing at angle of attack. Lift and drag coefficient data for a 69.5° delta wing has been published by Jarrah (1988 and 1989) for angles of attack from 0-90°. Jarrah's data has been corrected for blockage effects. Note that this data is for a wing with a thickness ratio of 2.8% and a Reynolds number of 450,000, as opposed to 4.6% and 250,000 for the current study. Jarrah's data has been fit to sixth order curves over the range of 0-60° angle of attack. These equations were then used to generate the C_L^2 curve shown in Fig. 4.13. Thus, for a given angle of attack the lift coefficient can be calculated, and then the separation drag coefficient can be deduced.

Both Maskell's equation and Pass' adaptation were applied to the current data. It was found that Maskell's equation resulted in slightly better agreement of the data. However, Pass' adapted equations take into account angle of attack and aspect ratio and thus are considered to be more applicable to the current data. In addition, Maskell's equation tended to substantially reduce the magnitude of the pressure coefficient. Pass' method left the steady pressure data with more reasonable magnitudes (when compared to data from the literature). Note that the corrective equations were derived by Pass expressly for his experimental data, and the current application of those equations assumes the validity of using lift and force data from a separate study.

Figure 4.14 shows the corrected steady surface pressure data (using Pass' method). The three parts of this figure correspond to the uncorrected data shown in Figs. 4.9a, 4.9b, and 4.10a. Each data point shown has been corrected, although for the low angles of attack the correction is negligible. By using Pass' correction the agreement between the data from the three different size wings can be improved. As shown in Fig. 4.14, the agreement from 20-35° has been significantly improved (compare to Fig. 4.9). In addition,
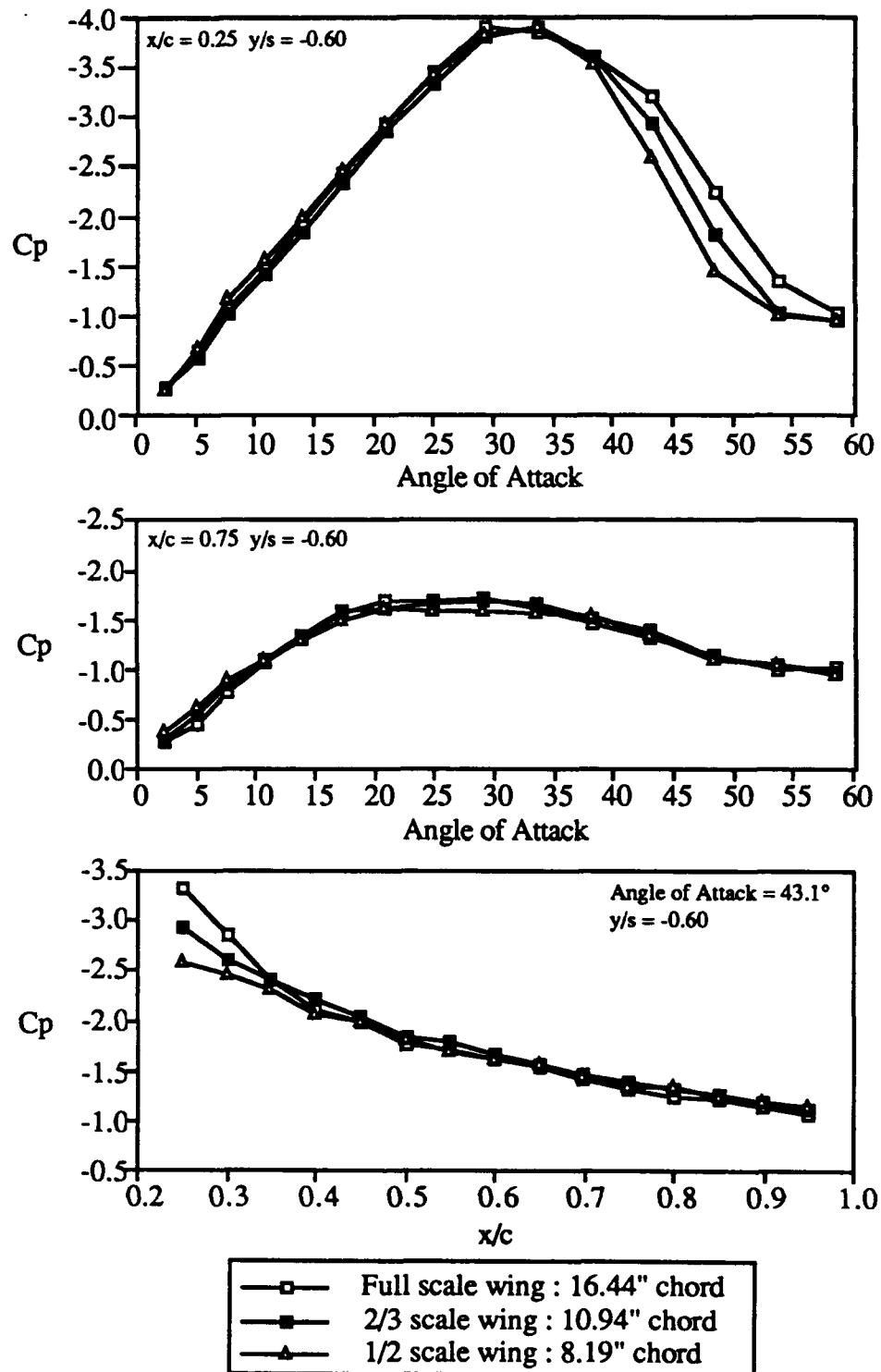
Figure 4.14   Corrected Steady Pressure Data. Compare to Data Shown in Figs. 4.9a,

4.9b, and 4.10a.

the agreement at surface locations aft of x/c = 0.40 has also been improved (compare to Fig. 4.10).

However, for the forwardmost surface locations at high angles of attack the data still shows distinct differences due to wing size. The correction method is least successful for pressures measured at chord locations of x/c = 0.25-0.30 and angles of attack from 43-55°.

As mentioned in section 4.4.1, these are the surface locations with the poorest location accuracy. However, the spanwise pressure gradient from 43-55° is small; the spanwise pressure profile has begun to flatten (this has also been noted by O'Neil et al., 1989). The chordwise gradient has also begun to decrease by 43°, although not to the same extent. By comparing the uncertainty of the surface location to the local pressure gradient, an uncertainty in the pressure coefficient at the nominal surface location can be estimated. For the smallest wing this uncertainty in C_p is ±0.05 at 43° and x/c = 0.25. This is the uncertainty due to the possibly incorrect location of the pressure tap. This amount decreases as the incidence increase. The uncertainty of the C_p measurement itself (for the smallest wing at 43° and 0.25c) is ±0.06. Neither of these sources of uncertainty is sufficient to account for the differences in the corrected data.

Figure 4.15 again shows the same steady pressure as Fig. 4.14 (which shows the corrected form of the data). In Fig. 4.15 the data has been nondimensionalized without defining a pressure coefficient (and thus not using the freestream dynamic pressure). A similar procedure was applied to the unsteady data shown in Fig. 4.12c; the object being to eliminate the freestream fluctuation from the differences present in the data from the three wings. As for the unsteady case, this method of nondimensionalization results in increased agreement between the three wings, although differences still exist at large angles of attack.

Cunningham and Bushlow (1990) applied a similar correction technique to their steady force data for a series of flat plate delta wings, straked wings, and fighter aircraft models. Using angles of attack up to 90°, they measured a reduction in the freestream

dynamic pressure as a function of incidence similar to that seen in the current study. However, rather than nondimensionalizing the force data with respect to the dynamic pressure at the actual angle of attack, they used the dynamic pressure measured with the model at 0° angle of attack. This essentially accomplished the same effect as that seen in Fig. 4.15. As with the current data, Cunningham and Bushlow increased the agreement of their data by using this method.
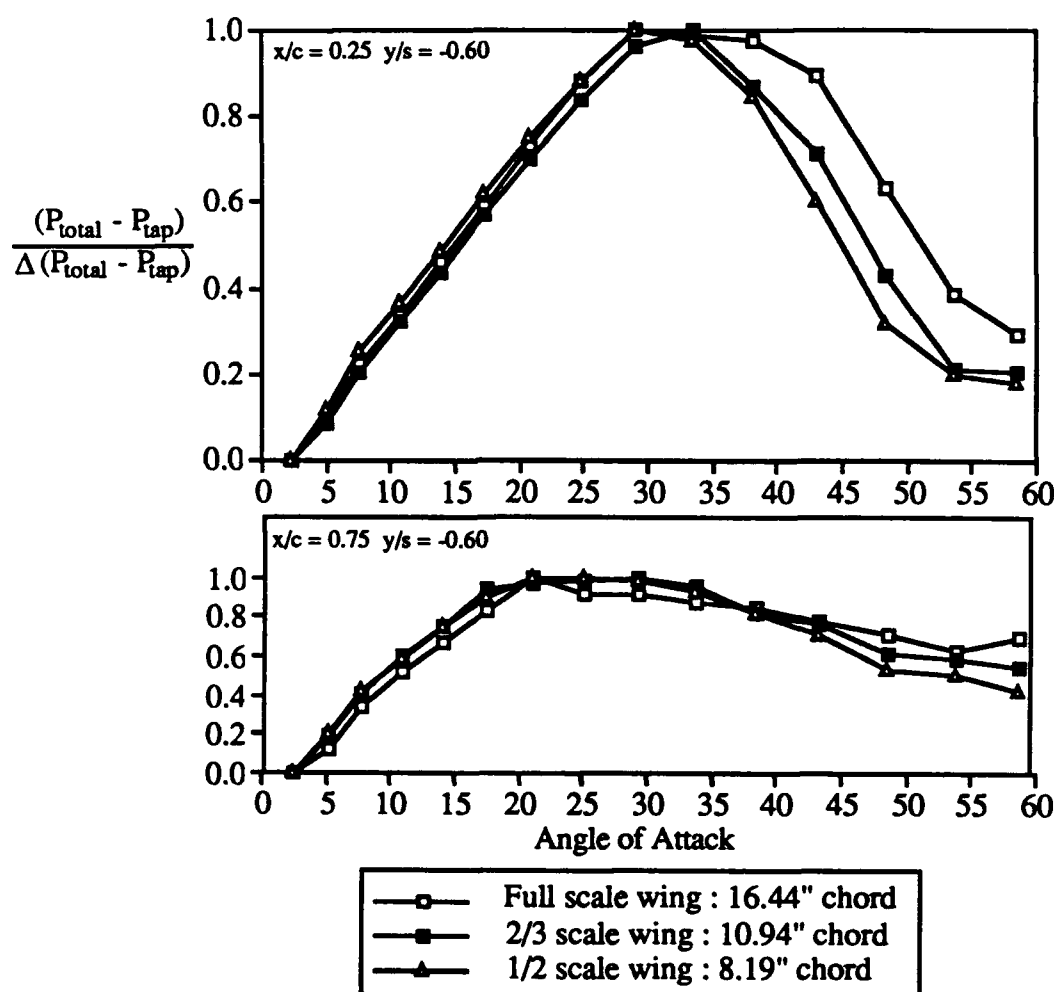
Figure 4.15   Steady Pressure Data Nondimensionalized without Freestream Conditions. Corrected Version of this Data Shown in Fig. 4.14.

However, the agreement was not satisfactory at angles of attack beyond stall (as is the case for the current data). Thus, they empirically developed an equation to correct the data at post-stall angles of attack. This equation was a function of the angle of attack, the stall angle, and the model planform area. The equation was originally developed to correct the normal force and pitching moment coefficients. Note that both Pass and Cunningham and Bushlow developed their corrective techniques by assuming one set of data to be free of any blockage effects.

Figure 4.15 also demonstrates the effect of Pass' correction method. By comparing Fig. 4.15 to Fig. 4.14 (the corrected data), it can be seen that the agreement shown in each set of curves is effectively the same. This indicates that Pass' method corrects the standard definition of the pressure coefficient for the variation of the freestream dynamic pressure.

Correction methods for unsteady data are considerable less prevalent. Cunningham and Bushlow (1990) developed a preliminary unsteady correction method that was dependent on pitching frequency. Using their method they substantially improved the agreement between water tunnel data and wind tunnel data.

An attempt has been made to correct the current unsteady pressure data for blockage effects using Pass' method. However, rather than using the steady lift and drag coefficients, the unsteady coefficients have been used. As before, the unsteady force data was obtained from Jarrah (1988) for a reduced pitch frequency of $k = 0.08$. Figure 4.16 shows the corrected unsteady data. Fairly good agreement is obtained, particularly over the region of the curve corresponding to the high angle of attack regime where the flow is totally separated (between the two suction peaks). This is the region where differences in the curves could not be attributed to variations in the freestream dynamic pressure. However, the magnitudes of the suction peaks remain different for each wing.
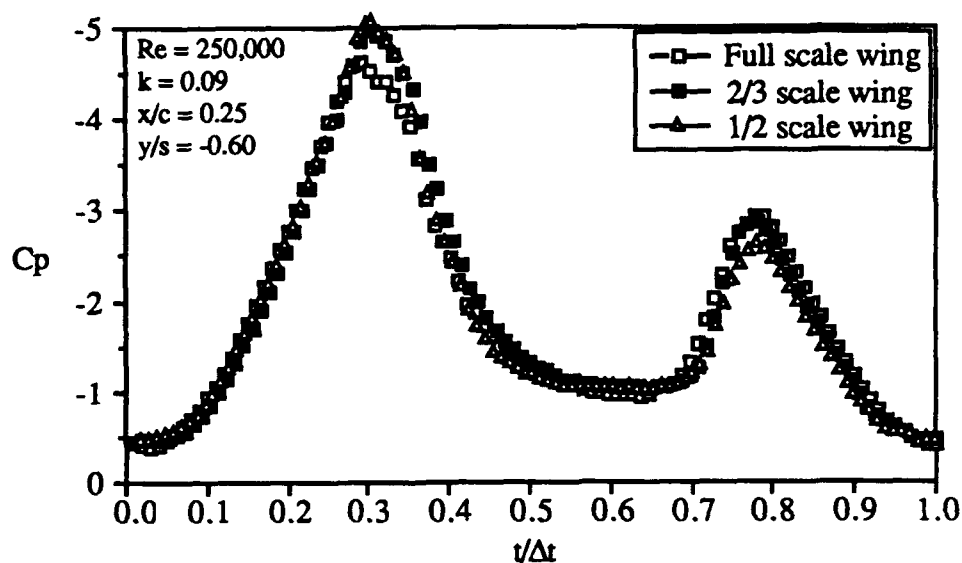
Figure 4.16   Corrected Unsteady Pressure Data. Compare to Data Shown in Fig. 4.12.

4.4.5   Conclusions

The location of vortex breakdown did not show a conclusive effect due to wing size. The steady location of breakdown over the wing for the full scale wing and the two-thirds scale wing was effectively the same. However, differences did exist for the one-half scale wing. For a given angle of attack the steady breakdown was aft of the corresponding location for the two larger wings. This was not consistent though, and considering that a full range of breakdown location data did not exist for the sub-scale wings, a conclusive statement cannot be made. The possibility exists that this was an effect of the obstruction caused by the wing support hardware. The size of this hardware relative to the one-half scale wing may have been significant. However, the corresponding surface pressure data did not show a similar effect and thus does not show evidence of support interference.

However, the steady flow visualization tests did show an effect at the trailing edge of the models. The location of breakdown when it first appeared was farther into the wake with decreasing wing size. In addition, the effect of the trailing edge as an impedance to the forward and aft motion of the breakdown was decreased as the wing size decreased. The ability of the breakdown to reach a steady state in the wake was increased. This is probably a result of the decrease in the pressure gradient at the trailing edge as the wing size decreases (due the decrease in acceleration of the freestream around the model).

A similar effect was evident in the unsteady flow visualization data, where the breakdown again showed an increased ability to exist in the wake, as the wing size decreased. However, that was effectively the only difference between the unsteady breakdown data for the three wings. For locations over the wing, the three sets of unsteady data showed very good agreement, at both reduced frequencies examined. This agreement reinforces the similarity of the steady breakdown location data, and further suggests that the differences seen for the one-half scale wing are not an effect of the decrease in blockage, but rather an effect of a different parameter.

Although the location of vortex breakdown over the wing did not show a consistent effect due to wing size, the steady surface pressures did. As the wing size was successively decreased from the full scale wing to the two-thirds scale wing, then to the one-half wing, the surface pressures increased (for both the steady and unsteady cases). This is probably a result of the decrease in blockage and thus the decrease in local acceleration of the flow. However, the magnitude of this effect was not consistent between wings. The pressure data suggested the presence of an asymptote at which a further decrease in wing size would not have a noticeable effect on the data, i.e. the blockage effects would be negligible.

The unsteady pressure data showed similar trends. However, this was in part due to the fluctuation of the freestream velocity, which is contained in the definition of the pressure coefficient. When the unsteady pressure was examined without being nondimensionalized by the freestream conditions the differences due to wing size were significantly decreased. Considering the relative lack of blockage effect on the unsteady breakdown data it seems that a significant effect of the wing size is on the freestream conditions. This in turn effects the pressure coefficient by its definition.

However, removing the freestream condition from the nondimensionalization does not completely remove the differences due to wing size. The remaining differences occurred almost exclusively during the portion of the motion where the flowfield is fully separated. These differences could not be attributed to the accuracy of the surface location of the pressure taps.

Methods of steady blockage corrections available in the literature were examined and a suitable correction was used with the steady pressure data. The agreement of the data was significantly improved. Differences still remained in the data for large angles of attack and surface locations from $x/c = 0.25$-0.30. The correction method was then employed on the unsteady pressure data, with the addition of using the *unsteady* force coefficients. This also resulted in significantly improved agreement of the data. This was particularly true for large angles of attack where the differences in the data could not be attributed to variations of the freestream dynamic pressure. However, differences still remained in the magnitudes of the suction peaks.

The blockage effect seen on the surface pressures was most noticeable for angles of attack where breakdown was present; for both steady and unsteady cases. At low angles of attack (less than 20°) the steady surface pressures showed comparatively little effect due to

wing size; above this angle the differences in the data drastically increased. This is within a few degrees of the angle at which breakdown moves onto the wing for each case.

It was consistently seen that the most dramatic blockage effects occurred at angles for which breakdown existed. However, it is unclear if one is a cause and one an effect, or if they are both symptoms caused by a different variable. While the blockage does not seem to effect the location of breakdown, it may be effecting it in a way that in turn effects the surface pressures.

This observation reinforces the idea that the aerodynamics of a pitching delta wing are significantly different for ranges of motion including and excluding vortex breakdown. As noted by other researchers (Ashley, Jarrah, Katz, and Vaneck, 1990), ranges of motion including the presence of breakdown are associated with significant unsteady effects. Conversely, ranges not including breakdown are associated with quasi-steady behavior.

Consistent quantitative differences were seen in the pressure data as a function of the wing size. This was true for both steady and unsteady tests. However, the trends seen were consistent throughout the data regardless of wing size. Although the blockage effects changed the magnitudes of the data for the full scale wing, the qualitative effect on the data was small. This suggests that this type of unsteady testing can be successfully accomplished in relatively small wind tunnels such as the one used here. As noted by Erickson (1981) the leading edge vortices are very sensitive to a variety of factors, thus it is the qualitative characteristics that should be stressed. Thus the full scale wing has been used to obtain the majority of the data used in this research due to the increased surface resolution and range of Reynolds numbers available with this wing. Furthermore it is assumed that the behavior of the vortex system and the pressure field over this wing are representative of and comparable to the behavior of other wings.

V   RESULTS: FLOW VISUALIZATION DATA

5.1   Overview

The results of the flow visualization experiments are divided into steady cases and unsteady cases. The steady data for each of the flow visualization models (see section 2.3) will be presented first. The presentation of the unsteady data includes some data available in the literature. A summary of the significant trends then concludes the chapter.

5.2   Steady Flow Visualization Data

Steady flow visualization experiments were conducted at several angles of attack ranging from 0-65°. Reynolds numbers of 150,000 and 450,000 were used; this approximated the range of Reynolds numbers used during the surface pressure experiments, while maintaining useful flow visualization quality. Only the left side vortex (relative to a top view) was visualized.

Steady breakdown location data was obtained for three flow visualization models, as described in sections 2.3.1 and 2.3.2. By using these three models the effect of both wing thickness ratio and leading edge geometry could be examined. The majority of the data for the first model has been previously published (LeMay, Batill, and Nelson, 1990; Thompson, Batill, and Nelson, 1991). The third wing is the wing used to obtain the majority of the surface pressure data (sections 6 and 7) and blockage effect data (section 4).

Figure 5.1 shows the steady breakdown location as a function of angle of attack for the third (single bevel) wing. Increasing angles of attack and decreasing angles of attack (quasi-statically) are shown separately. This case is for a Reynolds number of 150,000.

126

Each point shown is the average of ten points taken at that angle of attack; the error band is the standard deviation (Equation 3.6) of the average. Note that instantaneous fluctuations of ±3-5% are possible at each point due to the unsteadiness of the breakdown. A discussion of the unsteadiness of the breakdown location for a steady angle of attack is included in section 3.5.3 (and Fig. 3.5).
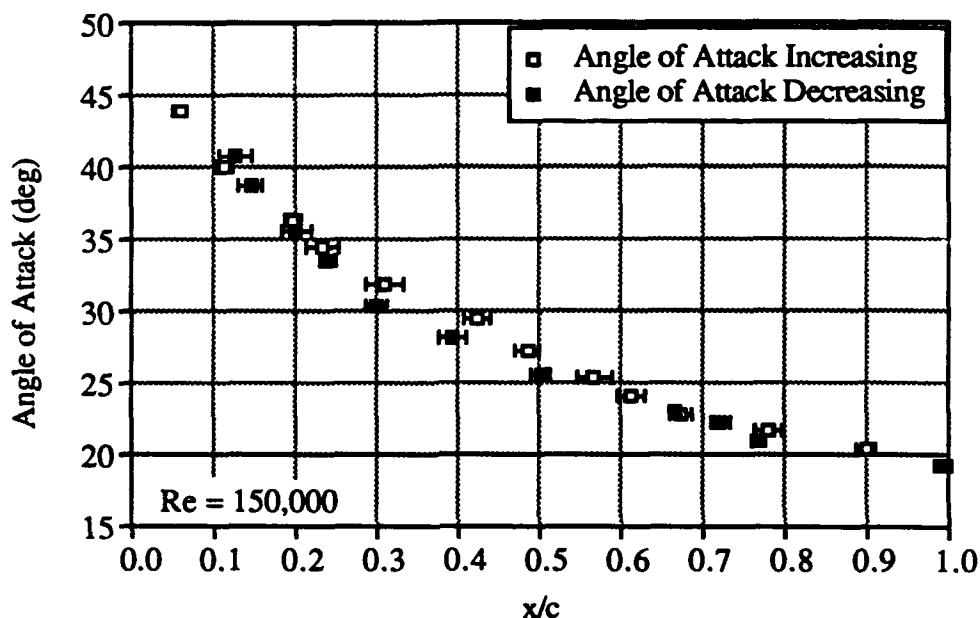
Figure 5.1   Steady Vortex Breakdown Location for Single Bevel 70° Wing.

For increasing angles of attack, breakdown did not exist up to 18.9°. The next measurement was at 20.3°, at which point the breakdown first occurred and was located at x/c = 0.90. The breakdown then progressed forward on the wing with increasing angle of attack. The last measurable position was at 43.9° and x/c = 0.06. By 54° the flow over the wing appeared to be fully separated, similar to flow around a bluff body.

For decreasing angles of attack the vortex reformed with breakdown near the apex of the wing; the first measurable position was at 40.7° and x/c = 0.13. The breakdown then proceeded aft with decreasing incidence. A difference in the two curves exists at the

trailing edge. Breakdown moves onto the wing at 20.3°, but remains there until 19.2°, at which point it is located 10% farther aft than for the increasing incidence case.

This difference at the trailing edge is evidence of a steady hysteresis in the breakdown location. Further evidence exists near the center of the wing, where for decreasing angles of attack the breakdown is slightly forward of the location for increasing angles. This ranges extends from approximately $x/c = 0.25$-0.55 (25-33°). Although the unsteadiness of the breakdown is sufficient to account for this difference, the scatter due to the digitized points is not; thus the difference is considered to be significant. The effect is most apparent from 28-30° where the difference in the two curves is approximately 10% of the chord.

Data was also obtained at Re = 450,000; the data for this case was on the same curve as data for the Re = 150,000 case shown in Fig. 5.1; however, a difference did exist near the trailing edge. The initial and final locations of breakdown were both at $x/c = 0.77$. This occurred at 21.2° for increasing incidence; and at 20.2° for decreasing incidence. Comparatively, for the Re = 150,000 case, breakdown had steady state positions much closer to the trailing edge, particularly for decreasing incidence. The data for Re = 450,000 was very similar to the Re = 150,000 data shown in Fig. 5.1, excluding the two data points closest to the trailing edge.

Figure 5.2 shows the steady height-above-wing location (z) of vortex breakdown. This figure shows a qualitative similarity to the chordwise location of breakdown. As in Fig. 5.1, a difference exists between the angle of attack increasing and decreasing portions of the data from 25-33°. The data obtained at Re = 450,000 did not show any significant difference from Fig. 5.2, similar to the chordwise location data.
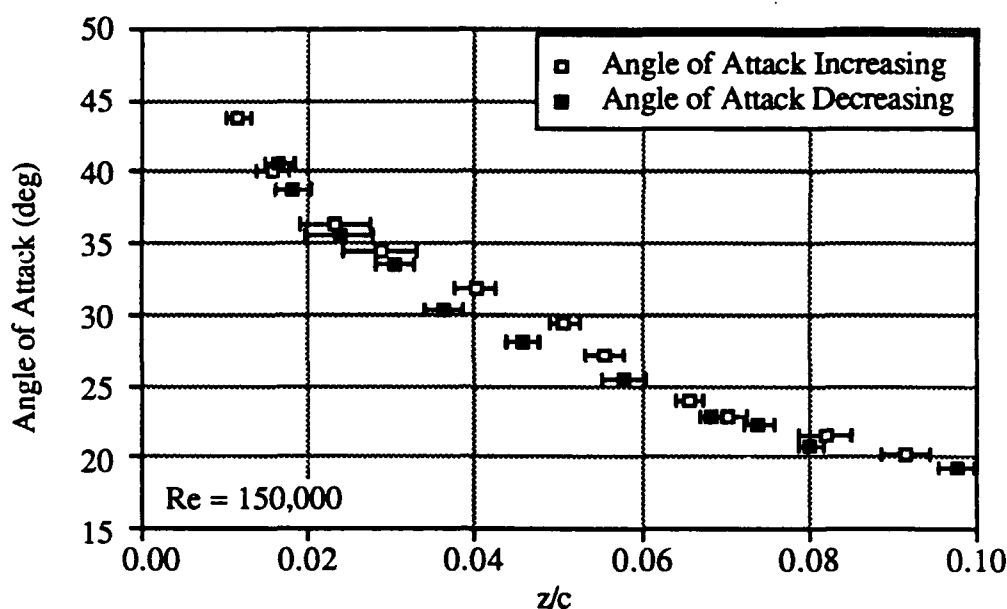
Figure 5.2   Steady Vortex Breakdown Location (Height Above Wing) for Single Bevel 70° Wing.

Figure 5.3 shows a comparison of the steady breakdown location for three wings of varying thickness ratios or leading edge geometry (though all have a 70° sweep angle and comparable chord lengths). The "two bevel" wings have leading edges that are beveled on both pressure and suction sides, while the "one bevel" wing is beveled on only the pressure side. These three wings are shown in Figs. 2.3a-c. The data for the 0.50" thick wing is from LeMay (see LeMay, 1988; or LeMay, Batill and Nelson, 1990). The data for the one bevel 0.75" wing is the same data shown in Fig. 5.1. Note that the Reynolds number is different for each of the three wings in Fig. 5.2; for LeMay's data Re = 260,000, while for the two bevel 0.75" wing Re = 420,000 (and for the data shown in Fig. 5.1 Re = 150,000). Note that each of these wings was tested in the same facility, thus the tunnel blockage is equivalent for each wing.
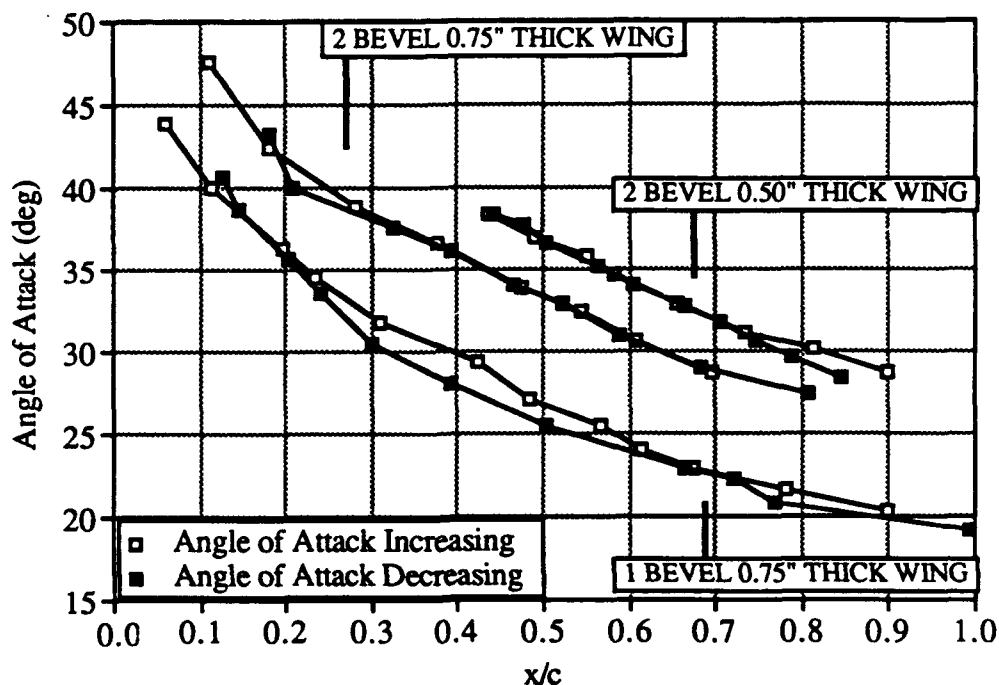
Figure 5.3   Steady Breakdown Location: Thickness and Leading Edge Geometry

Effects (data for 0.50" wing from LeMay, 1988)

Figure 5.3 shows consistent differences between the data for each wing. Changing the thickness or leading edge geometry of the wing appears to a significant effect on the breakdown location. This difference is probably not attributable to the differences in Reynolds number, as indicated by the current experiments (at Re = 150,000 and 450,000) performed on the single bevel wing. O'Neil et al. (1989) also found a substantial effect on the breakdown location due to leading edge shape. They tested wings with the same thickness ratio but different leading edge geometries; among them a single beveled wing and a double beveled wing similar to the ones shown in Fig. 5.3. As in Fig. 5.3, O'Neil et al. found that a change from one bevel to two bevel resulted in a farther aft breakdown location for a given angle of attack. O'Neil et al. measured this difference to be from 10-15% of the chord, whereas Fig. 5.3 shows differences of as much as 20%.

The addition of an upper surface bevel effectively adds camber to the wing. For a wing with symmetric upper and lower surface bevels, the camber line is the same as the chord line, thus the wing has zero camber. However, a wing with only a lower surface bevel has a negative camber. Thus the addition of an upper surface bevel increases the camber from a negative value to zero. An increase in camber then has the effect of decreasing the local angle of attack as seen by the leading edge. Thus, a downstream change in breakdown would be expected.

However, the change in effective angle of attack is probably insufficient to account for the change in breakdown location shown in Fig. 5.3. Examining the camber line of the single bevel model (relative to its chord line) suggests a change in effective angle of attack of no more than 2°. This amount is not enough to account for the difference in the two curves shown in Fig. 5.3.

A change in thickness also results in a breakdown location farther aft as seen in Fig. 5.3. However, the angle at which breakdown first occurs remains within a degree for both the 0.50" and 0.75" thick wings. The effect due to thickness is opposite that documented in some of the following sources in the literature. Although no data was included, McKernan (1983) noted that the difference in breakdown location for otherwise identical models of thicknesses 0.25" and 0.75" was from 15-55% of the chord length (with the thicker model having the breakdown location farther aft). Additionally, Earnshaw (1968) documented a downstream shift with increasing thickness.

However, in both those cases, the thickness effect could not be conclusively isolated. Due to anomalies present in the data, Earnshaw stated that the effects of Reynolds number and Mach number could have been significant. He was not able to resolve the contribution of each parameter. McKernan used a different model support system between his two (0.25" and 0.75") wings. He mentions that the support for the thin model (a rear mount) could have caused an upstream movement of the breakdown.

Although the 0.50" and 0.75" wings shown in Fig. 5.3 were supported on the exact same mount, the ability to draw conclusions is limited. The contradictory nature of

the data in the literature, the fact that the data was obtained by different researchers using different techniques, the slight difference in the leading edge geometries (bevel angle), the difference in Reynolds numbers (260,000 as opposed to 150,000 for the current study); all these contribute an unknown amount to the breakdown location.

From Fig. 5.3 it can be seen that, for two of the wings, no difference exists between the increasing and decreasing incidence cases at the central portion of the wings; unlike in Fig. 5.1. However, similar to that data, the data for the other two wings does show differences near the trailing edge. For the 0.50" wing, this was described by LeMay as a steady state hysteresis (LeMay, 1988). Similarly, a steady state hysteresis in breakdown location has been documented by Lowson (1964). For each of the three wings shown, breakdown remains over the wing to a lower angle of attack than the angle at which it first occurred (similar to the findings of Lowson).

Figure 5.3 demonstrates the sensitivity of the breakdown to the specific wing geometry. Each wing shown in this figure has a leading edge sweep of 70°, yet at a given angle of attack the breakdown position varies by as much as 40% of the chord length depending on thickness and leading edge shape.

This sensitivity is also shown in Fig. 5.4. Figures 5.3 and 5.4 both serve to illustrate the difficulty and ambiguity that arise when making measurements involving vortex breakdown, even for the steady case. Figure 5.4 shows the steady breakdown location over a 70° wing from several sources available in the literature. The data from the current research (as shown in Fig. 5.1) is also shown. The frontal area blockage ratio at a specific angle of attack of 30° (chosen arbitrarily for comparison) is indicated for each study.
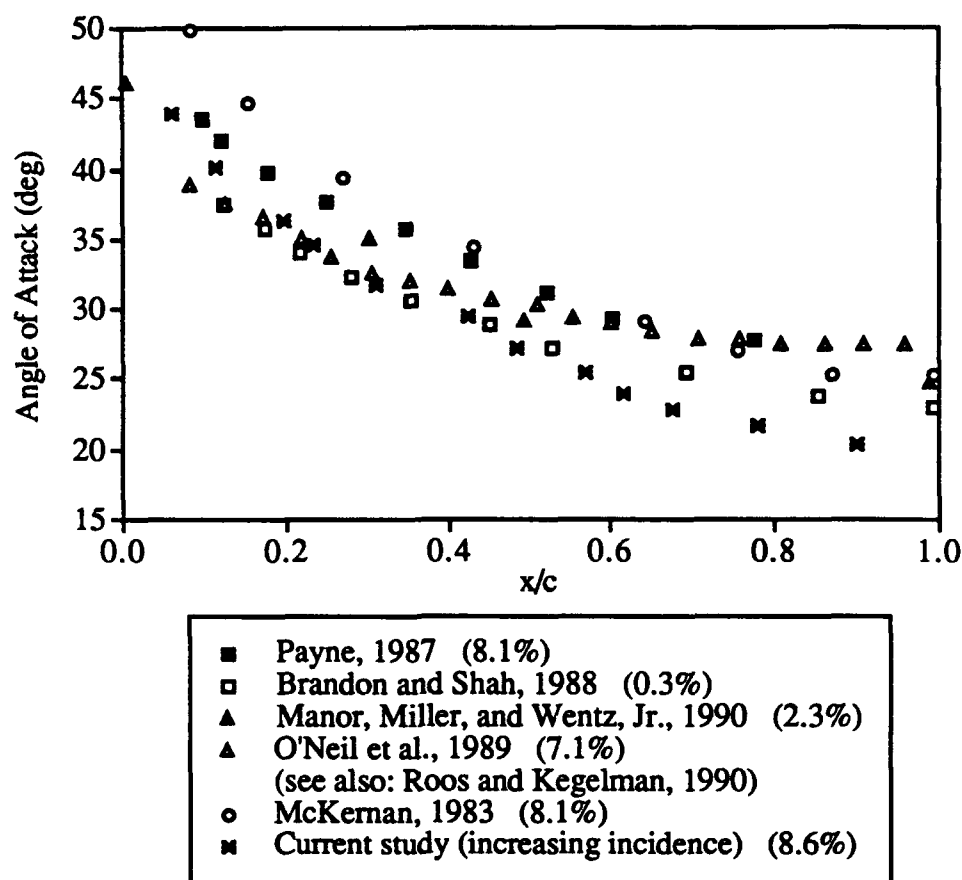
Figure 5.4   Steady Vortex Breakdown Location from Sources in the Literature for a 70°

Delta Wing. Frontal Area Blockage Ratio at 30° Indicated for each Study in Parentheses.

As shown in Fig. 5.3, a wide range of chordwise locations exists at a specific angle of attack, even though the sweep angle is the same for each wing. Additional factors such as thickness ratio, tunnel blockage, and downstream pressure gradient have to be considered. Each of the wings for which data is shown has a single bevel, with the exception of that of Manor, Miller, and Wentz (1990). The data from McKernan (1983) and the current study are for wings with thickness ratios from 4.5-4.7%, while the remainder of the data is for wings from 1.2-1.6% thick. In addition, with the exception of the current study it is unknown whether the remainder of the data was obtained for

increasing or decreasing angles of attack, or some average value. As seen by both the current study and by LeMay, Batill, and Nelson (1988 and 1990), this can cause a difference in breakdown location. Figure 5.4 illustrates the unsteadiness of the phenomenon of breakdown itself, and the sensitivity of breakdown to a variety of conditions.

An interesting aspect of the data shown in Fig. 5.4 involves the difference between the data from the current research and the data from McKernan. These two studies utilized wings with very similar thickness ratios and yet significant differences exist in the breakdown location; as much as 20% for a fixed angle of attack. A difference of that magnitude is probably not attributable to the measurement technique. However, the reason for the difference is unknown. In general, the differences apparent in Fig. 5.4 can be attributed to some of the following:

- Leading edge geometry

- Thickness ratio

- Measurement technique / Researcher definition of breakdown point

- Blockage (model size relative to tunnel cross section)

- Wind tunnel streamwise pressure gradient

- Wing support interference

- Direction of quasi-steady motion: increasing or decreasing incidence

- Reynolds number

Figure 5.5 shows the steady vortex core trajectory at four increasing angles of attack; three prior to the occurrence of vortex breakdown and one showing the initial occurrence of breakdown. The Reynolds number is 150,000 as in the previous figures. The core first becomes visible at 5°. It may actually form at a slightly lower angle before being effectively visualized by the present technique. Figure 5.5 demonstrates that the vortex core is not a perfectly straight line (in this plane). A slight waviness of the core can be detected with the naked eye for each of the four angles shown. The characteristic

continues to exist when breakdown exists over the wing (as can be seen at 20.1°). It can also be seen that beyond the trailing edge the core begins to align itself with the freestream, which is moving from left to right perpendicular to the model support.
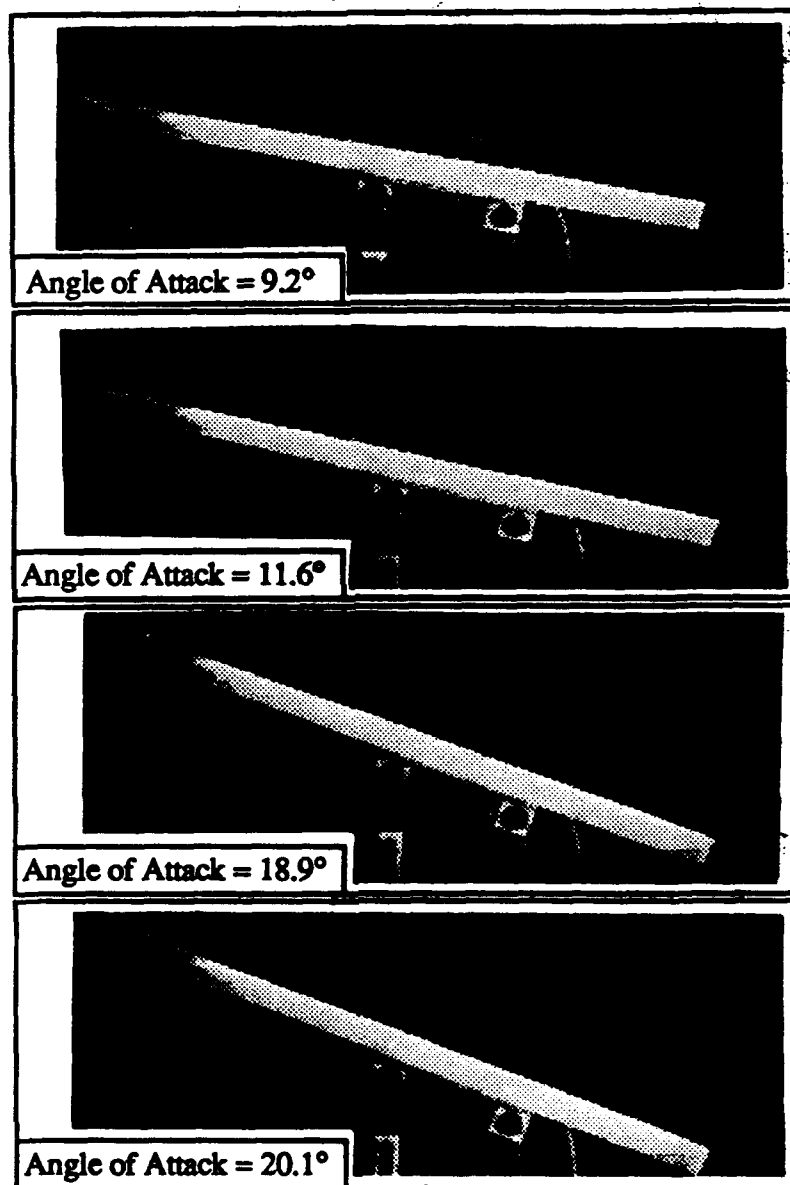
Figure 5.5   Steady Vortex Core Trajectory at four Angles of Attack. Re = 150,000.

Once breakdown had occurred, it moved forward along a path defined by the vortex core as shown in Fig. 5.5 (at 20.1°). The shape of the core did not measurably change as breakdown moved forward. A similar trend was seen for decreasing angles of attack and the associated aft progression of breakdown.

Flow visualization tests were not performed from a view perpendicular to the surface of the wing; thus, no spanwise information on the core linearity or breakdown location was obtained.

Note from Fig. 5.5 that throughout the angle of attack range shown, the locations of the core and its irregularities maintain roughly the same relative position as the wing changes angle of attack. This can be examined by measuring the angle that the vortex core makes with the wing as compared to the angle of attack of the wing. To do this, a straight line is fit to the core for the length of the core visualized. The angle of this line can then be measured relative to the wing. This information is shown in Fig. 5.6, which shows the angle of the core (θ) as a function of angle of attack. The error bands are the uncertainty
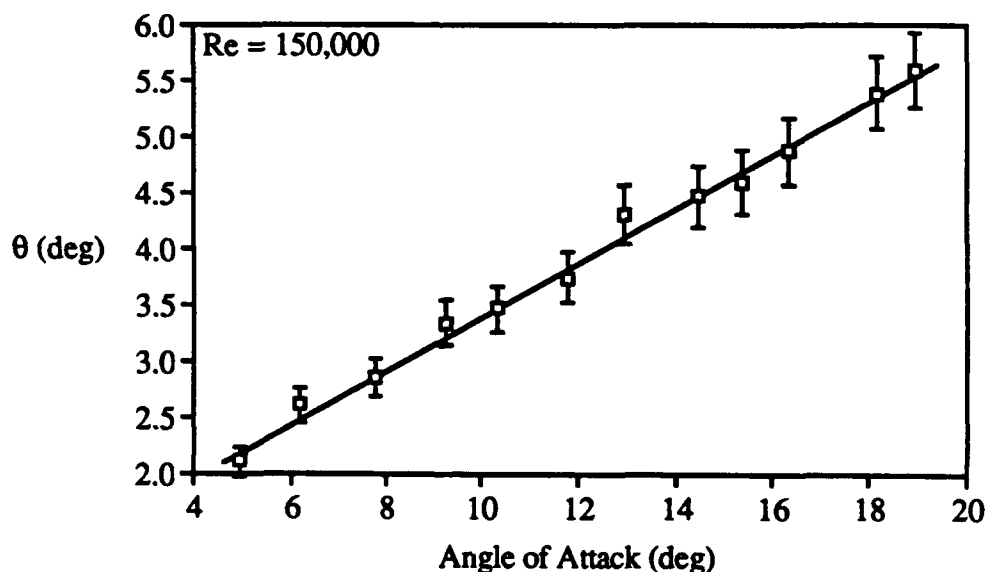
Figure 5.6   Angle of the Steady Vortex Core (θ) Relative to the Wing Surface

in θ due to the uncertainty in fitting a linear curve to the nonlinear core trajectory. A straight line has been fit to the data in Fig. 5.6 to demonstrate its linearity; a 1° increase in angle of attack results in a 0.25° increase in θ.

Similar data has been shown for a 70° sweep wing by Elle (1958), Morris et al. (1988), and O'Neil et al, (1989). Each of these three studies showed an approximately linear increase in core angle (θ) with increase in pitch angle of the wing, as is shown in Fig. 5.6.

Elle's data showed the core angle increasing from 3° to 6° over an angle of attack range of 10-26°. The data from O'Neil et al. data showed the core angle increasing from 4° to 6° for angles of attack from 15-30°. The slopes of the data from Elle and O'Neil et al. are smaller than that of the current data, but the magnitudes of θ compare well. However, the data from Morris et al. showed a change in core angle from 7° to 27° for pitch angles from 10-35°. These magnitudes are significantly larger than those shown in Fig. 5.6. This difference may be attributable to the fact that Morris' data was obtained in a water tunnel rather than a wind tunnel. Similarly large angles of the vortex core relative to the wing have been seen previously in water tunnels, for angles of attack up to 35° (Ng and Malcolm, 1990). This type of behavior is not typically seen in wind tunnels.

5.3   Unsteady Flow Visualization Data

Unsteady flow visualization experiments were performed at a Reynolds numbers of 250,000. Four reduced frequencies were used at each Reynolds number: k = 0.03, 0.06, 0.09 and k = 0.12. These corresponded to a range of pitch frequencies from 0.11-0.42 Hz, respectively. The angle of attack range used was 0-60°; approximately the same as the range used during a portion of the unsteady pressure testing. The type of motion was a sinusoidal pitching oscillation.

Additional unsteady flow visualization experiments were performed with the two bevel wing (see section 2.3.2). A Reynolds numbers of 420,000 and reduced frequencies of 0.076 and 0.153 were used.

In addition, a set of experiments was conducted using a transient pitching motion. This involved both increases and decreases in angle of attack. These experiments have been documented in Thompson, Batill, and Nelson (1989 and 1991). Important results and conclusions will be reviewed later in this section (and shown in Fig. 5.13).

Figures 5.7a and 5.7b present some of the unsteady breakdown data. The unsteady chordwise location of breakdown is shown as a function of instantaneous angle of attack. Figure 5.7a shows the unsteady case relative to the steady case, while Fig. 5.7b shows the effect of varying reduced frequency. The direction of motion is indicated on each by arrows. A single cycle of unsteady data is shown; not an average. The data shown in Fig. 5.7a was also shown in Fig. 4.11 in examining blockage effects.
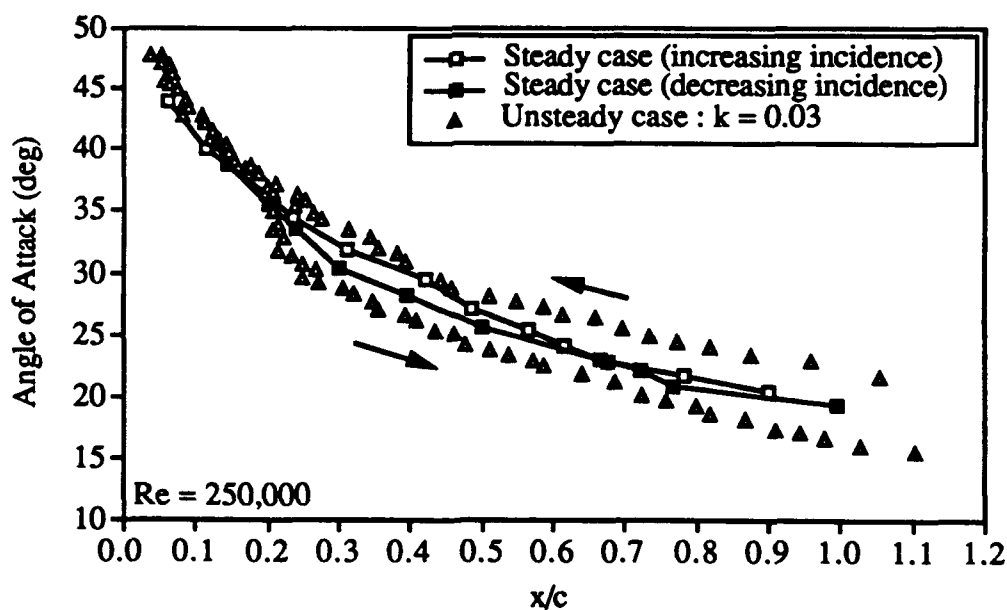
Figure 5.7a   Unsteady Breakdown Location for 0-60° Oscillation. Steady Data also Shown.

From Fig. 5.7a it can be seen that the unsteady data brackets the steady data over most of the range of travel of the breakdown. The hysteresis loop is readily visible. The width of this loop is typically 20-30% of the chord length. On the upstroke (increasing incidence) the breakdown continues moving forward up to $x/c = 0.10$; however, the downstroke (decreasing incidence) data does not begin until the reformation of the vortex and breakdown at approximately 37°. The breakdown then remains relatively stationary while the model pitches down from 37-31° before beginning to move aft. This introduces the lag in chordwise position that remains throughout the motion. Note that the angle of attack at which breakdown first occurs is higher than for the steady case. Similarly, for the downstroke the breakdown remains on the wing to a lower angle of attack compared to the steady case. Note that the gradient of the data for both the upstroke and the downstroke are roughly the same aft of $x/c = 0.30$, indicating similar breakdown propagation velocities.

Figure 5.7b shows the effect of varying pitch frequency. Data for reduced frequencies of $k = 0.03$, 0.06, 0.09, and 0.12 are shown. A line has been drawn connecting the points of each data set in order to maintain clarity. The steady data has not been included (however, Fig. 5.7a can be used as a reference). A hysteresis loop can be seen for each case, the width of the loop increasing with increasing reduced frequency. Similar results have been seen in the breakdown location by LeMay, Batill, and Nelson (1988) and in the normal force coefficient by both Brandon and Shah (1988) and Jarrah (1989).

As k increases, breakdown remains on the wing to lower angles of attack; for $k = 0.12$ breakdown still exists at 10.7°. At the high angles of attack there is a downstream shift in the breakdown locations between the two lower reduced frequencies (0.03 and 0.06) and the two higher (0.09 and 0.12). Another difference between these two that can be seen in Fig. 5.7a at the low angles of attack of the upstroke, when breakdown first occurs. For $k = 0.09$ and 0.12 the breakdown moves onto the wing at a significantly lower angle of attack than for the $k = 0.03$ and 0.06 cases. The gradient of the data is then
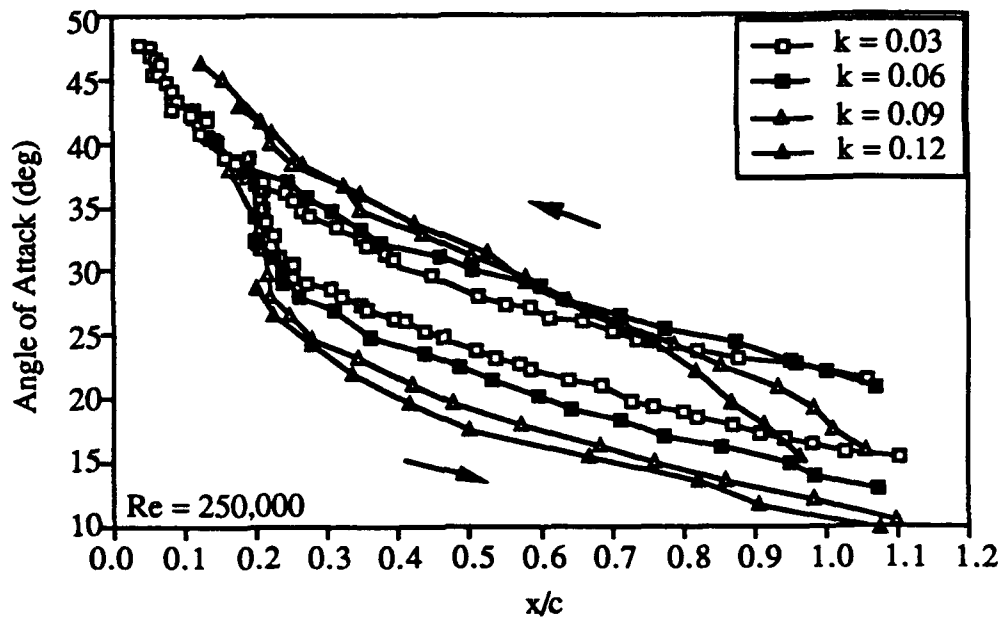
Figure 5.7b   Unsteady Breakdown Location for 0-60° Oscillation. Four Pitch

Frequencies Shown.

steeper (breakdown propagation speed is lower) until roughly 25° at which time the curves have effectively merged.

From Fig. 5.7b it can be seen that when the breakdown reforms during the downstroke it is located from x/c= 0.20-0.25. Here the gradient is nearly vertical; the breakdown remains stationary in that region during approximately ten degrees of model motion (40-30°). The angle at which breakdown begins to move aft decreases with k, and thus the width of the hysteresis loop increases. Jarrah (1989) noted that during a sinusoidal oscillation the unsteady effect was greater during the downstroke due in part to the lag in formation of the leading edge vortex system. This can also be seen in the downstroke data in Fig. 5.7b. Upon reformation the breakdown briefly remains at a constant chord location while the wing continues to pitch down.

Figure 5.8 graphically shows the hysteresis in unsteady breakdown position relative to the steady case. Three frames are shown, each at the same instantaneous angle of attack, 23°. The upper frame is for the upstroke portion of an unsteady motion, while the lower frame is for the downstroke portion. The center frame shows the steady case. The unsteady data is the same as that shown in Fig. 5.7b for k = 0.06. From Fig. 5.8 the
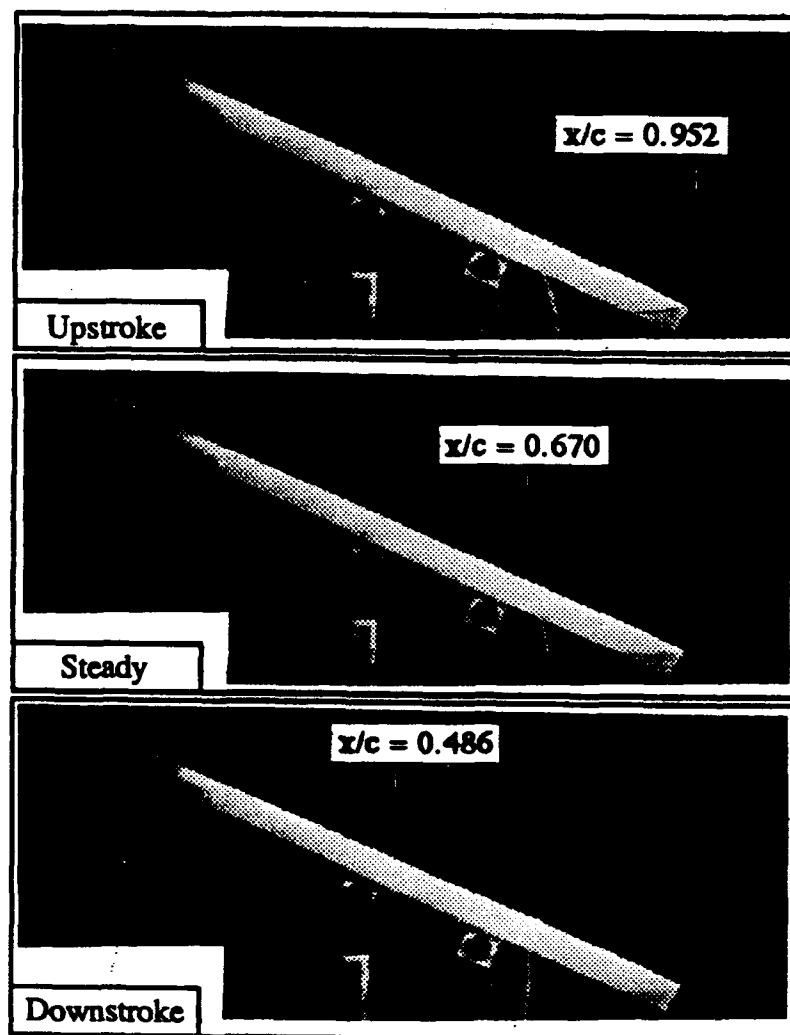
Figure 5.8   Instantaneous Breakdown Location for Upstroke, Downstroke, and Steady Case. Angle of Attack ≈ 23°, Re = 250,000, k = 0.06.

difference in the breakdown behavior due to the direction of motion can be easily seen; a difference of almost 50% of the chord length exists between the upstroke and the downstroke locations (with the steady location in between the two). It can also be seen that the shape of the breakdown varies between frames; this occurs at a steady angle of attack as well. Note also that the waviness of the core, as discussed in section 5.2, can be seen in this figure.

Figure 5.9 shows data covering six cycles of unsteady motion, illustrating the difference in the data for the same case. The reduced frequency is 0.09; this case was also shown in Fig. 5.7b. The data shown in that figure is shown in Fig. 5.9 as cycle 2. The six cycles shown in Fig. 5.9 occurred in consecutive order.
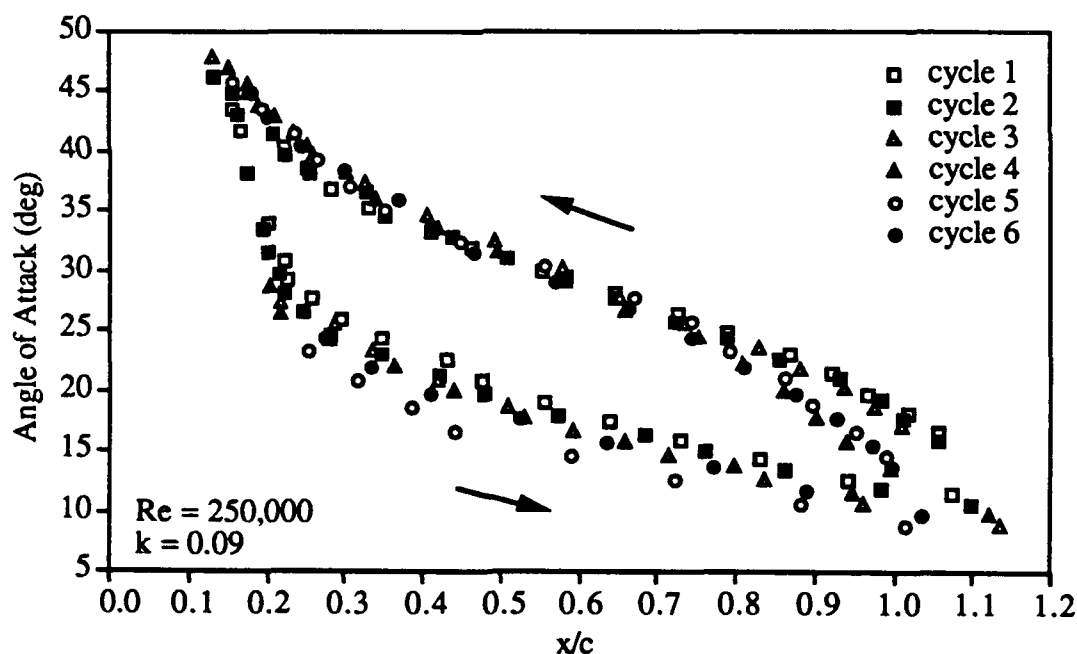
Figure 5.9   Breakdown Location for 6 Cycles of Unsteady Motion.

For the majority of the upstroke the data for each cycle lies on the same curve. However, some differences do exist near the trailing edge. Note that cycles 4-6 show a steeper gradient than cycles 1-3. A similar trend was seen in Fig. 5.7b as a result of increased reduced frequency. By 25° the curves have merged.

The downstroke data contains more scatter than the upstroke data. This is indicative of the difference in the point at which breakdown reforms over the wing, a difference that then propagates through the remainder of the motion. However, each cycle has a region at the high angles of attack where the breakdown position is relatively constant even though the wing is continuing to pitch down.

No consistent difference can be seen between cycles 1-3 and cycles 4-6 that could be associated with the differences seen during the upstrokes of those cycles. This indicates that the differences seen in the downstroke do not continue to exist as the wing begins pitching upwards again, thus propagating to the next cycle of motion.

Fig. 5.9 shows data that was digitized from consecutive frames of a video. Considering that the frame rate for the video camera is a known quantity, it is thus possible to extract time dependent information such as breakdown propagation speed from the videotape. This has been done for each of the four cases (k = 0.03-0.12) shown in Fig. 5.7b and is presented in Fig. 5.10.

The speeds shown in Fig. 5.10 were obtained by the following procedure. First, the unsteady breakdown location was plotted as a function of time. A curve was then fit to this data. In order to accomplish this with the downstroke data it was necessary to remove the points where breakdown remained stationary (as shown in Figs. 5.7 and 5.9). The curve fit was consistently within 5% of the measured data. This curve was then differentiated to obtain the absolute breakdown propagation speed as a function of time. The angle of attack time history is known from the videotape, thus the speed is shown in Fig. 5.10 as a function of instantaneous angle of attack. This figure shows the breakdown
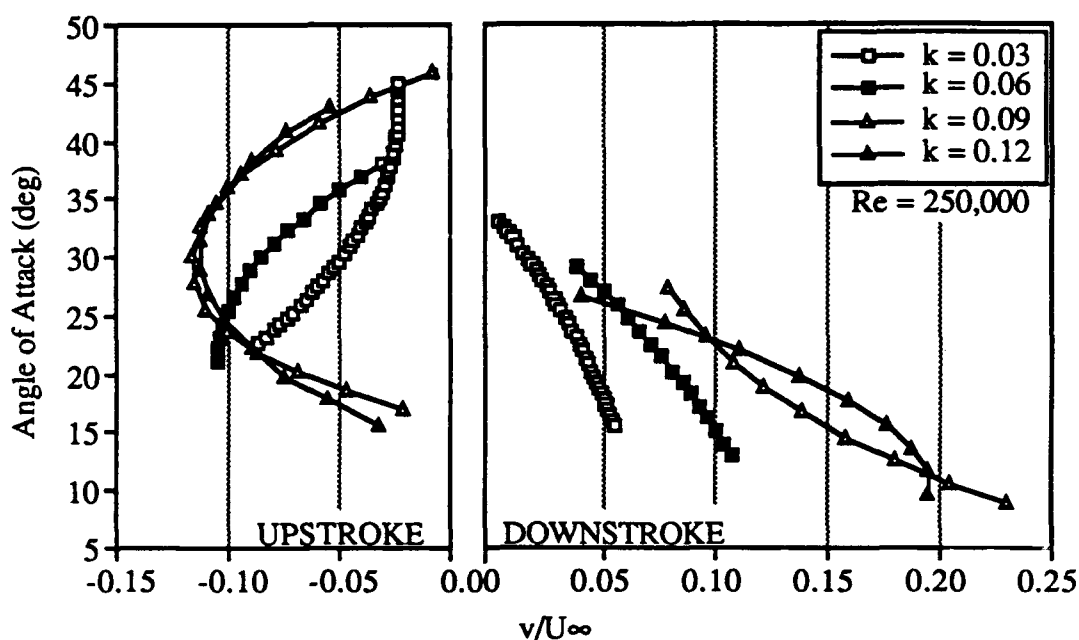
Figure 5.10   Breakdown Propagation Velocity for Four Pitch Frequencies. Velocity Nondimensionalized by the Nominal Freestream Velocity.

propagation speed nondimensionalized by the nominal freestream velocity (30 ft/s for Re = 250,000). If the varying, time dependent freestream velocity (see section 4.3) had been used, the effect would not have significantly altered the curves shown in Fig. 5.10.

Upstroke and downstroke have been separated; note that the upstroke speeds are negative. This is indicative of the upstream motion of breakdown (and thus opposite to the freestream direction). Thus the downstroke speeds are positive. Although each pitch frequency shows different characteristics in Fig. 5.10, no conclusive effect due to increasing reduced frequency can be detected.

As seen in the breakdown position, the upstroke and downstroke portions of the motion produce different results. The upstroke velocities are consistently less than 12% of the freestream while the downstroke velocities are as high as 23%. Note that the curve for

the k = 0.09 and 0.12 cases are similar what would be expected for the wing velocity (peak velocity at the mean angle of attack).

Figure 5.11 shows unsteady flow visualization data for the two bevel wing (a schematic of this wing is shown in Fig. 2.3b). The angle of attack range is 0-60°. A single cycle of unsteady data is shown, along with the steady data. This data can be compared to the data for the one bevel wing as shown in Fig. 5.7a-b (note that both the Reynolds number and reduced frequency are larger for the two bevel wing than for the one bevel wing).
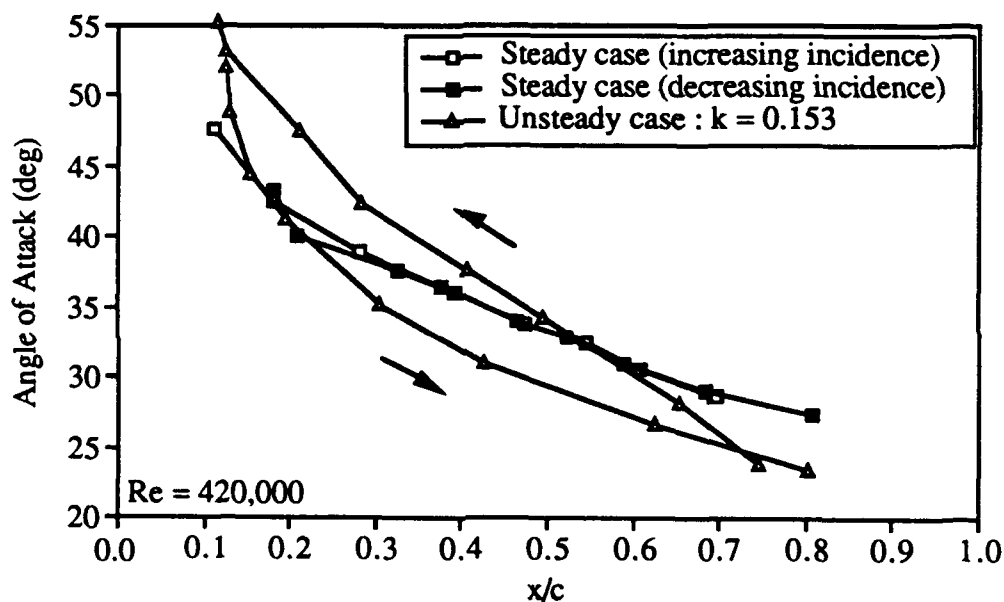
Figure 5.11   Unsteady Breakdown Location over Two Bevel Wing for 0-60° Oscillation. Steady Data also Shown.

The data for the two bevel wing shown in Fig. 5.11 shows characteristics very similar to the data for the one bevel wing. When the breakdown reforms during the downstroke, it remains stationary for roughly seven degrees of wing travel before beginning to move aft.

For the one bevel wing it was seen that an increase in reduced frequency resulted in two trends: first, the data at high angles of attack for the upstroke shifted downstream; and second, at low angles of attack for the upstroke the curvature of the data changed and began to close off the hysteresis loop. Both these trends can be seen in Fig. 5.11 for the two bevel wing.

However, the data for the two bevel wing forms a smaller hysteresis loop than the data for the one bevel wing (note that the vertical scale in Fig. 5.11 has been expanded from that of Fig. 5.7). The difference between the two bevel upstroke and downstroke data in Fig. 5.11 is as much as 20%. This is close to the difference for the one bevel wing with $k = 0.03$. However, as k was increased to 0.12 for the one bevel wing, the hysteresis loop widened to as much as 50% of the chord length. This is significantly larger than the size of the loop for the two bevel wing, even though the two bevel data is for an even larger value of k, 0.1528.

Figures 5.12 and 5.13 show comparative data for other ranges and types of motion. Figure 5.12 shows the unsteady breakdown location for a sinusoidal oscillation from 29-39°, while Fig. 5.13 shows the unsteady breakdown location for a transient motion from 30.5-39.5°. The data in Fig. 5.12 has been presented in LeMay (1988) and LeMay, Batill, and Nelson (1988 and 1990). The transient data shown in Fig. 5.13 has been presented in Thompson, Batill, and Nelson (Jan. 1989 and 1991).

For the range of motion of 29-39°, breakdown existed over the wing throughout the entire motion. The data for this range of motion forms a hysteresis loop as did the data for 0-60° of motion. The width of this loop is significantly smaller even though the reduced frequency (k) is considerably larger; the difference seen between the upstroke location and the downstroke location is typically 12-14%. Similar to the data seen previously, the unsteady data brackets the steady data. Additionally, LeMay noted that an increase in reduced frequency over the range 0.1-0.3 increased the size of the hysteresis loop.
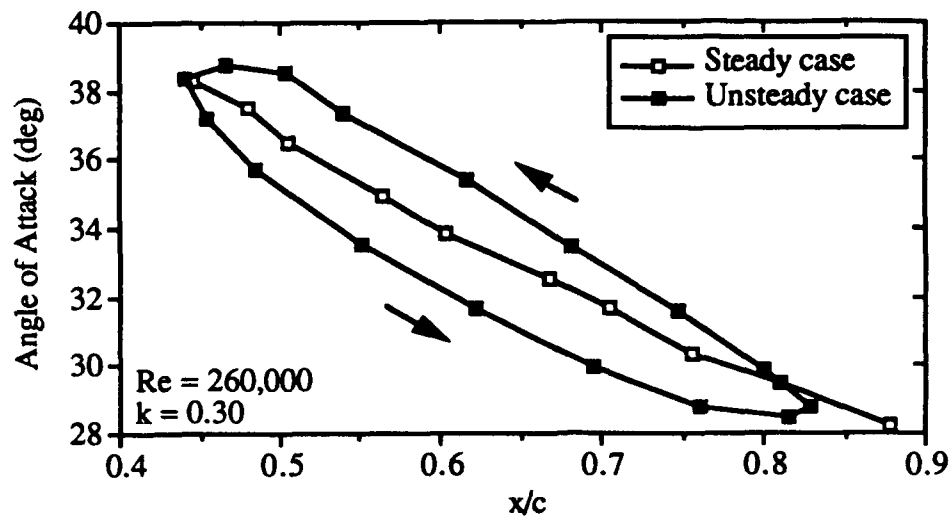
Figure 5.12   Unsteady Location of Vortex Breakdown: 29-39°. Figure from LeMay,

1988.

Figure 5.13 shows the unsteady breakdown location during a transient pitching motion from 39.5° down to 30.5°; the wing begins at a steady angle then pitches down to a steady angle. The motion is not oscillatory. Data for three pitch frequencies is shown. Note that the reduced frequency k is defined for an oscillatory motion and thus is not truly appropriate for use with a transient motion. The values of k shown in Fig. 5.13 correspond to oscillatory motion at the same pitch frequency as that of the transient motion. This has been done (rather than showing a transient reduced frequency) so that the data may be compared to that of the previous figures, all of which are defined by k.

As the wing pitches down, the breakdown is consistently forward of the steady location. Upon completion of the maneuver (at 30.5°) the breakdown continues to move aft even though the wing is now stationary. For the k = 0.50 case the breakdown can be seen to reach the steady curve. However, for the other two cases the data record is not sufficiently long to detect the final position of the breakdown. Similarly, Reynolds and Abtahi (1987) found that breakdown did not reach the steady position after fifteen convective time units for a transient maneuver (the data shown in Fig. 5.13 continues for
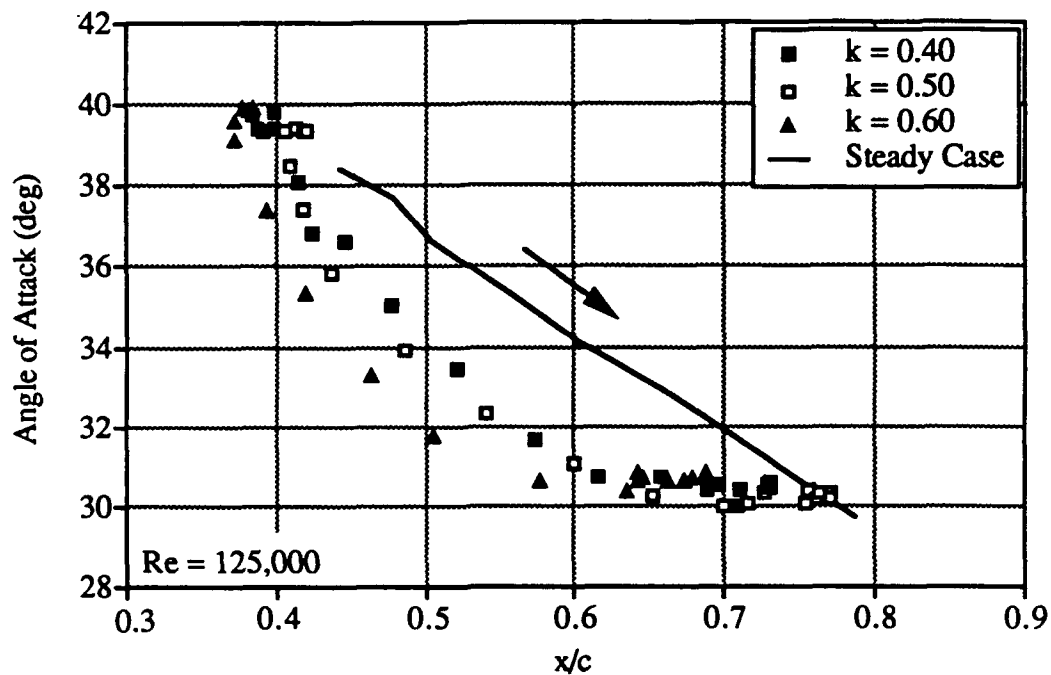
Figure 5.13   Breakdown Location for Transient Pitch-Down Motion. Steady Case Also Shown. Figure from Thompson, Batill, and Nelson, 1991.

less than ten convective time units after completion of the maneuver). Magness et al. (1989) found that breakdown could continue to move as much as 50% of the chord length upon completion of the maneuver. From Fig. 5.13 it appears that an increase in k results in a larger difference between the steady and unsteady data; however this effect is inconclusive because the position at the beginning of the motion is not constant between the three cases shown. This difference in initial position may then propagate throughout the motion.

It was seen that upon completion of the motion the breakdown would typically have traveled 80% of the distance to the steady location. The pitch-down response was not necessarily the same as the pitch-up response. Furthermore, by combining the two it was

not possible to recreate the response for a continuous oscillatory motion. Similar results have been documented in the literature for the aerodynamic forces.

5.4   Summary

The chordwise location of steady vortex breakdown was seen to progress forward with increasing angle of attack, and aft with decreasing angle of attack; both in a smooth fashion. No consistent change in position occurred due to a change in Reynolds number from 150,000 to 450,000. The steady location was seen to depend on the direction of (quasi-static) motion, particularly near the trailing edge. Similar results have been seen by other researchers. In addition, a difference was detected near the center portion of the wing, where as much as 10% of the chord length was measured between the increasing and decreasing incidence cases.

During the course of the steady tests angles of attack of up to 60° were utilized in order to examine the full scale separation of the flow and the subsequent reformation of the vortex system. This reformation of the vortex system may be responsible for the difference in steady breakdown location seen over the center wing between the increasing and decreasing incidence cases. If the angle of attack had been increased only up to a point where breakdown still exists (for example, 40°), then decreased, the midwing hysteresis would not have been as significant. However, the hysteresis seen at the trailing edge would occur for either case. This is a hypothesis drawn from the steady (and unsteady) data; a test was not conducted to validate the concept.

A consistent change in breakdown location was measured for both a change of wing thickness and a change of leading edge geometry. The effect due to thickness consisted of an upstream shift in breakdown location with increased thickness. This effect was not consistent with the effect documented in the literature. The effect due to leading

edge shape was a downstream shift in breakdown location due to addition of an upper surface bevel (effectively increasing the camber). This effect was consistent with data documented in the literature.

The steady vortex core trajectory was recorded and seen to have some curvature. This occurred for angles of attack at which breakdown did not exist as well as angles at which breakdown did exist over the wing. The angle that the mean location of the vortex core made with the wing surface was measured to be proportional to the wing angle of attack.

The unsteady location of breakdown was measured primarily for an oscillatory motion from 0-60°. The general behavior of the data agreed well with data available in the literature. The unsteady data was seen to bracket the steady case over most of the range of motion. An increase in reduced pitching frequency increased the lag of the breakdown from the steady location, in effect widening the hysteresis loop formed by the data. Similar results were found for both the single bevel and double bevel wings.

As the reduced frequency was increased, a change occurred in the breakdown behavior at the trailing edge during the upstroke. At higher reduced frequencies the breakdown moved onto the wing at a lower angle of attack, and with a smaller propagation velocity.

During the downstroke portion of the motion it was seen that the breakdown would reform near the apex, then remain relatively stationary while the wing continued to pitch down through 5-10 degrees of motion. The breakdown would then begin moving aft, being consistently forward of the steady position. This point at which the breakdown remains stationary is near the mean angle of attack, where the angular velocity of the wing is highest.

From examining several cycles of unsteady data it was seen that the downstroke data typically contained greater fluctuations that the upstroke data. This may be indicative of a difference in the point of reformation of the vortex system during the downstroke. A small difference in the angle of attack at which breakdown reforms propagates through the remainder of the pitching cycle. It was seen that any difference in the downstroke data did not in turn effect the data during the upstroke of the proceeding cycle.

The chordwise propagation velocity of breakdown was calculated by fitting a curve to the time dependent breakdown location data. Excluding the downstroke data when breakdown had first reformed, the data could be fit easily to a third order polynomial. This was then differentiated to obtain velocity. The breakdown velocity did not show a conclusive effect due to reduced frequency. In addition, as seen in the breakdown location, the upstroke and downstroke characteristics were consistently different.

VI.   RESULTS: STEADY PRESSURE DATA

6.1   Overview

For both the steady and unsteady surface pressure measurements the data was obtained using the full size ($16\frac{7}{16}$ in. root chord) 70° delta wing. Surface pressures were also measured with the subscale wings at similar flow conditions; that data is discussed in chapter 4. This chapter focuses on the full size wing.

Steady surface pressure distributions were measured at three surface locations: y/s = -0.60, x/c = 0.75, and x/c = 0.50. All pressure orifices were located on the left side of the model. Fifteen steady angles of attack ranging from 2-61° were examined, as well as four Reynolds numbers ranging from 150,000-500,000.

6.2   Steady Pressure Data

The steady data at Re = 250,000 is presented in Figs. 6.1-6.3. The data in these figures has been split into two angle of attack ranges for clarity. Each figure has two graphs; one showing data at 2.4-33.5° and one showing data at 33.5-60.9°. The pressure distribution for 33.5° is shown in each graph as a reference between them. The angle of attack of each pressure distribution is indicated within each figure.

Figures 6.1a and 6.1b show data measured at a constant span location of y/s = -0.60 and varying x/c locations. The pressure coefficients decrease consistently as angle of attack is increased up to 29.1°. Further increase to 33.5° results in little distinguishable change in the pressure distribution. It is near this angle of attack that 70° delta wings typically achieve maximum lift coefficient (McKernan, 1983; Jarrah, 1988). The

152

Figure 6.1a   Surface Pressure Distribution at y/s = -0.60. Angles of Attack: 2.4-33.5°.
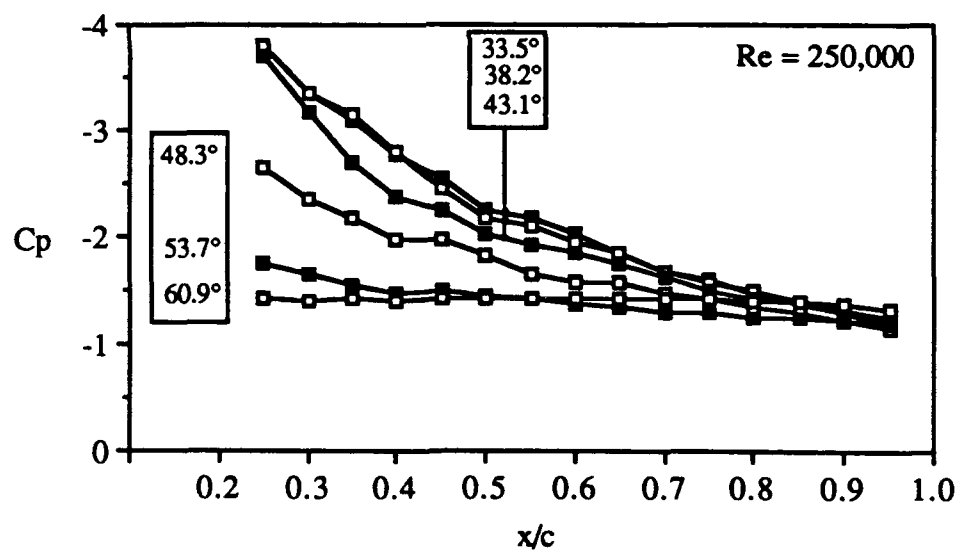
Figure 6.1b   Surface Pressure Distribution at y/s = -0.60. Angles of Attack: 33.5-60.9°.

chordwise pressure gradient can be seen to increase with increasing incidence, up to approximately the stall angle. At this point the pressures begin increasing; by 53.7° the distribution is flat, indicative of fully separated leeward surface flow. No drastic change in pressure gradient occurs with a change in angle of attack. Note that the approximately uniform pressure distribution at 60.9° ($C_p \approx -1.5$) could possible be used as a first approximation of the base pressure coefficient, as defined by Maskell's (1963) method of blockage correction. This method was discussed in Section 4.4.4.

Figures 6.2a and 6.2b present the steady data from a constant chord location of x/c = 0.75. As in the constant span data, the pressure coefficients reach minimum values by 33.5°, and a further increase in incidence results in a flattening of the pressure distribution. An effect of breakdown can be detected in these two figures. At both 13.9° and 17.3° there is a suction peak located at y/s = -0.60; this is due to the presence of the leading edge vortex. However, by 33.5° the pressure peak has spread out and appears as a gradual curve. This is indicative of the presence of vortex breakdown upstream of the x/c = 0.75 station. This effect of breakdown is small; it is certainly not sufficient to infer the location of breakdown from the surface pressure distributions. Similarly, Visser (1991) found that the breakdown could not be identified from the steady surface pressure.
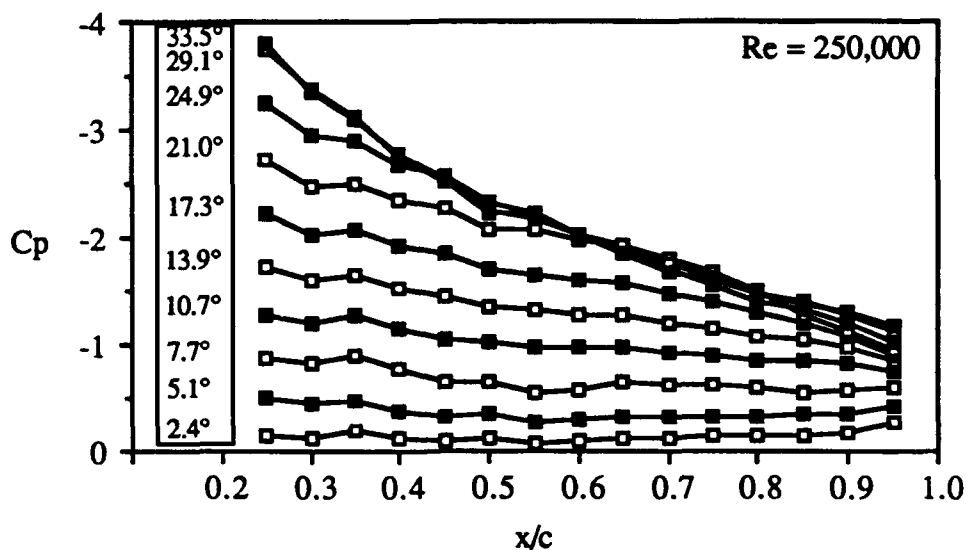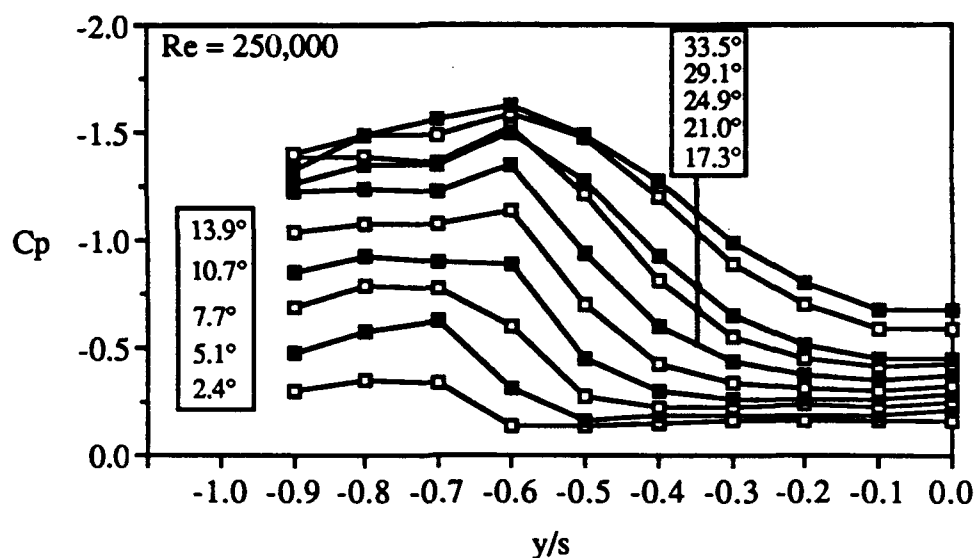
Figure 6.2a   Surface Pressure Distribution at x/c = 0.75. Angles of Attack: 2.4-33.5°.
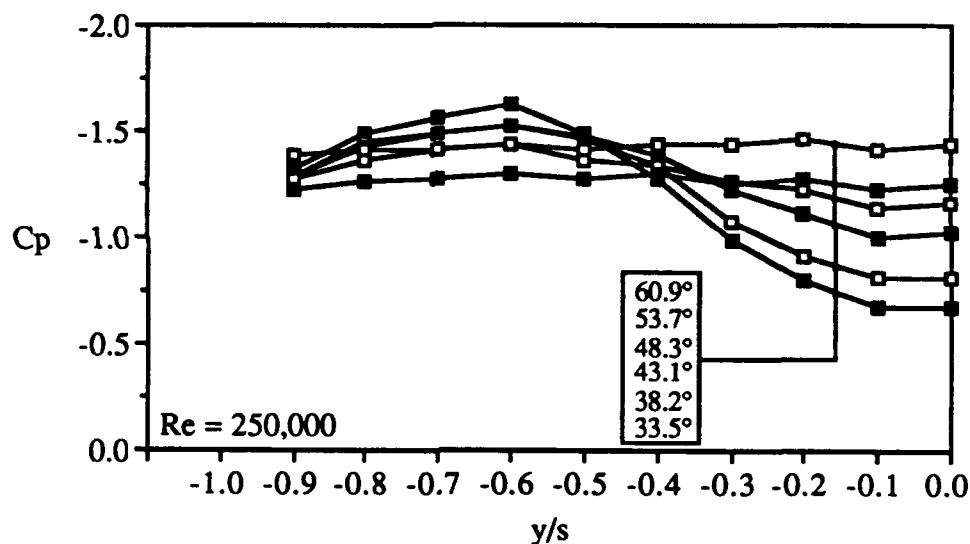
Figure 6.2b   Surface Pressure Distribution at x/c = 0.75. Angles of Attack: 33.5-60.9°.

Additional constant chord pressure distributions are shown in Figs. 6.3a and 6.3b. This data was obtained at x/c = 0.50 and varying span location. This data is similar to the x/c = 0.75 distributions shown. However, the suction peak appears at a different span position; at x/c = 0.75 the suction peak was located at y/s = -0.60, but at x/c = 0.50 the

suction peak is closer to y/s = -0.70. This indicates a change in the spanwise location of the vortex core between these two chord locations.

As in the previous figures, the suction peak flattens out by 33.5°, and further increase in angle of attack causes an increase in pressures eventually leading to a completely flat profile.
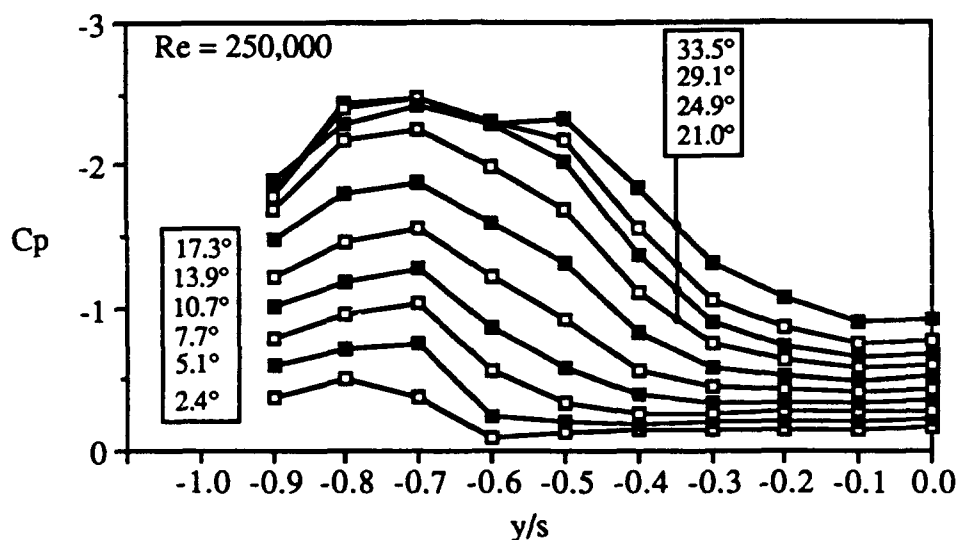
Figure 6.3a   Surface Pressure Distribution at x/c = 0.50. Angles of Attack: 2.4-33.5°.
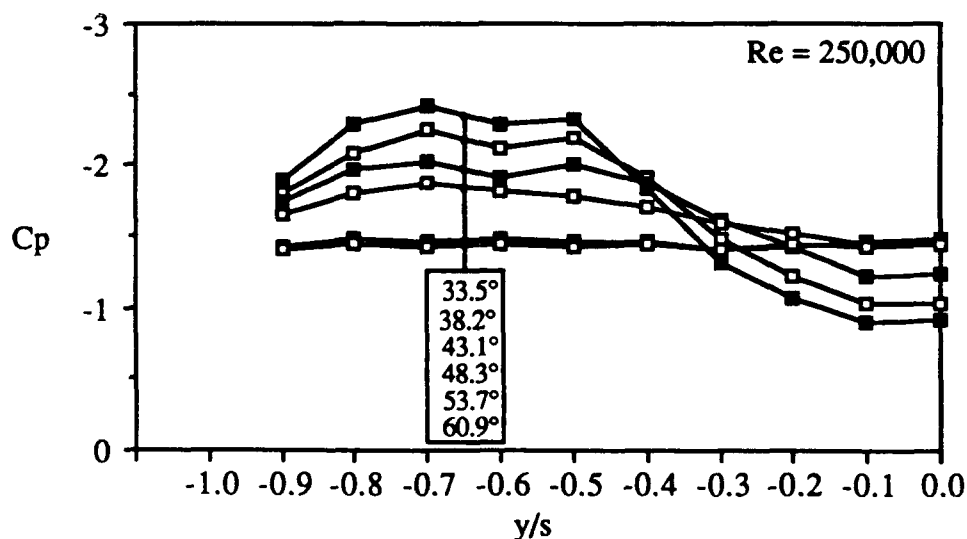
Figure 6.3b   Surface Pressure Distribution at x/c = 0.50. Angles of Attack: 33.5-60.9.

Steady pressure data was obtained at four Reynolds numbers: 150,000, 250,000, 400,000, and 500,000. Over this range a small yet consistent change in the surface pressures was noted. Figure 6.4 shows chordwise pressure distributions at 33.5° for each of the four Reynolds numbers. For chord locations from x/c = 0.45-0.95 the difference in the data is not significant. However, for chord locations forward of 45%, an increase in Reynolds number results in a decrease in pressure. Also note from Fig. 6.4 that this portion of the data appears to be grouped by Reynolds number into two sets: 150,000 and 250,000, and 400,000 and 500,000. This suggests that a change in the flow structure is occurring between Re = 250,000 and 400,000.
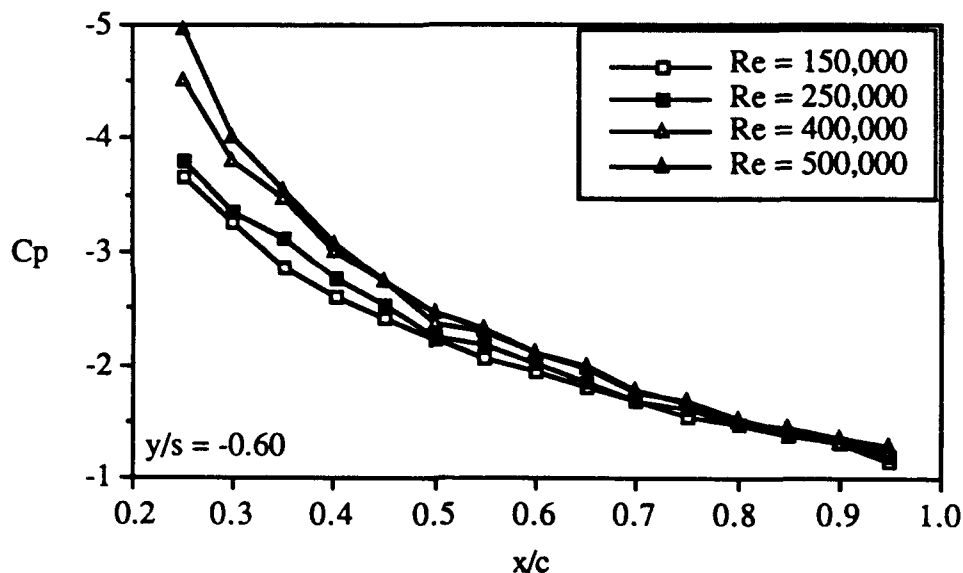
Figure 6.4   Chordwise Pressure Distribution at 33.5° Angle of Attack

Note that the data shown in Fig. 6.4 has not been corrected for the effects of blockage. However, the blockage corrections discussed in section 4.4 are independent of Reynolds number per se; thus, the differences apparent in Fig. 6.4 would continue to exist after correction.

Figure 6.5 shows the surface pressure from one surface location, x/c = 0.25, as a function of angle attack. Again, data for all four Reynolds number is shown. The effects seen at x/c = 0.25 diminish down the length of the wing; by x/c = 0.50 no distinguishable difference exists due to Reynolds number. As in Fig. 6.4, the data for Re = 150,000 and 250,000 lies effectively on the same curve, while for the two higher Reynolds numbers the pressures begin to change. From Fig. 6.5 it can be seen that the Reynolds number effect is most prevalent over a range of approximately 20-47°; this is consistent with the other surface locations exhibiting this behavior. This angle of attack range, within a few degrees, is the same as the range for which vortex breakdown exists over the wing.
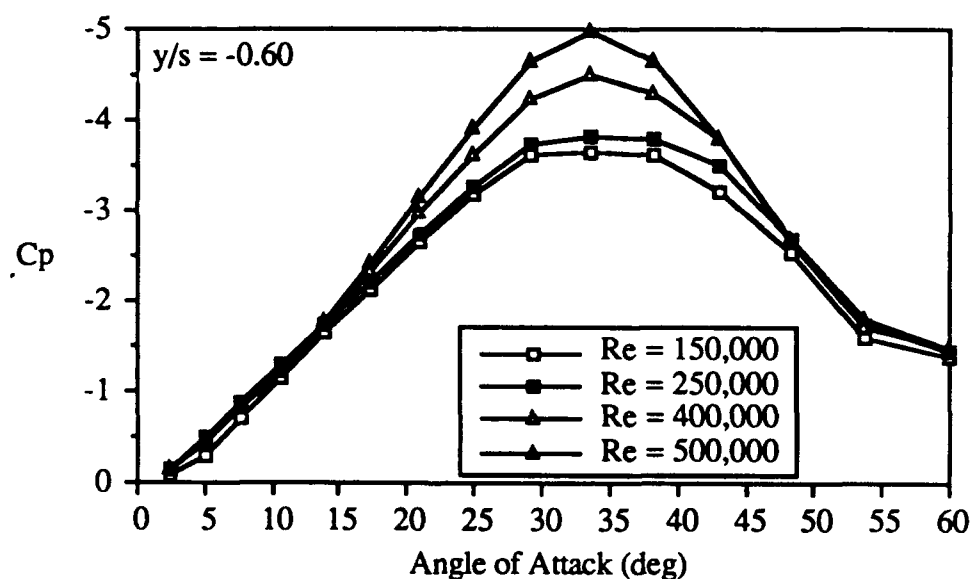
Figure 6.5   Steady Surface Pressure at x/c = 0.25.

An additional view of this Reynolds number effect is shown in Fig. 6.6, which shows the spanwise pressure distribution at 17.3° for each of the four Reynolds numbers, at a chord station of x/c = 0.75. This figure clearly shows the change in the pressure

distribution that occurs between 250,000 and 400,000. For the two lower Reynolds number, a single suction peak can be seen at 60% of the semi-span. However, for the two higher Reynolds numbers, an additional suction peak can be seen at 80% of the semi-span. The two peaks have similar magnitudes. The second peak could be indicative of the secondary vortex having a stronger effect on the surface pressures. This could be due to the increase in Reynolds number effecting the secondary vortex, either strengthening it or relocating it (i.e. closer to the wing surface). Flow visualization tests did not reveal any qualitative information on the nature of the secondary vortex.
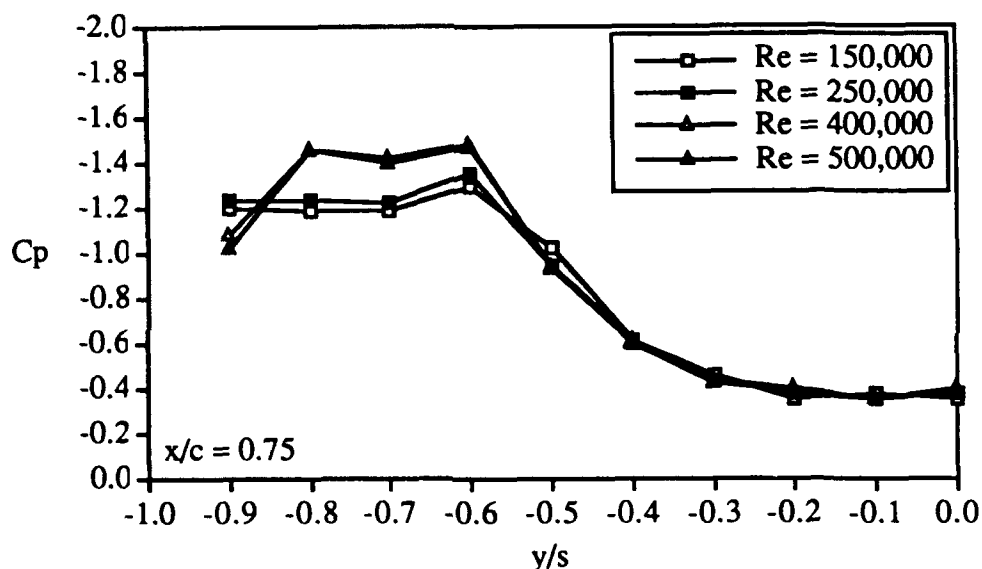
Figure 6.6   Spanwise Pressure Distribution at 17.3° Angle of Attack.

This change in the form of the suction peak seen in Fig. 6.6 can be seen in each of the spanwise pressure distributions for angles of attack from 7.8°-17.3°. Note that the vortex forms near 5°.

A Reynolds number effect over this range of Reynolds numbers has been documented by both LeMay (1988; see also LeMay, Batill, and Nelson, 1990) and O'Neil et al. (1989). LeMay measured a consistent downstream shift in unsteady breakdown

location with an increase in Reynolds number from 175,000 to 250,000. This occurred during an oscillation from 29-39° of a 70° wing with a thickness ratio 33% smaller than the current wing, and with a dual beveled leading edge.

A change in the spanwise pressure distribution similar to that shown in Fig. 6.6 was seen by O'Neil et al (1989). O'Neil et al. documented a change in the pressure distribution for a change in Reynolds number from 400,000 to 1,000,000. This consisted of an increase in the suction pressure at both pre- and post-stall angles of attack. For pre-stall angles of attack, O'Neil et al. attributed the effect to a transition of the secondary separation from laminar to turbulent (citing the work of Hummel, 1978). This increase in suction pressure was limited to forward surface locations, with the result being no net change in the lift coefficient.

This effect of laminar and turbulent separation was previously documented by Hummel (1978). Hummel used a 76° delta wing at a Reynolds number of 900,000 and an incidence of 20.5°. Hummel found that by inducing turbulent secondary flow (by use of a trip wire on the wing surface) the spanwise pressure distribution could be altered in a manner similar to that seen by both O'Neil and the current study (as shown in Fig. 6.6).

However, O'Neil saw a difference in the Reynolds number effect depending on the angle of attack. For post-stall angles the increase in suction pressure was seen to occur at *all* surface locations. O'Neil et al. correlated this with a Reynolds number effect measured in the lift coefficient for post-stall angles. They did not have an explanation for this post-stall Reynolds number effect.

The current pressure data also showed a Reynolds number effect at both pre- and post-stall angles of attack. However, the number of pressure taps used was insufficient to determine if the suction increase was localized, or if it was contributing to a net change in the loading.

Figure 6.7 shows a comparison of the current data with the data from O'Neil. Two angles of attack are shown. The current data is for Re = 400,000 while O'Neil's data is for Re = 300,000. Note also that O'Neil's data at x/c = 0.70 is compared to the current data at x/c = 0.75. Neither O'Neil's data nor the current data is corrected for blockage effects.
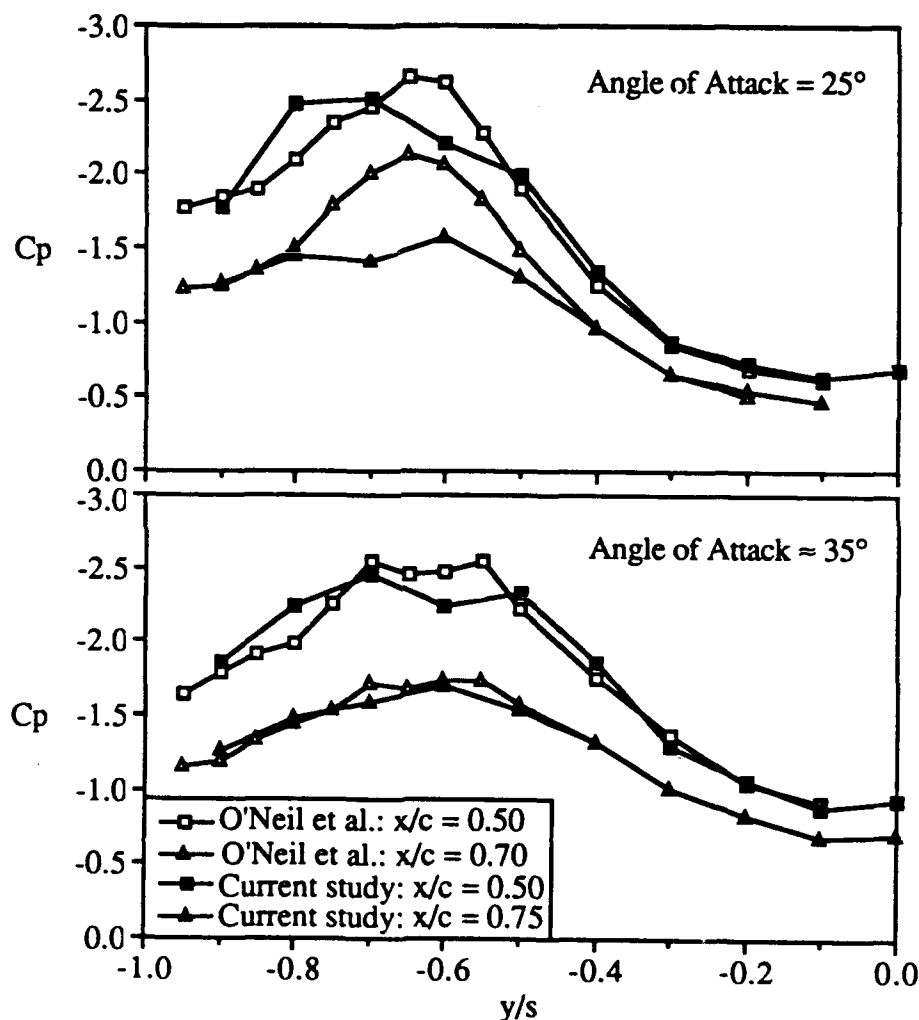
Figure 6.7   Comparison of Current Spanwise Pressure Distribution with Data from O'Neil et al. (1989). Two Chord Locations and Two Angles of Attack Shown

The largest difference in the data occurs at 25° for x/c = 0.70 and 0.75. O'Neil's data shows a considerably more defined suction peak, whereas the current data shows a flat profile. This is a result of the location of vortex breakdown for each wing. For the current study the breakdown is located upstream of x/c = 0.75, thus the suction peak no longer exists. However, for O'Neil's wing the breakdown does not even first occur over the wing until roughly 27°, thus the surface pressure at 25° still shows a distinct peak due to the vortex core. The information on the breakdown location has been shown previously in Fig. 5.4. The difference in breakdown location may be due to a difference in the thickness ratios of the two wings; O'Neil's wing had a thickness ratio of 1.7% while the current wing had a thickness ratio of 4.6%.

The remainder of the data shows good agreement, particularly at 35°. At this angle of attack the agreement was very good at all surface locations. At 25° a difference exists in the location of the suction peak at x/c = 0.50. This is caused by a difference in the location of the primary vortex, which is in turn caused by a difference in the type of secondary separation. For the current case the flow has been shown to change from laminar to turbulent at a Reynolds number between 250,000 and 400,000; thus, the data shown in Fig. 6.7 is for the turbulent case. However, O'Neil's data indicated transition occurring between Re = 400,000 and 1,000,000; thus his data is for the laminar case. As documented by Erickson (1981) the vortex core position for the turbulent case is outboard of the position for the laminar case. This behavior can be seen in Fig. 6.7 despite differences is wing geometry.

The chordwise pressure gradient can be estimated from the steady chordwise data shown in Figs. 6.1a-b. That data was fit to a third order equation, which was then differentiated to obtain the gradient in the chordwise direction. The curve fits yielded pressure coefficient values within 2.7% (on average) of the measured values. The pressure gradient at a surface location and angle of attack corresponding to those shown in Figs.

6.1a-b can be calculated. Values for intermediate locations and angles can then be interpolated from those values.

Figure 6.8 contains data on the chordwise pressure gradient in relation to the steady location of vortex breakdown. This type of correlation has also been shown by O'Neil et al. (1989) for a 70° delta wing. The current data on steady breakdown location (shown in Fig. 5.1) was used in Fig. 6.8; thus Fig. 6.8 shows data for quasi-statically increasing and decreasing angles of attack. For each steady measurement of breakdown, the chordwise pressure gradient was calculated at *that specific chord location*, using the steady pressure data. This information is plotted along the ordinate of Fig. 6.8. The angle of attack of the wing (α) and the sweep angle ($\Lambda = 70°$) were then used to calculate the value of the abscissa, γ. The sweep angle Λ is included as a scaling factor to make the data comparable to data for wings of other sweep angles (as done by O'Neil). This same method of analysis has been used on the unsteady pressure data and will be presented in Chapter VII.
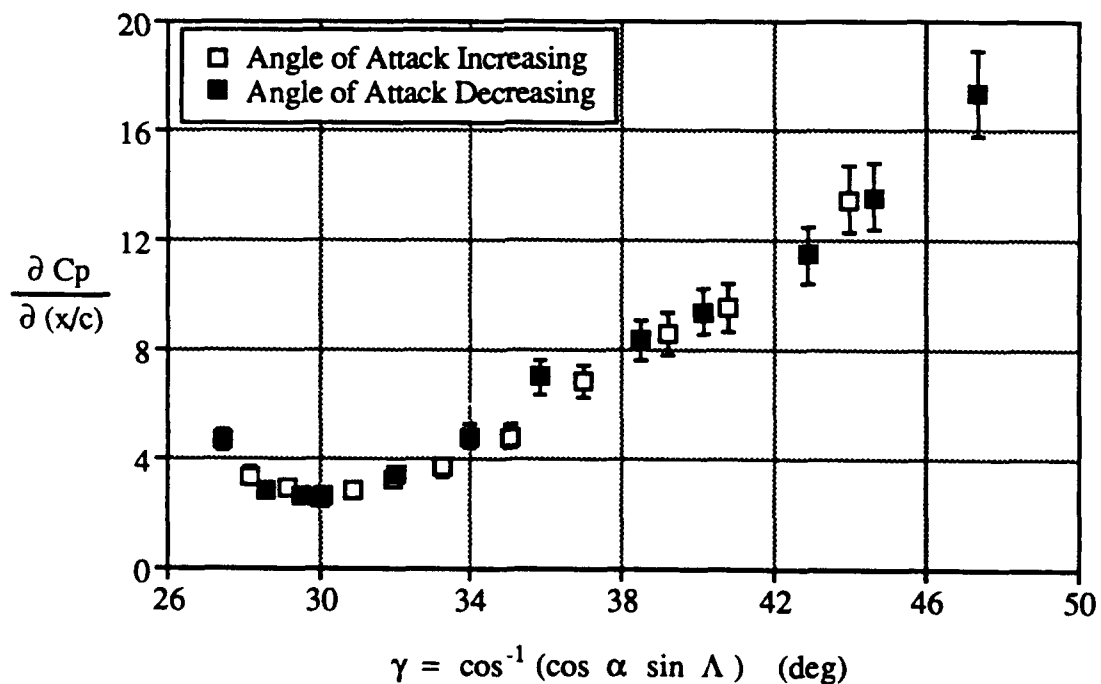
Figure 6.8   Steady Chordwise Pressure Gradient Correlated to Steady Location of
Vortex Breakdown for 70° Sweep Wing

The uncertainty in the the measured angle of attack and the sweep angle are small; less than the size of the symbols used in Fig. 6.8. The uncertainty in the process of calculating the pressure gradient and interpolating the values for each location of breakdown has been estimated as 9% and is shown in Fig. 6.8 as vertical error bands.

This data compares very well to data shown by O'Neil et al. for a 70° wing. The magnitudes of $\frac{\partial C_P}{\partial (x/c)}$ ranged from 5-16 for O'Neil's data, for values of γ from 34-42°. As noted previously, breakdown moves onto the current wing at a lower angle of attack than was seen by O'Neil, thus lower values of γ are present in Fig. 6.8. Additional differences between the current data and O'Neil's data may be attributable to blockage effects. At 40° angle of attack, O'Neil's wing had a maximum frontal area blockage ratio of 9% while the current wing had a blockage ratio of 11.0%.

The pressure gradients shown in Fig. 6.8 has a minimum at roughly $\gamma = 30°$. This corresponds to angles of attack for which breakdown exists close to the trailing edge. For values of γ above and below this point the pressure gradient increases. This type of behavior appears to exist in O'Neil's data; however, an insufficient number of data points exists for it to be conclusively detected. For values of γ above 33°, breakdown is located forward of 0.50c, and the curve is effectively linear. O'Neil et al. concluded from their data that the linear correlation indicated the existence of "a unique pressure gradient which will cause bursting of the leading-edge vortex."

Steady pressure data was also obtained for the model with the leading edge beveled on both the upper and lower surfaces. This data has been presented in Thompson, Batill, and Nelson (Jan. 1990 and Aug. 1990) and in Nelson, Arena, and Thompson (1991). Figure. 6.9 shows a comparison of that data with the data for the single bevel model. Spanwise pressure distributions for three angles of attack are shown. The difference in the vortex core position due to the leading edge geometry can be seen by the difference in the suction peak. By 24°, the breakdown is located upstream of x/c = 0.75 for the single bevel
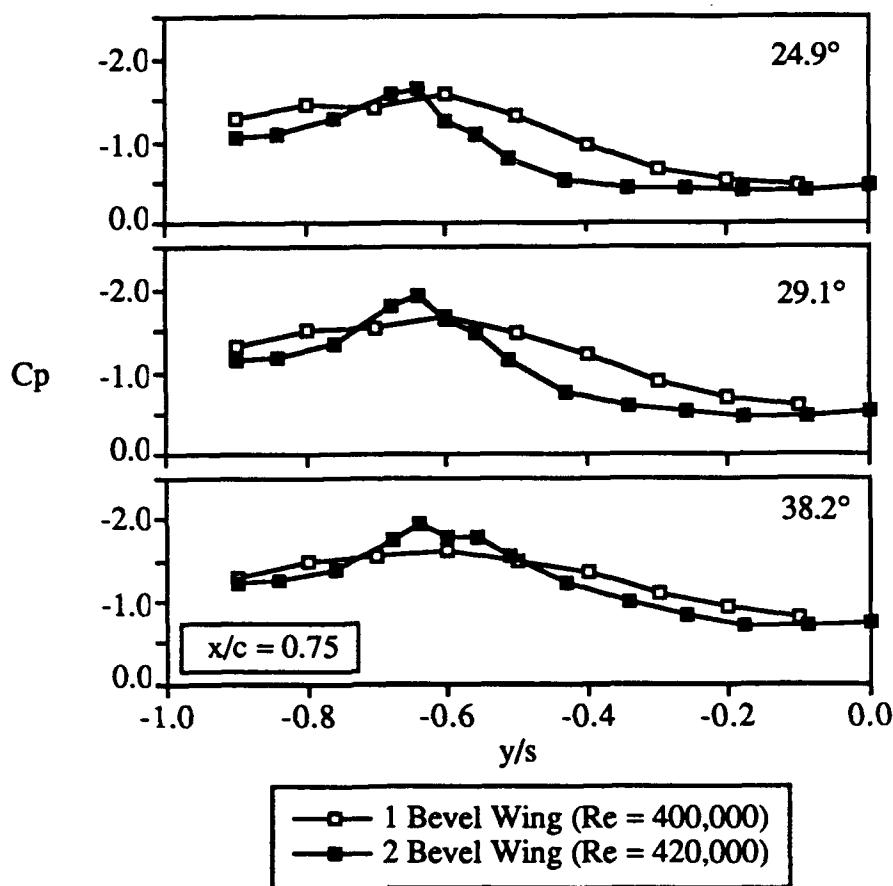
Figure 6.9   Comparison of Steady Pressure Data for Different Leading Edge
Geometries.

model, while breakdown does not yet exist for the double bevel model. Thus, a distinct peak is still apparent in the pressure profile for the double bevel model.

A difference in the form of the suction peak would be expected for a change in the leading edge geometry. By using a double bevel wing an effective camber is added to the upper surface of the wing. This causes a change in the location of the secondary separation, which in turn effects the location of the primary vortices. The more distinct peak shown shown in Fig. 6.9 for the double bevel wing indicates that the effective camber is causing either a stronger vortex, or one closer to the wing surface.

As the angle of attack is increased to 38.2°, the double bevel pressure profile continue to decrease while the single bevel profile begins to flatten. O'Neil et al. (1989) measured the lift for wings with similar leading edge geometries and found that over the range from 25-40° the double bevel wing had a consistently higher lift coefficient. This can be inferred from the current data by the consistently lower surface pressures at those angles of attack.

6.3   Summary

Surface surface pressure distributions were obtained over a Reynolds number range from 150,000-500,000. Angles of attack from roughly 0-60° were examined. This range includes the formation of the core, the occurrence of breakdown, stall, and full scale flow separation.

In general, both the magnitudes of the pressures and the effect of angle of attack were similar to data for a 70° wing available in the literature. The surface pressures typically reached their lowest values near the stall angle (this angle obtained from the literature). Further increase in angle of attack resulted in flat pressure profiles for both chordwise and spanwise distributions. This is indicative of the full scale flow separation occurring at very large angles of attack.

The presence of the vortex core could be detected by a distinct suction peak visible in the spanwise pressure distributions. This spanwise position of this peak was a function of the chord location. The occurrence of vortex breakdown upstream resulted in a flatter pressure profile, without the distinct peak. However, the effect of breakdown on the surface pressure was not sufficient to permit the determination of the breakdown location from the surface pressure data.

A consistent Reynolds number effect was seen in the surface pressures. The effect consisted of a decrease in the pressure with an increase in Reynolds number from 250,000 to 400,000. This was consistent with a Reynolds number effect documented in the literature for a 70° wing. The decrease in pressure is probably a result of the transition of the secondary flow from laminar to turbulent. The Reynolds number effect was seen at both pre- and post-stall angles of attack. However, the number of surface locations examined was insufficient to determine if a net change in the loading was occurring.

The chordwise pressure gradient was calculated from the steady pressure data. This gradient was then correlated to the steady location of vortex breakdown. The data compared well to data available in the literature. The relation between the pressure gradient (at the specific location of breakdown) and the angle of attack was essentially linear for breakdown positions upstream of 0.50c.

Steady surface pressures were also measured for the model having both the upper and lower surfaces beveled at the leading edge. Consistent differences in the shape of the spanwise pressure distributions were observed, particularly in relation to the suction peak. The chordwise distributions were qualitatively similar. The differences in the suction peak are indicative of a difference in the location of the vortex core as a result of the effective camber of the double bevel wing. The difference in vortex breakdown location between the two wings was correlated to a difference in the high angle of attack behavior of the suction peak. At angles near the stall angle, the double bevel model had lower surface pressures, indicative of the higher lift coefficient for that leading edge geometry.

VII.   RESULTS: UNSTEADY PRESSURE DATA

7.1   Overview

Data for unsteady pitching motions can be separated into three different angle of attack regimes: low angles of attack, which preclude the occurrence of vortex breakdown and stall; and high angles of attack, where breakdown exists over the wing for at least a portion of the motion. The high angle of attack motions can then be further divided into ranges for which breakdown exists over the wing throughout the motion, and ranges for which breakdown moves onto and off of the wing during the motion. These different ranges of motion typically exhibit different unsteady characteristics (Thompson, Batill, and Nelson, Aug. 1990; Thompson, Arena, Nelson, and Batill, 1990; Ashley, Jarrah, Katz, and Vaneck, 1990). This will also be shown by the unsteady pressure data presented in the following discussion.

This chapter has been divided into sections according to the particular angle of attack range of the unsteady motion. The mean angles of attack have ranged from 15-35°, with ranges of travel from 11-58°. In each case the motion is a sinusoidal oscillation of angle of attack. Section 7.2 contains data for the range of motion of 0-30°, section 7.3 is for the range of motion of 29-40°, and section 7.4 is for two ranges; 4-40° and 9-45° (these tests were conducted for identical Reynolds numbers and pitch frequencies and thus will be presented together). Section 7.5 then contains data for very large angle of attack excursions, 3-50° and 2-60°. A summary of the significant trends then concludes the chapter.

Figure 7.1 shows schematics of each range of motion relative to the steady lift curve for a 70° delta wing (as shown in Fig. 1.3). The specific range of motion and the

168

section in which data for that range is discussed is listed beneath each schematic. At the beginning of each of the following sections, the appropriate schematic is shown as a reference for that particular angle of attack range.
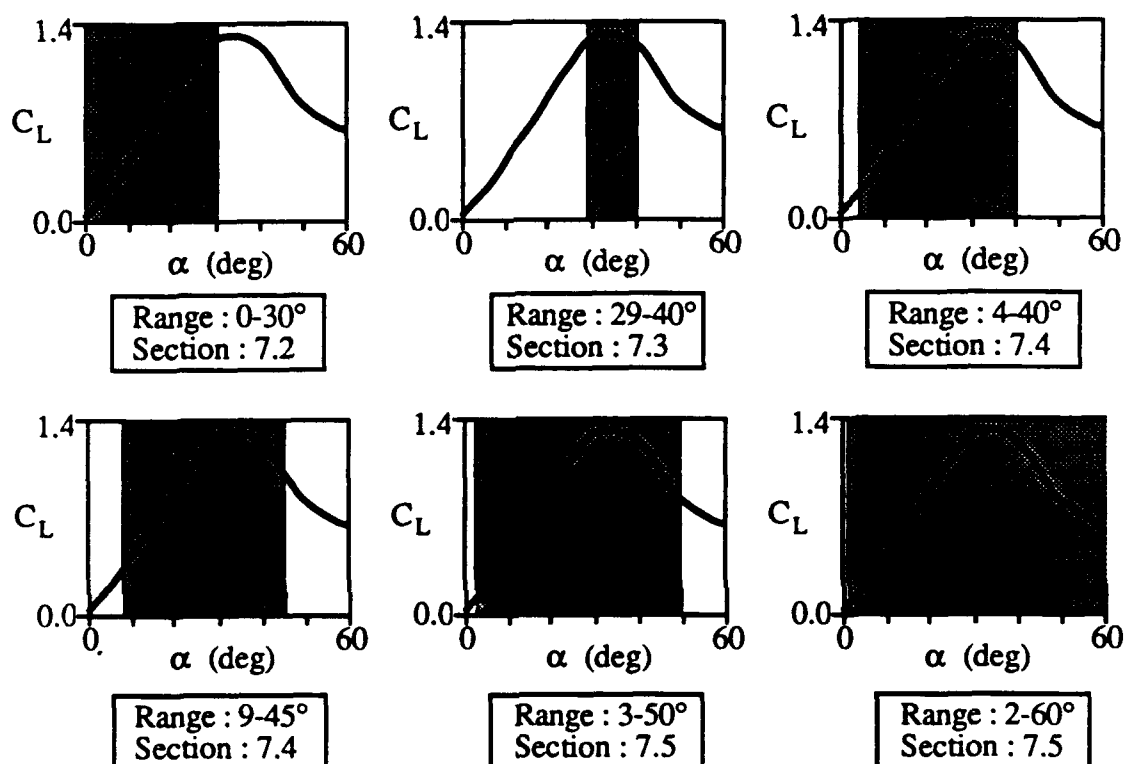
Figure 7.1   Schematics of Ranges of Motion for Unsteady Pressure Tests Relative to Steady Lift Curve for 70° Wing.

Several values of Reynolds numbers and pitch frequency have been examined for each angle of attack range. The Reynolds numbers have ranged from 150,000-500,000 and the reduced pitch frequencies have ranged from 0.050-0.300. The effects of Reynolds number and pitch frequency variation will be discussed in each section. Table 7.1 summarizes the unsteady pressure test conditions, showing the different ranges of motion

and also which wing was used during each test. Note that two different wings were used during the surface pressure testing, a double bevel wing and a single bevel wing (as described in section 2.3). The single bevel wing was used to examine the effect of the

TABLE 7.1

UNSTEADY PRESSURE TEST CONDITIONS

Note : Tests performed during blockage effect experiments not included (see Table 4.5)

Range	Re/1000	U (ft/s)	k	f (Hz)	Geometry	Surface Locations
0-30°	420	50	0.076 0.153	0.45-0.90	2 bevel	-60% y/s
29-40°	250 335 420 500	30 40 50 60	0.100 0.200 0.300	0.35-2.10	2 bevel	-60% y/s 50% x/c 75% x/c
4-40°	550	66	0.015 0.045 0.075	0.11-0.31	2 bevel	-60% y/s
9-45°	550	66	0.015 0.045 0.075	0.11-0.31	2 bevel	-60% y/s
3-50°	250 335 42()	30 40 50	0.050 0.092 0.300 0.400	0.17-1.40	2 bevel	-60% y/s
2-60°	420	50	0.076 0.153	0.45-0.90	2 bevel	-60% y/s 50% x/c 75% x/c
2-60°	250 500	30 60	0.030 0.060 0.090 0.120	0.10-0.84	1 bevel	-60% y/s 50% x/c 75% x/c

leading edge geometry (relative to the double bevel wing), as well as to improve the comparison with unsteady aerodynamic load data available in the literature. As this body of data would be unwieldy to present in its entirety, representative data will be shown while conclusions will be drawn from all the data. The bulk of the data, including individual data plots, can be found in a data report prepared by Thompson and Nelson (1992).

7.2   0-30° Range of Motion
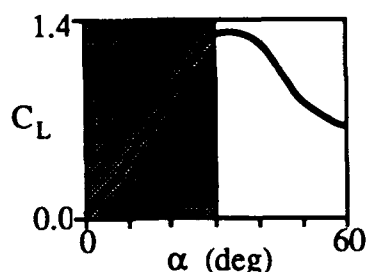
The range of 0-30° was chosen for two reasons: so that the data was comparable to data in the literature on the unsteady aerodynamic forces on a 70° delta wing (Jarrah, 1988 and 1989), and to examine the effects of a range for which breakdown did not exist on the wing. The double bevel wing (see Figure 2.3) was used for these tests. The angle of attack at which breakdown first occurs over a wing of this sweep and geometry is typically from 28-30° (LeMay, 1988; LeMay, Batill, and Nelson, 1988; Roos and Kegelman, 1990).

Figure 7.2 shows a time history of the unsteady pressure data obtained from a line of pressure taps located at y/s = -0.60. Time has been nondimensionalized with respect to Δt, the duration of one pitching cycle. The lower portion of this figure shows a schematic of the angle of attack time history. This data is for the lower of the two reduced pitch frequencies used with this angle of attack range. The corresponding dimensional pitch frequency is indicated in the figure. Each curve represents the ensemble average of fifty cycles of unsteady data.
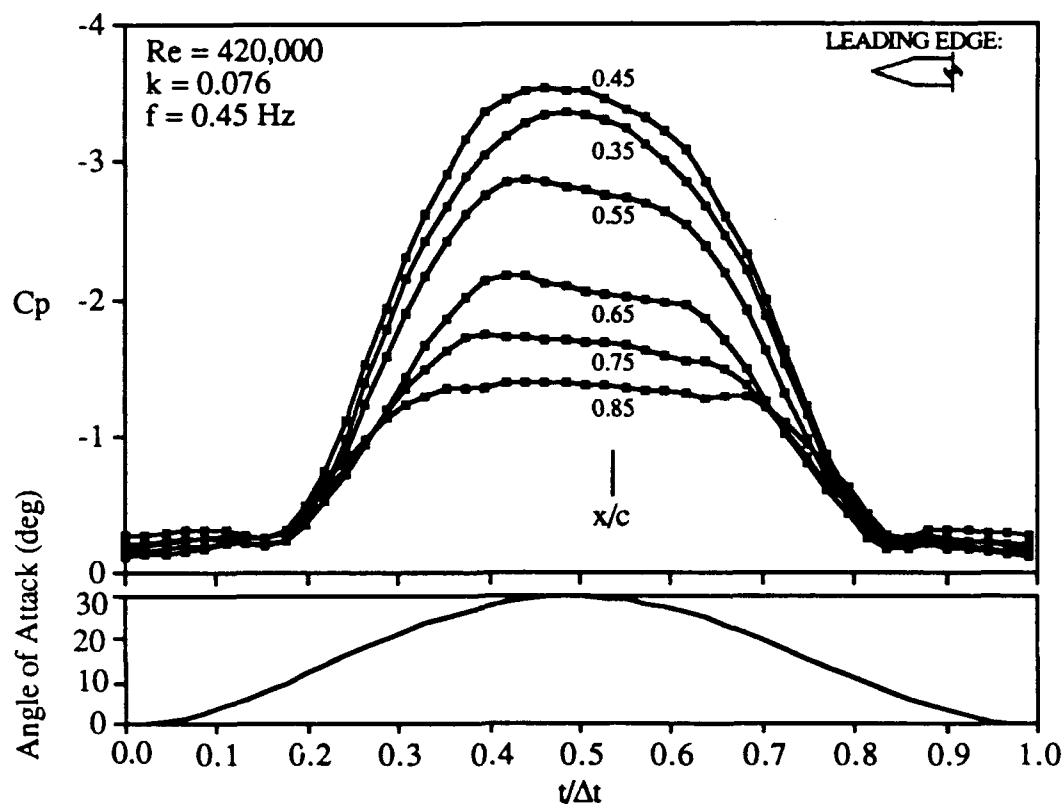
Figure 7.2   Unsteady Pressure Data for 0-30° Range of Motion. Span Location y/s =
-0.60.

For angles of attack less than 10° the unsteady pressures are approximately constant at each of the chord locations shown.   An increase in angle of attack results in decreasing surface pressures. At any given instantaneous angle of attack, the pressure decreases with decreasing distance from the apex. The exception to this occurs at x/c = 0.35, where the pressures are higher than at x/c = 0.45. A similar trend was evident in the steady data for this wing. Due to the presence of the upper surface bevel on this wing, the 0.35c surface location is actually on the face of the bevel. This was seen to result in atypical behavior, such as a drastic change in the chordwise pressure gradient as shown in Fig. 7.2.

Some distortion of the pressure curve is evident for surface locations from 0.55c-0.85c. This consists of a plateau in the curve at the high angles of attack. This is most

evident at 0.85c, where the pressure is essentially constant for angles above 26° This behavior is evidence of the presence of vortex breakdown over the wing. The steady flow visualization data for this wing showed breakdown first occurring at 28° and moving to 0.65c by 30° (see Fig. 5.3).

Over this angle of attack range the surface pressure is well behaved and exhibits relatively small differences between the upstroke (angle of attack increasing) and downstroke (angle of attack decreasing) portions of the motion. This can be seen in Fig. 7.3, which shows the pressure as a function of instantaneous angle of attack.

Data from three surface locations, 0.45c, 0.55c, and 0.65c has been shown in Fig. 7.3. The lower portion of the figure shows the same data superimposed on the steady data for those locations. The direction of motion is indicated on the upper half of the curve. By comparing the steady case to the unsteady case it can be seen that the unsteady surface pressure reacts in a quasi-steady manner, although consistent unsteady effects are apparent. A small hysteresis loop is formed at angles of attack above 26°. The direction of motion is indicated on the figure (for the 0.65c data). Here the loop is small, and the data does not truly "overshoot" the steady data. However, the loop that is present is the beginning of the overshoot typically seen for unsteady high angle of attack delta wing aerodynamics (as discussed in section 1.5). The unsteady effects seen in Fig. 7.3 compare well qualitatively to effects seen in the unsteady force data measured by Jarrah (1988 and 1989) for a 76° wing pitching from 0-30°.

The formation of a substantial hysteresis loop is typically considered to be due to the occurrence of vortex breakdown (Ashley, Jarrah, Katz, and Vaneck, 1990). For angles of attack precluding breakdown, quasi-steady behavior has been documented in the loads (Jarrah, 1988 and 1989). This reinforces the conclusion that breakdown is in fact occurring over the wing during the 0-30° motion, and as a result a hysteresis loop forms in the pressure data at the high angles of attack.
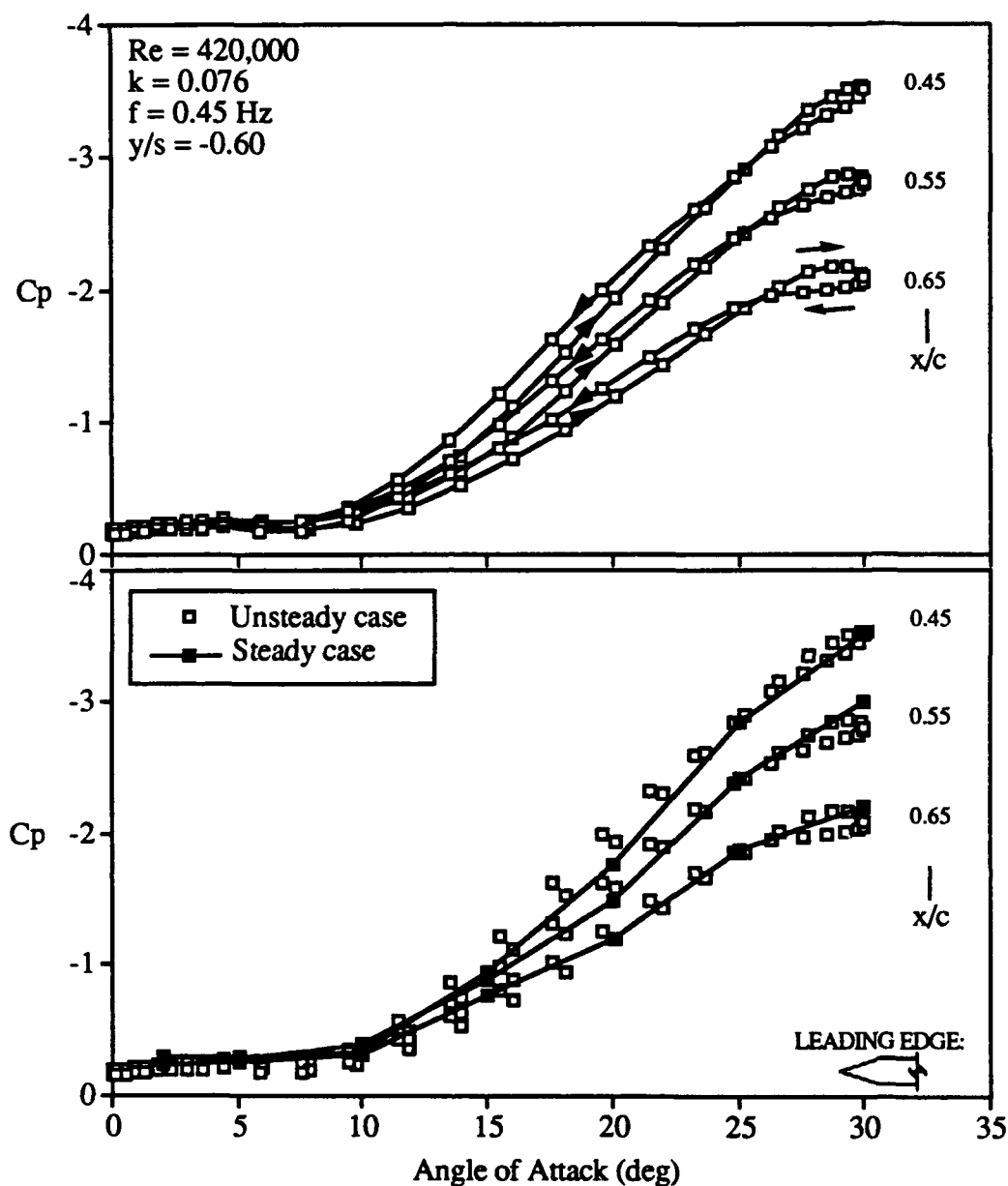
Figure 7.3   Unsteady Pressure Data for 0-30° Range of Motion. Pressure Coefficient as a Function of Instantaneous Angle of Attack. Steady Data Shown in Lower Half.

Note that the pressure curves each form a "figure eight" shape, in that the upstroke pressures are lower (relative to the downstroke pressures) at low angles of attack, and

higher at high angles of attack. This behavior was seen to increase with increasing nondimensional pitch frequency, k. The effect of k is shown in Fig. 7.4.

Figure 7.4 shows the time history for four surface location, each for two values of k. The difference due to k is small, certainly within the uncertainty of the measurement. However, this effect was seen throughout the data for this range of motion and is thus considered to be significant. Note that the effect of k increases with increasing chord location (as does the size of the hysteresis loop). This corresponds to the surface locations at which breakdown exists for a longer portion of the motion; hence the unsteady effects are more pronounced.
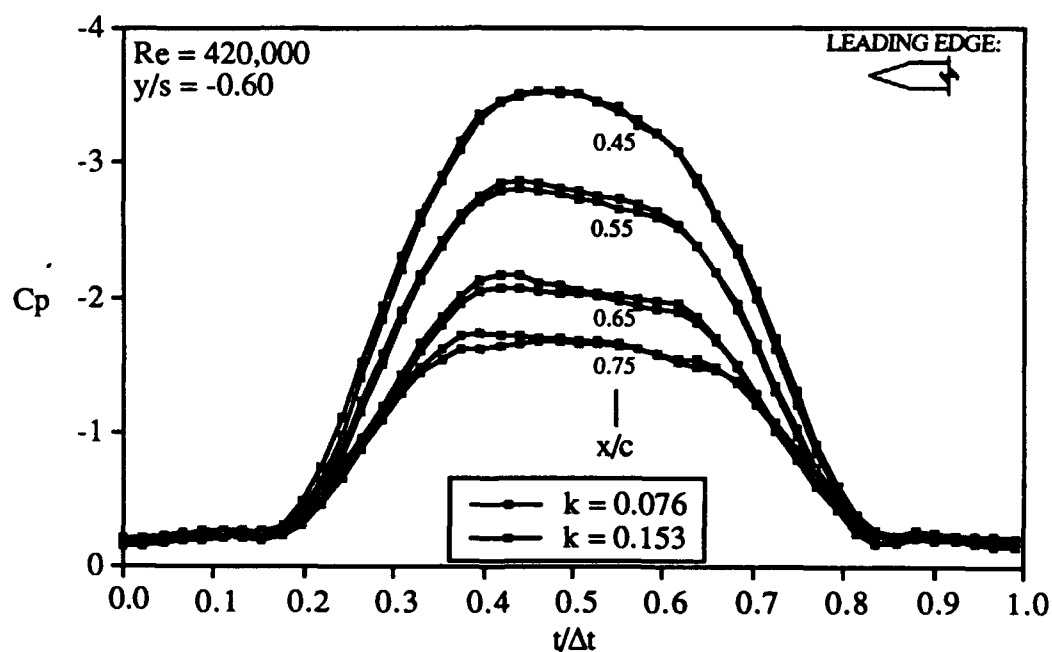
Figure 7.4   Unsteady Pressure Data for 0-30° Range of Motion. Data for Two Pitch Frequencies Shown.

7.3   29-40° Range of Motion
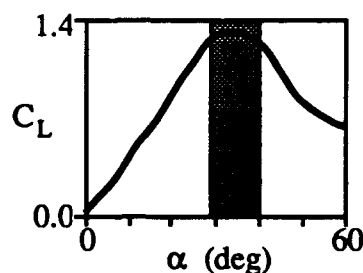
The range of 29-40° was chosen for two reasons: so that the data was comparable to data in the literature (the both the unsteady breakdown location (LeMay, Batill, and Nelson, Apr. 1988, June 1988, and 1990), and to examine the effects of a range for which breakdown was continually over the wing.

As with the 0-30° pressure data, the 29-40° data was obtained using the double bevel wing. Pressure distributions were obtained at four Reynolds numbers ranging from 250,000-500,00 and four reduced pitching frequencies ranging from 0.10-0.30. The chordwise pressure distributions have already been presented in Thompson, Batill, and Nelson, July, 1989 and Jan. 1990. Figure 7.5 shows data obtained at the spanwise pressure taps. These curves were obtained by ensemble averaging fifty cycles of unsteady data. The top part is for array of pressure taps at 0.50c, the center part is for 0.75c, and the lower part is a schematic of the angle of attack time history. Data from three span locations (y/s) are shown at each chord station.

Note that the amount of fluctuation of the pressure coefficients is relatively small compared to the 0-30° data. This was also seen in the chordwise data. The chordwise data was obtained at a constant local semi-span of y/s = -0.60; thus two of the curves shown in Fig. 7.5 were also presented with the chordwise data. The amount of fluctuation of the two y/s = -0.60 curves shown is roughly 10% (about the mean of the unsteady data). This fluctuation was roughly constant at each of the chordwise stations measured. It was

concluded that a 10% fluctuation of the surface pressure was to be expected as the lift coefficient also has roughly a 10% fluctuation from 28-40°. However, notice that the fluctuation at 0.50c and y/s = -0.48 is closer to 25%. This may be due to the location of the vortex core closer to that span location than to y/s = -0.60.
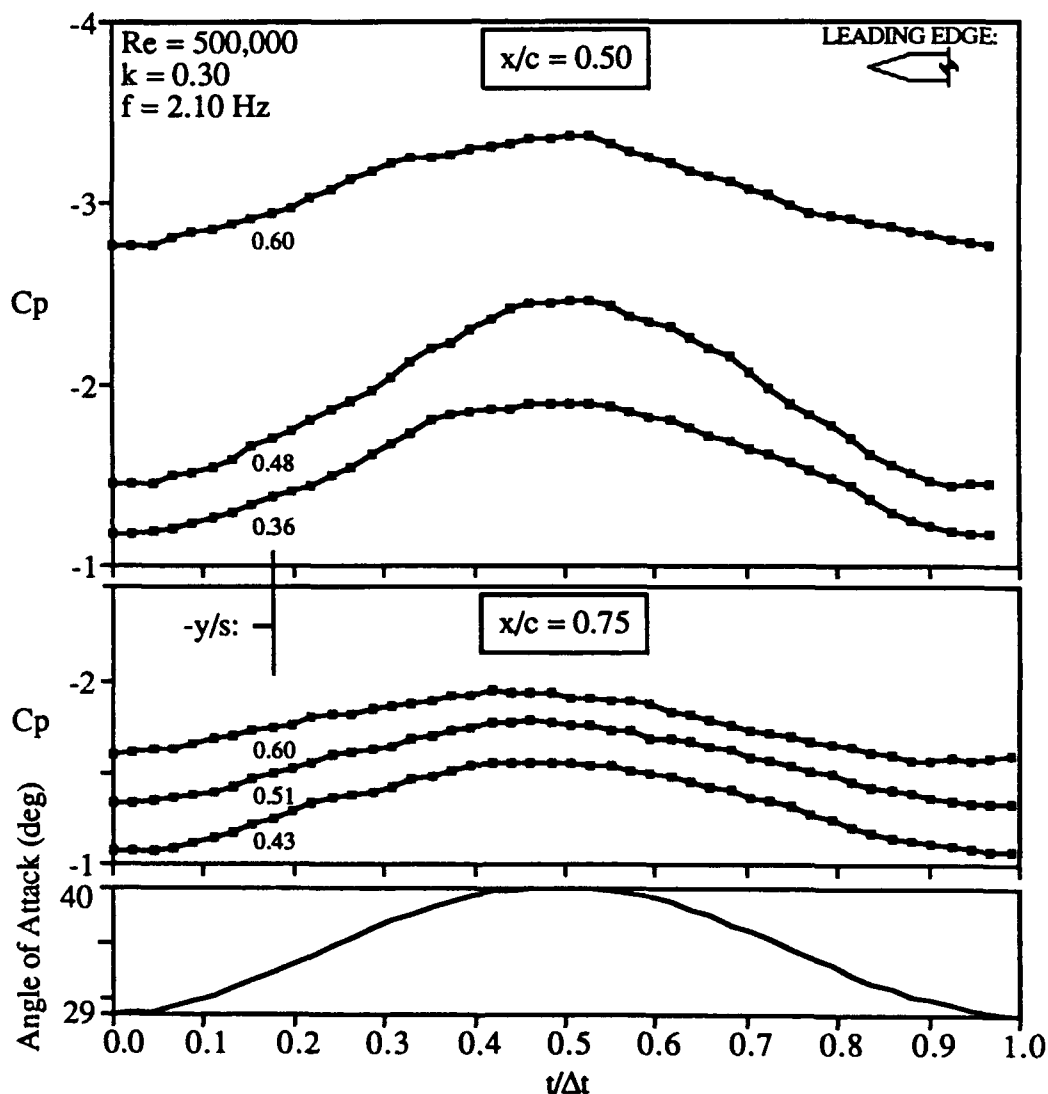
Figure 7.5   Unsteady Pressure Data for 29-40° Range of Motion. Data for Two Chord

Locations Shown.

Vortex breakdown exists over the wing throughout the pitching cycle, but the change in breakdown location could not be detected by the surface pressures data. The effect of breakdown is not readily apparent in Fig. 7.5. This conclusion was also drawn from the chordwise data. This was also true of most of the chordwise pressure data. However, at the farthest forward pressure tap locations, 0.35c and 0.40c, an effect of the breakdown could be detected for angles from 38-40°. This effect consisted of an increase in the pressure with an increase in incidence (opposite to the expected pressure decrease). This increase resulted in a pressure signal (at these two specific locations) oscillating at approximately twice the pitching frequency. However, the increase in pressure was not distinct or drastic enough to identify the location of breakdown strictly from the surface pressure distribution. The ability to detect an effect of breakdown at these two locations and not at the downstream locations could be due in part to the lower pressure (and thus increased resolution) at these locations.

From Fig. 7.5 it can be seen that the pressures oscillate in phase with the model motion. Plotting this data as a function of angle of attack does not result in a hysteresis loop; rather, quasi-steady behavior can be seen. From the 0-30° data it was concluded that the presence of breakdown at the peak of the motion was resulting in hysteretic behavior of the pressures. However, for the 28-40° breakdown exists throughout the motion. This suggests that the presence and motion of breakdown over the wing is not a major contribution to the severe unsteady load effects seen in the literature; rather that it is the motion of breakdown onto and off of the wing that causes the hysteresis in the surface pressures.

A change of reduced pitching frequency was seen to have a small impact on the unsteady surface pressures over this range. The pressures continued to oscillate at roughly the pitching frequency (with the exception of the surface locations effected by breakdown). No substantial change in the unsteady characteristics were seen.

7.4   4-40° and 9-45° Ranges of Motion
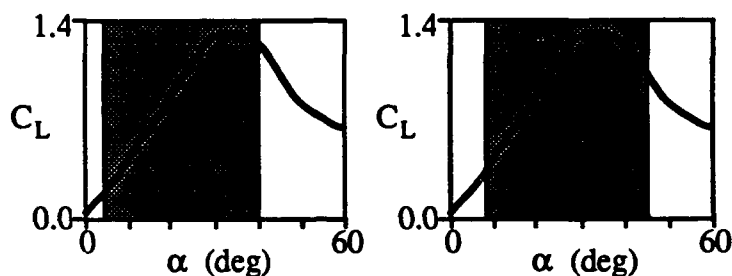
This section contains the results from two ranges of motion: 4-40° and 9-45°. Note that for each, the amplitude of motion is 36°, but with a different beginning angle of attack (4° and 9°, respectively). These ranges have been chosen to correlate with the unsteady force data obtained by Brandon and Shah (1988). In addition, they provide a transition between the low angle of attack motions and the high angle of attack motions. The 4-40° data shows trends which are characteristic of ranges of motion for which quasi-steady behavior occurs. However, the 9-45° data shows trends which are characteristic of ranges for which significant unsteady effects occur.

This data was obtained using the double bevel wing and the chordwise array of pressure taps located at a semi-span of y/s = -0.60. As for the preceding angle of attack ranges, fifty cycles of unsteady data were ensemble averaged to yield the data shown below.

Time histories of these two angle of attack ranges are shown in Figs. 7.6 and 7.7. As before, the angle of attack is indicated beneath the data plot. Chord locations from 0.35c-0.85c are shown. Note that the pressures at 0.35c are lower than at 0.45c; this is different that the behavior for the 0-30° data. As mentioned previously, the 0.35c pressure tap is located on the face of the upper surface bevel.

The curves shown in Fig. 7.6 continue the trends seen in the 0-30° data. The pressures decrease with increasing angle of attack. At a certain angle of attack the

pressures remain roughly constant until the incidence again decreases below that value. The angle at which this "plateau" occurs increases with decreasing chord location. At 0.85c this occurs near 24°, while at 0.35c this occurs near 34°. This plateau is readily apparent at the upstream locations of 0.35c and 0.45c, whereas it was not for the 0-30° data. This reinforces the conclusion that the plateau is an effect of breakdown occurring at these chord locations as the angle of attack increases to 40°.
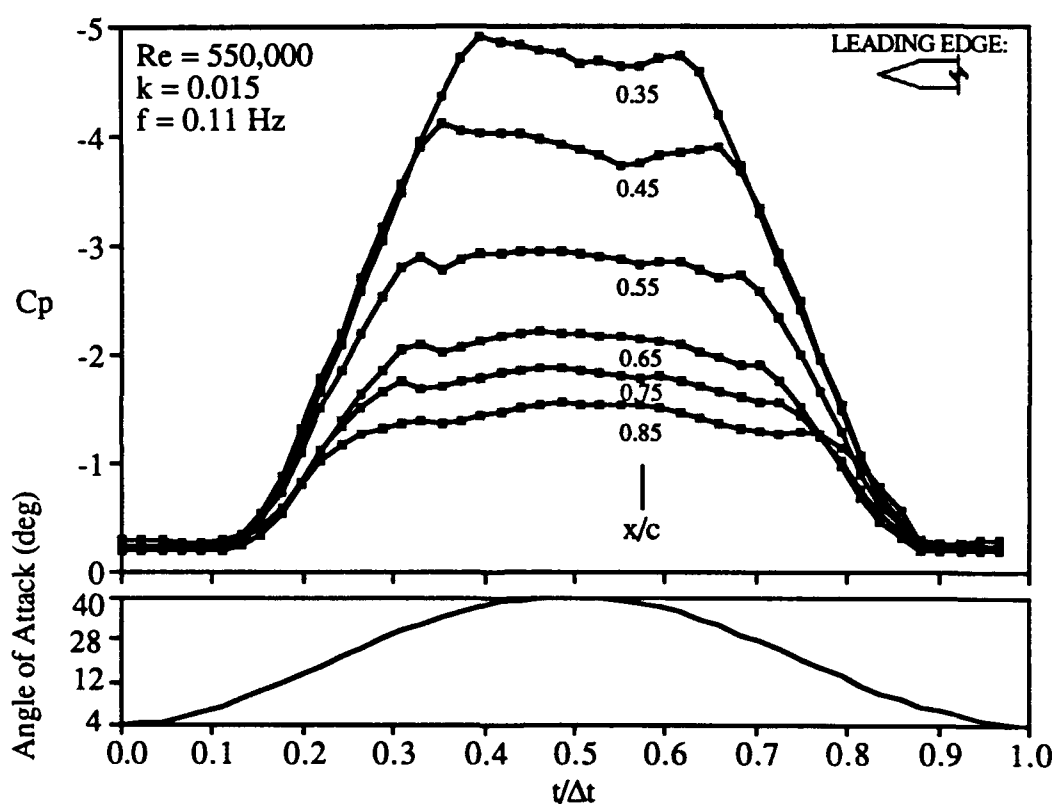
Figure 7.6   Unsteady Pressure Data for 4-40° Range of Motion. Span Location y/s = -0.60.

181
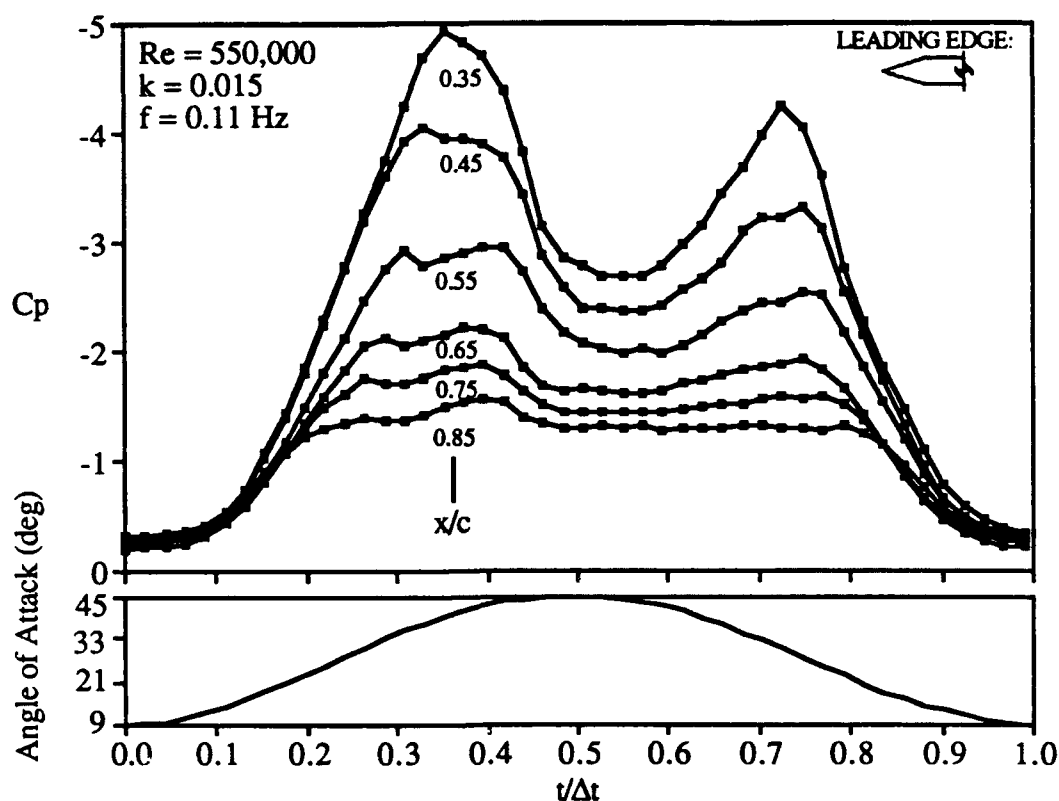
Figure 7.7   Unsteady Pressure Data for 9-45° Range of Motion. Span Location y/s =
-0.60.

Figure 7.7 is for a range of motion of 9-45°. This has the same amplitude of motion as the 4-40° range; 36°. However, the initial angle of attack has been increased by 5°. The resulting data shows considerably different trends. The pressures no longer oscillate in a quasi-steady manner. While the plateau still exists at 0.85c, by 0.65c the data has begun to acquire a double peaked characteristic. This is particularly visible at the upstream locations, 0.35c and 0.45c. It was be shown in the following sections that this behavior is typical of the very high angle of attack motions, while 4-40° more closely typifies the low and medium angle of attack motions.

This double peaked nature of the time history can be explained by considering the flow visualization data. As the angle of attack increases the pressures uniformly decrease. With the occurrence of breakdown on the wing the pressure gradient begins to decrease, first at the downstream locations. Further increase in angle of attack moves the breakdown to the apex. This precedes the total separation of the lee side, and as a result the pressures begin increasing due to the lack of an organized flow structure over the wing. However, before the pressure field can become relatively uniform (as at very high angles of attack for the steady case), the model begins pitching down again, until the point is reached at which the leading edge vortex structure reforms (with breakdown near the apex). Thus a pressure recovery begins and the pressures begin decreasing. Breakdown then moves down the length of the wing and into the wake. Concurrent with this behavior of the vortex is a partial recovery of the suction pressures, evidenced by the secondary suction peaks visible in Fig. 7.7. Further decrease in angle of attack (i.e. increase in time) results in a collapse of the vortex system and the vortex induced pressure field.

Note that the recovery of the pressures and the resulting second peak in the data can be seen to a lesser extent in the 4-40° data as well, at 0.35c and 0.45c. As the wing pitches down breakdown moves aft of these surface locations. Thus the vortex core exists just long enough to cause a small recovery of the suction pressure before the angle of attack decreases too far to sustain the low pressures.

The collapse and reformation of the vortex field give rise to the hysteresis loops and large unsteady effects seen in the force data available in the literature. Figure 7.8 shows data for both ranges, 4-40° and 9-45°, plotted as functions of instantaneous angle of attack. Chord locations of 0.45c and 0.65c are shown. Note the relatively small hysteresis loop formed by the 4-40° data as compared to the 9-45° data. The "figure eight" nature of the curve can also be seen, as for the 0-30° data. The hysteresis loop formed by the 0-30° data is even smaller than that shown in Fig. 7.8 for the 4-40° data (note that the 0-30° data was plotted with an expanded scale). The 9-45° clearly shows the type of unsteady effect

expected for high angle attack motions. Significant differences exist between the upstroke pressures and the downstroke pressures. Similar effects have been documented for the unsteady forces for these two ranges of motion (Brandon and Shah, 1988).
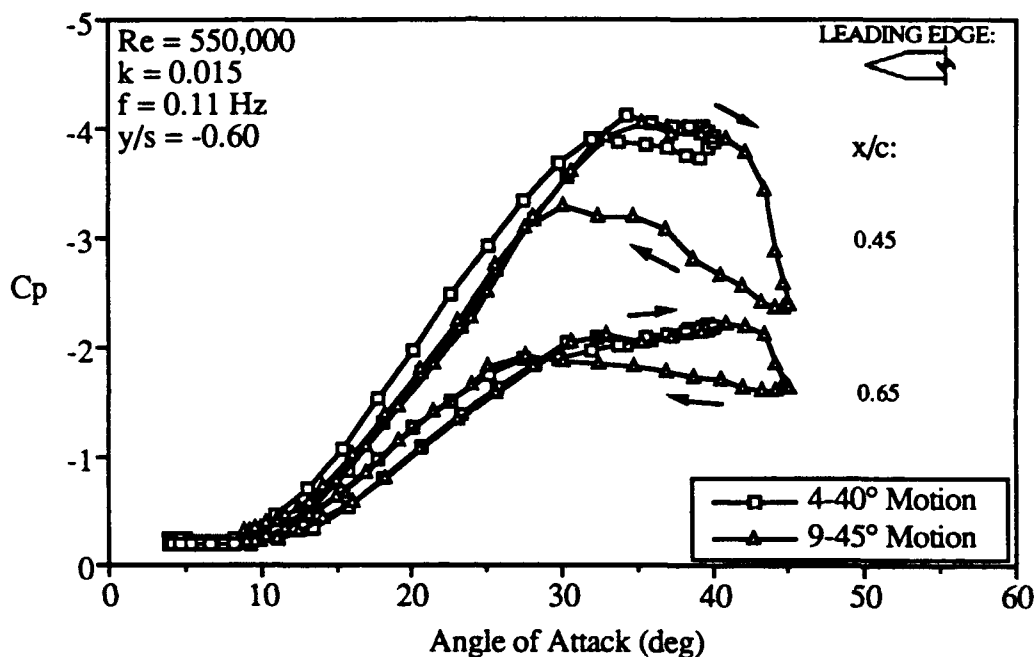
Figure 7.8   Unsteady Pressure Data for 4-40° and 9-45° Ranges of Motion. Data for Two Chord Locations Shown.

Figure 7.9 demonstrates the effect of reduced pitching frequency on the data for these two angle of attack ranges. Again, the effects seen for the 4-40° data are representative of the low and medium angle of attack ranges while the 9-45° data is representative of the high angle of attack ranges. The 4-40° data shown in Fig. 7.8 shows
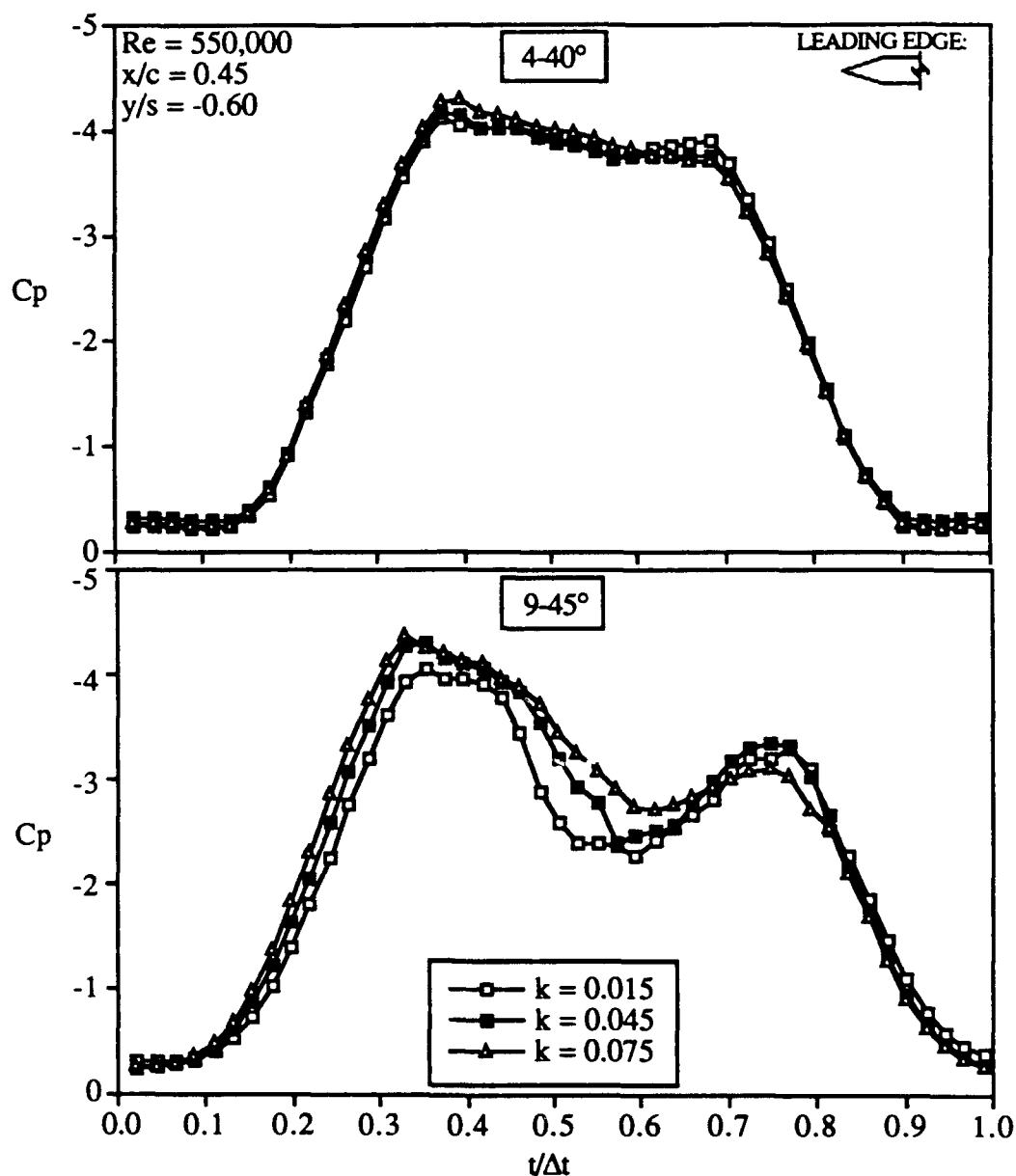
Figure 7.9   Unsteady Pressure Data for 4-40° and 9-45° Ranges of Motion. Data for

Three Pitch Frequencies Shown.

little substantial effect due to an increase in k, as seen for the 0-30° data. However the 9-
45° shows three consistent effects: an increase in the magnitude of the first suction peak, a
decrease in the magnitude of the second peak, and a decrease in the pressure gradient

between the two peaks. It will be shown in the following section that this has the effect of expanding the size of the hysteresis loop formed by the data.

The decrease in the magnitude of the second suction peak (caused by the reformation of the vortex field during the downstroke) is a result of the increased pitching frequency of the model. For a quasi-steady model motion, both suction peaks would have equal magnitudes. However, as the pitching frequency is increased, the pressure field has less time to recover (during the downstroke) before the angle of attack decreases to the point where the leading edge vortices no longer exist.

7.5   3-50° and 2-60° Ranges of Motion
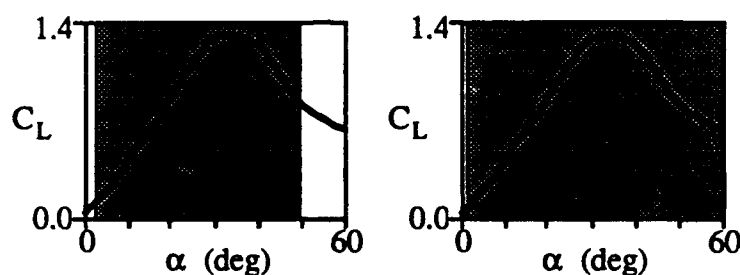
Compared to the smaller ranges presented in sections 7.2 and 7.3, these large ranges display much more drastic unsteady effects, and thus are of greater interest when exploring the possibility of expanding aircraft maneuvering envelopes by exploiting the dynamic effects. This was first seen in section 7.4 for the 9-45° range of motion. The data for that range exhibited characteristics which continue to be seen for the 3-50° and 2-60° ranges.

Figure 7.10 shows the time history for the 3-50° data. This is again for the two bevel model. Note that this data closely resembles the data for 9-45° motion. The shape of the curves and the magnitudes of the pressure coefficients are similar, with the exception of

the data at 0.35c. A significant reduction in the magnitude of the suction peaks can be seen by comparing the 3-50° data with the 9-45° data.
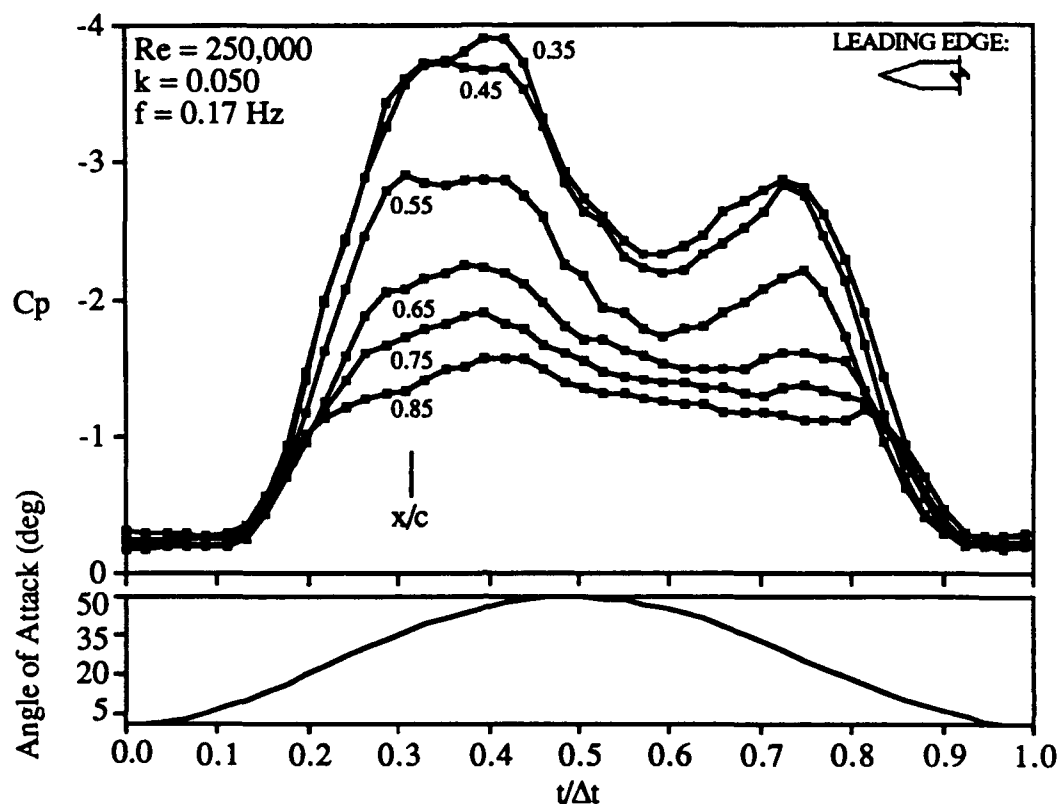
Figure 7.10   Unsteady Pressure Data for 3-50° Range of Motion. Span Location y/s = -0.60.

A possible explanation for this involves the Reynolds number. The 9-45° data was obtained for Re = 550,000, while the 3-50° data was for Re = 250,000. For the steady data, these two values were seen to cause turbulent and laminar secondary separation, respectively (as shown in Figs. 6.4-6.6). For the steady data the turbulent case resulted in a larger and more defined suction peak. A similar difference exists in the 0.35c data for the 9-45° and 3-50° ranges of motion. This could be due to a change in the vortex core location as the secondary separation transitions from laminar to turbulent.

Figure 7.11 shows data for two surface locations plotted as functions of instantaneous angle of attack. The steady data has also been shown in this figure. Both the sizeable hysteresis loop and the crossover of the upstroke and downstroke data can be seen. The unsteady data can be seen to follow the steady data during the upstroke, before overshooting during the highest angles of attack. For 0.45c this unsteady overshoot is as much as 30% of the magnitude of the steady pressure coefficient. Similarly, there is then an undershoot during the downstroke of the motion. This gives rise to the problem of taking advantage of the unsteady effects: how to the exploit the benefits of the overshoot
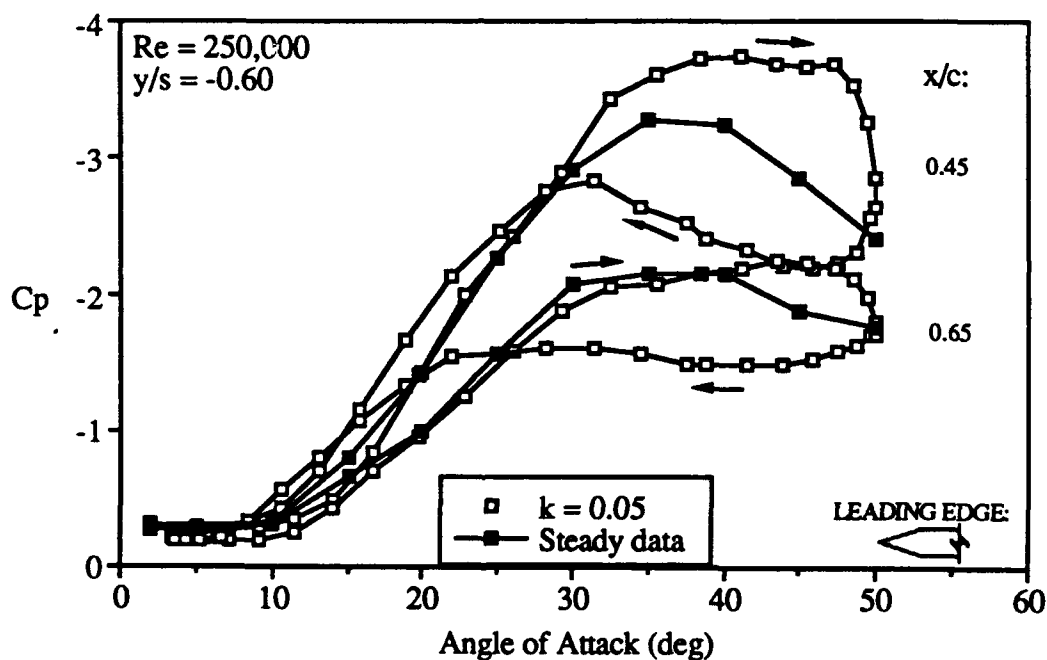
Figure 7.11   Unsteady Pressure Data for 3-50° Range of Motion. Data for Two Chord Locations Shown.

while avoiding the degraded performance of the undershoot. The downstroke data then crosses over the upstroke portion of the curve before collapsing entirely at the low angles of attack.

The effect of reduced frequency is shown in Fig. 7.12. This data shows trends very similar to those seen in Fig. 7.9 for the 9-45° data. Although the increase in the magnitude of the first suction peak is not consistent, the decrease in the magnitude of the second peak and the decrease in the pressure gradient are readily apparent. For k = 0.30 and 0.40 the second suction peak is essentially nonexistent. At these pitch frequencies (corresponding to 1.05 and 1.40 Hz) the surface pressure has insufficient time to recover from the full flow separation condition at the high angles of attack before the leading edge vortices cease to exist at the low angles of attack.
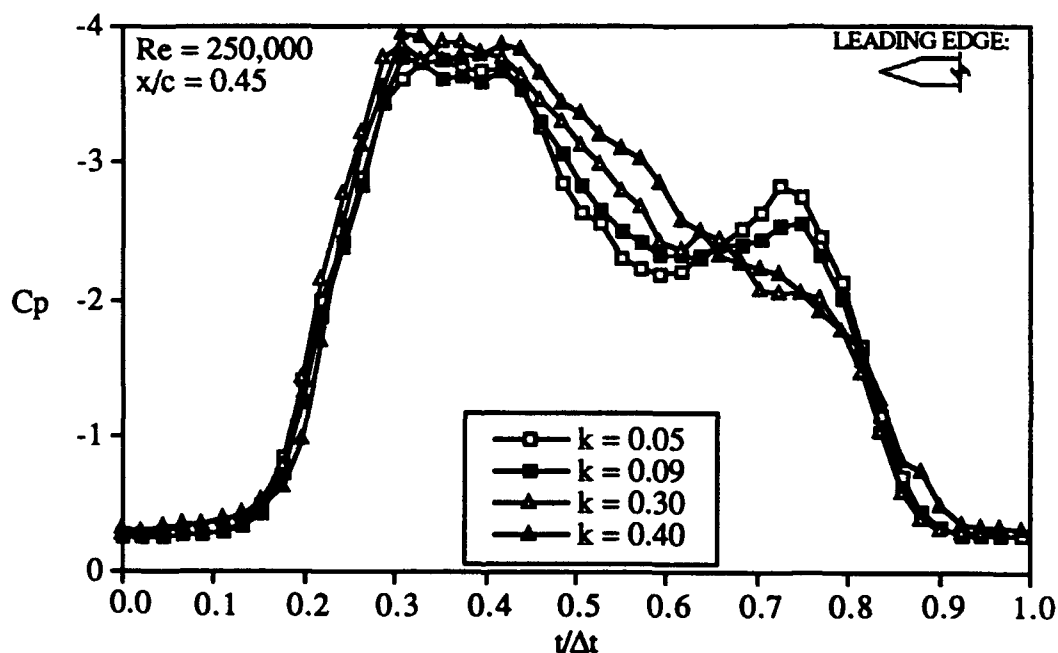
Figure 7.12   Unsteady Pressure Data for 3-50° Range of Motion. Data for Four Pitch Frequencies Shown.

Figure 7.13 shows the first of the unsteady data for the 2-60° range of motion. Data was obtained over this range for both the single and double bevel model; the double bevel data is presented first. Figure 7.13 shows the typical trends for the high angle of attack unsteady pressures. The sizes of the first suction peaks relative to the second peaks are larger than for the 3-50° case.
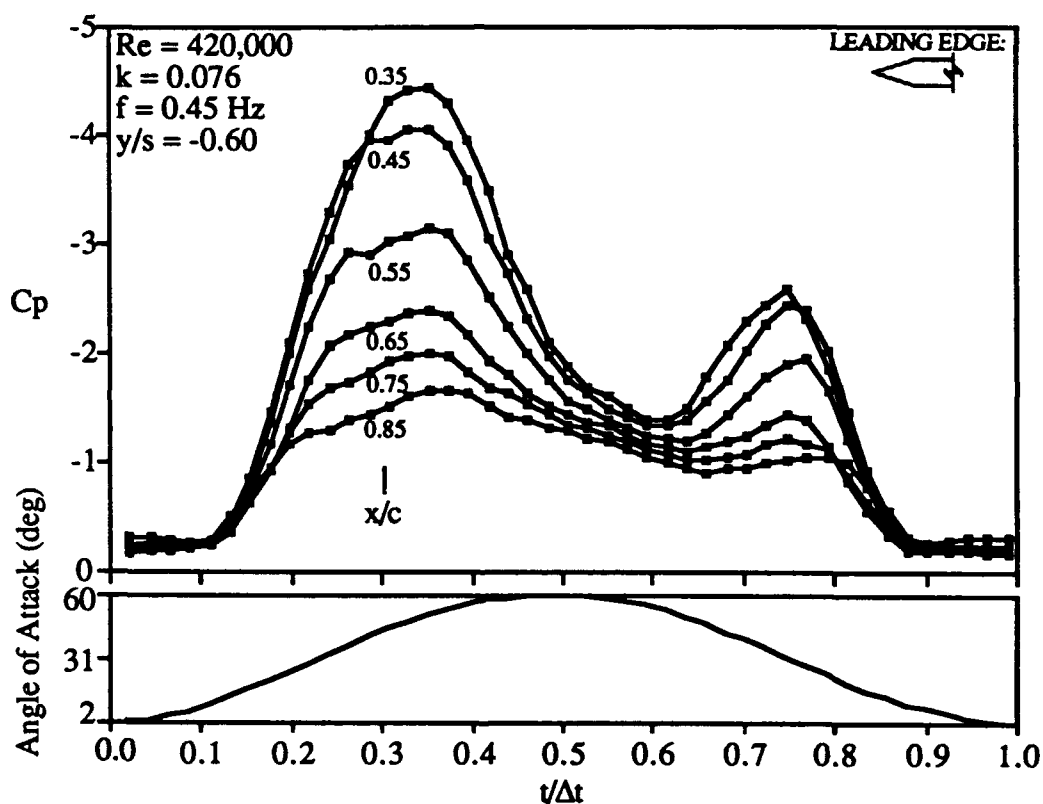
Figure 7.13   Unsteady Pressure Data for 2-60° Range of Motion. Span Location y/s = -0.60.

For the 2-60° angle of attack range, spanwise pressure distributions were also obtained; at 0.50c and 0.75c. Data from 0.75c is shown in Fig. 7.14. This figure shows five sets of plots, each at a different instantaneous angle of attack (indicated on the figures). The spanwise pressure distribution is shown for both the upstroke and the downstroke. Representative steady data has also been shown as a reference. Note that this data is at twice the pitching frequency as the 2-60° data shown in Fig. 7.13.

Significant differences exist between the upstroke and downstroke distributions at each angle of attack shown. Generally the upstroke data compares better to the steady data than the downstroke data does. This was also seen in the 3-50° data. For angles from 13-20° a difference can be detected in the unsteady location of the suction peak. The upstroke location is outboard of the downstroke location. This may indicate a difference in the location of the vortex core during the unsteady motion. A computational model of leading edge vortices by Arena (1992) has shown the suction peak to depend on both the core location and the axial flow velocity.

For angles above 25° no significant difference exists in the location of the suction peak. In addition, for span locations inboard of y/s = -0.48, no significant difference exists between the unsteady data and the steady data. For the double bevel, 70° wing used, these surface locations were relatively insensitive to the unsteady motion of the wing and the corresponding time lag of the breakdown location and the aerodynamic loads.
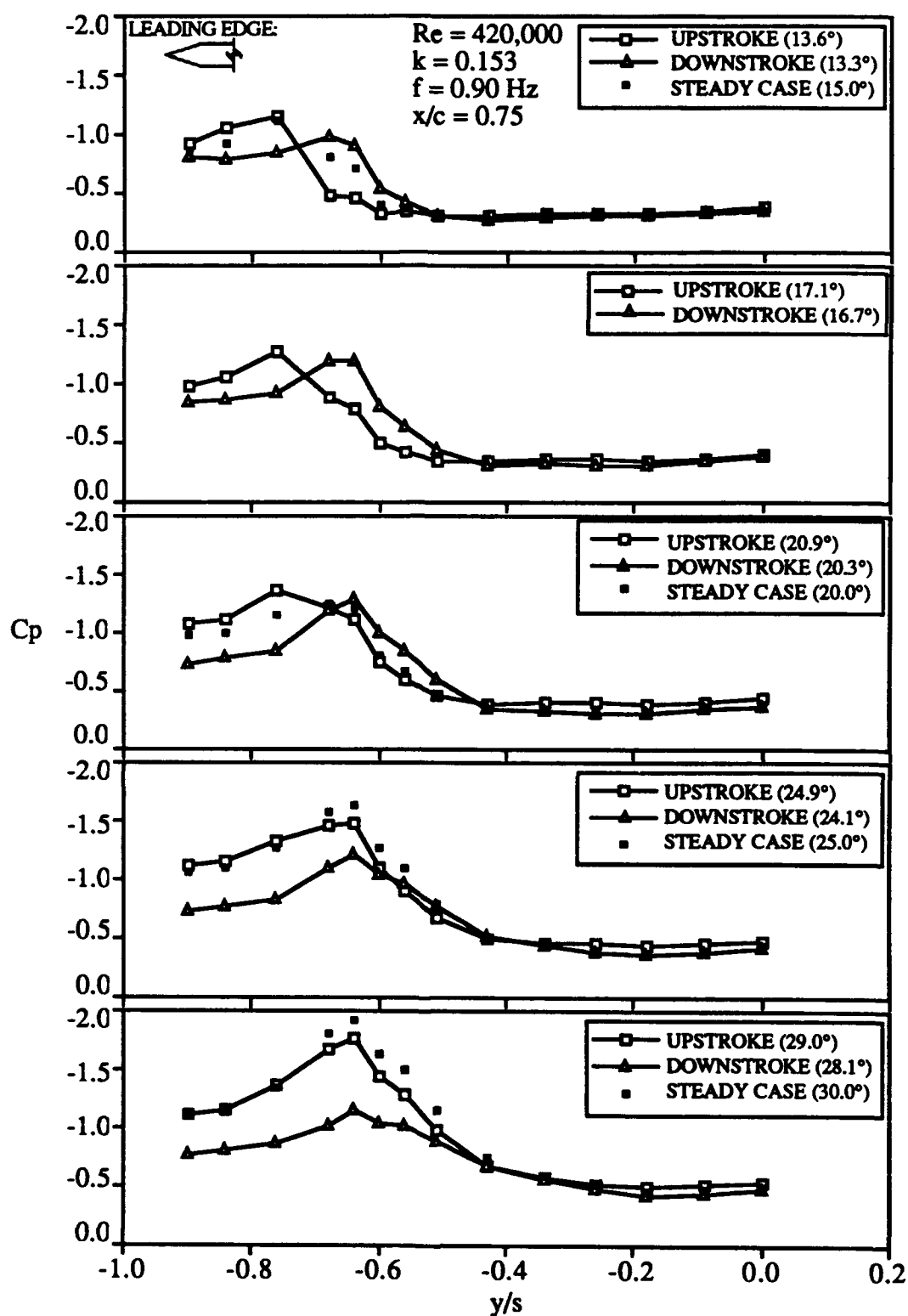
Figure 7.14   Unsteady Pressure Data for 2-60° Range of Motion. Spanwise

Distributions for Five Instantaneous Angles of Attack.

The data which has already been discussed for the preceding six ranges of motion was obtained using the double bevel delta wing model. Figure 7.15 shows a comparison of the unsteady pressure measured at the 0.35c location for five of these locations. The data for the 29-40° range was excluded since the Reynolds number was 250,000 and the question of laminar or turbulent secondary separation still exists for that case. The steady data is also shown in Fig. 7.15.
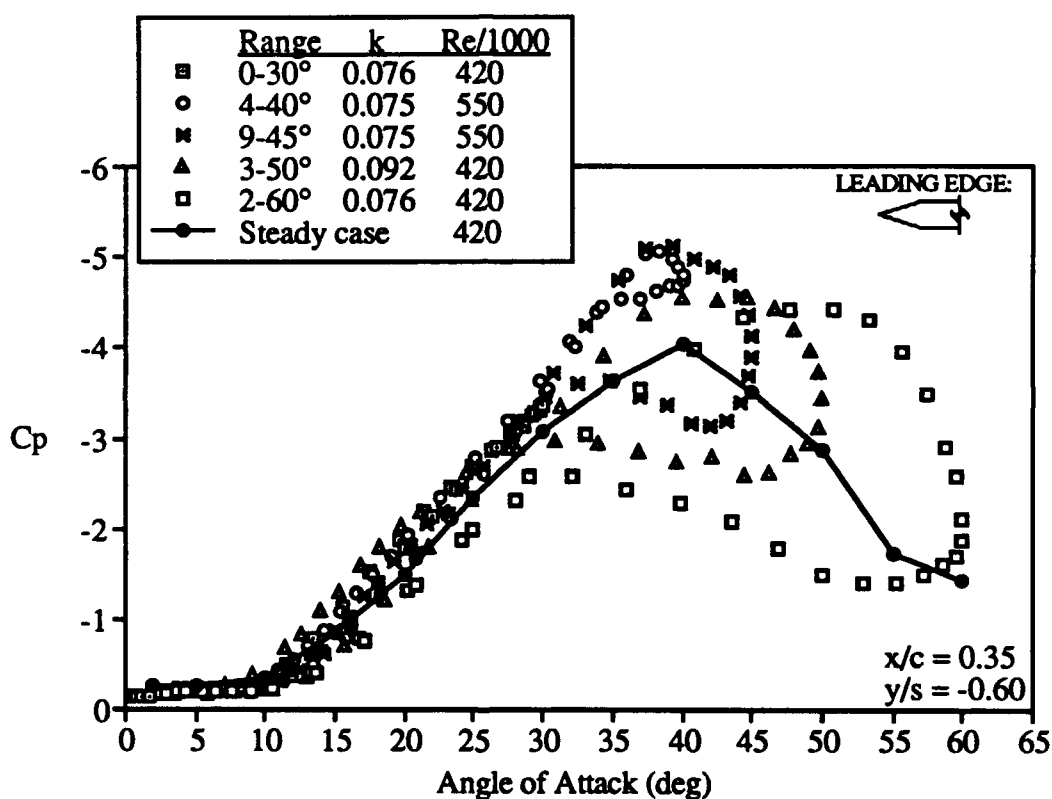
Figure 7.15   Unsteady Pressure Data for Several Ranges of Motion. Steady Data also Shown.

Note that this figure can be dividing into two portions: angles less than 30°, for which quasi-steady behavior occurs, and angles greater then 30°, for which the most significant unsteady effects exists. Since this is approximately the angle at which

breakdown first occurs over this wing, this is in keeping with the concept that the motion of breakdown onto and off of the wing, as well as complete separation, contributes to the large unsteady effects.

The expansion of the hysteresis loop with an increase in the range of motion can be seen in Fig. 7.15. The width of the loop consistently enlarges with increasing range. The magnitude of the overshoot actually decreases for the 2-60° range. However, for the most part the lowest pressure coefficient obtained remains nearly the same while the magnitude of the undershoot decreased, in effect widening the loop. For example, comparing the 3-50° data with the 2-60°, it can be seen that each reaches a $C_p \approx -4.5$. Yet the 2-60° curve achieves this value during a higher angle of attack range, thus, its *percent* overshoot is considerably larger than that of the 3-50° data, since the steady pressure is rapidly increasing (compare to the steady curve shown). The 2-60° data then has a larger undershoot during the downstroke portion of the motion. This type of comparison can be made between the data for each of the ranges shown in Fig. 7.15.

Figure 7.16 shows data for the single bevel wing undergoing a 2-60° range of motion. This wing was equipped with a greater number of pressure taps than the double bevel wing, thus pressures at chord locations from 0.25c-0.95c are shown. For the single bevel wing, twenty five cycles of unsteady data were ensemble averaged. It was found that this number of cycles yielded a representative average while substantially decreasing the computational time required. Beneath Fig. 7.16, Fig. 7.17 shows the instantaneous location of vortex breakdown during the unsteady motion.

By comparing the data in Fig. 7.16 to the double bevel data shown in Fig. 7.13 it can be seen that the trends are quite similar. In general, the magnitudes of the single bevel pressures are smaller for a given chord location. However, the single bevel data is for a Reynolds number of 250,000; the steady pressure data indicated that this was in the range of laminar secondary separation. If this also applies to the unsteady case, then higher pressure
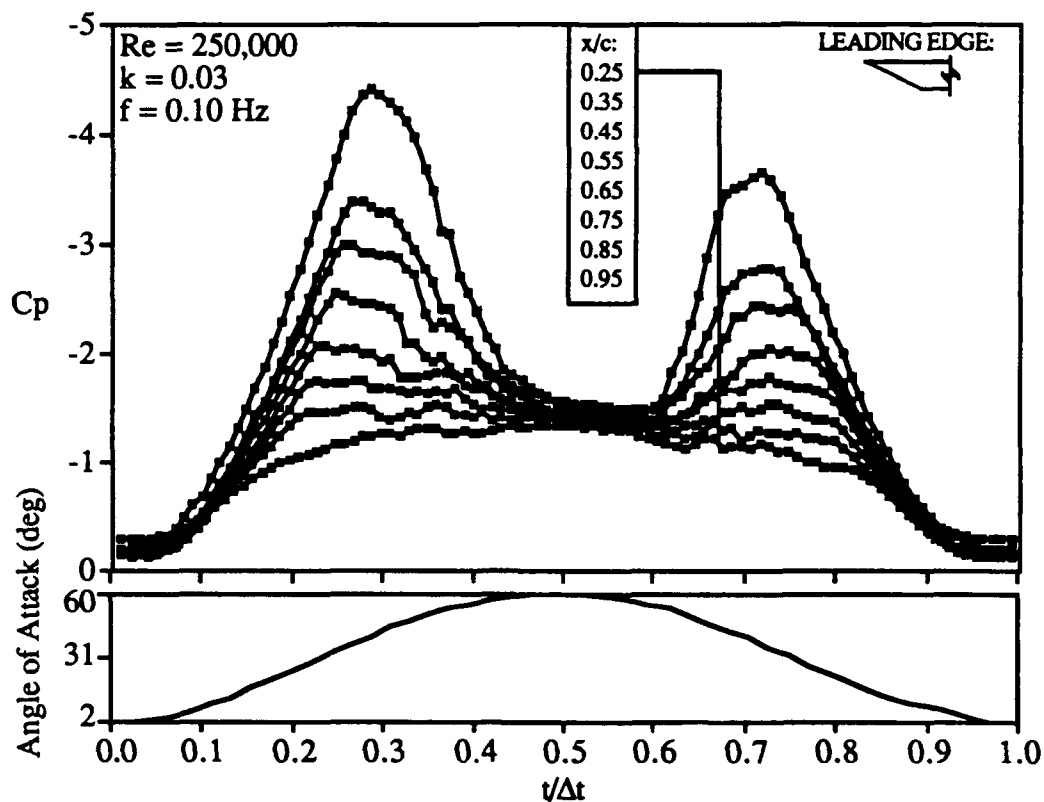
Figure 7.16   Unsteady Pressure Data for 2-60° Range of Motion. Span Location y/s =

-0.60.
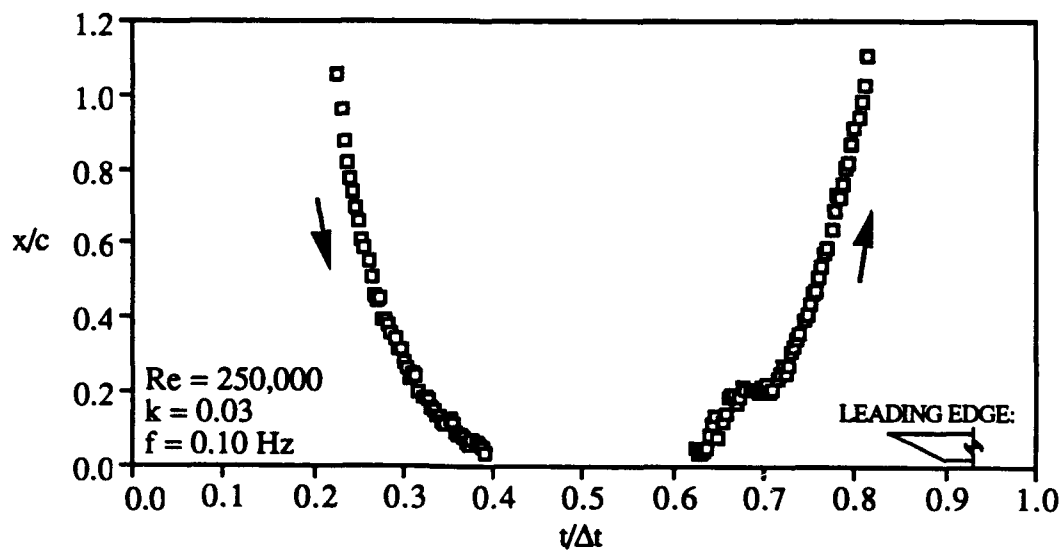
Figure 7.17   Unsteady Breakdown Location for 0-60° Oscillation.

(relative to the double bevel wing) could result, as shown in Fig. 7.13. A direct comparison of the single and double bevel at comparable Reynolds numbers is included later in this section.

The pressure recovery seen in Fig. 7.16 during the downstroke of the motion becomes most apparent for chord locations upstream up 0.75c. At 0.25c a strong suction peak is recovers prior to the collapse of the leading edge vortex at low angles of attack. For chord locations from 0.75c-0.95c, no substantial suction peaks are formed. This is due to the fact that breakdown exists upstream of these locations for a large portion of the motion; there is only a small portion of the motion for which a leading edge vortex exists (without breakdown over the wing) to cause the pressure drop seen at locations closer to the apex.

The unsteady location of breakdown is shown in Fig. 7.17. This same data has been shown previously in Fig. 5.7a. Here the chordwise breakdown location during one cycle of motion is shown as a function of nondimensional time. The Reynolds number and reduced frequency are the same as for the pressure data shown in Fig. 7.16. The unsteady pressures reach minimum values at roughly $t/\Delta t = 0.30$, at which time the breakdown is located near 0.2c. The breakdown reforms during the downstroke at $t/\Delta t = 0.62$, the same time that the suction pressure recovery begins to be seen in the surface pressure data.

From $t/\Delta t = 0.40$-0.60 full scale flow separation is occurring over the wing as seen by the flow visualization data; breakdown has moved to the apex and disappears as the leading edge vortex system ceases to exist. This corresponds to the collapse of the surface pressure field as each the pressures at each chordwise position measured begin increasing to similar values.

The 0.25c and 0.75c data shown in Fig. 7.16 is shown as hysteresis loops in Fig. 7.18. The steady data has also been shown. Data for two pitching frequencies is shown to demonstrate the effect of k on the shape of the hysteresis loop. Note that the scale is the same for each part of Fig. 7.18; the data for 0.25c and 0.75c can be directly compared to each other. During the upstroke the pressures are essentially the same up to 30-35°

degrees. The increase in pitching frequency then clearly results in an increase of both the overshoot and the undershoot (relative to the steady data) at higher angles of attack. The "figure eight" nature of the curve is also increased, but only slightly for the 0.25c data. However, for this data the point of crossover of the upstroke and downstroke data occurs 5° higher as k increases from 0.03 to 0.12.
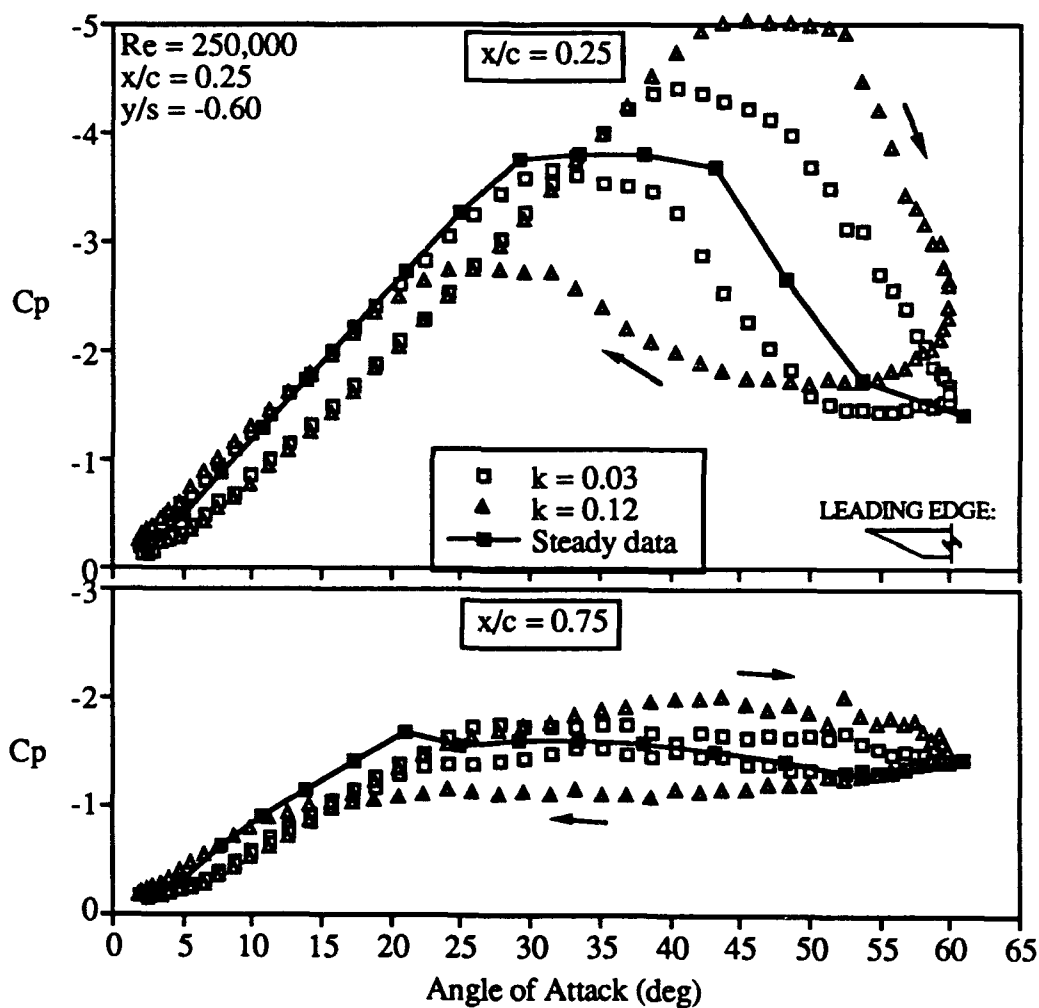
Figure 7.18   Unsteady Pressure Data for 2-60° Range of Motion. Data for Two Chord Locations Shown.

The trend of increasing loop width with increasing reduced frequency was typical throughout the pressure data. This was also shown in Fig. 7.15 for the double bevel wing and several different ranges of motion. It was consistently seen that the *nondimensional* pitching frequency (k) determined the shape of the hysteresis loop, and not the dimensional pitch rate (f).

For example, the case of Re = 500,000 and k = 0.06 has the same dimensional pitching frequency as the case of Re = 250,000 and k = 0.12 (0.42 Hz). However, the hysteresis loop formed by the Re = 500,000 data more closely resembles the loop formed by the Re = 250,000 data with k = 0.06.

Figure 7.19 again shows the effect of k; here the time history is shown. Data for four values of k is shown. This figure shows trends seen previously for the 49-45° and 3-
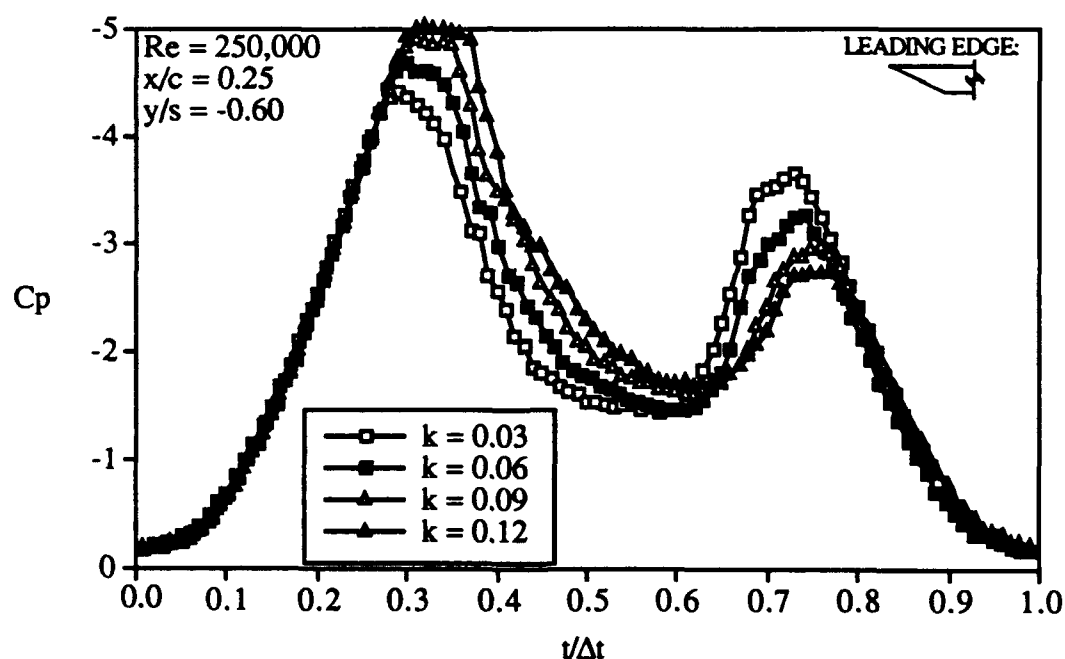
Figure 7.19   Unsteady Pressure Data for 2-60° Range of Motion. Data for Four Pitch Frequencies Shown.

50° data. The magnitude of the first suction peak is increased and that of the second peak is decreased. However, the pressure gradient between the two peaks is roughly constant for each value of k shown in Fig. 7.19.

Figure 7.20 shows the effect of Reynolds number on the unsteady surface pressure. In Chapter 6 it was shown that a Reynolds number effect existed in the steady pressures; this was attributed to the transition of the secondary separation from laminar to turbulent (see Figs. 6.4, 6.5, and 6.6). This occurred between Reynolds numbers of 250,000 and 500,000.
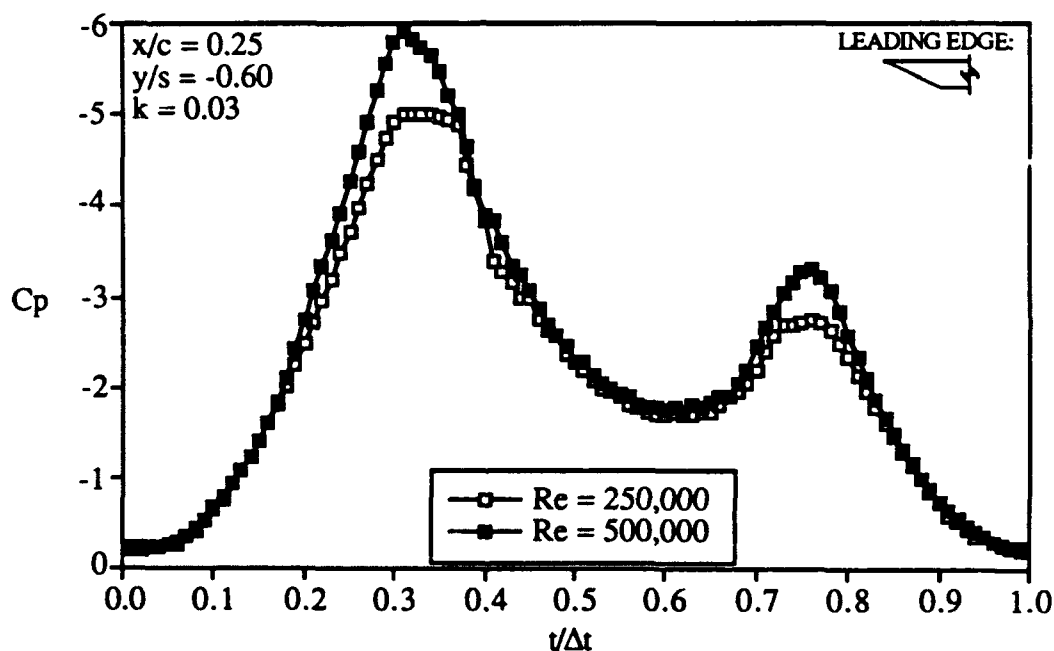
Figure 7.20   Unsteady Pressure Data for 2-60° Range of Motion. Data for Two
Reynolds Numbers Shown

Figure 7.20 shows unsteady pressure time histories for the 0.25c location at two Reynolds numbers. Reduced pitching frequency is constant. The data for the higher Reynolds number shows a significant difference from the lower Re nolds number data,

particularly at the two peaks. This behavior exactly parallels the pressure decrease caused by the increase in Reynolds number for the steady case. Similar behavior was seen at higher pitching frequencies as well.

Note that this effect may be limited to the specific surface location shown in Fig. 7.20 (0.25c, -0.60s). The transition of the secondary flow results in a change in the location of the vortex core (outboard and closer to the wing surface). Thus, it is logical to assume that at some surface locations the surface pressure could remain constant or possibly increase as a result of transition, due to the shift of the core farther from that surface location. However, it was seen in the steady data that at $x/c = 0.25$ and $y/s = -0.60$, transition causes a decrease in pressure.

Figure 7.21 shows the pressure profiles at an instantaneous angles of attack of $50°$. One chordwise profile ($y/s = -0.60$) and two spanwise profiles ($x/c = 0.50$ and 0.75) are shown. The steady data is also shown. By referring to the hysteresis loops shown in Fig. 7.18 it can be seen that $50°$ corresponds to one of the widest parts of the loop. The large difference between the upstroke and downstroke pressures are readily apparent in Fig. 7.21. The upstroke pressures indicate that organized flow continues to exist over the wing, while the steady pressure have already begun to collapse as full flow separation occurs. The consistency of the lower upstroke pressures suggests that the unsteady aerodynamic loads on the wing (the integrated effect) is also large relative to the steady loads.
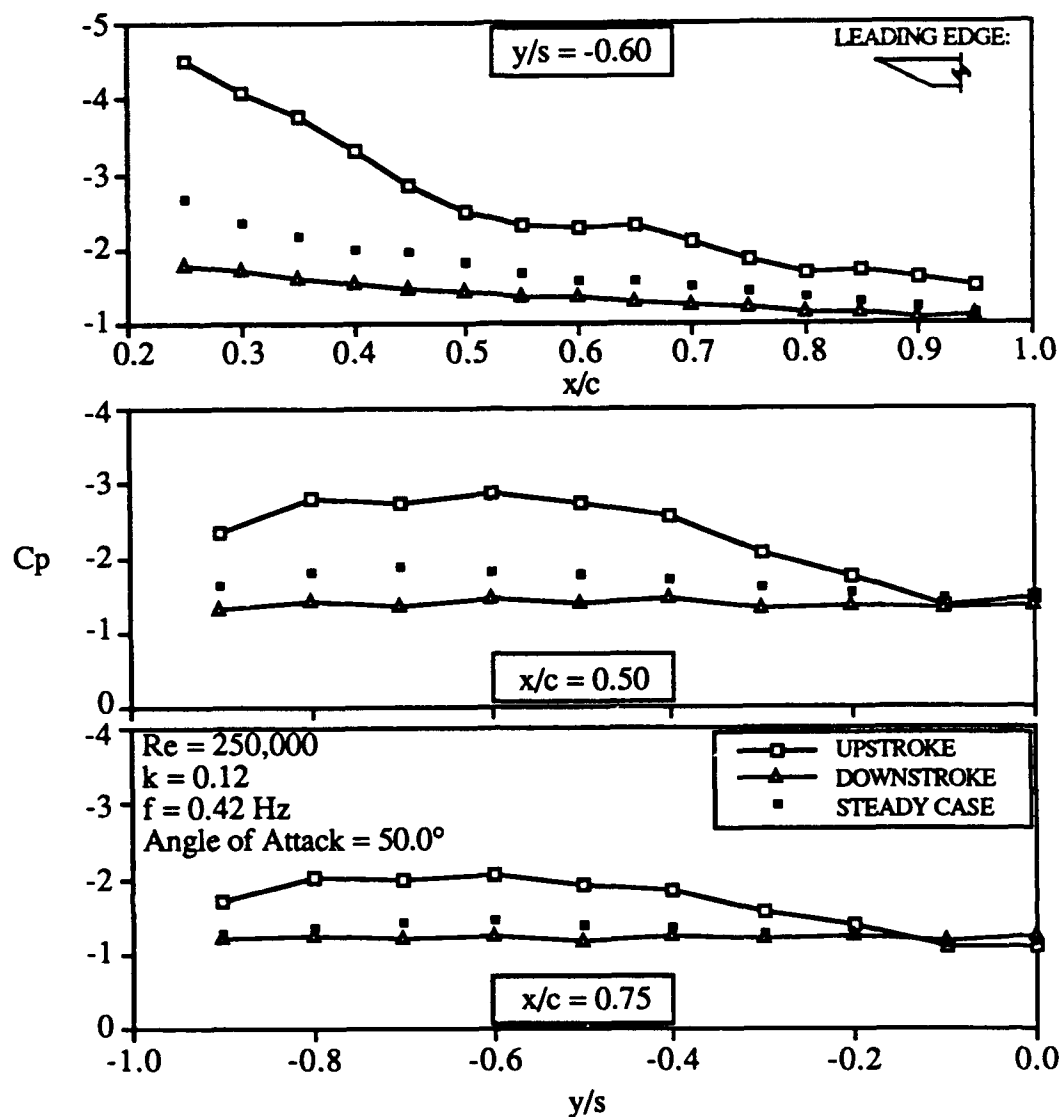
Figure 7.21   Unsteady Pressure Data for 2-60° Range of Motion. Chordwise and
Spanwise Distributions at an Instantaneous Angle of Attack of 50.0°.

Figure 7.22 shows additional spanwise pressure distributions for the 2-60° single
bevel data. Here the instantaneous angle of attack is 17.3°. Note that the instantaneous
spanwise profile for the double bevel wing at this angle has been shown as part of Fig.
7.14. Data for two Reynolds numbers is shown in Fig. 7.22. There are two points to

make about this data: one involving the dynamic location of the suction peak, and the other involving the effect of Reynolds number.
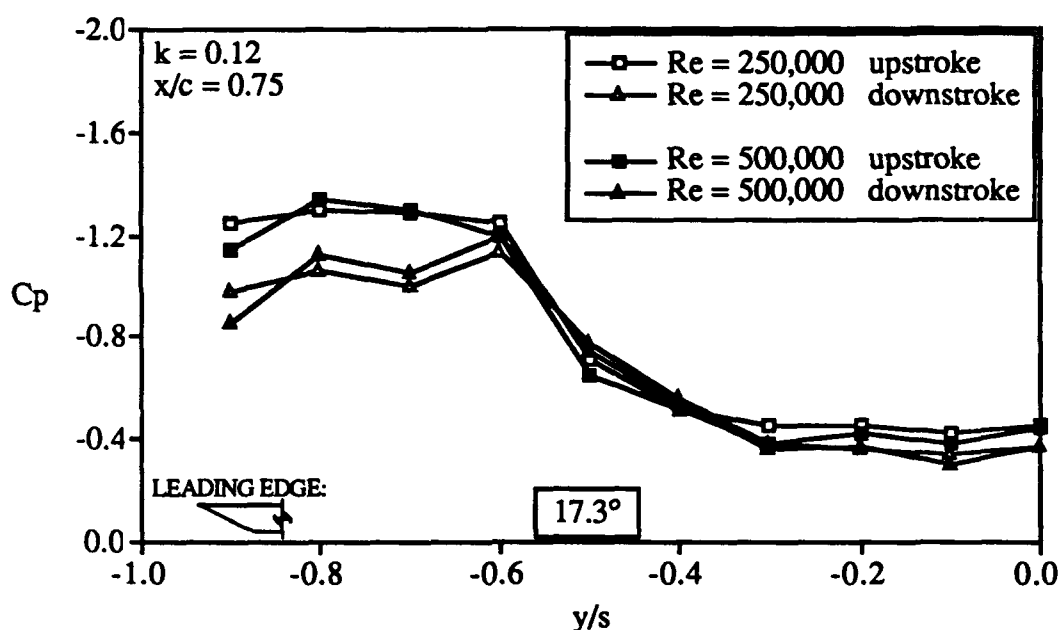
Figure 7.22   Unsteady Pressure Data for 2-60° Range of Motion. Suction Peak as a

Function of Reynolds Number

Unlike the data for the double bevel wing, a clear difference in the location of suction peak for the upstroke and the downstroke is not apparent in Fig. 7.22. The double bevel data showed the downstroke location to be almost 15% of the semi-span inboard of the upstroke location. The single bevel data does show distinct differences between the upstroke profile and the downstroke profile, but the suction peak is not clearly defined. This is particularly true for the upstroke profile (at both Reynolds numbers shown). This behavior was also seen in the steady data for each wing; the double bevel spanwise profiles (at x/c = 0.75) showed a much more sharply defined suction peak than did the single bevel profiles (see Fig. 6.2a).

The effect of Reynolds number is also unclear in the spanwise profiles shown in Fig. 7.22. The transition of the secondary separation was clearly visibly in the steady data. This was also true for some of the unsteady data as shown in Fig. 7.20 for x/c = 0.25. However, the effect of transition on the suction peak could not be conclusively determined. Spanwise pressure profiles were obtained for Re = 250,000 and Re = 500,000 and four reduced frequencies. The data shown in Fig. 7.22 represents the difficulties in determining laminar or turbulent separation from the spanwise profiles.

Transition from laminar to turbulent separation has two effects: a decrease in the pressures (as shown in the unsteady data in Fig. 7.20) and a change in the form of the suction peak (see Fig. 6.6). The Re = 250,000 data shown in Fig. 7.22 resembles the laminar profile on the upstroke, but the turbulent profile on the downstroke. However, this is also true for the Re = 500,000. Yet both the steady data and the unsteady data at 0.25c for Re = 500,000 have indicated turbulent secondary separation.

This type of conflicting behavior was seen in all the unsteady spanwise profiles. It suggests that for the unsteady case transition depends not only on Reynolds number, but also on reduced frequency and direction of motion.

Figure 7.23 contains data on the unsteady instantaneous chordwise pressure gradient in relation to the unsteady instantaneous location of vortex breakdown for a 2-60° motion. The data shown is for the single bevel wing at a Reynolds number of 250,000 and a reduced frequency of k = 0.12. The steady pressure data was presented in a similar manner, as shown in Fig. 6.8, and can be used as a comparison to Fig. 7.23 (the scales are the same). Clearly, a difference exists in the data depending on the direction of motion. Note also that the unsteady data does not bracket the steady data (from Fig. 6.8). For the most part, the unsteady pressure gradient is smaller than the steady pressure gradient.
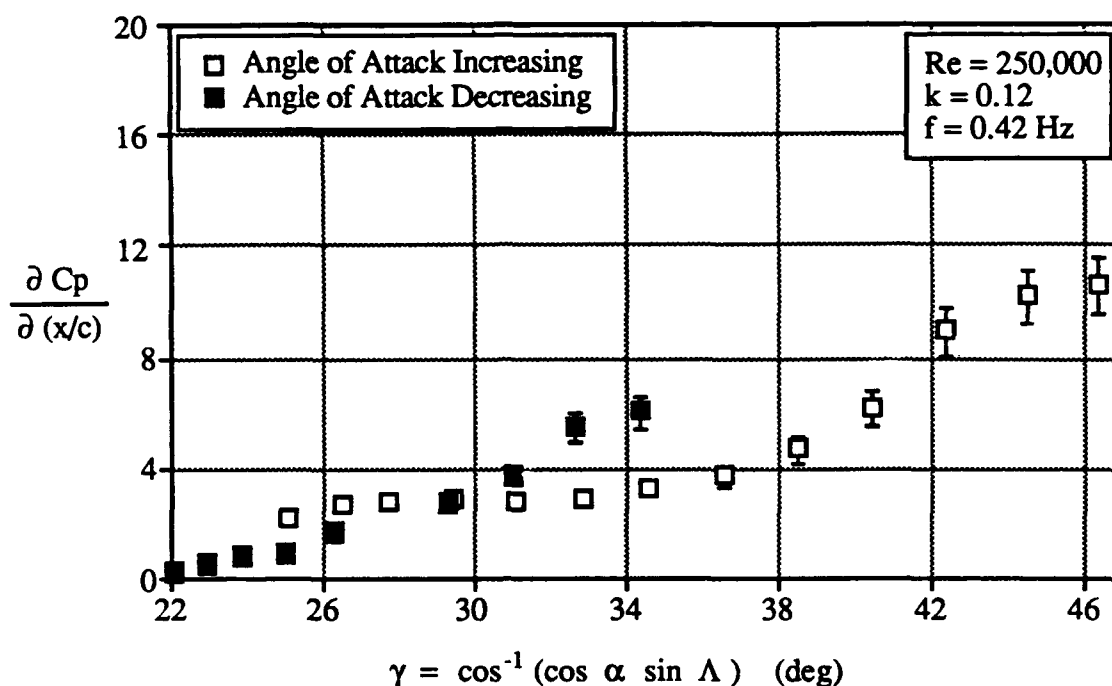
Figure 7.23   Unsteady Chordwise Pressure Gradient Correlated to Unsteady Location of

Vortex Breakdown for 70° Sweep Wing

Figure 7.24 contains a comparison of data for the double bevel wing with data for

the single bevel wing. The angle of attack range for each is 2-60°. The Reynolds number

is different for each wing; however, both wings are in the turbulent separation range for the

steady case. Data for two chord locations are shown, 0.35c and 0.45c. Note that the

0.35c location is on the bevel face for the double bevel wing. While the reduced frequency

is slightly larger for the single bevel wing, the effect of this difference is not

distinguishable.
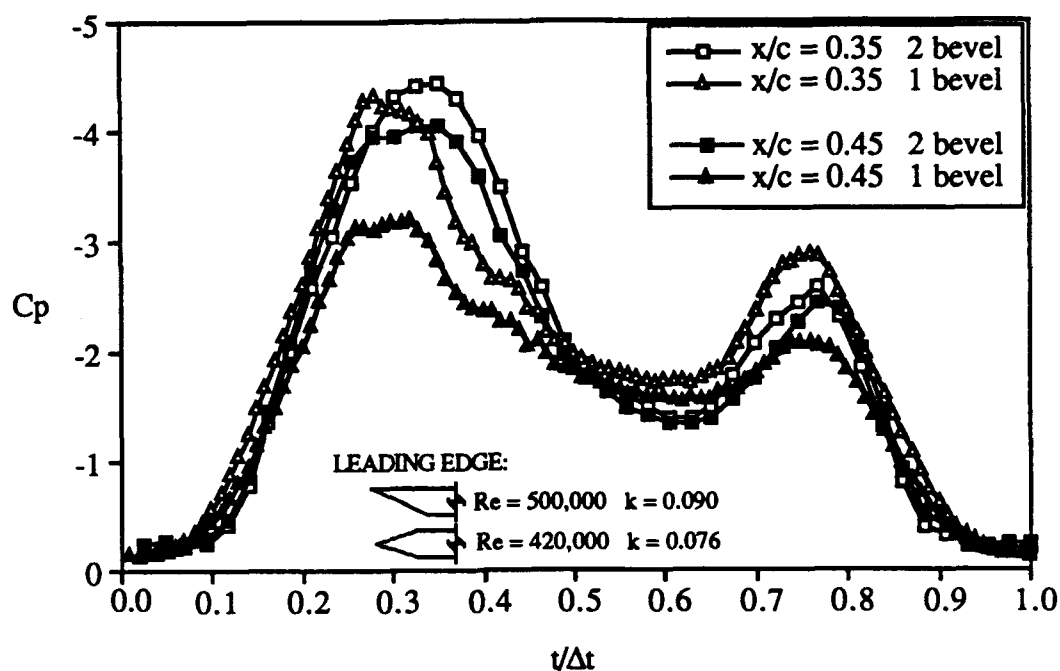
Figure 7.24   Comparison of Unsteady Pressure Data for Single Bevel and Double Bevel

Models. Data for Two Chord Locations Shown.

Both the magnitudes and the trends of the 0.35c pressures compare well between wings. The first suction peak forms slightly earlier for the single bevel wing, i.e. at a lower angle of attack. This also occurs for the 0.45c data. This type of difference was also seen between the steady pressure data for the two wings. The surface pressures for the single bevel wing typically reached a minimum by 30° while the pressures for the double bevel wing continued to decrease up to 40°. Thus, an earlier peak would be expected in the unsteady data. The second (recovery) suction peaks are closer in phase with each other.

Notice that the 0.45c is consistently lower for the double bevel wing.   This was also seen in the steady data. For the single bevel wing a minimum C_p of -2.7 occurred at this surface location, while for the double bevel wing a value of -3.3 was reached. The unsteady values shown in Fig. 7.24 show a similar trend.

7.6   Summary

Unsteady pressure distributions were obtained for six angle of attack ranges and two leading edge geometries. Several values of Reynolds number and reduced pitching frequency were used during each test. A sinusoidal oscillation of angle of attack was used throughout the tests.

For an angle of attack range of 0-30° the unsteady effects on the surface pressures were relatively small. The pressures oscillated in phase with the model motion. The occurrence of breakdown at the peak angles of attack of the motion resulted in an increase in the pressures at several surface locations near the trailing edge (where breakdown first occurs). This in turn increased the unsteady effects, resulting in a small hysteresis loop when the data is plotted as a function of instantaneous angle of attack.

Data for the 29-40° range of motion again showed the unsteady pressures to behave in a quasi-steady manner. The exception to this occurred near the apex, where the effect of breakdown again caused an increase in surface pressure. This effectively doubled the frequency of oscillation of the surface pressure to roughly twice the pitching frequency. The percent fluctuation of the pressures was close to the percent fluctuation of the lift coefficient from 29-40°; 10%. Similar behavior was recorded for Reynolds numbers from 250,000-500,000 and reduced frequencies from 0.10-0.30.

The data for the 4-40° and 9-45° ranges typified low angle of attack motions and high angle of attack motions, respectively. The same Reynolds number, reduced frequencies, and range of travel were used in both cases; the difference between the two cases was a change in the mean angle of attack from 22° to 27°. This resulted in very different unsteady effects.

The 4-40° data was similar to the 0-30° data. However, the higher angles of attack resulted in the occurrence of breakdown as far forward on the wing as 0.35c, resulting in uniform pressure increases at all the surface locations sampled. As with the 0-30° data, this resulted in hysteresis loops being formed by the data.

The 9-45° data showed the double peak nature of the very large angle of attack unsteady pressures. A peak is formed during the upstroke but begins to collapse as the angles of attack becomes large enough to encompass breakdown reaching the apex and the beginning of full scale lee side separation. However, before the pressures can uniformly collapse, the wing begins to pitch down again, resulting in a reformed vortex. Correspondingly, breakdown reforms near the apex and moves aft. As this happens a recovery of the suction pressures occurs. The surface pressures begin to decrease again. For a quasi-steady motion, the amount of the recovery would equal the pressure drop during the upstroke. However, for the unsteady case the magnitude of the second suction peak is less than that of the first peak. This is due to the continued downward motion of the wing as the pressure recovery occurs. Before the recovery is complete the wing has reached an angle of attack too low to sustain the low surface pressures.

This effect decreases with increasing chord location, since less time exists between breakdown moving past that surface location, and the angle of attack becoming too low to sustain the low pressures. Hence the second peak is larger for the upstream surface locations. This effect was visible to a small extent in the 4-40° data, at the forwardmost surface location sampled.

The 2-60° data and 3-50° data continued to show the trend of a sharp pressure drop on the upstroke followed by a momentary collapse of the pressure field, followed by a partial recovery of the suction pressure. Using unsteady flow visualization data, the collapse of the pressure field was correlated to the full scale separation of the leeward side

flow field. The suction pressure recovery was seen to occur upon reformation of the vortex system (with breakdown near the apex) during the downstroke.

The effects for these large amplitude motions were more significant than for the 9-45° range. Correspondingly, the size of the hysteresis loops formed by the data were larger. These loops are a very effective way to present the data since they clearly show the overshoot and undershoot of the unsteady data relative to the steady data.

The hysteresis loops were seen to have a "figure eight" shape in that the upstroke pressures were higher than the downstroke pressures for part of the motion, and lower for part of the motion.

The effect of reduced frequency was consistent for the 9-45°, 3-50°, and 2-60° data. An increase in reduced frequency primarily resulted in a decrease in the magnitude of the suction pressure recovery during the downstroke. This can be explained by considering that when the model is pitching at a faster frequency, there is less time for the pressure field to recover during the downstroke before the angle of attack decreases to the point where the leading edge vortex system no longer exists. Hence, the extent of the recovery is less. The time required for a complete pressure recovery was not examined. In addition, in some cases an increase in reduced frequency increased the magnitude of the first peak, and decreased the pressure gradient between the two peaks.

Some differences due to the leading edge geometry were also noted. For the double bevel wing a clear difference in the spanwise location of the suction peak was detected between the upstroke data and the downstroke data. This was not true for the single bevel wing. This correlates with the steady pressure data for the two wings; the double bevel wing consistently had a more defined spanwise suction peak.

However, the general behavior of the unsteady surface pressures was very similar for each wing. The hysteresis at the high angles of attack and the suction pressure recovery during the downstroke were seen for both single and double bevel wings.

The transition of the secondary separation from laminar to turbulent was detectable in some of the unsteady pressure data, particularly at surface locations near the apex (such as $x/c = 0.25$). This occurred between Reynolds numbers of 250,000-500,000. A decrease in pressure was caused by the transition. Both the Reynolds number range and the magnitude of the pressure drop compared well to the steady pressure data.

Unlike for the steady data, the effect of transition on the unsteady spanwise pressure profile (specifically the suction peak) was not conclusive. It appears that for the unsteady case transition is related not only to Reynolds number, but also the pitching frequency and direction of motion (angle of attack increasing or decreasing).

In general, the data fits into two categories depending on the range of motion: ranges with quasi-steady behavior (0-30°, 29-40°, 4-40°), and ranges with drastic unsteady effects (9-45°, 3-50°, 2-60°). Unsteady effects were visible for both categories, but considerably more so for the high angle of attack ranges.

However, the unsteady effects seen at the small ranges served to explain the unsteady effects seen at the large ranges. The data for 0-30° and 4-40° suggested that the unsteady effects were related to the occurrence of vortex breakdown. However, for the 29-40° data breakdown existed throughout the motion, yet the unsteady effects were small. Together these two observations suggest than the most significant unsteady effects are caused by angles of attack which include the *formation* of breakdown. This includes angles near 20-30° where breakdown first occurs, and angles near 45-50° where breakdown ceases to exist as full scale separation occurs.

The flow visualization data (steady and unsteady) showed that breakdown is sensitive to the location of the trailing edge and can treat it as an obstacle to its smooth forward or aft motion. In addition, during an unsteady motion encompassing full scale flow separation, when breakdown reformed during the downstroke it would stay relatively motionless while the wing continued to pitch down, before moving aft. The hysteresis effects seen in the breakdown location were primarily instigated at the trailing edge or at the apex; where breakdown formation is involved.

For the high angle of attack motions, the unsteady effects were the most substantial during the high angle of attack portion of the motion, i.e. during roughly 30-60° for a 2-60° angle of attack oscillation. The size of the hysteresis loop formed at these angles was seen to correlate well with the *reduced* pitching frequency, not the dimensional pitching frequency. The unsteady effects for cases with matched reduced frequencies were much more similar than those for cases with matched dimensional pitching frequencies.

An increase in the pitching frequency (reduced or dimensional) clearly results in an increase of *both* the overshoot and the undershoot of the unsteady pressures relative to the steady pressures. If the goal is to exploit the overshoot developed during the upstroke, then the obstacle is the undershoot the develops during the downstroke. Relative to the steady case the magnitude of the undershoot can be as large or larger than that of the overshoot. The problem therefore changes from how to exploit the overshoot to how to exploit the overshoot while avoiding any detrimental effects of the undershoot.

The undershoot is dependent to some extent on the magnitude of the pressure recovery that occurs as the vortex system reforms. The more complete the recovery, the closer the pressure gets to the steady value. No recovery at all would result in a larger and more persistent undershoot. *Increasing* the pitching frequency *decreases* the magnitude of the pressure recovery; the wing is moving faster thus less time exists for the suction pressure to recovery before the angle of attack has become too low to sustain the low

pressures. Thus the overshoot is increased, but the undershoot is also increased. A second issue now involves determining if it is possible to increase the overshoot without increasing the undershoot. A simple change in pitching frequency did not accomplish that in the present research. For an airframe undergoing an unsteady maneuver, it may be possible to accept an undershoot of a certain magnitude, thus it would be beneficial to maximize the overshoot without altering the undershoot.

VIII   CONCLUSIONS

The present experimental research was conducted in order to examine the relationship between the aerodynamic loads and the vortex flow characteristics of a highly swept wing undergoing both quasi-steady and unsteady pitching motions. Extensive testing was conducted that consisted primarily of the measurement of surface pressure and vortex breakdown location as functions of angle of attack. The effects of several parameters were examined, including motion amplitude, pitching frequency, Reynolds number, and leading edge geometry. The data obtained here was then correlated to data available in the literature on the aerodynamic loads and the surface flow characteristics for wings of similar geometry. Tests were also conducted to examine the effects of wing size and blockage.

Chapters IV through VII present the experimental results of this research. Each of these Chapters is concluded with a summary of the significant trends apparent in the data. These summaries can be referred to for more detailed discussion of the results.

This research was one of the first experimental studies to obtain unsteady surface pressures for a pitching delta wing. This was accomplished for several angle of attack ranges and surface locations (in addition to the parameters listed above). A description and validation of the experimental procedure used to measure the unsteady pressures can be found in Chapter IV.

The unsteady surface pressure data was correlated to the unsteady behavior of the vortex breakdown during an oscillatory pitching motion encompassing both low and high angles of attack (including post-stall angles). Initially during such a motion, at the low angle of attack, the pressure distribution (both chordwise and spanwise) was uniform. As

211

the wing pitched up the surface pressure began to decrease. Minimum pressures occurred at a given surface location near the angle at which breakdown crossed that location (on its way forward). The breakdown then reached the apex, and additional increase in angle of attack resulted in full separation. Full separation here implies the elimination of the leading edge vortex system and the loss of leeward surface flow reattachment (similar to bluff body flow). As full separation occurred, the pressures began increasing. Before the pressure distribution reached an approximately uniform value, the wing began pitching down again, and the vortex system reformed, with breakdown near the apex. Breakdown then moved aft as the wing continued pitching down. As this occurred, the surface pressures began to decrease again, resulting in a partial recovery of the suction pressure. The amount of the suction pressure recovery was greater at upstream chord locations, where the leading edge vortices existed (without the presence of breakdown) for a greater portion of the downward motion, i.e., between the reformation of the vortex system and the collapse of the vortex system as the angle of attack became too low to sustain the leading edge separation.

Unsteady surface pressures were measured for a sinusoidal angle of attack oscillation over several ranges of angle of attack. The pressure data could be divided into two categories, depending on angle of attack range: data for which the unsteady effects were relatively small (quasi-steady behavior), and data for which significant unsteady effects occurred.

It appeared that the formation of vortex breakdown contributed significantly to the large unsteady effects seen in the surface pressure. For a range of motion where breakdown *always* existed, or a range excluding breakdown altogether, the unsteady effects were relatively small. However, for motions where breakdown moved onto and off of the wing, the unsteady effects were large. This was also true for motions which included full scale separation. A similar trend has been noted in the literature.

A consistent difference was seen in the unsteady data due to variations in the reduced pitching frequency. The amount of hysteresis in the unsteady breakdown location increased with increasing reduced frequency. The unsteady surface pressures also showed a consistent difference. The magnitudes of the upstroke pressure peak increased, and the magnitude of the downstroke (or recovery) peak decreased with increasing reduced frequency. This has the effect of widening the hysteresis loop formed by the data. The form of the hysteresis loop was seen to be dependent on the *reduced* frequency and not the dimensional pitching frequency.

No consistent effect due to Reynolds number was detected in the steady breakdown location over the range of 150,000-450,000. However, the steady pressure data did show a consistent effect due to Reynolds number. This occurred between Reynolds numbers of 250,000 and 400,000. The Reynolds number effect was consistent with data available in the literature and was attributed to the transition of the secondary surface flow from laminar to turbulent. The decrease in pressure with increase in Reynolds number occurred for angles of attack below and above the stall angle. Data in the literature suggested that despite the local change in surface pressure, no change in the net loading occurs. However, this was only for angles of attack *below* stall (as determined by the maximum lift coefficient). For post-stall angles a net change in both the surface pressures and the net loading has been documented in the literature. This phenomenon could not be examined using the current pressure data due to the limited number of surface locations at which pressures were measured; net loads could not be accurately inferred.

A consistent difference in breakdown location was measured between the single bevel wing and the double bevel wing; the location for the double bevel wing was downstream of that of the single bevel wing. The change in camber (and thus effective

angle of attack) due to the addition of an upper surface bevel was not considered to be sufficient to account for the magnitude of the change in breakdown location.

In addition to examining the relationship between the unsteady loads and the unsteady vortex system, the effects of model size and blockage were also examined. This was accomplished through the use of three differently sized but geometrically similar delta wing models. The effects of blockage on both the surface pressure and the breakdown location were examined.

Consistent effects due to wing size were measured in the surface pressures. A decrease in wing size resulted in an increase in the surface pressure at the same relative surface location on each wing. This occurred for both steady and unsteady motions. This may be due in part to a greater acceleration of the flow around the larger wings, resulting in larger local flow velocities and thus lower pressures.

It was also found that the large angles of attack (up to 60°) used during this research were affecting the freestream dynamic pressure, particularly for the unsteady case. This change in dynamic pressure was found to be responsible for some of the differences in the surface pressure coefficients (by definition of the pressure coefficient). By nondimensionalizing the surface pressure *without* using the instantaneous freestream condition a significant improvement was found in the agreement of the data (a similar strategy has been used by sources in the liter ure to "correct" for blockage effects).

Although the wing size was seen to change the magnitudes of the surface pressure coefficients, the trends seen in the data were qualitatively the same for each of the three wings. This suggests that, qualitatively, this type of unsteady testing can be successfully accomplished in relatively small wind tunnels such as the one used here.

Various methods of correcting for steady and unsteady blockage were examined for use with the surface pressure data. Correction methods available in the literature were applied with limited success in correlating the pressure data for the three wings. The

corrections applied to the steady pressure data typically resulted in good correlation for angles of attack below 40° and surface locations aft of 0.40c. A correction method was then adapted for use with the unsteady pressure data by replacing the *steady* drag coefficient with the instantaneous *unsteady* drag coefficient (for a similar unsteady maneuver). Differences in the magnitudes of the suction peaks were amplified by using this procedure. However, the agreement for angles of attack where the flowfield was fully separated (typically 50-60°) was significantly improved.

IX   CONSIDERATIONS FOR FUTURE INVESTIGATION

This section contains two different types of recommendations for future investigation. The first involves critical factors to be considered during future research of a similar nature. The second involves tangent areas of interest that should be investigated to help understand the data obtained during the current research and make it more applicable towards the improvement of current airframe design and control.

During the course of the current research, in particular the actual experimental testing, certain factors were found to be of critical importance in obtaining and analyzing the data. It is considered that these factors need to be handled with particular care and thus are listed here to benefit similar investigations that may take place in the future.

The first of these factors is the angle of attack time history. Measurement of the instantaneous angle of attack should be as accurate as possible. A convenient method of displaying the data involves plotting it as a function of the instantaneous angle of attack, and even a small bias in the angle of attack measurements can result in a significant change in the form of the hysteresis loops formed by the data.

The next factor involves the placement of the pressure taps. Large surface pressure gradients can be present on a highly swept wing, and as such even a small error in the location of a pressure tap can substantially alter the form of the pressure distributions. Care must be taken in the placement of the pressure taps.

Third, a knowledge of the response of the freestream conditions to the unsteady model motion is important. It was seen during the current research that the variation of the freestream dynamic pressure due to the model motion could significantly affect the surface pressure coefficients (by definition of the pressure coefficient). It may be desirable to use

216

the time averaged freestream conditions rather than the instantaneous conditions, but a knowledge of the instantaneous conditions is still useful when making comparisons with data in the literature.

The final recommendation of this nature involves the data acquisition technique. When attempting to obtain unsteady time dependent data for several variables it is crucial to be able to relate the time histories of each variable. Simultaneous data sampling would be preferred but is not always practical. Sequential data sampling can be used but it is important to be aware of the precise times at which data is obtained for each variable.

The remainder of this section highlights some areas of potential research that have stemmed from the current research. The first area is an extension of the current research. It involves unsteady pressure measurements for an oscillatory pitching motion, but for difference angle of attack ranges. It was seen in the current research that the *formation* of breakdown was important in determining the extent of the unsteady effects. This could be examined further by measured surface pressures and vortex breakdown trajectories for angle of attack ranges with initial angles of 30-50° (for example, 30-60 or 40-60°).

The next area involves additional measurement of unsteady surface pressures; however, a transient pitching motion should be used. This type of motion more is more typical of an unsteady maneuver performed by an actual airframe. This should include motions involving only a pitch up or a pitch down, as well as motions involving only one cycle of oscillatory motion. This type of test should involve measurement of the unsteady effects during the wing motion as well as the persistence of the unsteady pressure effects upon completion of the maneuver. The characteristics of the decay of the unsteady effects should be examined. This would yield an estimate of the time needed for a complete recovery of the pressure field during an unsteady pitching motion, as opposed to the partial recovery seen in the current data.

The third area involves a more in depth examination of the trailing edge effects. It was seen during the current research that the breakdown motion could develop a lag by having to cross the trailing edge (in either direction). In some cases the breakdown sees the trailing edge as a obstacle, possibly due to the downstream pressure gradient in that region. This study should examine if this effect is related to the amount of blockage of a given wing. A decrease in blockage may decrease the pressure gradient and decrease the effect of the trailing edge on the location of vortex breakdown. This in turn may alter the unsteady pressure effects.

Another useful research topic involves the effect of the transition of the secondary separation on the vortex behavior and the surface pressures. Transition from laminar to turbulent separation was seen to have an effect on the steady surface pressures in the current research. This effect should be examined in more detail, including the effect of surface roughness or irregularities such as pressure orifices on the transition characteristics. The effect, if any, of transition on the breakdown location should also be examined.

Research which utilized wing planforms other than simple delta wings would also be helpful. Unsteady tests similar to those conducted in the current research could be applied to models such as wing/fuselage or wing/strake combinations. Generic swept-wing aircraft models could also be employed.

In addition, a study on the differences between data for a half-span wing and a full span-wing would be helpful. This type of study would serve two purposes. First, if it was found that half-span data was comparable to full span data (for specific angles of attack of sweep angles), then half-span models could be used, thus allowing for larger models and better spatial resolution and larger loads. Second, knowing the differences between data for half-span wings and full span wings would allow for more and better comparisons with data available in the literature.

X   BIBLIOGRAPHY

Agrawal, S., Barnett, R. M., and Robinson, B. A., "Investigation of Vortex Breakdown on a Delta Wing Using Euler and Navier-Stokes Equations," AGARD 67th Fluid Dynamic Panel Symposium, Oct. 1990.

Arena, Andrew A. Jr., "An Experimental and Computational Investigation of Slender Wings Undergoing Wing Rock", *Ph. D. Dissertation, University of Notre Dame*, April, 1992.

Ashley, H., Jarrah, M. A. M., Katz, J., and Vaneck, T., Unsteady Aerodynamic Loading of Delta Wings for Low and High Angles of Attack," Jun. 1990.

Atta, R., and Rockwell, D., "Hysteresis of Vortex Development and Breakdown on an Oscillating Delta Wing," *AIAA Journal*, Vol. 25, Nov. 1987, pp. 1512-1513.

Atta, Rasheed, and Rockwell, Donald, "Leading-Edge Vortices Due to Low Reynolds Number Flow Past a Pitching Delta Wing," *AIAA Journal*, Vol. 28, Jun. 1990, pp. 995-1004.

Bragg, M.B., and Soltani, M.R., "An Experimental Study of the Effect of Asymmetrical Vortex Bursting on a Pitching Delta Wing," AIAA Paper 88-4334, Aug. 1988.

Brandon, Jay M., and Shah, Gautam H., "Effect of Large Amplitude Pitching Motions on the Unsteady Aerodynamic Characteristics of Flat-Plate Wings," AIAA Paper 88-4331, Aug. 1988.

Brandon, Jay M., and Shah, Gautam H., "Unsteady Aerodynamic Characteristics of a Fighter Model Undergoing Large-Amplitude Pitching Motions at High Angles of Attack," AIAA Paper 90-0309, Jan. 1990.

Brendel, Michael, and Huber, Arthur F. II, "An Experimental Investigation of Flow Quality in an Indraft Subsonic Wind Tunnel Using a Single Hot Wire Anemometer," University of Notre Dame Department of Aerospace and Mechanical Engineering Internal Report, Nov. 1984.

Brown, D., Lee, B. H. K., and Tang, F. C., "Some Characteristics and Effects of the F/A-18 Lex Vortices."

Carcaillet, R., Manie, F., Pagan, D., and Solignac, J. L., "Leading Edge Vortex Flow over a 75 Degree-Swept Delta Wing - Experimental and Computational Results," ICAS, Sept. 1986.

Cunningham, Atlee M. Jr., "A Critique of the Experimental Aerodynamic Data Base for an Oscillating Straked Wing at High Angles," Fourth Symposium on Numerical and Physical Aspects of Aerodynamic Flows, Jan. 1989.

Cunningham, Atlee M. Jr., and Bushlow, Todd, "Steady and Unsteady Force Testing of Fighter Models in a Water Tunnel," AIAA Paper 90-2815, Aug, 1990.

Cunningham, A. M. Jr., and den Boer, R.G., "Low-Speed Unsteady Aerodynamics of a Pitching Straked Wing at High Incidence - Part II: Harmonic Analysis," *AIAA Journal of Aircraft*, Vol. 27, Jan. 1990, pp. 31-41.

Cunningham, Atlee M. Jr., and den Boer, Ruud G., "Steady and Unsteady Aerodynamics of a Pitching Straked Wing Model at High Angles of Attack," AGARD 67th Fluid Dynamic Panel Symposium, Oct. 1990.

den Boer, R. G., and Cunningham, A. M. Jr., "Low-Speed Unsteady Aerodynamics of a Pitching Straked Wing at High Incidence - Part I: Test Program," *AIAA Journal of Aircraft*, Vol. 27, Jan. 1990, pp.23-30.

Earnshaw, P. B., "An Experimental Investigation of the Structure of a Leading-Edge Vortex," *Aeronautical Research Council Reports and Memoranda*, No. 3281, Mar., 1961.

Earnshaw, P. B., "Measurements of the Effects of Thickness on Vortex Breakdown Position on a Series of Sharp-Edged Delta Wings," *Aeronautical Research Council Current Papers*, No. 1018, Feb. 1968.

Earnshaw, P. B., and Lawford, J. A., "Low-Speed Wind-Tunnel Experiments on a Series of Sharp-Edged Delta Wings," *Aeronautical Research Council Reports and Memoranda*, No. 3424, Mar. 1964.

Ekaterinaris, J. A., and Schiff, Lewis B., "Vortical Flows over Delta Wings and Numerical Prediction of Vortex Breakdown," AIAA Paper-90-0102, Jan. 1990.

Ekaterinaris, J. A., and Schiff, Lewis B., "Numerical Simulation of the Effects of Variation of Angle of Attack and Sweep Angle on Vortex Breakdown over a Delta Wing," AIAA Paper 90-3000, Aug. 1990.

Elle, B. J., "An Investigation at Low Speed of the Flow near the Apex of Thin Delta Wings with Sharp Leading Edges," *Aeronautical Research Council Reports and Memoranda*, No. 3176, Jan. 1958.

Elsenaar, A. and Hoeijmakers, H. W. M., "An Experimental Study of the Flow over a Sharp-Edged Delta Wing at Subsonic and Transonic Speeds," AGARD-CP-494, Oct. 1990.

Er-El, J., "Effect of Wing/Canard Interference on the Loading of a Delta Wing," *AIAA Journal of Aircraft*, Vol. 25, Jan. 1988, pp. 18-24.

Erickson, Gary E., Schreiner, John A., and Rogers, Lawrence W., "Canard-Wing Vortex Interactions at Subsonic Through Supersonic Speeds," AIAA Paper 90-2814-CP, Aug. 1990.

Erickson, Gary E., "Vortex Flow Correlation," Wright Air Force Base Technical Report AFWAL-TR-80-3143, Jan. 1981.

Ericsson, L., "Another Look at High-Alpha Support Interference," AIAA Paper 90-0188, Jan. 1990.

Ericsson, L. E., "Unsteady Flow Separation on Slender Bodies at High Angles of Attack," AIAA Paper 90-2835-CP, Aug. 1990.

Gad-el-Hak, M. and Ho., C.M., "The Pitching Delta Wing," *AIAA Journal*, Vol. 23, Nov. 1985, pp. 1660-1665.

Gibbs-Smith, Charles H., *Aviation: An Historical Survey from its Origins to the end of World War II*, Her Majesty's Stationery Office, London, 1970.

Gili, P. A., Pastrone, D. M., Quagliotti, F. B., and Barbantini, E., "Blockage Corrections at High Angles of Attack in a Wind Tunnel," *Journal of Aircraft*, Vol. 27, May 1990, pp. 413-417.

Greenwood, John T., editor, *Milestones of Aviation*, Hugh Lauter Levin Associates, Inc., New York, 1989.

Hanff, E. S., and Ericsson, L. E., "Multiple Roll Attractors of a Delta Wing at High Incidence," AGARD Symposium on Vortex Flow Aerodynamics, Oct. 1990.

Hanff, E. S., "Non-Linear Representation of Aerodynamics of Wing Rock of Slender Delta Wings," AIAA Paper 85-1831, Aug. 1985.

Hawk, J., Barnett, R., and O'Neil, P., "Investigation of High Angle of Attack Vortical Flow over Delta Wings," AIAA Paper 90-0101, Jan. 1990.

Heiman, Grover, *Jet Pioneers*, Duell, Sloan, and Pearce, New York, 1963.

Hemsch, M. J., "Similarity for High Angle-of-Attack Subsonic/Transonic Slender-Body Aerodynamics," AIAA Paper 88-0216, Jan. 1988.

Hemsch, Michael J., "Engineering Analysis of Slender-Body Aerodynamics Using Sychev Similarity Parameters," *AIAA Journal of Aircraft*, Vol. 25, Jul. 1988, pp. 625-631.

Hemsch, Michael J., "Similarity for High-Angle-of-Attack Subsonic/Transonic Slender-Body Aerodynamics," *AIAA Journal of Aircraft*, Vol. 26, Jan. 1989, pp. 56-66.

Hemsch, Michael J., and Luckring, James, M., "Connection Between Leading-Edge Sweep, Vortex Lift, and Vortex Strength for Delta Wings," *AIAA Journal of Aircraft*, Vol. 27, May 1990, pp. 473-474.

Hummel, D., "On the Vortex Formation over a Slender Wing at Large Angles of Incidence," AGARD-CP-247, 1978.

Hummel, D., and Srinivasan, P. S., "Vortex Breakdown Effects on the Low Speed Aerodynamic Characteristics of Slender Delta Wings in Symmetrical Flow," *Journal of the Royal Aeronautical Society*, Vol. 71, April 1967, pp. 319-322.

Jarrah, Mohammad-Ameen M., "Unsteady Aerodynamics of Delta Wings Performing Maneuvers to High Angle of Attack," *Ph.D. Dissertation, Stanford University*, Dec. 1988.

Jarrah, Mohammad-Ameen M., "Low-Speed Wind-Tunnel Investigation of Flow About Delta Wings, Oscillating in Pitch to Very High Angle of Attack," AIAA Paper 89-0295, Jan. 1989.

Jarrah, M. A. M., "Visualization of the Flow about a Delta Wing Maneuvering in Pitch to Very High Angle of Attack," *International Symposium on Nonsteady Fluid Dynamics*, Jun. 1990.

Jones, Robert T., "Wing Plan Forms for High Speed Flight," *National Advisory Committee for Aeronautics (NACA) Technical Note*, No. 1033, Mar. 1946.

Kegelman, J. T., and Roos, F. W., "Effects of Leading-Edge Shape and Vortex Burst on the Flowfield of a 70-Degree-Sweep Delta Wing," AIAA Paper-89-0086, Jan. 1989.

Kegelman, J. T., and Roos, F. W., "The Flowfields of Bursting Vortices Over Moderately Swept Delta Wings," AIAA Paper 90-0599, Jan. 1990.

Kline, S. J., "The Purposes of Uncertainty Analysis," *ASME Journal of Fluids Engineering*, Vol. 107, Jun. 1985, pp. 153-160.

Krist, Sherrie L., "An Embedded Grid Formulation Applied to a Delta Wing," AIAA Paper 90-0429, Jan. 1990.

Laidlaw, W. R., "Theoretical and Experimental Pressure Distributions on Low Aspect Ratio Wings Oscillating in an Incompressible Flow," MIT Aeroelastic and Structures Research Laboratory Technical Report 51-2, Sept. 1954.

Lambourne, N. C., and Bryer, D. W., "Some Measurements in the Vortex Flow Generated by a Sharp Leading Edge having 65° Sweep," *Aeronautical Research Council Current Papers*, No. 477, July 1959.

Lambourne, N. C., and Bryer, D. W., "The Bursting of Leading-Edge Vortices - Some Observations and Discussion of the Phenomenon," *Aeronautical Research Council Reports and Memoranda*, No. 3282, Apr. 1961.

Lambourne, N. C., Bryer, D. W., and Maybrey, J. F. M., "The Behavior of the Leading-Edge Vortices over a Delta Wing Following a Sudden Change in Incidence," *Aeronautical Research Council Reports and Memoranda*, No. 3645, Mar. 1969.

Lee, G. H., "Note On the Flow Around Delta Wings with Sharp Leading Edges," *Aeronautical Research Council Reports and Memoranda*, No. 3070, Sept. 1955.

Leibovich, Sidney, "Vortex Stability and Breakdown: Survey and Extension," *AIAA Journal*, Vol. 22, Sept. 1984, pp. 1192-1206.

LeMay, S.P., "Leading Edge Vortex Dynamics on a Pitching Delta Wing," *Master's Thesis, University of Notre Dame*, Apr. 1988.

LeMay, S.P., Batill, S.M., and Nelson, R.C., "Leading Edge Vortex Dynamics on a Pitching Delta Wing", AIAA Paper 88-2559-CP, Jun. 1988.

LeMay, S.P., Batill, S.M., and Nelson, R.C., "Vortex Dynamics on a Pitching Delta Wing," *AIAA Journal of Aircraft*, Vol. 27, Feb. 1990, pp. 131-138.

Liccini, Luke L., "Effects of 45° Sweepback on the High-Speed Characteristics of a Wing Having a Modified NACA 16-012 Airfoil Section," *National Advisory Committee for Aeronautics (NACA) Research Memoranda*, No. L6K18a, July 1947.

Lippisch, Alexander, *The Delta Wing - History and Development*, Iowa State University Press, Ames, Iowa, 1981.

Lowson, M. V., "The Separated Flows on Slender Wings in Unsteady Motion," *Aeronautical Research Council Reports and Memoranda*, No. 3448, Sept. 1963.

Lowson, M. V., "Some Experiments with Vortex Breakdown," *Journal of the Royal Aeronautical Society*, Vol. 68, 1964, pp. 343-346.

Magness, C., Robinson, O., and Rockwell, D., "Control of Leading-Edge Vortices on a Delta Wing," AIAA Paper 89-0999, Mar. 1989.

Manor, David, Miller, Leonard, and Wentz, William H. Jr., "Static and Dynamic Water Tunnel Tests of Slender Wings and Wing-Body Configurations at Extreme Angles of Attack," AIAA Paper 90-3021, Aug. 1990.

Maskell, E. C., "A Theory of the Blockage Effects on Bluff Bodies and Stalled Wings in a Closed Wind Tunnel," *Aeronautical Research Council Reports and Memoranda*, No. 3400, Nov. 1963.

McCune, James E., "Unsteady Wing Theory - The Kármán/Sears Legacy," AIAA Paper 88-3540, Jul. 1988.

McKernan, John F., "An Investigation of the Breakdown of the Leading Edge Vortices On a Delta Wing at High Angles of Attack," *Master's Thesis, University of Notre Dame*, Jan. 1983.

Meyers, James F., and Hepner, Timothy E., "Measurement of Leading Edge Vortices from a Delta Wing Using a Three Component Laser Velocimeter," AIAA-88-2024, May 1988.

Morris, Steven L., Ward, Donald T., Malcolm, Gerald N., and Ward, Donald T., "Nonintrusive Measurements of Vortex Flows on Delta Wings in a Water Tunnel," AIAA Paper 88-2595-CP, Jun. 1988.

Mueller, T. J., "Smoke Visualization of Subsonic and Supersonic Flows (The Legacy of F. N. M. Brown)," AFOSR Contractor Report No. TN-3412-1, June 1978.

Nakamura, Y., "Vortex Breakdown Simulation," AIAA Paper 85-1581, July, 1985.

Nelson, R. C., Arena, A. S. Jr., and Thompson, S. A., "Aerodynamic and Flowfield Hysteresis of Slender Wing Aircraft Undergoing Large-Amplitude Motions," 68th AGARD Fluid Dynamics Panel Specialists Meeting on "Manoeuvering Aerodynamics," AGARD-CP-497, May, 1991.

Nelson, R. C., and Visser, K. D., "Breaking Down the Delta Wing Vortex - The Role of Vorticity in the Breakdown Process," AGARD-CP-494, Oct. 1990.

Ng, T. Terry, and Malcolm, Gerald N., "Effect of Leading Edge Roundness on a Delta Wing in Wing-Rock Motion," AIAA Paper 90-3080-CP, Aug. 1990.

Ng, T. Terry, "On Leading Edge Vortex and its Control," Extended Abstract submitted for AIAA Atmospheric Flight Mechanics Conference, Aug. 1989.

O'Neil, P. J., Roos, F. W., Kegelman, J. T., Barnett, R. M., and Hawk, J. D., "Investigation of Flow Characteristics of a Developed Vortex," Naval Air Development Center Final Report, May 1989.

Parker, A. G., "Aerodynamic Characteristics of Slender Wings with Sharp Leading Edges - A Review," *AIAA Journal of Aircraft*, Vol. 13, Mar. 1976, pp. 161-168.

Payne, Francis M., "The Structure of Leading Edge Vortex Flows Including Vortex Breakdown," *Ph.D. Dissertation, University of Notre Dame*, May, 1987.

Payne, Francis M., Ng, T. Terry, and Nelson, R. C., "Visualization of Leading Edge Vortices on a Series of Flat Plate Delta Wings," NASA Contractor Report 4320, Apr. 1991.

Pass, C. Q., "A Wake Blockage Correction Method for Small Subsonic Wind Tunnels," AIAA Paper 97-0294, Jan. 1987.

Peckham, D. H., "Low-Speed Wind-Tunnel Tests on a Series of Uncambered Slender Pointed Wings with Sharp Edges," *Aeronautical Research Council Reports and Memoranda*, No. 3186, Dec. 1958.

Peckham, D. H., and Atkinson, S. A., "Preliminary Results of Low Speed Wind Tunnel Tests on a Gothic Wing of Aspect Ratio 1.0," *Aeronautical Research Council Current Papers*, No. 508, Apr. 1957.

Pisano, D. A. and Lewis, C. S., eds., *Air and Space History - An Annotated Bibliography*, Garland Publishing, Inc., New York, 1988.

Polhamus, E. C., "Predictions of Vortex Lift Characteristics by a Leading Edge Suction Analogy," *AIAA Journal of Aircraft*, Vol. 8, April 1971, pp. 193-199.

Pope, Alan, and Harper, J. J., *Low-Speed Wind Tunnel Testing*, John Wiley and Sons, New York, 1966.

Portnoy, H., "Unsteady Motion of Vortex-Breakdown Positions on Delta Wing," ????

Rae, William H. Jr., and Pope, Alan, *Low-Speed Wind Tunnel Testing, 2nd Edition*, John Wiley and Sons, New York, 1984.

Randall, D. G., "Oscillating Slender Wings with Leading-Edge Separation," *The Aeronautical Quarterly*, Vol. 17, Nov. 1966, pp. 311-331.

Rediniotis, O. K., Hoang, N. T., and Telionis, D. P., "Multi-Sensor Investigation of Delta Wing High-Alpha Aerodynamics," AIAA-91, Jan. 1991.

Reynolds, G.A., and Abtahi, A.A., "Instabilities in Leading-Edge Vortex Development," AIAA Paper 87-2424, Aug. 1987.

Robinson, A., "The Wave Drag of Diamond-Shaped Aerofoils at Zero Incidence," *Aeronautical Research Council Reports and Memoranda*, No. 2394, May 1946.

Robinson, A., "Aerofoil Theory of a Flat Delta Wing at Supersonic Speeds," *Aeronautical Research Council Reports and Memoranda*, No. 2548, Sept. 1946.

Robinson, A., and Hunter-Tod, J. H, "Bound and Trailing Vortices in the Linearised Theory of Supersonic Flow, and the Downwash in the Wake of a Delta Wing," *Aeronautical Research Council Reports and Memoranda*, No. 2409, Oct. 1947.

Robinson, A., and Hunter-Tod, J. H., "The Aerodynamic Derivatives with respect to Sideslip for a Delta Wing with Small Dihedral at Zero Incidence at Supersonic Speeds," *Aeronautical Research Council Reports and Memoranda*, No. 2410, Dec. 1947.

Rockwell, D., Atta. R., Kuo, C. H., Hefele, C., Magness, C., and Utsch, T., "On Unsteady Flow Structure from Swept Edges Subjected to Controlled Motion."

Roos, F. W., and Kegelman, J. T., "An Experimental Investigation of Sweep-Angle Influence on Delta-Wing Flows," AIAA Paper 90-0383, Jan. 1990.

Roper, Gwendolen M., "The Flat Plate Delta Wing at Incidence, at Supersonic Speeds, when the Leading Edges Lie Outside the Mach Cone of the Vertex," *The Quarterly Journal of Mechanics and Applied Mathematics*, Vol. 1, 1948, pp. 327-343.

Sawyer, R., and Sullivan, J., "Lift Development on Delta Wings Undergoing Constant Acceleration From Rest," AIAA Paper 90-0310, Jan. 1990.

Schiff, Lewis B., and Degani, David, "Numerical Simulation of Vortex Unsteadiness on Slender Bodies of Revolution at Large Incidence," AIAA Paper 89-0195, Jan. 1989.

Scott, Matthew T., and McCune, James, E., "Nonlinear Aerodynamics of Two-Dimensional Aerofoils in Severe Maneuver," AIAA Paper 88-0129, Jan. 1988.

Stewart, H. J., "The Lift of a Delta Wing at Supersonic Speeds," *Quarterly of Applied Mathematics*, Vol. 4, Oct. 1946, pp. 246-254.

Thompson, D. H., "A Visualization Study of the Vortex Flow Around Double-Delta Wings," Australian Defense Science and Technology Organisation, Report No. ARL-AERO-R-165, Aug. 1985.

Thompson, S. A., Arena, A. S. Jr, Nelson, R. C., and Batill, S. M., "Dynamic Surface Pressure Measurements on a Delta Wing Constrained to a Pitching or Rolling Motion," NASA High Angle-of-Attack Technology Conference, Oct. 1990.

Thompson, S. A., Batill, S. M., and Nelson R. C., "The Separated Flow Field on a Slender Delta Wing Undergoing Transient Pitching Motions," AIAA Paper 89-0194, Jan. 1989.

Thompson, S. A., Batill, S. M., and Nelson R. C., "Surface Pressure Distributions on a Delta Wing Undergoing Large Amplitude Pitching Oscillations," *Master's Thesis, University of Notre Dame*, July 1989.

Thompson, S. A., Batill, S. M., and Nelson R. C., "Unsteady Surface Pressure Distributions on a Delta Wing Undergoing Large Amplitude Pitching Motions," AIAA Paper 90-0311, Jan. 1990.

Thompson, S. A., Batill, S. M., and Nelson R. C., "Delta Wing Surface Pressures for High Angle of Attack Maneuvers," AIAA Paper 90-2813, Aug. 1990.

Thompson, S. A., Batill, S. M., and Nelson R. C., "The Separated Flow Field on a Slender Wing Undergoing Transient Pitching Motions," *AIAA Journal of Aircraft*, Vol. 28, Aug. 1991, pp. 489-495.

Thompson, S. A., and Nelson R. C., *University of Notre Dame Department of Mechanical and Aerospace Engineering Data Report*, No. 2420-23444, Apr. 1992.

Tucker, Warren A., "Characteristics of Thin Triangular Wings with Constant-Chord Full-Span Control Surfaces at Supersonic Speeds," *National Advisory Committee for Aeronautics (NACA) Technical Note*, No. 1601, July 1948.

Verhaagen, Nick G., and Naarding, Steven H. J., "Experimental and Numerical Investigation of Vortex Flow over a Sideslipping Delta Wing," *AIAA Journal of Aircraft*, Vol. 26, Nov. 1989, pp. 971-978.

Verhaagen, N., and van Ransbeeck, P., "Experimental and Numerical Investigation of the Flow in the Core of a Leading Edge Vortex," AIAA Paper 90-0384, Jan. 1990.

Visser, K. D., Ng, T., and Nelson, R.C., "Method of Cold Smoke Generation for Vortex Core Tagging," *AIAA Journal of Aircraft*, Vol. 25, Nov. 1988, pp.1069-1071.

Visser, K. D., "An Experimental Analysis of Critical Factors Involved in the Breakdown Process of Leading Edge Flows," *Ph.D. Dissertation, University of Notre Dame*, May, 1991.

Weinberg, Zvi, "Tunnel Wall Effect on Vortex Breakdown Location over Delta Wings," submitted to AIAA Journal of Aircraft, 1991.

Wentz, William H. Jr., and McMahon, Michael C., "Further Experimental Investigations of Delta and Double-Delta Wing Flow Fields at Low Speeds," NASA Contractor Report, No. CR-714, Feb. 1967.

Wilson, Herbert A. Jr., and Lovell, J. Calvin, "Full-Scale Investigation of the Maximum Lift and Flow Characteristics of an Airplane Having Approximately Triangular Plan Form," *National Advisory Committee for Aeronautics (NACA) Research Memoranda*, No. L6K20, Feb. 1947.

Wolffelt, K.W., "Investigation of the Movement of Vortex Burst Position with Dynamically Changing Angle of Attack for a Schematic Delta Wing in a Water Tunnel with Correlation to Similar Studies in Wind Tunnel," AGARD Paper CPP-413, Oct. 1986.

Wonnacott, Thomas H., and Wonnacott, Ronald J., *Introductory Statistics for Business and Economics, 3rd Edition*, John Wiley and Sons, New York, 1984.

Woodgate, L., "Measurements of the Pitching-Moment Derivatives on a Sharp Edged Delta Wing in Incompressible Flow," *Aeronautic Research Council Reports and Memoranda*, No. 3379, Oct. 1963.